frontiers | Research Topics

Hydrological connectivity and sustainable watershed management in a changing environment

Edited by
Yang Yu, Mariano Moreno De Las Heras, Hu Liu,
Peng Shi, Omer Yetemen and Patricia Saco

Published in
Frontiers in Environmental Science

FRONTIERS EBOOK COPYRIGHT STATEMENT

The copyright in the text of individual articles in this ebook is the property of their respective authors or their respective institutions or funders. The copyright in graphics and images within each article may be subject to copyright of other parties. In both cases this is subject to a license granted to Frontiers.

The compilation of articles constituting this ebook is the property of Frontiers.

Each article within this ebook, and the ebook itself, are published under the most recent version of the Creative Commons CC-BY licence. The version current at the date of publication of this ebook is CC-BY 4.0. If the CC-BY licence is updated, the licence granted by Frontiers is automatically updated to the new version.

When exercising any right under the CC-BY licence, Frontiers must be attributed as the original publisher of the article or ebook, as applicable.

Authors have the responsibility of ensuring that any graphics or other materials which are the property of others may be included in the CC-BY licence, but this should be checked before relying on the CC-BY licence to reproduce those materials. Any copyright notices relating to those materials must be complied with.

Copyright and source acknowledgement notices may not be removed and must be displayed in any copy, derivative work or partial copy which includes the elements in question.

All copyright, and all rights therein, are protected by national and international copyright laws. The above represents a summary only. For further information please read Frontiers' Conditions for Website Use and Copyright Statement, and the applicable CC-BY licence.

ISSN 1664-8714
ISBN 978-2-8325-2877-8
DOI 10.3389/978-2-8325-2877-8

About Frontiers

Frontiers is more than just an open access publisher of scholarly articles: it is a pioneering approach to the world of academia, radically improving the way scholarly research is managed. The grand vision of Frontiers is a world where all people have an equal opportunity to seek, share and generate knowledge. Frontiers provides immediate and permanent online open access to all its publications, but this alone is not enough to realize our grand goals.

Frontiers journal series

The Frontiers journal series is a multi-tier and interdisciplinary set of open-access, online journals, promising a paradigm shift from the current review, selection and dissemination processes in academic publishing. All Frontiers journals are driven by researchers for researchers; therefore, they constitute a service to the scholarly community. At the same time, the *Frontiers journal series* operates on a revolutionary invention, the tiered publishing system, initially addressing specific communities of scholars, and gradually climbing up to broader public understanding, thus serving the interests of the lay society, too.

Dedication to quality

Each Frontiers article is a landmark of the highest quality, thanks to genuinely collaborative interactions between authors and review editors, who include some of the world's best academicians. Research must be certified by peers before entering a stream of knowledge that may eventually reach the public - and shape society; therefore, Frontiers only applies the most rigorous and unbiased reviews. Frontiers revolutionizes research publishing by freely delivering the most outstanding research, evaluated with no bias from both the academic and social point of view. By applying the most advanced information technologies, Frontiers is catapulting scholarly publishing into a new generation.

What are Frontiers Research Topics?

Frontiers Research Topics are very popular trademarks of the *Frontiers journals series*: they are collections of at least ten articles, all centered on a particular subject. With their unique mix of varied contributions from Original Research to Review Articles, Frontiers Research Topics unify the most influential researchers, the latest key findings and historical advances in a hot research area.

Find out more on how to host your own Frontiers Research Topic or contribute to one as an author by contacting the Frontiers editorial office: frontiersin.org/about/contact

Hydrological connectivity and sustainable watershed management in a changing environment

Topic editors
Yang Yu — Beijing Forestry University, China
Mariano Moreno De Las Heras — University of Barcelona, Spain
Hu Liu — Northwest Institute of Eco-Environment and Resources, Chinese Academy of Sciences (CAS), China
Peng Shi — Xi’an University of Technology, China
Omer Yetemen — Istanbul Technical University, Türkiye
Patricia Saco — The University of Newcastle, Australia

Citation
Yu, Y., Moreno De Las Heras, M., Liu, H., Shi, P., Yetemen, O., Saco, P., eds. (2023). *Hydrological connectivity and sustainable watershed management in a changing environment*. Lausanne: Frontiers Media SA. doi: 10.3389/978-2-8325-2877-8

Table of contents

frontiers | Frontiers in Environmental Science

TYPE Editorial
PUBLISHED 16 June 2023
DOI 10.3389/fenvs.2023.1228835

Check for updates

OPEN ACCESS

EDITED AND REVIEWED BY
Angela Helen Arthington,
Griffith University, Australia

*CORRESPONDENCE
Yang Yu,
✉ theodoreyy@gmail.com

RECEIVED 25 May 2023
ACCEPTED 09 June 2023
PUBLISHED 16 June 2023

CITATION
Yu Y, Moreno-De-Las-Heras M, Liu H, Shi P, Yetemen O and Saco P (2023), Editorial: Hydrological connectivity and sustainable watershed management in a changing environment.
Front. Environ. Sci. 11:1228835.
doi: 10.3389/fenvs.2023.1228835

Editorial: Hydrological connectivity and sustainable watershed management in a changing environment

Yang Yu[1,2]*, Mariano Moreno-De-Las-Heras[3], Hu Liu[4], Peng Shi[5], Omer Yetemen[6] and Patricia Saco[7]

[1]School of Soil and Water Conservation, Beijing Forestry University, Beijing, China, [2]Jixian National Forest Ecosystem Research Network Station, CNERN, Beijing, China, [3]Mediterranean Environmental Research Group (GRAM), Department of Geography, University of Barcelona, Barcelona, Spain, [4]Northwest Institute of Eco-Environment and Resources, Chinese Academy of Sciences, Lanzhou, China, [5]State Key Laboratory of Eco-Hydraulics in Northwest Arid Region of China, Xi'an University of Technology, Xi'an, China, [6]Eurasia Institute of Earth Sciences, Istanbul Technical University, Istanbul, Türkiye, [7]Civil, Surveying and Environmental Engineering and Centre for Water Security and Environmental Sustainability, The University of Newcastle, Callaghan, NSW, Australia

KEYWORDS

hydrological connectivity, soil and water conservation, hydrological modeling, watershed management, climate change

Editorial on the Research Topic
Hydrological connectivity and sustainable watershed management in a changing environment

Increasing environmental impacts caused by climate change and human disturbances are progressively leading to the degradation of vast areas worldwide, also producing changes in land use dynamics and ecological services. Land and water management are especially critical as the use of upstream watersheds can drastically affect a large number of people living in downstream watersheds, as well as the ecosystem services of the land and waterways on which they depend. Integrated watershed management, which stresses both the importance of landscape processes, participatory planning, and the institutional and technical constraints and opportunities, is therefore necessary.

In recent years, research on multi-scale hydrological connectivity has grown in popularity and has been recognized for its potential to provide an integrated approach to the study of complex land-water systems. As a method to develop a more holistic approach to watershed assessment and management, the concept of hydrological connectivity is often put at the forefront. Hydrological connectivity can be seen as the patterns and strength of the water-mediated linkages between discrete units of the landscape, and as such, it facilitates our knowledge and understanding of the mechanisms driving runoff initiation, cessation, and the flow regimes of receiving waterways and wetlands. Much of the interest attracted by hydrological connectivity is attributed to its potential to enhance our ability to gain insights into multiple areas of expertise, including process dynamics, numerical model building, conceptualization on the effects of human interventions in our landscape, and the development of simplified watershed management tools.

Water-limited ecosystems are undergoing drastic changes in vegetation cover and plant community composition in response to shifts in climatic conditions and anthropogenic activities on land, therefore, it is necessary to establish close connections between research in the physical and the ecological sciences in order to provide a process-based understanding of the interactions existing between the hydrosphere and the biosphere. At the watershed scale, efficient management requires us to protect vegetation and soil resources and reduce the vulnerability of landscapes to soil erosion. Consequently, raising awareness of issues, causes, consequences, and preventive measures of hydrological processes, and of their impacts on water-limited ecosystems at the watershed scale, is crucial for stakeholders and policymakers around the world.

This Research Topic was proposed with the purpose of collecting the recent methodological developments and studies to detect the influences of anthropogenic activities and climate changes on sustainable watershed management for different regions. This Research Topic of papers gathers novel contributions that explore different research approaches in the field of watershed ecosystem protection and restoration, and new methods/models used in the sustainable watershed management. A total of twelve manuscripts were collected, including studies from China and South America. Different approaches to watershed management research are presented, using new methods, models and tools in the context of both natural and anthropogenic disturbances, and climate change.

In the area of field-based research and *in situ* landscape monitoring, Zhang et al. selected a desert section along the eastern shore of Qinghai Lake as a study area. Plant communities, soil physical and chemical properties, and differences in soil moisture in diverse sand-fixating communities were carefully analyzed. Overall, they explored differences and variations among plant, soil, and water availability, providing scientific support to improve sand-fixation effectiveness by introducing plant species. Further, Li et al. explored the effect of the Porous Fiber Material (PFM, rock wool) on soil erosion and crop growth of winter wheat, based on rainfall simulations and the use of the Entropy-Critic comprehensive evaluation method. The study illustrates the comprehensive application effect of PFM in agricultural production, pollution control and urban landscape, and provides an important basis for promoting the stability of farmland ecosystem. Zhang et al. studied the South-to-North Water Diversion Middle Route Project, a significant infrastructure alleviating water scarcity but suffering from non-traditional sediment sources in Northern China. The characteristics of the sediment and the siltation period were surveyed. Siltation mainly occurs from March to October, while almost no siltation occurs in winter. The main source of siltation in the middle route project is not from traditional sediment sources, but is due to the remnants of the algae that proliferate in large numbers when temperature is suitable, attaching to the sediment particles and gradually growing downstream with the flow.

On a watershed-scale study of eco-hydrological processes using hydrological modeling, Bai et al. conducted a comparative analysis in two adjacent catchments in Northwestern China. The influences of precipitation and land use change on streamflow were studied for the period 1956–2019. The results of this work shed light on the quantitative understanding of streamflow changes in small catchments, offering a scientific basis for sustainable water management in other inland river basins. Yu et al. determined appropriate thresholds of ecological runoff in the middle reaches of the Bailong River (northwest China) under the influence of human activities. Using data from long-term hydrological stations, seven suitable hydrological methods were applied to analyze ecological discharge in the middle reaches of the river. The runoff satisfaction degree was studied, and monthly ecological flows and thresholds for the river were determined in the study area. These results provide a useful reference for ecological restoration and ecosystem management in the middle reaches of the Bailong River Basin and other similar areas. Ju et al. proposed a coupled soil-moisture and heat-transfer model in terms of the physical processes of water and heat movement in frozen soil. Measured data on soil temperature and frost/thaw depth at 19 stations in and around the Three-River Source Region of China were used for model calibration and validation. The results showed that this frozen-soil model can accurately capture freezing-thawing processes acting in this region. The relationship between model parameters, climate conditions and vegetation factors was identified using both observation and remote sensing data. The proposed method can be applied to other cold regions with little observation data to obtain parameters and simulate soil freezing-thawing processes. Zhou et al. developed an improved module of the WetSpa model, which they used for the simulation of runoff at different time scales for the Hanjiang River Basin. Reservoir inflow data correction and water storage/outflow calculation without measured data were considered in the improved model. Their results showed that the improved WetSpa model has good applicability in the Hanjiang River Basin, thus suggesting that predictions of the future runoff variations using this model will be more accurate. Hou et al. analyzed the evolution of both historical and future water yield coefficients in the Yiluo River Basin. Water yield was simulated for 2000–2020 and 2030–2050 under four Shared Socioeconomic Pathways (including SSP126, SSP245, SSP370 and SSP585). A geographical detector model was used to study the impacts of climate, land use and terrain factors on the water yield coefficient. Land use showed the strongest explanatory capacity to determine water yield coefficient for 2000–2020, and will increase its influence for 2030–2050. This research provides scientific support for adopting precise watershed management of water and land resources.

In terms of regional-scale hydrological and geomorphological processes and water resources research, Rojas et al. examined the hydrogeomorphology of the Peruvian tropical wetland of Pacaya Samiria in Western Amazonia, and its role in the distribution of aquatic habitats. The hydrogeomorphological connectivity that bounds the Pacaya Samiria National Reserve is characterized by ancient to modern processes. The effect of geomorphology on the spatial distribution of fishing zones was assessed. This methodological approach, based on understanding wetland connectivity, hydrogeomorphological behavior and their influence on commercial fisheries, was developed and shown to support decision-making in conservation actions for Amazonian environments. Xu et al. proposed a scenario-based framework for a PLES (production, living, and ecological spaces) water resources assessment, analyzing the temporal and spatial changes of land and water resources on the North Slope of Tianshan Mountain, China. They indicate that the vulnerability of regional ecosystems should be taken into account in the future socio-economic development of the North Slope of Tianshan Mountain, where production should be controlled according to the existing water resources and ecological capacity to reduce the pressure on the regional environment. Qin et al. presented an evaluation of the water-resources carrying capacity for the regional economic development of Chicheng County, Zhangjiakou City, China. The carrying capacity of water resources for both present and future planned conditions does not exceed total water consumption, therefore satisfying the economic and social development of the region. However, problems such as river pollution, low sewage treatment capacity and weak pollution supervision need to be solved urgently. This research provides a basis for regional water resources management, contributing to the stability of water ecological environments. Last but not least, Chen et al. reviewed the progress of phytoplankton population ecology research in the Pearl River Estuary, discussing the main environmental factors affecting phytoplankton growth. Species diversity of phytoplankton generally shows a downward trend in the region. Further, the abundance of phytoplankton in the nearshore waters is higher than that in open waters, suggesting that human activities have a great influence. Overall they conclude that relevant guidelines must be developed and implemented for promoting the ecological health of the Guangdong-Hong Kong-Macao Greater Bay Area and ensuring its sustainable development.

In the past few decades, a wide range of *in situ* monitoring, methodological, and hydrological tools have been developed to help locals to develop sustainable watershed management. However, as shown by the contributions to this Research Topic, methods accounting for the influence of connectivity on the structure and function of ecosystem are under-developed. Although these contributions help to understand the relationship between climate change and the hydrological cycle, research on connectivity and integrated watershed management needs to be strengthened in the future, so as to provide a basis for the formulation of watershed management strategies.

Author contributions

All authors listed have made a substantial, direct, and intellectual contribution to the work and approved it for publication.

Funding

YY was supported by the National Natural Science Foundation of China (No. 42177310). MM-D-L-H is beneficiary of a Serra Hunter fellowship on Physical and Environmental Geography funded by the Generalitat de Catalunya (UB-LE-9055). HL was supported by the Strategic Priority Research Program of the Chinese Academy of Sciences (XDA2003010102). PS acknowledges support from the Australian Research Council Future Fellowship scheme (FT140100610).

Acknowledgments

The guest editors would like to express our sincere thanks to all authors who contributed their studies, irrespective of being accepted or not to this particular Research Topic. We also appreciate all reviewers, editors, and the Editor-in-Chief for their continuous assistance in making this Research Topic a success.

Conflict of interest

The authors declare that the research was conducted in the absence of any commercial or financial relationships that could be construed as a potential conflict of interest.

Publisher’s note

frontiers | Frontiers in Environmental Science

TYPE Original Research
PUBLISHED 26 July 2022
DOI 10.3389/fenvs.2022.927588

Online monitoring and sampling analysis of siltation in the middle route of the south-to-north water diversion project

Dawei Zhang[1,2], Xiaolin Han[3], Qiang Zhong[3,4]*, Shulei Wang[5], Liuqian Ding[1], Yuan Liu[3], Qigang Chen[6] and Fujun Wang[3,4]

[1]China Institute of Water Resources and Hydropower Research, Beijing, China, [2]Research Center on Flood and Drought Reducton, Ministry of Water Resources, Beijing, China, [3]College of Water Resources and Civil Engineering, China Agricultural University, Beijing, China, [4]Beijing Engineering Research Center of Safety and Energy Saving Technology for Water Supply Network System in China Agricultural University, Beijing, China, [5]Construction and Administration Bureau of South- to-North Water Diversion Middle Route Project, Beijing, China, [6]School of Civil Engineering, Beijing Jiaotong University, Beijing, China

The middle route project (MRP) of the South to North Water Diversion Project is a significant infrastructure and alleviating water scarcity in Northern China. MRP suffered from untraditional siltation problems. Obvious siltation occurred in the regulating reservoir at the end of the channel and some locations with weak hydrodynamic conditions in the channel when the mineral siltation concentration in the flow is very low. To study the characteristics of the siltation and the siltation time period, an IoT based automatic siltation monitoring system using cloud was installed at the outlet of the inverted siphon project on Xiao River. Three years of online monitoring data since 2018 and the siltation samples at five sites for particle size analysis were collected. The monitoring data shows that siltation mainly occurs during March to October, and almost no siltation occurs in winter. The maximum siltation speed can reach 390 mm per day. The particle size of the siltation gradually increases from upstream to downstream, which mainly occurs in the range above 100 m. The organic matter contained in the siltation shows a significant increase from 40.3 to 86.4% at upstream and downstream sampling position, respectively. Monitoring results shows the main body of the siltation in the MRP is not the traditional siltation but the remnants of the algae that proliferate in large numbers. During March to October, the temperature is suitable for the proliferation of algae which attaches to the sediment particles and gradually grows downstream with the flow.

KEYWORDS

south-to-north water diversion project, water quality, siltation problem, online monitoring, sampling analysis

OPEN ACCESS

EDITED BY
Yang Yu,
Beijing Forestry University, China

REVIEWED BY
Hao Wang,
Fuzhou University, China
Qin Ju,
Hohai University, China

*CORRESPONDENCE
Qiang Zhong,
qzhong@cau.edu.cn

SPECIALTY SECTION
This article was submitted to Freshwater Science,
a section of the journal
Frontiers in Environmental Science

RECEIVED 24 April 2022
ACCEPTED 28 June 2022
PUBLISHED 26 July 2022

CITATION
Zhang D, Han X, Zhong Q, Wang S, Ding L, Liu Y, Chen Q and Wang F (2022), Online monitoring and sampling analysis of siltation in the middle route of the south-to-north water diversion project.
Front. Environ. Sci. 10:927588.
doi: 10.3389/fenvs.2022.927588

Introduction

The South-to-North Water Diversion Project (SNWD) is a multi-decade infrastructure mega-project in China. The main purpose of the project is to alleviate the water shortage in the north area of China. According to the plan, the project is divided into three canal systems as shown in Figure 1 (Liu and Zheng, 2002): the eastern route through the course of the Grand Canal; the middle route from the upper reaches of Han River (the biggest tributary of Yangtze River) via the open channel to Beijing and Tianjin; the western route which goes from three tributaries of Yangtze River in Sichuan province to the northwest China. The east and the middle route have been completed and started operation, and the west route is still under planning. The middle route project (MRP) runs from Danjiangkou Reservoir on the Han River to Tuancheng Lake in the summer Palace in Beijing along approximately 1,277 km long open channel. The first phase of the MRP has been completed and started running from 12 December 2014 (Long et al., 2020). By the end of 2021, the MRP supplied a total of 4.41 × 10^{11} m^3 water to the four provinces of Henan, Hebei, Beijing and Tianjin along the project (Agency, 2021a), and it has played a huge role in supporting residential water and environmental improvement in the areas along the route (Long et al., 2020). For example, 70% of the water used by residents in Beijing comes from the water transfer of the MRP at present (Agency, 2021b).

After the operation of the MRP, unexpected siltation problem has occurred in areas with weak hydrodynamic conditions. Figure 2 shows the satellite images of Tuancheng Lake in the summer Palace in different years, which is the regulating reservoir between the end of the channel of the MRP and municipal water supply system of Beijing. Before the MRP started running, Tuancheng Lake was clear and there was basically no obvious siltation in 2010 (see Figure 2A). Since the MRP started operation in 2014, more and more siltation has accumulated in the lake as shown in Figures 2B–F.

Various types of siltation have occurred frequently in the channels, the most common type is in the bends of rivers, where suspended sediment settles due to reduced flow velocity and sediment transport capacity (Nguyen, et al., 2013). Causes of other types of siltation include the influx of tributaries (Pan, et al.,

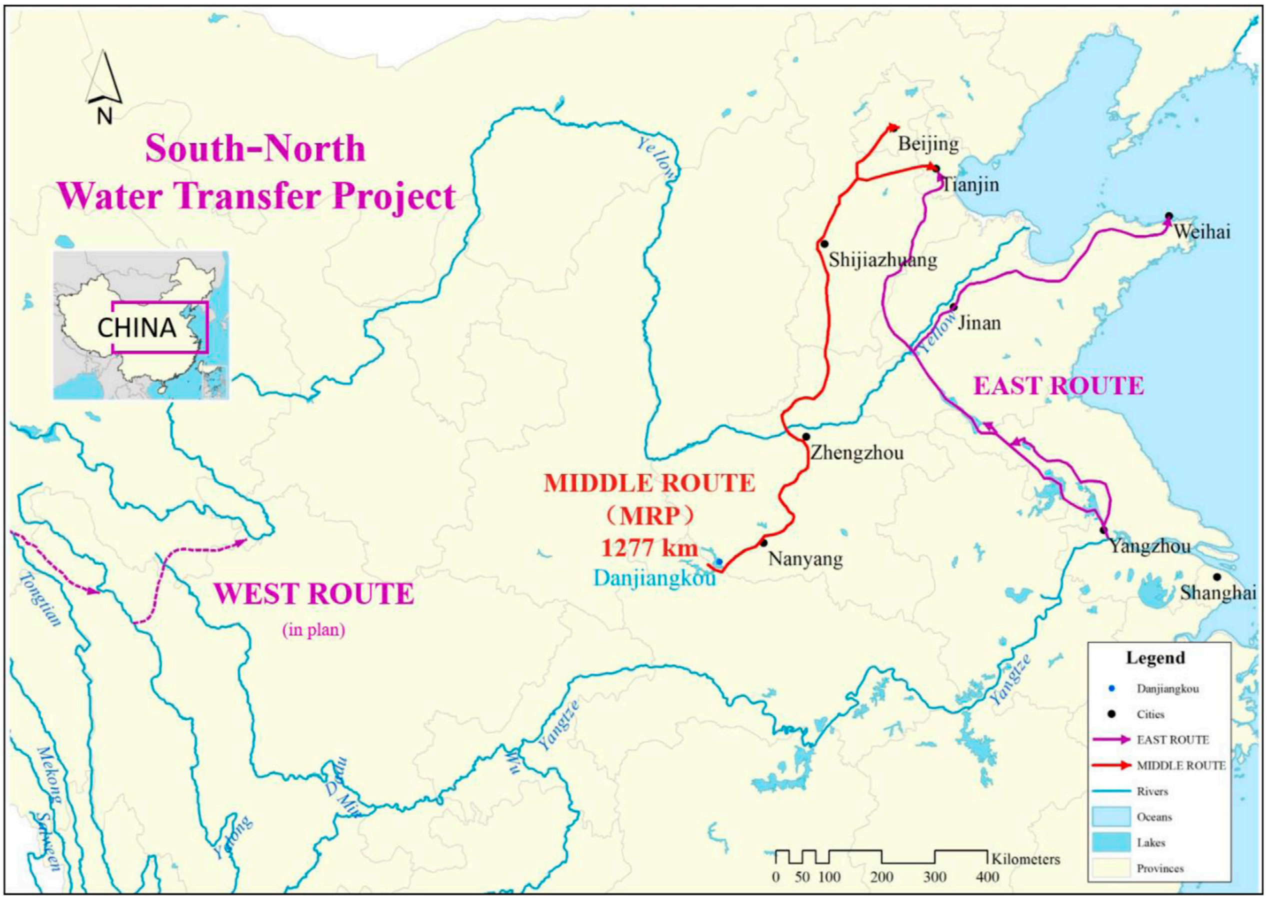

FIGURE 1
The eastern, middle and western route of the South-to-North Water Diversion Project.

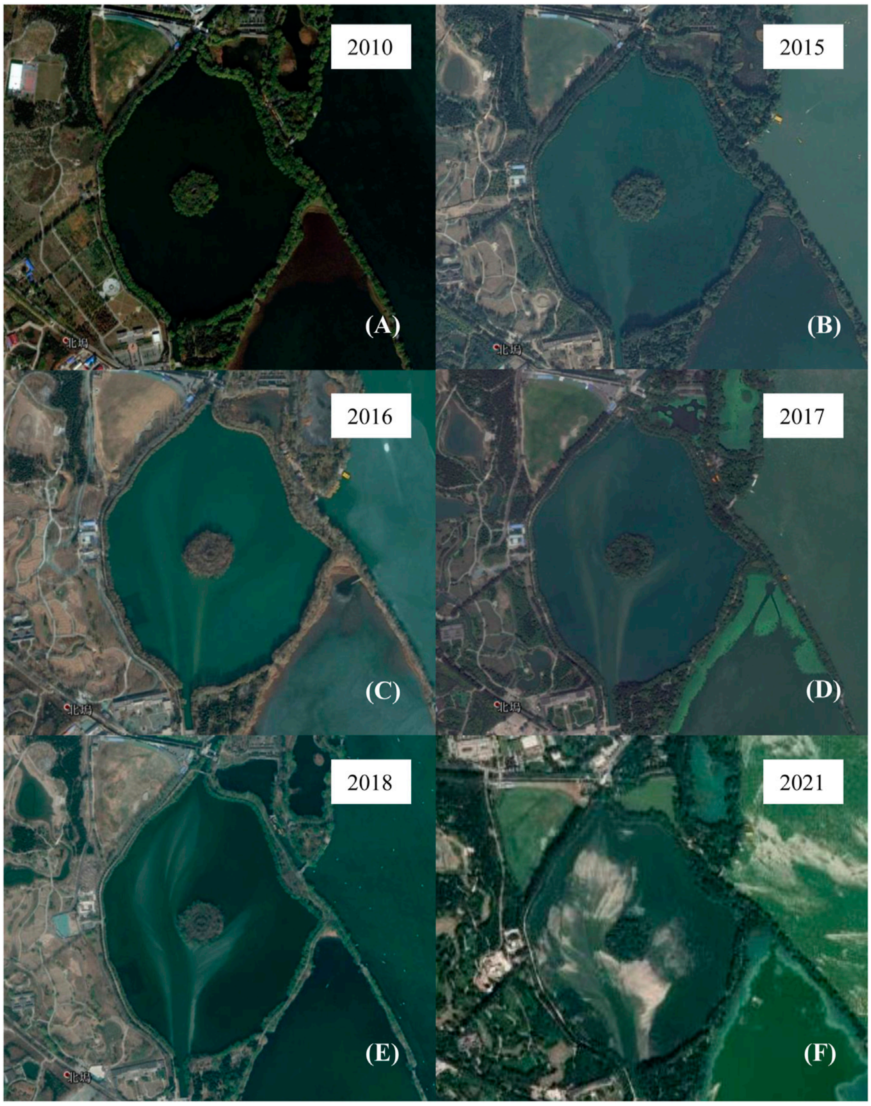

FIGURE 2
Satellite images of Tuancheng Lake from Google Earth over the past 10 years. **(A)** In 2010. **(B)** In 2015. **(C)** In 2016. **(D)** In 2017. **(E)** In 2018. **(F)** In 2021.

2015; Lee, et al., 2019), rill/interrill erosion or gully/channel erosion (Ben Slimane, et al., 2016) and man-made land reclamation (Obodoefuna, et al., 2020). Siltation in MRP is found to be an unusual siltation problem different from them since there is no source of large amounts of mineral sediment along the channel. Firstly, the MRP introduces the clean water with extremely low siltation concentration (lower than 0.1 kg/m^3) from the surface water body in Danjiangkou reservoir (see Figure 1), and the water quality there maintains at an “excellent” level that can be even directly consumed (Nong et al., 2020). Secondly, the MRP is a completely independent channel system of other rivers, thus there is no sediment entering the channel from the rivers along the way. Finally, the region through which the MRP channel passes is not an area where sandstorms frequently occur, and there is no such problem of a large amount of dust entering the channel. Therefore, most of published studies on MRP have focused on the water quality (Li et al., 2011; Tang et al., 2014; Nong et al., 2020), water resource scheduling and distribution (Wei et al., 2010; Zhao et al., 2017; Zhu et al., 2021) and the social and environmental impacts of the project (Long et al., 2020; Zhang et al., 2020; Zhang, 2009), with little attention paid to the problem of siltation.

This unconventional siltation problem has affected the normal operation of the project. The siltation of Tuancheng Lake weakens its regulating and storage function, and siltation of some channels has weakened their water carrying capacity, and

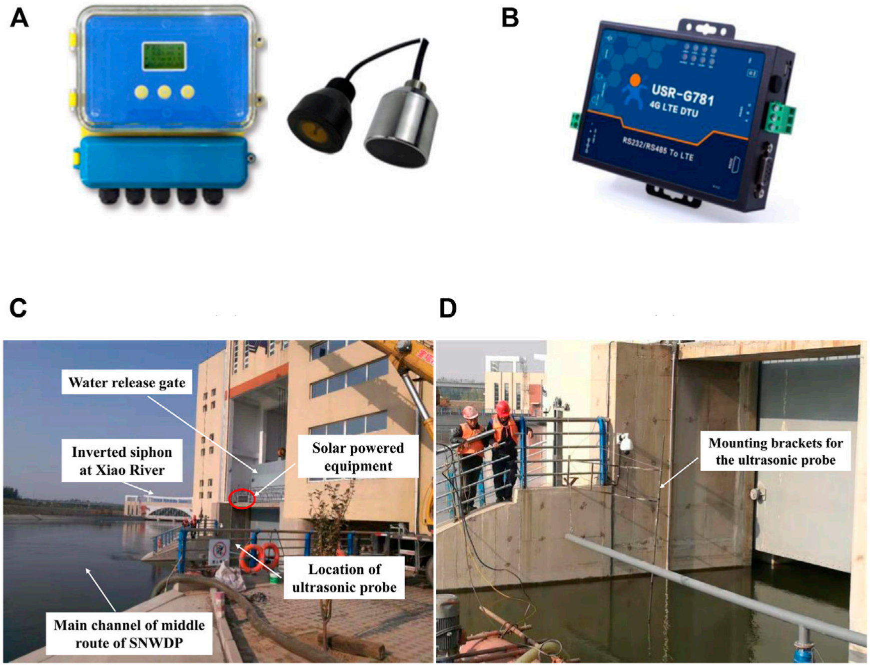

FIGURE 3
Online automatic monitoring system for the siltation in front of the water release gate on the Xiao River: **(A)** ultrasonic probe; **(B)** 4G data terminal unit module; **(C)** installation site of the online automatic monitoring system for siltation; **(D)** mounting bracket for the ultrasonic probe.

the serious siltation before some water release gates brings hidden dangers to the safe and stable operation of the project. At present, the operation department of the project has to use a large number of equipment to continuously dredging in areas with serious siltation.

In order to solve this siltation problem of the MRP, we first need to study temporal and spatial characteristics of siltation and physical properties of siltation. This study developed an Internet of Things (IoT) based automatic siltation monitoring system using cloud and arranged it in the middle reaches of the channel of the MRP to monitor the siltation deposition rate in real time, and 3 years of observational data were collected. The siltation samples at five sites with significant siltation in the MRP were collected for the particle size distribution analysis. The following *Methods* Section introduces the equipment and data processing methods. *Results* Section presents the analysis of the data and the results. Finally, a summary is given in *Cause of siltation* Section.

Methods

Online monitoring system for siltation

In order to automatically monitor the siltation in the MRP, this study has developed an IoT based automatic siltation monitoring system using cloud similarly as (Sheng et al., 2020). The whole system is divided into three parts, the data collection device, the data transmission layer, and the data storage terminal on the cloud. The data collection device includes an ultrasonic probe, solar powered equipment and mounting bracket (see Figure 3C). The ultrasonic probe (ultrasonic underwater ranging probe, Anbuleila Ultrasonic Ltd., Figure 3A) measures the distance using the time it takes for the ultrasonic wave to arrive at the probe after it is emitted and reflected on the surface of the siltation. The measurement range of the probe is 0.3–8 m, and the measurement resolution is 5 mm. The solar powered equipment provide power to all other devices. The system can continue working for 5 days under the power of the battery fully charged when the solar panel cannot work (for example the continuous rainy days). The mounting bracket (Figure 3D) fixed the probe in the middle of the channel in front of the water release gate, and ensured that the probe height is fixed and will not shake with the flow.

The data transmission layer includes a 4G data terminal unit module (4G DTU USR-G780 V2, USR IOT Technology Ltd., Figure 3B) and the 4G mobile phone signal network. The data storage terminal is a remote cloud platform (USR IOT cloud, USR IOT Technology Ltd.). The ultrasonic probe collects data once per 5 min, and the data is transmitted to the 4G DTU module through a RS485 serial port. Then the 4G DTU module sends the data to the cloud by the 4G mobile phone signal network. We can access the cloud through web access or smart phone client to view and download real-time and historical data.

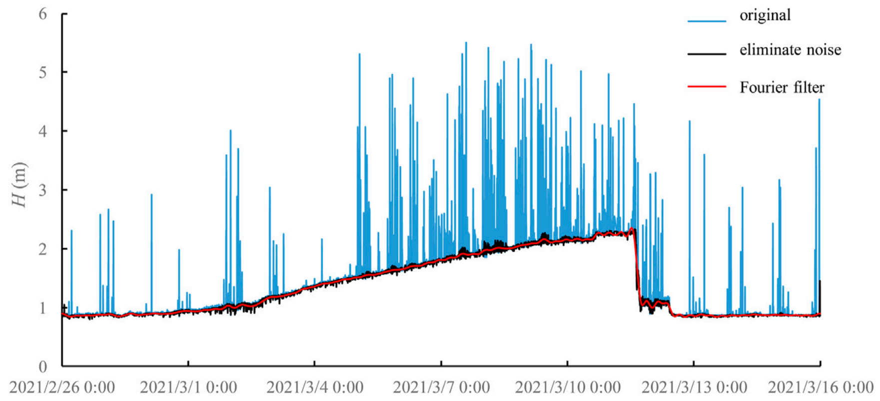

FIGURE 4
Data processing: the blue line is the original measurement data; the black line is the data after removing measurement noise; the red line is the general trend after removing small-scale fluctuations through Fourier filtering.

The collected data of distance d from the probe to the siltation surface needs to be converted to the thickness H of the siltation:

$$H = h_{\mathrm{p}} - d \tag{1}$$

where h_{p} is the distance from the probe to the channel bed, which was measured when the probe was mounted. The online monitoring system for siltation was installed in front of the water release gate of the inverted siphon project on Xiao River of the MRP (see Figure 5A), located in Shijiazhuang City in Hebei Province on 31 October 2018.

Data processing

The original data of the siltation thickness H needs to be post-processed to remove the fluctuations caused by the influence of equipment and the environment noise. There are many fishes in the channel and the ultrasonic probe will report the distance of the fish from the probe rather than the distance between the siltation surface and the probe when the fish swims across the ultrasound transmission route. Hence, there are many sudden values of extreme large siltation thickness as the blue line in Figure 4, and these violent fluctuations should be removed before further analysis. The local standard deviation is used as a threshold to eliminate these noises:

$$\sigma_i = \sqrt{\frac{\sum_{j=i-N}^{j=i+N} \left(H_j - \mu_i\right)^2}{51}} \tag{2}$$

$$\mu_i = \frac{\sum_{j=i-N}^{j=i+N} H_j}{2N+1} \tag{3}$$

in which $N = 25$ thus a total of 50 min of data before and after instantaneous i participated in the calculation; σ_i is the standard deviation of the 50 min data before and after instantaneous i, and μ_i is the average siltation thickness of the 50 min data. When $H_i > \mu_i + \sigma_i$, the H_i will replace by μ_i. This process was executed twice, and the violent fluctuations are basically eliminated as shown by the black line in Figure 4. Then, the Fourier transform is performed on the data to filter out high-frequency noise and to obtain the main trend of the siltation. In spectral space, signals with a period less than 7 days are all set to 0, thus in the results the fluctuations with a period less than 7 days are all smoothed as the red line in Figure 4.

Siltation sampling

In September 2019, the siltation samples were collected at five different sites in the MRP, which are the inverted siphon at Qi River in Hebi city (Henan Province), the inverted siphon at Liyang River in Xingtai city (Hebei Province), the inverted siphon at Xiao River in Shijiazhuang city (Hebei Province), the water division at Xihei mountain in Baoding city (Hebei Province), and the outlet sluice at Waihuan River in Tianjin city from upstream to downstream, as shown in Figure 5A. A barrel with a diameter of 8 cm and a height of 20 cm is used for sampling (see Figure 5B and Figure 5C) The collected samples are dried and then the particle size distribution was obtained by the laser diffraction particle size analyzer (Mastersizer 3,000). Then the samples were burned to remove organic matter, and the particle size distribution was obtained again to compare the difference before and after burning.

Results

Siltation online monitoring

Figure 6 shows the siltation thickness of continuous observation from 31 October 2018. The meaning of the black

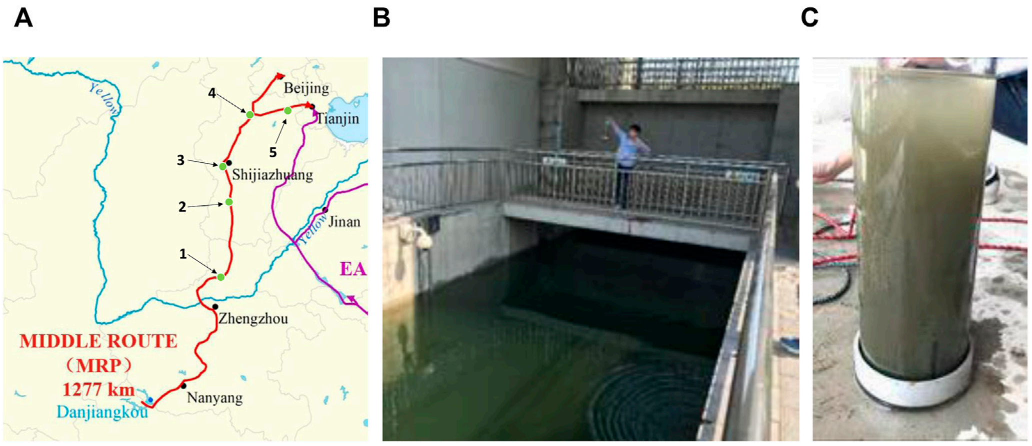

FIGURE 5
The siltation sampling. **(A)** the position: 1. the inverted siphon at Qi River in Hebi city, Henan Province; 2. the inverted siphon at Liyang River in Xingtai city, Hebei Province; 3. the inverted siphon at Xiao River in Shijiazhuang city, Hebei Province; 4. the water division at Xihei mountain in Baoding city, Hebei Province; 5. the outlet sluice at Waihuan River in Tianjin. **(B)** Sampling site photo at the outlet sluice at Waihuan River in Tianjin and **(C)** the photo of the sample in the sampling barrel.

and red solid lines in the figure are the same as in the Figure 4. It can be seen from Figure 6 that there was a rapid siltation from October 31 to the early morning of November 6 and the average siltation speed reached 80 mm/day at the measuring point. The siltation at the measuring point has basically stopped from November 6, which may be affected by the dredging operations in front of the gate in the area between the measuring point and the main channel. The dredging operation time is marked by the green color in Figure 6. As a result of the dredging operation at the measuring point, the thickness of the siltation was reduced by approximately 300 mm in a short time starting around 2 p.m. on November 12. Then, the thickness of the siltation at the measuring point showed a slow decreasing trend throughout the winter. The thickness of the siltation changed from approximately 2.54–2.27 m until 6 January 2019, and the decreasing speed of the thickness of the siltation was about 4.3 mm/day. There may be two possible reasons for this reduction. The first one is that the incoming siltation from upstream was reduced during the winter and the siltation in front of the gate was gradually carried downstream by the mainstream. The second possible reason is the siltation was gradually compacted by itself.

During the spring, the thickness of the siltation experienced a rapid increase. From March 10 to 17 March 2019, the increasing speed of the thickness of the siltation reached about 133 mm/day. From March 17 to April 29, the thickness of the siltation still increased rapidly, but the increasing speed gradually decreased, with an average acceleration of the siltation thickness is 2.7 mm/day, and the thickness of the siltation reached 4.66 m on April 29. The decay of siltation velocity may be due to the gradual decrease of the upstream incoming siltation during this period, or may be caused by the movement of the severely silted locations to the main channel after the thickness of the siltation at the measuring point is significantly higher than that of the main channel. The dredging operation at the measuring point on April 29 caused the thickness of the siltation to decrease to 2.9 m. After the dredging, the measuring point immediately entered a state of rapid siltation. The average siltation speed in the early stage reached 70 mm/day. As the siltation thickness gradually increased, the siltation speed gradually decreased again. The thickness of the siltation was up to the maximum value of 5.6 m in the monitoring data on August 15th, and the surface of the siltation is only 0.6 m away from the water surface. After that, due to continuous dredging operations, the thickness of the siltation dropped to 2.5 m on September 10. Throughout spring, summer and autumn, we can see that after dredging operations the thickness of the siltation reduced significantly, followed by a rapid siltation process until the siltation reaches a relatively high height. For example, the siltation speed reached 220 mm/day from September 6 to September 15.

Monitoring data for 2020 and 2021 are similar to 2019. Long-term monitoring results show that the siltation presents obvious seasonality. During the whole winter, there was no obvious siltation, and the thickness of the siltation is slowly decreasing. The period of rapid siltation is from March to October. During the 3-year monitoring period, the maximum and second largest siltation speed occurred during March 16–19, 2020 (Figure 6C) and September 7–15, 2019 (Figure 6B), respectively. The maximum siltation speed reached an astonishing 390 mm per day. This implies that there is a high density of siltation concentration in the mainstream of the MRP channel at the monitoring point in spring, summer and autumn.

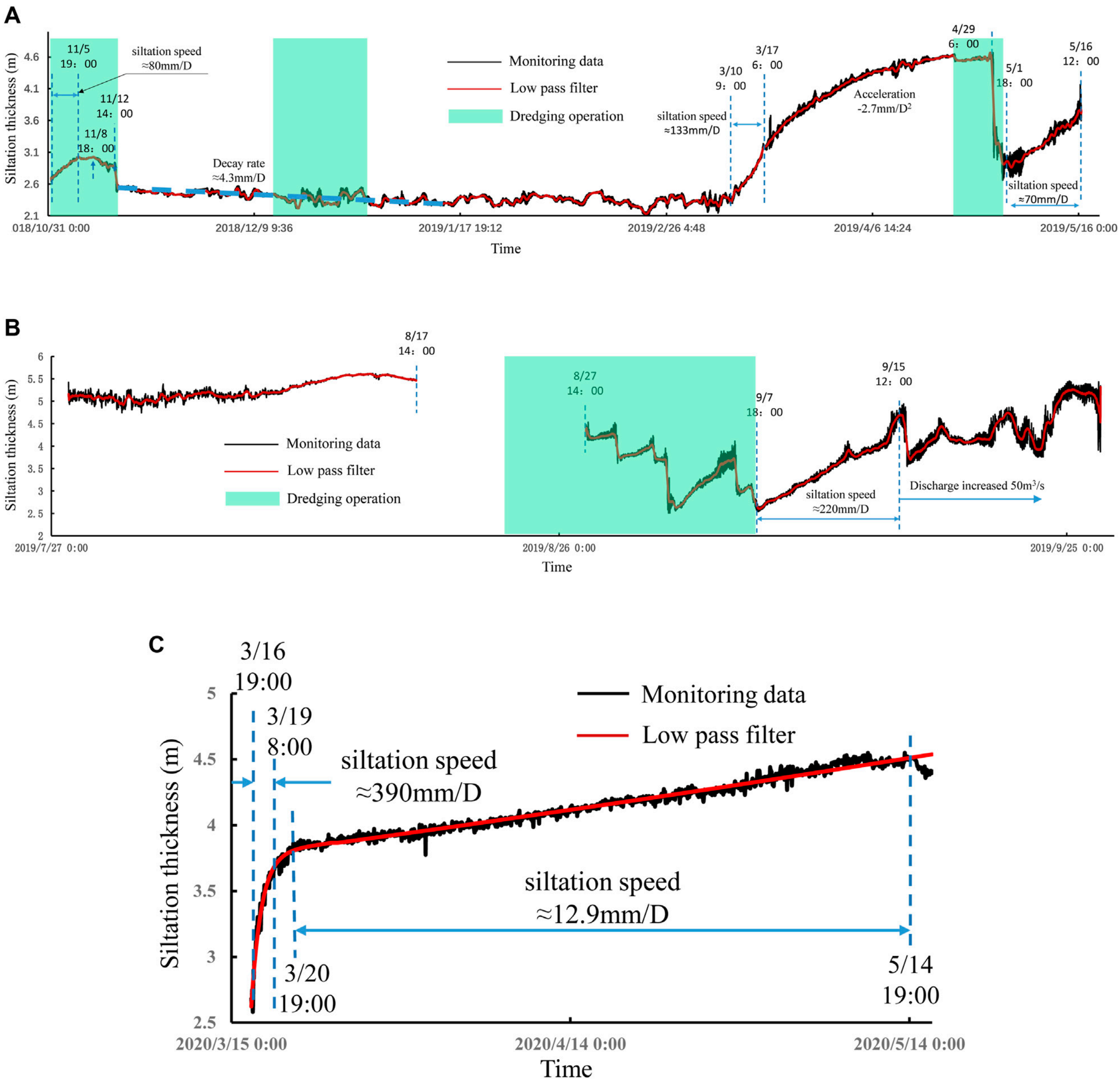

FIGURE 6
Changes in the thickness of the siltation. **(A)** Changes in the thickness of siltation from 31 October 2018 to 16 May 2019. **(B)** Changes in the thickness of siltation from 27 July 2019 to 25 September 2019; **(C)** Changes in the thickness of siltation from 15 March 2020 to 14 May 2019.

The siltation speed is related to the thickness of the siltation. If the thickness of the siltation is small, rapid siltation is prone to occur. In contrast, the siltation speed decreases. For example, the siltation speed gradually reduced to 12.9 mm per day after the serious siltation from March 16 to 19 March 2020 (Figure 6C). In addition, hydrodynamic condition can also affect the siltation speed. In order to reduce the flood control pressure of the water source Danjiangkou Reservoir and increase the water supply, the flow discharge at the head of the MRP has gradually increased by 50 m^3/s from 12 September 2019 and the total flow discharge at last reached 350 m^3/s for the first time. In Figure 6B, it can be seen that with the increase of hydrodynamic conditions, the siltation thickness decreased significantly after September 15, and the average siltation speed decreased after that.

Based on these test results, we can infer that throughout the spring, summer and winter, the flow in the main channel transports a large amount of siltation from upstream to downstream, and rapid siltation will occur in areas where

TABLE 1 Analysis of siltation particle size.

Position	Median diameter (μm)		Average diameter (μm)	
	Original	Burned	Original	Burned
Qi River	31.0	26.1	46.0	39.2
Liyang River	40.7	27.4	60.7	106.6
Xiao River	33.4	23.1	51.3	34.7
Xihei mountain	46.3	23.8	66.3	37.7
Waihuan River	38.6	24.6	61.9	36.6

local hydrodynamic conditions are weakened. It should be noted that due to the needs of equipment maintenance, dredging operations and the power outages caused by the continuous rain, the monitoring from May 16 to July 27 and August 17 to August 27 was interrupted, but from the monitoring data in the following years, the basic conclusions are consistent.

Siltation sampling analysis

The median and average particle size analysis results of the siltation samples collected from different locations are shown in Table 1. From Table 1, it can be seen that the original median and average diameters roughly increase from upstream to downstream. The median and average diameters after burning are significantly smaller than the original ones and there is no significant change in the diameters of the burning samples from upstream to downstream. Since the burning of the sample removes the organic components and only the inorganic material remains, Table 2 analyzed the organic matter in siltation particles based on the median diameters before and after burning. From Table 2 the content of organic matter shows a significant increase from upstream to downstream. For the sample at Qi River which is the most upstream sampling point in this study, the organic ratio of the siltation particles is 40.3%, and the organic ratios at two points, Liyang River and Xiao River in the middle section are close to 70%, and the downstream point Xihei mountain reaches 86.4%. The results shown in Table 1 and Table 2 indicate that the siltation of MRP are composed by the tiny inorganic sand particles and a large amount of organic matter surrounding it. The volume of organic matter accounts for most of the particles, the organic matter content increases significantly from upstream to downstream. At the same time, there is no significant difference among the diameters of inorganic sand particles from upstream to downstream.

The median and average radius can only show the overall characteristics of the siltation particles. In order to further analyze the particle size composition of siltation particles, Figure 7 shows the particle size distributions from the laser diffraction particle size analyzer. Figure 7A plots the cumulative probability density curves of the diameter of the original samples from different locations. It can be seen that the curves generally move towards the direction of the larger particle size as the locations move from upstream to downstream, which is consistent with the median and average particle size results in Table 1. Figure 7B compares probability density curves of the diameter of the original samples from different locations. The probability density in the small diameter area gathered in 19 and 39 μm two positions, which are around the average particle size after burning as seen in Table 1. On the contrary, the probability density increases in the large diameter area from upstream to downstream. To further determine the cause of the change in particle size, Figure 7C plots the probability density curves of the diameter of the burned samples from different locations. It can be seen that all curves show a much better similarity than the curves in Figure 7B, which means there is no essential change in the size distribution of inorganic siltation particles from upstream to downstream. This indicates that the inorganic siltation in the water body from upstream to downstream should have the same source. Figure 7D compares the particle size distribution of the original and burned samples. Since the results at different locations are similar, only the result at the inverted siphon at Xiao River is plotted in Figure 7D. Unsurprisingly, the original sample curve shifted to the large particle size. It is worth noting that there are also more small particles of about 1 μm in the original sample than that in the burned sample. This may be organic matter shed from intact organic matter.

Cause of siltation

To investigate the cause of siltation, in the previous studies, (Pan, et al., 2015), analysed samples, but did not monitor the changes in siltation in real time. Lee et al. (2019) deployed two ADCPs to monitor the siltation flux at the entrance of a harbour over a month but ADCP is expensive, which is not suitable for long-term monitoring. Whereas, this study combines 3 years of monitoring data and analysis of multiple samples. The results of monitoring and sampling analysis strongly suggest that the main cause of siltation in the MRP is not the traditional siltation but

TABLE 2 Analysis of organic matter in siltation particles.

Position	Median diameter (μm)		Average volume (mm^3)		Organic volume ratio (%)
	Original	Burned	Organic	Inorganic	
Qi River	31.0	26.1	6289.2	9309.4	40.3
Liyang River	40.7	27.4	24529.7	10770.9	69.5
Xiao River	33.4	23.1	13055.1	6454.1	66.9
Xihei mountain	46.3	23.8	44909.9	7058.8	86.4
Waihuan River	38.6	24.6	22318.7	7794.8	74.1

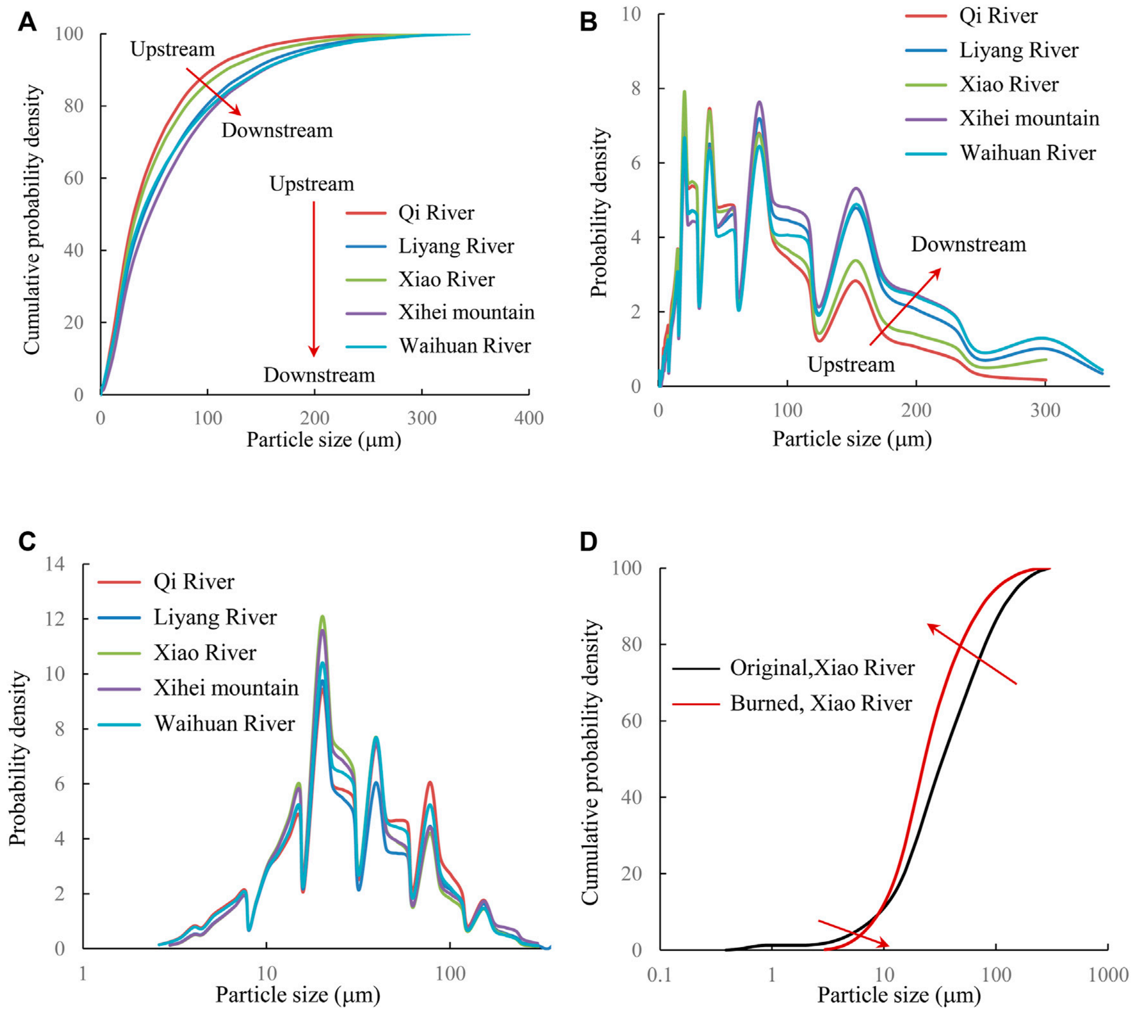

FIGURE 7
Particle size distribution of siltation samples in the MRP. **(A)** cumulative probability density curves of the diameter of the original samples; **(B)** probability density curves of the diameter of the original samples; **(C)** probability density curves of the diameter of the burned samples **(D)** cumulative probability density curves of the original and burned samples at Xiao river.

the massively multiplying organisms. Since 2016, the project operators observed that rapid algae growth has occurred in areas of the main canal of MRP in the spring and autumn (Zhu et al., 2019). Then researchers started to focus on risk of water quality deterioration from algae growth (Jing et al., 2021; Nong et al., 2021; Wang et al., 2022). A model prediction results based on the principal component analysis shows that algal density along the canal differs to the greatest extent in summer, followed by spring and autumn, and is the weakest in winter (Jing et al., 2021). Changes in hydrodynamic conditions also affect algal density (Zhu et al., 2019). In addition, (Xu, et al., 2021; Long, et al., 2022), have also mentioned the algae problems in Middle Route of South-to-North Water Diversion Project.

Combined with previous algae study results and current research, the conclusion can be given that the siltation in the MRP is most likely the aquatic algae. In winter, the temperature is too low thus the algae reproduce slowly. Since the concentration of algae in the water body is low, there is basically no siltation. When the ambient temperature raises to a temperature suitable for algae growth during March, algae attach to the inorganic sediment particles in the water and begin to grow rapidly, then the concentration of algae in the water body increases sharply. The maximum siltation speed can reach 390 mm/day at the monitoring points. March to October is the period of vigorous algae blooming, and the concentration of algae residue in the water body maintained at a high level. The algae gradually grow in the process of migrating downstream with the flow. Therefore, the particle size of the original sample of the siltation increases from upstream to downstream.

Conclusion

The water quality from the Danjiangkou reservoir at the channel entrance of the MRP is pretty good and contains almost no siltation. However, during the operation of the MRP, a large amount of obvious siltation occurred in locations with weak hydrodynamic conditions in front of the outlet or the outlet gate. In order to study the time and particle size distribution characteristics of the siltation, an IoT based automatic siltation monitoring system using cloud was developed and installed in the water release gate of the inverted siphon project on Xiao River. Three years' data are collected since 31 October 2018. The siltation at five sites was also collected for particle size analysis. The main findings are as follows:

1) The siltation mainly occurs from March to October, and almost no siltation occurs in winter. The maximum siltation speed can reach 390 mm per day at the monitoring points. The huge siltation speed indicates there is a high density of siltation concentration in the mainstream of the MRP channel at the monitoring point in spring, summer and autumn. The monitoring data also showed that hydrodynamic condition in the MRP channel can also affects the siltation speed.
2) The particle size of the siltation gradually increases from upstream to downstream, and this growth mainly occurs in the range above 100 μm. The particle size distribution after burning remains basically unchanged from upstream to downstream. The organic matter shows a significant increase from 40.3% at the inverted siphon at Qi River to 86.4% at Xihei mountain downstream.
3) Combining previous research and the results of this study, the main body of the siltation in the MRP is not the traditional siltation but the remnants of the algae that proliferate in large numbers.

Data availability statement

The raw data supporting the conclusions of this article will be made available by the authors, without undue reservation.

Author contributions

QZ contributed to design of the study. DZ, SW, and LD finished the field experiments. YL performed the data analysis. XH wrote the first draft of the manuscript. QZ, DZ, and FW wrote sections of the manuscript. All authors contributed to manuscript revision, read, and approved the submitted version.

Funding

The study was supported by the National Natural Science Foundation of China (Grant Nos. 52179081, 51809268, 51879138) and the IWHR Research and Development Support Program (WH0145B022021, WH015B042021).

Conflict of interest

The authors declare that the research was conducted in the absence of any commercial or financial relationships that could be construed as a potential conflict of interest.

Publisher's note

References

Agency, X. N. (2021a). "The South-to-North Water Diversion Project has provided approximately 49.4 billion water for 140 million people in the past 7 years," in *Construction and administration bureau of South-to-North water diversion middle route project*.

Agency, X. N. (2021b). "The South-to-North Water Diversion Project has transferred nearly 50 billion water to the north China in 7 years," in *Website of the central people's government of the people's Republic of China*.

Ben Slimane, A., Raclot, D., Evrard, O., Sanaa, M., Lefevre, I. E. N., Le Bissonnais, Y., et al. (2016). Relative contribution of rill/interrill and gully/channel erosion to small reservoir siltation in Mediterranean environments. *Land Degrad. Dev.* 27 (3), 785–797. doi:10.1002/ldr.2387

Jing, Z., Chen, H., Cao, H., Tang, X., Shang, Y., Liang, Y., et al. (2021). Spatial and temporal characteristics, influencing factors and prediction models of water quality and algae in early stage of Middle Route of South-North Water Diversion Project. *Environ. Sci. Pollut. Res.* 29, 23520–23544. doi:10.1007/s11356-021-16917-5

Lee, G., Shin, H., Kim, Y. T., Dellapenna, T. M., Kim, K. J., Williams, J., et al. (2019). Field investigation of siltation at a tidal harbor: North port of incheon, korea. *Ocean. Dyn.* 69 (9), 1101–1120. doi:10.1007/s10236-019-01292-0

Li, S., Li, J., and Zhang, Q. (2011). Water quality assessment in the rivers along the water conveyance system of the Middle Route of the South to North Water Transfer Project (China) using multivariate statistical techniques and receptor modeling. *J. Hazard. Mater.* 195, 306–317. doi:10.1016/j.jhazmat.2011.08.043

Liu, C., and Zheng, H. (2002). South-to-north water transfer schemes for China. *Int. J. Water Resour. Dev.* 18 (3), 453–471. doi:10.1080/0790062022000006934

Long, D., Yang, W., Scanlon, B. R., Zhao, J., Liu, D., Burek, P., et al. (2020). South-to-North Water Diversion stabilizing Beijing's groundwater levels. *Nat. Commun.* 11 (1), 3665. doi:10.1038/s41467-020-17428-6

Long, Y., Feng, M., Li, Y., Qu, J., and Gao, W. (2022). *Comprehensive risk assessment of algae and shellfish in the middle route of South-to-North water diversion project*.

Nguyen, V., Zheng, J., and Zhang, J. (2013). Mechanism of back siltation in navigation channel in Dinh an Estuary. *Vietnam. Water Sci. Eng.* 6 (2), 178–188. doi:10.3882/j.issn.1674-2370.2013.02.006

Nong, X., Shao, D., Zhong, H., and Liang, J. (2020). Evaluation of water quality in the South-to-North Water Diversion Project of China using the water quality index (WQI) method. *Water Res.* 178, 115781. doi:10.1016/j.watres.2020.115781

Nong, X., Shao, D., Shang, Y., and Liang, J. (2021). Analysis of spatio-temporal variation in phytoplankton and its relationship with water quality parameters in the South-to-North Water Diversion Project of China. *Environ. Monit. Assess.* 193 (9), 593. doi:10.1007/s10661-021-09391-6

Obodoefuna, D. C., Fan, D., Guo, X., and Li, B. (2020). Highly accelerated siltation of abandoned distributary channel in the Yangtze Delta under everchanging social-ecological dynamics. *Mar. Geol.* 429, 106331. doi:10.1016/j.margeo.2020.106331

Pan, B., Pang, H., Zhang, D., Guan, Q., Wang, L., Li, F., et al. (2015). Sediment grain-size characteristics and its source implication in the Ningxia-Inner Mongolia sections on the upper reaches of the Yellow River. *Geomorphology* 246, 255–262. doi:10.1016/j.geomorph.2015.06.028

Sheng, Y., Zhang, J., Chen, W., Xie, Y., Sun, G., and Lin, H. (2020). *Design of a big data platform for water quality monitoring based on IoT, paper presented at international conference on artificial intelligence and security*. Springer.

Tang, C., Yi, Y., Yang, Z., and Cheng, X. (2014). Water pollution risk simulation and prediction in the main canal of the South-to-North Water Transfer Project. *J. Hydrology* 519, 2111–2120. doi:10.1016/j.jhydrol.2014.10.010

Wang, C., Zhang, H., Lei, P., Xin, X., Zhang, A., Yin, W., et al. (2022). Evidence on the causes of the rising levels of CODMn along the middle route of the South-to-North Diversion Project in China: The role of algal dissolved organic matter. *J. Environ. Sci.* 113, 281–290. doi:10.1016/j.jes.2021.06.003

Wei, S., Yang, H., Abbaspour, K., Mousavi, J., and Gnauck, A. (2010). Game theory based models to analyze water conflicts in the middle route of the South-to-North water transfer project in China. *Water Res.* 44 (8), 2499–2516. doi:10.1016/j.watres.2010.01.021

Xu, Y., Liang, J., Lin, J., Lei, X., Ding, G., Yuan, R., et al. (2021). A study on the phytoplankton community structure in the diaohe river section of the middle route of the South-to-North water diversion project in winter. *Water Supply* 21 (3), 959–970. doi:10.2166/ws.2020.247

Zhang, C., Duan, Q., Yeh, P. J. F., Pan, Y., Gong, H., Gong, W., et al. (2020). The effectiveness of the South-to-North water diversion middle route project on water delivery and groundwater recovery in North China plain. *Water Resour. Res.* 56 (10), e2019WR026759. doi:10.1029/2019wr026759

Zhang, Q. (2009). the South-to-North water transfer project of China: Environmental implications and monitoring strategy. *JAWRA J. Am. Water Resour. Assoc.* 45 (5), 1238–1247. doi:10.1111/j.1752-1688.2009.00357.x

Zhao, Z.-Y., Zuo, J., and Zillante, G. (2017). Transformation of water resource management: A case study of the South-to-North water diversion project. *J. Clean. Prod.* 163, 136–145. doi:10.1016/j.jclepro.2015.08.066

Zhu, J., Lei, X., Quan, J., and Yue, X. (2019). Algae growth distribution and key prevention and control positions for the Middle Route of the South-to-North water diversion project. *Water* 11 (9), 1851. doi:10.3390/w11091851

Zhu, J., Zhang, Z., Lei, X., Jing, X., Wang, H., Yan, P., et al. (2021). Ecological scheduling of the middle route of south-to-north water diversion project based on a reinforcement learning model. *J. Hydrology* 596, 126107. doi:10.1016/j.jhydrol.2021.126107

Frontiers in Environmental Science

TYPE Original Research
PUBLISHED 17 August 2022
DOI 10.3389/fenvs.2022.980949

OPEN ACCESS

EDITED BY
Yang Yu,
Beijing Forestry University, China

REVIEWED BY
Jingwen Zhang,
University of Illinois at Urbana-Champaign, United States
Dehua Zhu,
Nanjing University of Information Science and Technology, China

*CORRESPONDENCE
Siyu Cai,
caisy@iwhr.com

SPECIALTY SECTION
This article was submitted to Freshwater Science,
a section of the journal
Frontiers in Environmental Science

RECEIVED 29 June 2022
ACCEPTED 13 July 2022
PUBLISHED 17 August 2022

CITATION
Zhou X, Chen W, Liu Q, Shen H, Cai S and Lei X (2022), Future runoff forecast in Hanjiang River Basin based on Wetspa model and CMIP6 model.
Front. Environ. Sci. 10:980949.
doi: 10.3389/fenvs.2022.980949

Future runoff forecast in Hanjiang River Basin based on Wetspa model and CMIP6 model

Xi Zhou[1,2], Wei Chen[3], Qingtao Liu[4], Hongxia Shen[4], Siyu Cai[5]* and Xiaohui Lei[1,2,5]

[1]Hebei Key Laboratory of Intelligent Water Conservancy, School of Water Conservancy and Hydropower, Hebei University of Engineering, Handan, China, [2]School of Water Conservancy and Hydropower, Hebei University of Engineering, Handan, China, [3]Song-Liao Water Resources Commission Basin Planning and Policy Research Center, Changchun, China, [4]Information Center, Ministry of Water Resources, Beijing, China, [5]China Institute of Water Resources and Hydropower Research, Beijing, China

In order to comprehensively consider the impact of human activities on runoff simulation and improve the accuracy of runoff simulation, so as to make a more accurate prediction of the future runoff of the Hanjiang River Basin, this study improved the reservoir module of the Wespa model, adding two parts: reservoir inflow data correction and water storage and outflow data calculation without measured data. Use the improved model to verify its applicability to the Hanjiang River Basin, then, choose the ones who has the most familiar trend with the historical data in the future climate model data (CMIP6). Put the selected data in the model to predict the runoff of Hanjiang River from 2021 to 2060. By analyzing the future runoff trend of Ankang, Huangjiagang and Huangzhuang in the Hanjiang River Basin from 2021 to 2060 and the changes of average runoff, seasonal runoff and monthly runoff compared with the historical period (1981–2020), the conclusions drawn are as follows: 1) The improved Wetspa model has good applicability in the Hanjiang River Basin; 2) The future runoff of Ankang section is decreasing, while that of Huangjiagang and Huangzhuang sections is increasing; 3) Compared with the reference period, the average runoff of the three sections in the future shows an increasing trend, which indicates that there will be flood risk in the future; 4) Compared with the reference period, the runoff proportion of the three sections will increase in spring and winter, and decrease in autumn. Attention should be paid to the risk of drought in autumn. In terms of months, the proportion of runoff from April to June increases, decreases from September to November, and increases and decreases in other months are uncertain.

KEYWORDS

Wetspa, Hanjiang River Basin, runoff simulation, CMIP6, reservoir regulation and storage

1 Introduction

Over the past century, the global climate has changed significantly. Climate change has brought new variations to the inherent laws of physical processes such as rainfall, runoff and evapotranspiration in the basin (Wang et al., 2013; Wang et al., 2017). As the largest tributary of the Yangtze River, the runoff change of the Hanjiang River has a great impact on the normal production and life of the people in the basin. Therefore, it is of great significance to study the runoff change trend of the Hanjiang River Basin under the future climate for the future water resources management and utilization of the Hanjiang River.

Domestic and foreign scholars use various hydrological models to predict the future runoff of different basins. For example, Wei et al. (2016) predicted the future runoff process of the Yellow River Basin based on VIC Model. The results show that the annual average runoff increased by 2.65%, 2.66%, and 8.07% respectively, and the increase gradually decreased with the passage of time, showing a downward trend in the long term; In terms of annual distribution, runoff increases in winter and decreases slightly in summer Guo et al. (2015) is based on Budyko's hydro thermal coupling equilibrium hypothesis, selected BCC-CSM1-1 global climate model and RCP4.5 emission scenarios, and the future runoff changes in the Yangtze River Basin are estimated. The results show that the relative change of future runoff in each sub watershed of the Yangtze River varies, and the maximum change range is about 10%; In the three periods of 2020s, 2050s, and 2080s, the runoff of the basins on the north and south banks of the Yangtze River will decrease in the south and increase in the north. The increase of runoff change on the north bank will gradually increase, and the decrease of runoff change on the south bank will gradually decrease Zhang and Yang. (2018). Studied the multi model integration (MME) and combined runoff prediction under climate change scenarios generated by eight rainfall runoff models in the Yellow River Basin by using genetic algorithm and Bayesian model averaging method. The results show that in most climate scenarios, the runoff is expected to decrease, which will threaten the water security of the basin Guo et al. (2012) used GCM and a hydrological model to forecast future runoff in the upper reaches of Hanjiang River under the A2 climate change scenario. The results show that, compared with the average runoff during the 1961 baseline period, the future runoff predicted based on the output of CGCM2 decreases in 2020s, increases in 2080s and does not change significantly in 2050s. For HadCM3, the two hydrological models increase in 2050s and 2080s, and different models predict different increasing and decreasing trends in 2020s. The results in the existing studies are not completely consistent, which may be related to the different hydrological models and meteorological model data used.

There are many influencing factors for future runoff change, and climate change is only one of the main influencing factors. In simulating future runoff, it is still necessary to consider the impact of human activities, such as reservoir regulation and storage (Homa et al., 2013; IPCC, 2014; Al-Faraj and Al-Dabbagh, 2015; Hayal et al., 2017; Yan et al., 2018). In particular, reservoir regulation and storage will change the size and annual distribution of runoff and affect the hydrological cycle in the basin (Yaghmaei et al., 2018). The existing research only simulates the future runoff through the correlation between climate change and runoff, without considering the impact of the reservoir on the future runoff, which may be caused by the lack of treatment of the reservoir part in the general model and the lack of an appropriate simulation method for reservoir discharge.

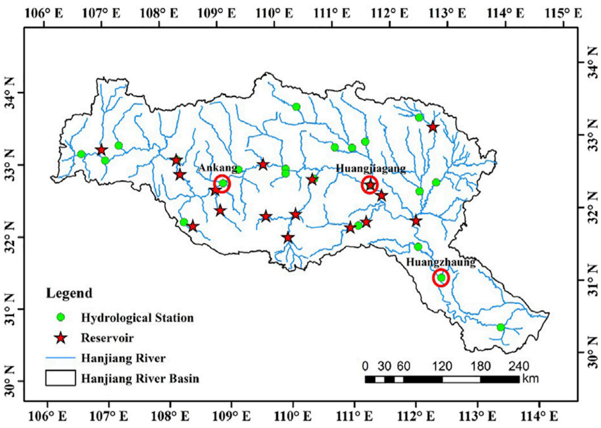

FIGURE 1
The location of hydrological stations and reservoirs in Hanjiang River Basin.

Based on the inaccurate reservoir simulation and the difficulty in predicting the reservoir outflow without measured data, this study improved the calculation method of the reservoir unit in the Wetspa model, corrected the zigzag fluctuation and extreme value of the reservoir inflow, put forward the method that the reservoir cannot predict the outflow in the future prediction period, and predicted the runoff change in the Hanjiang River Basin in the next 40 years based on the modified model using CMIP6 data. It is expected to provide reference for water resources planning and rational development in Hanjiang River Basin.

2 Materials and methods

2.1 Study regions

The Hanjiang River originates at the south foot of Qinling Mountains in Shaanxi Province. Its main stream flows through Shaanxi and Hubei provinces and joins the Yangtze River at the Longwang temple in Hankou. Hanjiang River has a total length of 1,577 km and a drainage area of 15.3×10^4 km^2, with longitude and latitude ranging from 106°15′–14°20′E,30°10′–34°20′N (Figure 1). The terrain is high in the West and low in the East, with medium and low mountains in the West and hills and plains in the East. The Hanjiang River Basin is located in the North-South climatic junction zone of China. The climate has obvious seasonality, cold in winter and hot in summer. The annual average temperature reaches 12–16°C, and the monthly average maximum temperature occurs in July and the minimum temperature occurs in January. The precipitation in the basin is mostly in the form of rainfall, snow and little hail. The annual average precipitation is 873 mm. The annual average precipitation decreases from upstream to downstream, reaching more than 1,100 mm in the downstream area and 700–900 mm in the Danjiangkou area. The precipitation in the year is unevenly distributed, reaching 50%–60% of the whole year for a maximum of four consecutive months, and mostly concentrated in April to July. The average annual runoff of the basin is 55.6 billion m^3, equivalent runoff depth 256 mm. The runoff varies greatly between years and is unevenly distributed throughout the year. The flood season can account for up to 65% of the annual runoff. It is the river with the largest change among the major tributaries of the Yangtze River.

2.2 Data

The input data of the model mainly includes: Geospatial data, meteorological data, various hydrological monitoring data and water intake monitoring data. Data sources are as follows:

2.2.1 Geospatial data

Geospatial data includes DEM, soil type, land use type and site location information. The first three are grid data, which are used to generate model parameters such as potential runoff coefficient, depression filling storage capacity, field water capacity, and runoff production parameters of each grid computing unit.

(1)DEM data.

DEM data is from the Federal Bureau of address investigation with a resolution of 1 km × 1 km grid data.

(2)Soil type.

The soil data is from the “1:1million soil classification map of China” of the second national soil survey, and the corresponding data such as soil texture and soil layer thickness are from the Chinese soil database and the Chinese soil records.

(3) Land use data.

The land use data is from the Vegetation Atlas of China (1: 1million).

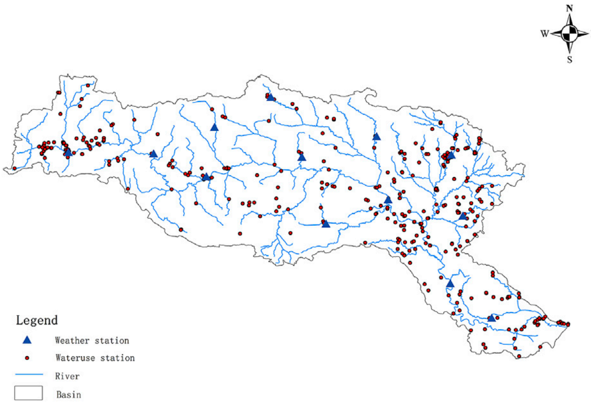

FIGURE 2
The distribution of water intake stations and meteorological stations.

2.2.2 Meteorological data

The meteorological data used in the modeling came from the daily meteorological element data of 13 meteorological stations in the Hanjiang River basin for 61 years (1960–2020) in the daily value data set of China’s surface climate data (V 3.0).

2.2.3 Hydrological monitoring data

There are 18 hydrological stations and 17 large reservoirs in the basin selected for modeling. The hydrological monitoring data comes from the national real-time water and rain database, including the water level and flow data of the hydrological stations, and the upper water level, storage capacity, inflow and outflow flow data of the reservoir. The monitoring data needs to be processed into daily scale data that meets the requirements of the model through data cleaning and integration.

2.2.4 Monitoring data of state-controlled water intake

The water intake monitoring data used in the study are from the state-controlled water intake monitoring stations of the National Water Resources Monitoring Capability Project. There are 569 water intake monitoring stations in the Hanjiang River Basin. The daily water intake monitoring data includes surface water intake and underground water intake. The data years are from 2016 to 2020.

The spatial distribution of meteorological stations and water intake monitoring stations is shown in the figure below (Figure 2).

2.2.5 Future scenario model data in CMIP6

The meteorological data used to simulate the future runoff is the future scenario model data in CMIP6. At present, the global climate model is one of the core tools to study the impact of future climate change (Ma et al., 2019; Zhao et al., 2020). CMIP6 is the Coupled Model Intercomparison Project (CMIP) organized and developed

TABLE 1 Information of 5 global climate models.

Model name	Institution	Country	Resolution ratio
CanESM5	Canadian Environment Agency (CCCma)	Canada	2.8125° × 2.8125°
MRI-ESM2-0	Meteorological Research Institute, Japan Meteorological Agency (MRI)	Japan	1.875° × 1.875°
IPSL-CM6A-LR	Pierre-Simon Laplace Institute (IPSL)	France	2.5° × 1.259°
NESM3	Nanjing University of Information Technology (NUIST)	China	1.875° × 1.875°
KACE-1-0-G	Institute of Meteorology, Korea Meteorological Administration (NIMS-KMA)	Korea	1.875° × 1.25°

by the World Climate Research Programme Working Group (Yang et al., 2010; Nashwan and Shahid, 2020). Considering the comprehensiveness and time length of various model data in cmip6, five global climate models CanESM5, MRI-ESM2-0,IPSL-CM6A-LR,NESM3,KACE-1-0-G and nesm3 are selected for follow-up research. In this paper, the grid data of daily average precipitation and daily maximum and minimum temperature output from the above five global climate models are used to simulate future runoff. In terms of scenarios, historical scenarios (1961–2011) and three future scenarios (2015–2060) are selected. The three future scenarios correspond to the forced scenarios of low (SSP1-2.6), medium (SSP2-4.5) and high (SSP5-8.5) emissions, respectively (Table 1).

2.3 Wetspa model

2.3.1 Model principle

Wetspa (A Distributed Model for Water and Energy Transfer Between Soil, Plants and Atmosphere) model is a distributed hydrological model based on physical mechanisms, which was proposed by Wang and Batelaan of Vrije Universiteit Brussels in Belgium in 1996. The model is based on the following assumptions: 1) The soil properties, geographical elevations, vegetation category and rainfall inputs of each grid in the sub watershed are identical; 2) When the soil moisture content is less than the wilting coefficient, the evapotranspiration process stops; 3) Deep evapotranspiration is limited by groundwater and only occurs when the soil dries up; 4) The grid has only one outflow direction; 5) The water conservancy radius is related to the geographical location and flood frequency, but does not change during a flood. The model is based on the grid as the calculation unit for calculation, and the model has good versatility and portability, and can more intuitively reflect the runoff process at any point and any time period (Batelaan et al., 1996; Wang et al., 1996; Liu et al., 2005).

The Wetspa model considers physical processes such as rainfall, closure, infiltration, evapotranspiration, seepage, ground and underground runoff, so multi-layer results are used to represent the water and energy balance of each unit (Liu and De Smedt, 2004; Liu et al., 2006; Zeinivand et al., 2007). As shown in the figure (Figure 3), the model is vertically divided into four layers, namely Plant canopies, Surface layer, Soil layer and Underground aquifer. The data required for model operation are DEM, Landuse data, soil type data, meteorological data, hydrological monitoring data and water intake monitoring data.

2.3.2 Model building

(1) Divide parameter partitions.

Parameter partitions refer to the control area of the survey stations in the basin, and each section will be calculated based on the parameter partition during model calculation. In this paper, reservoirs and hydrological stations are taken as control stations when dividing parameter partitions, and the relationship between upstream and downstream of each station is determined according to the topological map of the basin. When the zoning range of the upstream station is determined, the control area of the next station can be obtained according to the flow direction, elevation and other comprehensive parameters. After dividing the parameter partitions, calculate the sub-basin within this parameter zone or all sub-basins in the upstream according to the basin conditions and the specific calculation requirements. When there is a control station in the upstream, read the upstream calculation results according to the upstream downstream relationship and simulate the runoff generation and concentration process of the sub-basin within the parameter division of the station.

(2) Reservoir storage data correction.

This study mainly modifies the reservoir module of Wetspa. The initial reservoir simulation of the model is to directly simulate the outflow, that is, the inflow of the reservoir is simulated first in the internal calculation of the model, and the outflow of the reservoir is obtained through the water balance equation in combination with the measured storage capacity. However, there are cases where the calculated outflow is negative. To solve such problems, the reservoir module in the model is modified in this study. After correcting the abnormal in the measured data, put them in Wetspa to simulate the reservoir inflow and derive the outflow. Among them, the monitoring data of the reservoir is

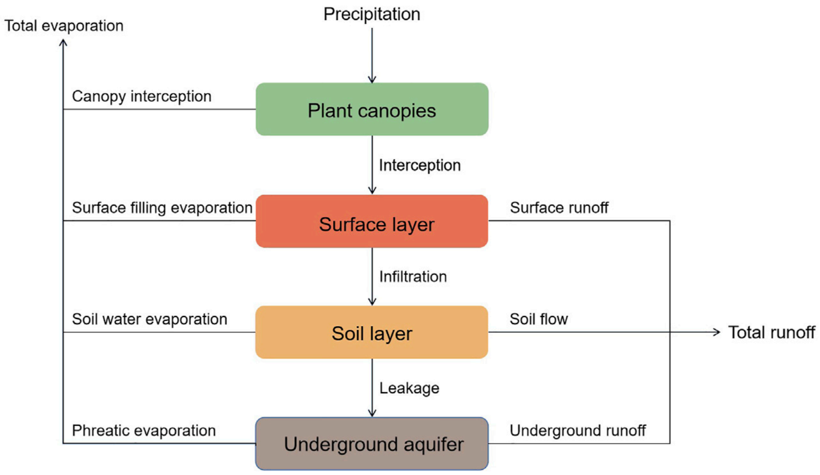

FIGURE 3
The construction of Wetspa flow generation model.

the measured data provided by the Hydrological Bureau, the storage capacity and outflow volume of the reservoir are the real-time monitoring data, and the inflow data is the data derived from the direct water consumption balance equation. However, the jagged fluctuation of the reservoir inflow obtained in this way is obvious, and the inflow is likely to be negative when the outflow is small. Therefore, this study adopts an improved calculation method of the reverse push-in flow process (Liu P. et al., 2017). The specific steps are as follows:

Use the continuity of the process of reservoir inflow to establish the optimization objective function:

$$\min F = \alpha\sum_{i=1}^{n-1}\left(I_{i+1} - I_i\right)^2 + (1-\alpha)\sum_{i=1}^{n+1}\left(V_i - V_i^0\right)^2 \qquad (1)$$

① Where, Ii+1 and Ii are the reservoir inflow water volume in the i+1 and i periods respectively; *α* is the weight coefficient, and the value range is [0,1]. The larger the value, the more attention is paid to the inflow continuity; V_i is the storage capacity of the reservoir in period i; $V_i^0 = f(Z_i)$, Z_i is the water level above the reservoir, and the function F represents the Water level-storage capacity relationship function; n represents the length of reservoir inflow series. After comparison, the *α* value was taken as 0.8 in the calculation of this study.

② According to the water balance equation, the inflow water in the optimization objective function is transformed into a reversed reservoir capacity, and the optimization objective function is converted into a function of outflow flow and reservoir storage capacity, and the Lagrangian function is used to find the partiality of Vi to obtain the analytical formula of the inflow flow of the reversed reservoir.

③ Set a weight coefficient, and bring the reservoir capacity V_i^0, reservoir outflow Ri and weight coefficient into the analytical formula to obtain the inverted reservoir capacity.

④ By introducing the back extrapolated reservoir capacity into the relationship between reservoir capacity and reservoir inflow, the back extrapolated reservoir inflow process can be obtained.

⑤ Negative values in the process of inbound flow after inversion are replaced by linear interpolation results.

(3) Reservoir discharge calculation.

Another improvement of the reservoir module is the part of calculating the outflow process. Since the calculation method of the reservoir in the model has been modified, the reservoir outflow needs to be calculated by the water balance equation with the simulated inflow and measured reservoir capacity. This method is feasible when simulating the period with measured data in the past, but it is difficult to implement in the future runoff forecast because there is no real-time monitoring data. Therefore, the model cannot predict the reservoir outflow. To solve such problems in the future, the following methods are used in this study to calculate the reservoir delivery data in the missing measurement period:

① The Wetspa model is used to simulate the inflow of the reservoir according to the method described above, so as to ensure that there is corresponding inflow in each simulation period.

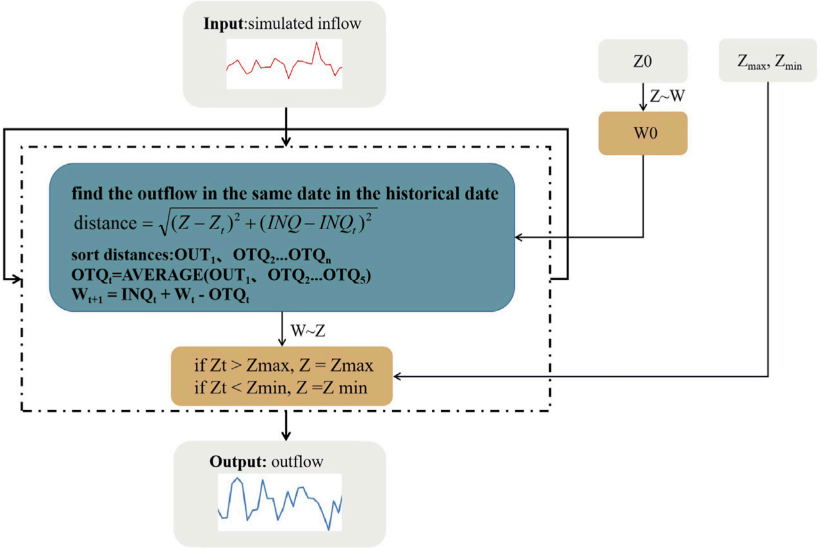

FIGURE 4
Flow chart of reservoir outflow process estimation.

② Set the initial water level value, which can be selected from the most familiar data corresponding to the inflow on the same date in the historical data. Set the maximum and minimum water level according to the historical data.

③ Through analyzing historical data, it is found that at the same or similar water level or storage, the corresponding reservoir outflow is not completely consistent, but it always fluctuates within a range. Therefore, this study uses this law when calculating the storage. In order to avoid the simulation value in the dry season matching to the flood season, the data in the history corresponding to the simulation value on the same day shall be found during the calculation, and use the Euclidean distance to find out the five groups of data that are closest to the simulated water level and storage capacity of the day (Liu and De Smedt, 2005; Ding et al., 2008; Li et al., 2004). The outflow is the mean value of the outflow corresponding to the five groups of data. Taking the mean value can effectively avoid the abnormal extrapolation result caused by taking the maximum or minimum value.

④ The corresponding storage capacity of the current reservoir is found according to the water level storage capacity curve. When the storage capacity is greater than the storage capacity corresponding to the maximum water level or less than the storage capacity corresponding to the minimum water level, the maximum or minimum storage capacity is used. If the queried storage capacity is within this range, the queried storage capacity can be directly used.

⑤ According to the water balance equation, the corresponding storage capacity of the next period is derived. The water level of the next period is queried by using the water level storage capacity curve. According to the above method, use the water level and the simulated stock of this period to query the stock out, and so on to deduce the stock out corresponding to all periods. The specific process is shown in the figure below (Figure 4).

2.3.3 Model evaluation indicators

In this study, Relative Bias (RB) and Nash-Sutcliffe Efficiency (NSE) are used as the evaluation indicators for the simulation results of flow process.

(1) Relative Bias (RB)

$$RB = \frac{\sum_{t=1}^{T}(Q_m^t - Q_o^t)}{\sum_{t=1}^{T} Q_o^t} \tag{2}$$

Where Q_m^t is the simulated flow value at time t, Q_o^t is the observed value at time t, and RB is the relative error between the simulated flow and the measured flow. The closer the RB value is to 0, the smaller the difference between the simulated flow and the measured flow, and the higher the simulation accuracy.

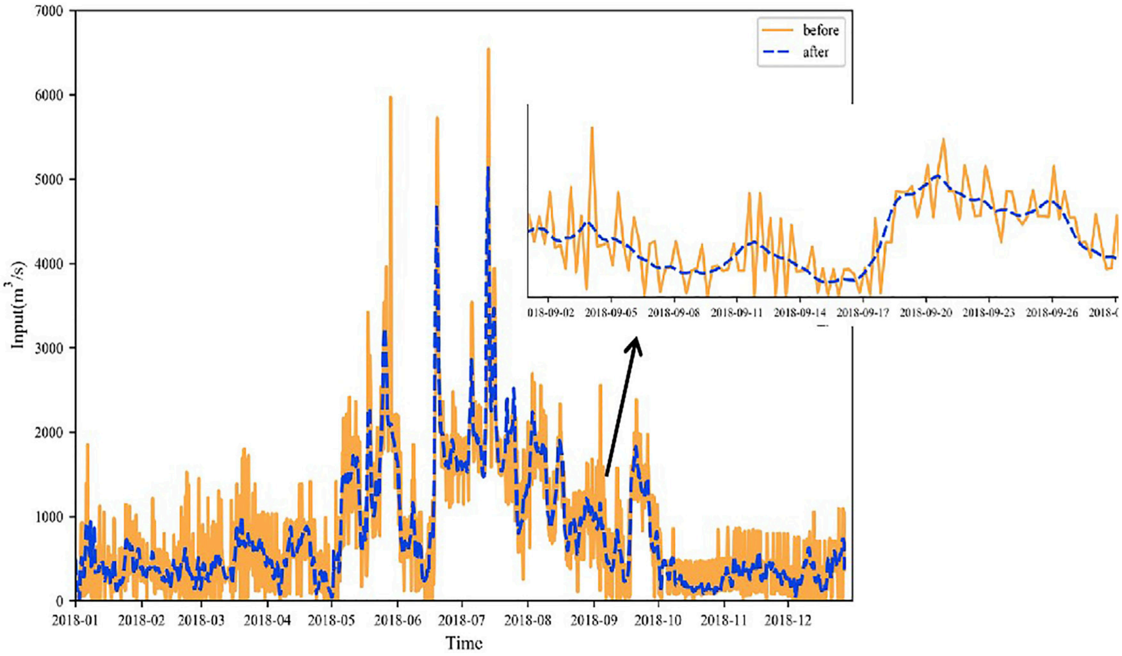

FIGURE 5
The comparison of data of Danjiangkou Reservoir in 2018 before and after correction.

(2) Nash -Sutcliffe Efficiency (NSE)

$$NSE = 1 - \frac{\sum_{t=1}^{T}\left(Q_o^t - Q_m^t\right)^2}{\sum_{t=1}^{T}\left(Q_o^t - \overline{Q_0}\right)^2} \tag{3}$$

Where the meaning of each variable is the same as before, $\bar{Q}_o$ is the average value of the measured flow series, and NSE is the Nash efficiency coefficient, reflecting the fitting effect of large flow. The optimal value of NSE coefficient is 1.

3 Results and analysis

3.1 Model evaluation results

(1) Simulation after model modification.

① Comparison between initial data and corrected data.

In order to ensure the continuity of reservoir inflow and reduce the occurrence of abnormal values, the method mentioned above is used to correct the inflow data of reservoirs in the basin. As shown in the figure (Figure 5), the corrected results of Danjiangkou Reservoir in 2018 are compared with the original data. It is obvious that the corrected inflow process is smoother, there is no zero value, and the “zigzag” fluctuation has been greatly improved.

② Model accuracy after warehousing correction

As mentioned above, this paper improves Wetspa’s reservoir treatment method when simulating runoff, and improves the calculation method of reservoir outflow in the original model while revising the inbound data. Compared with the previous model, the accuracy of the model has been improved; the comparison of the simulation results before and after the correction of the Danjiangkou Reservoir in 2018 is shown in the figure below (Figure 6).

Obviously, the model after correction (Figure 6B) has a higher degree of fit than before correction (Figure 6A). Subsequent cross-sectional simulation results are calculated based on the improved model.

Considering the data length of water intake monitoring data, this paper selects the daily data series from 2016 to 2020 to calibrate and verify the model parameters. Set 2016 as the warm-up period, 2017–2018 as the rate period, and 2019–2020 as the validation period. In this study, Ankang (AK) section in the upper reaches of Hanjiang River, Huangjiagang (HJG) section in the middle reaches and Huangzhuang (HZ) section in the lower reaches are selected as typical sections to verify the applicability of the model in the basin. As AK section is about 1.8 km away from Ankang reservoir (AKR) and HJG section is only 1.05 km away from Danjiangkou reservoir (DJK), the discharge of an upstream reservoir has a great impact on the simulation of downstream stations. It is unreasonable to directly use these

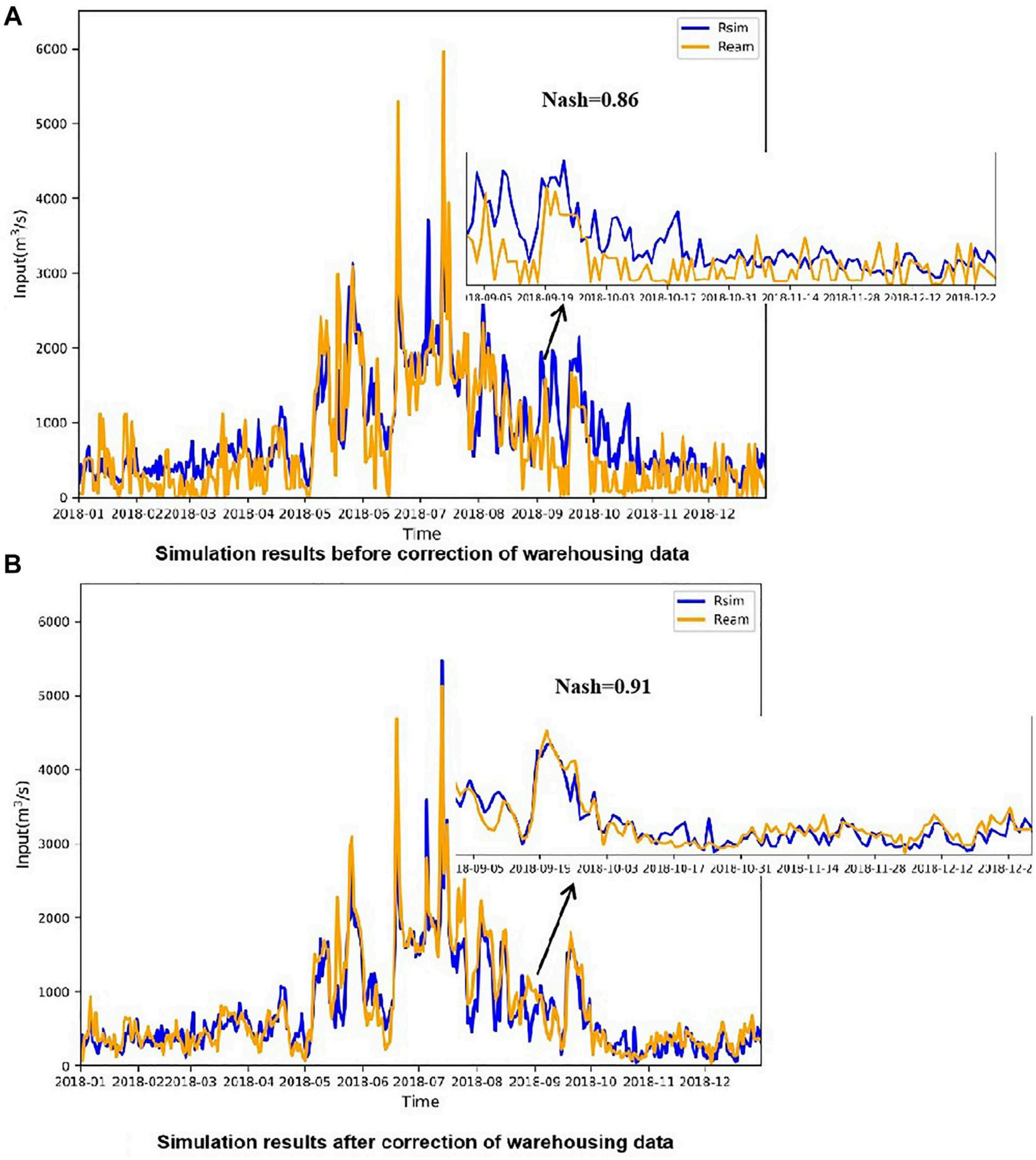

FIGURE 6
The comparison of simulation results of Danjiangkou reservoir after correction of 2018 inflow data. **(A)** shows the simulation results before correction. **(B)** shows the simulation results after correction.

two reservoirs as the measured upstream to simulate the downstream section. Therefore, in this study, the inflow of AKR and DJK and the discharge of HZ section are calibrated. After the parameter calibration is completed, the calculation results of the three stations in the calibration period and validation period are counted by using the above model evaluation indicators, and the statistical results are shown in the table below (Table 2).

TABLE 2 Index evaluation results of each section.

Parameter	AKR		DJK		HZ	
	RB	NSE	RB	NSE	RB	NSE
calibration (2017–2018)	−0.14	0.79	−0.05	0.94	−0.08	0.93
validation (2019–2020)	−0.17	0.73	−0.16	0.83	−0.03	0.85

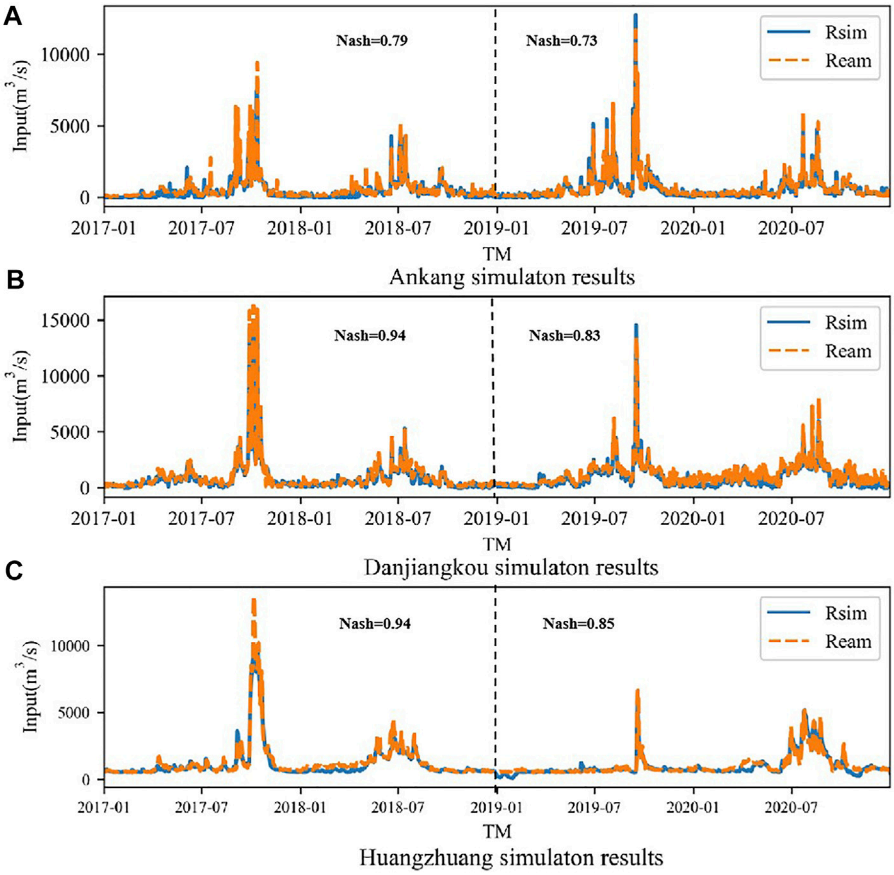

FIGURE 7
Simulation results of three section rates at calibration and validation periods (m^3/s). **(A–C)** are the simulation results of Ankang, Huangjiagang and Huangzhuang respectively.

It can be seen from the above table that the NSE coefficient of AKR, DJK, and HZ are all above 0.7, and the absolute value of Relative Bias is less than 20%. The simulation results are good (Figure 7). Based on the simulation results and various parameters, it can be considered that the Wetspa model can be better applied to the simulation of runoff process in the Hanjiang River Basin, and the model can be used for subsequent research and analysis.

3.2 Comparison and selection of climate model assessment

In this study, the runoff of the three typical sections of the Hanjiang River Basin in the next 40 years is simulated by selecting one of the five climate models with the most similar trend to the historical data of the Hanjiang River. According to the principle of the model, rainfall is the most significant elements for the runoff simulation results of the model, so rainfall is used as the basis for the evaluation and selection of climate models (Liu et al., 2005; Liu J. et al., 2017). The historical data of CMIP6 model are from 1961 to 2011. In order to ensure the time consistency of the two data, this study selects the historical data of Hanjiang River Basin from 1961 to 2011 and the historical data of the same time period under the five scenarios of CMIP6 for comparison, and takes the absolute difference and percentage deviation of the two as the selection indicators of model data. The more obvious the absolute difference and percentage deviation are, the more similar they are.

In order to more accurately reflect the future precipitation in the Hanjiang River Basin, this study uses Tyson polygon to calculate the weight of each station, multiply it by the rainfall of the corresponding station and sum it to obtain the area rainfall. The following table shows the multi-year average rainfall of the measured data and the five model data, as well as the absolute difference and percentage deviation of the area rainfall of each model relative to the measured value (Table 3). It can be seen from the table that there is the smallest absolute difference and percentage deviation between the simulated value under

TABLE 3 Difference between five model data and measured data.

Model	Average/mm	Difference/mm	Percentage deviation/%
Percentage deviation	778.73	—	—
CanESM	909.71	130.98	16.82
MRI-ESM2-0	916.41	137.68	17.68
IPSL-CM6A-LR	909.94	131.21	16.85
KACE-1-0-G	919.90	141.17	18.13
NESM3	909.54	130.91	16.80

NESM3 mode and the historical measured value from 1961 to 2011, which proves that the meteorological data under this model is more suitable for the Hanjiang River Basin.

3.3 Analysis of future rainfall data

The figure below shows the overall change trend from 2021 to 2060 under the three scenarios of NESM3 mode and the inter-annual change and trend every 10 years in the future (Figure 8). It can be seen from the figure that the inter-annual variation of rainfall is large, in which SSP1-2.6 shows a downward trend as a whole, while SSP2-4.5 and SSP5-8.5 show an upward trend, and the upward trend of SSP2-4.5 is more obvious than SSP5-8.5. Among them, the decline rate of SSP1-2.6 is 1.48 mm/a, the rising trend of SSP2-4.5 and SSP5-8.5 is 3.89 mm/a, and 3.19 mm/a respectively, and the multi-year average precipitation of SSP2-4.5 is greater than that of SSP5-8.5. In SSP1-2.6, although the overall trend of rainfall is declining, the decline rate slows down, and even there is an increasing trend from 2051 to 2060, but the increase rate is slow, only 0.51 mm/a. In SSP2-4.5, although the overall trend of rainfall increases, only the rainfall from 2031 to 2040 shows an increasing trend. Although the rainfall from 2051 to 2060 shows a decreasing trend, the multi-year average value in these 10 years is the largest, reaching 1089.31 mm. The rainfall of SSP5-8.5 shows an increasing trend from 2021 to 2050, but the rainfall starts to decrease at the rate of 3.25 mm/a from 2051 to 2060. The maximum and minimum rainfall during this period are the minimums in all future forecast periods.

3.4 Future runoff estimation

Based on the Wetspa model, this paper simulates the runoff of Hanjiang River Basin in 2021–2060 under different emission forcing scenarios of NESM3 model. In the future runoff forecast, the model simulates from upstream to downstream according to the divided parameter zoning. When simulating the reservoir section, the simulation results need to be corrected by the correction method in the previous article before the outbound calculation, so as to prevent the abnormal values in the simulated inbound from affecting the outbound results. The spatial and temporal variation of runoff in the Hanjiang River Basin in the future is analyzed from the inter-annual variation, average runoff, seasonal runoff and monthly runoff.

(1) Inter-annual variation of runoff.

The figure below shows the overall change of rainfall and runoff from 2021 to 2060 under three scenarios simulated by three typical sections (Figure 9). It can be seen from the figure that the annual runoff of AK section shows a downward trend under SSP1-2.6 and upward trends under SSP2-4.5 and SSP5-8.5, which is consistent with the overall future change trend under the three rainfall scenarios. The annual runoff changes of HJG section and HZ section show an upward trend.

The figure shows the change trend of runoff every 10 years for the three sections under the three scenarios of SSP1-2.6, SSP2-4.5, and SSP5-8.5 (Figure 10). According to the figure, except for individual years, the time corresponding to the maximum and minimum values of runoff in different years of the three sections is basically the same as that corresponding to the maximum and minimum values of rainfall in different years. In different scenarios, the runoff variation trends of the three sections in different prediction periods are also different. During the period from 2021 to 2030, the annual runoff of AK section shows a downward trend under SSP1-2.6 and SSP2-4.5, while it shows an upward trend under SSP5-8.5. During the same period, the runoff of HJG section shows an upward trend under all three scenarios, with a change range of 41.62 mm/(s*a) under SSP5-8.5. The annual runoff of HZ section shows a downward trend under SSP1-2.6, and an upward trend under the other two scenarios. From 2031 to 2040, the annual runoff of AK section shows a downward trend under SSP1-2.6 and SSP5-8.5, an upward trend under SSP2-4.5. The annual runoff of HJG shows an upward trend under SSP1-2.6 and SSP2-4.5, and a downward trend under SSP5-8.5, while the annual runoff of HZ section shows a downward trend under SSP1-2.6 and SSP5-8.5, and an upward trend under SSP2-4.5. From 2041 to 2050, AK section, HJG section and HZ section all show an upward trend under SSP1-2.6 and SSP5-8.5, and a downward trend under SSP2-4.5. From 2051 to 2060, the annual runoff of the three sections shows an upward trend

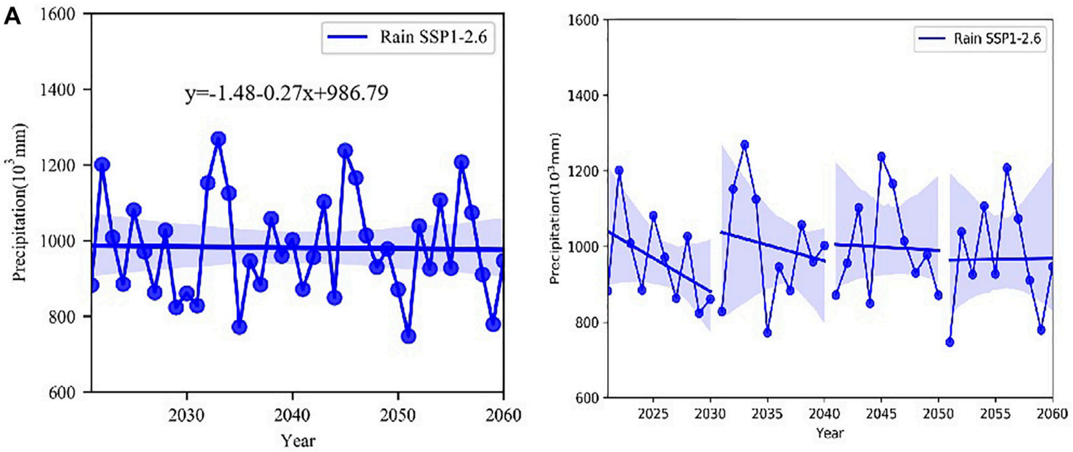

Inter-annual variation trend of rainfall under SSP1-2.6 scenario

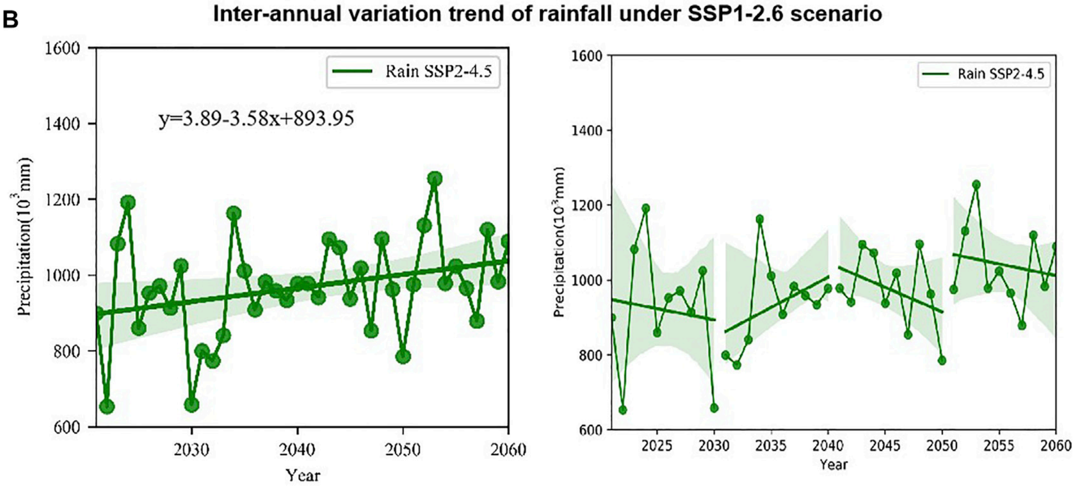

Inter-annual variation trend of rainfall under SSP2-4.5 scenario

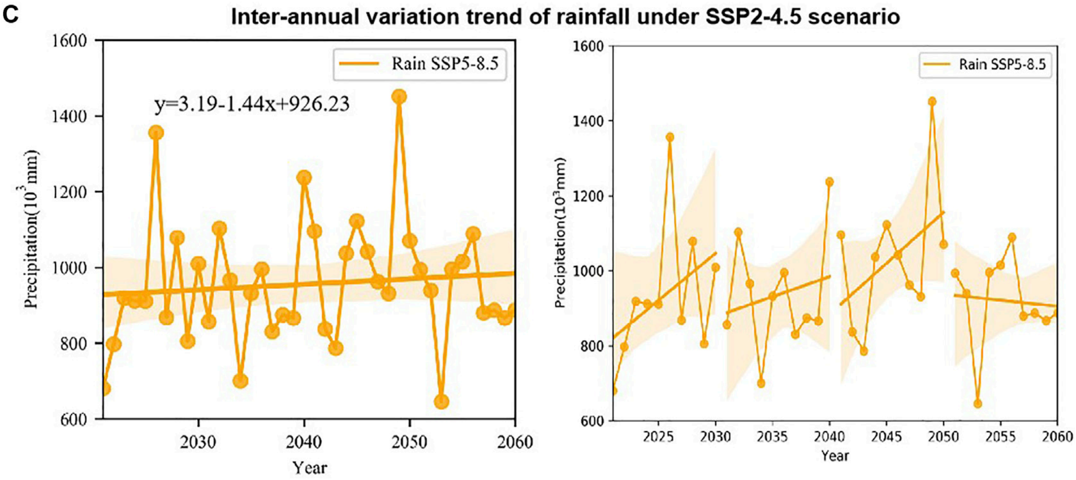

Inter-annual variation trend of rainfall under SSP5-8.5 scenario

FIGURE 8
Inter-annual variation trend of future rainfall under three scenario. **(A–C)** are the inter-annual variation of rainfall under SSP1-2.6, SSP2-4.5 and SSP5-8.5 scenarios respectively.

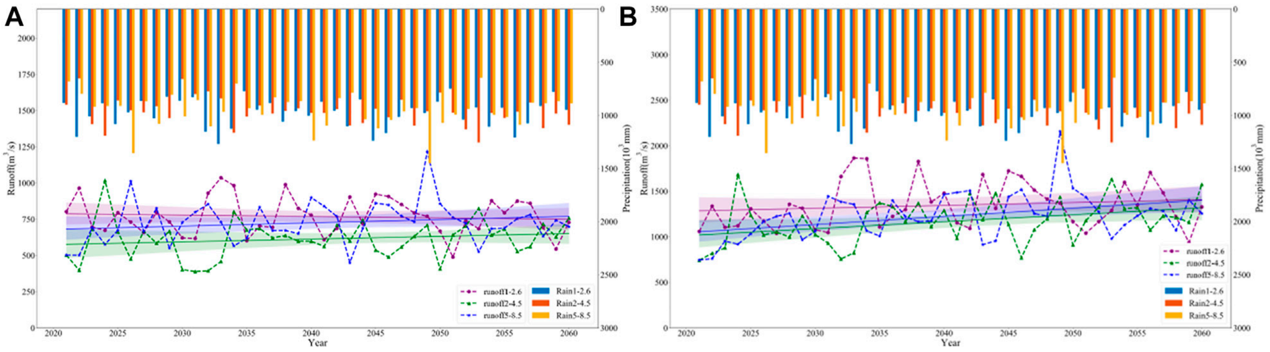

Future runoff change trend in AK

Future runoff change trend in HJG

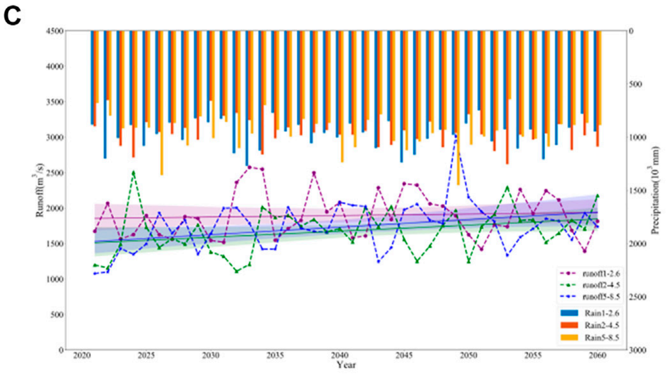

Future runoff change trend in HZ

FIGURE 9
Overall changes of rainfall and runoff from 2021 to 2060 under different scenarios simulated by three typical sections. **(A–C)** are the overall inter-annual variation trend of runoff in AK, HJG and HZ under SSP1-2.6, SSP2-4.5 and SSP5-8.5 respectively.

in SSP1-2.6 and SSP5-8.5 scenarios, and a downward trend in SSP2-4.5 scenarios.

② Average runoff variation.

Taking the measured data of 40 years from 1981 to 2020 as a reference, it is compared with the simulated runoff in the next 40 years. The difference between the average runoff of AK section, HJG section, HZ section in the future (2021–2060) and the reference period (1981–2020) is shown in the figure (Figure 11). The average flow of AK section, HJG section and HZ section under the three scenarios has an increasing trend compared with the reference period. Among them, the order of average runoff increments of AK, HJG, and HZ is SSP1-2.6 > SSP5-8.5 > SSP2-4.5.

③ Proportion of seasonal runoff.

The difference of the seasonal runoff proportion of the three sections under NESM3 model relative to the historical period is shown in the figure below (Figure 12). The four seasons in this study are divided according to the division method of the meteorological department, that is, from March to May is spring, from June to August is summer, from September to November is autumn, and from December to next February is winter. The three sections have a high proportion of summer runoff in the base period and the three scenarios, followed by spring and autumn, and the lowest proportion of winter runoff. Compared with the reference period, the runoff proportion of AK section decreases in autumn, and increases in spring, summer and winter; The proportion of runoff in HJG section decreased in summer and autumn, and decreased greatly in autumn, and increased in spring and winter; The runoff proportion of HZ section decreases in autumn and winter, and increases in spring and summer. To sum up, in three scenarios, the proportion of runoff in spring shows an increasing trend, while the proportion of runoff in autumn shows a decreasing trend. The increasing and decreasing trends of the three sections in summer and winter are different.

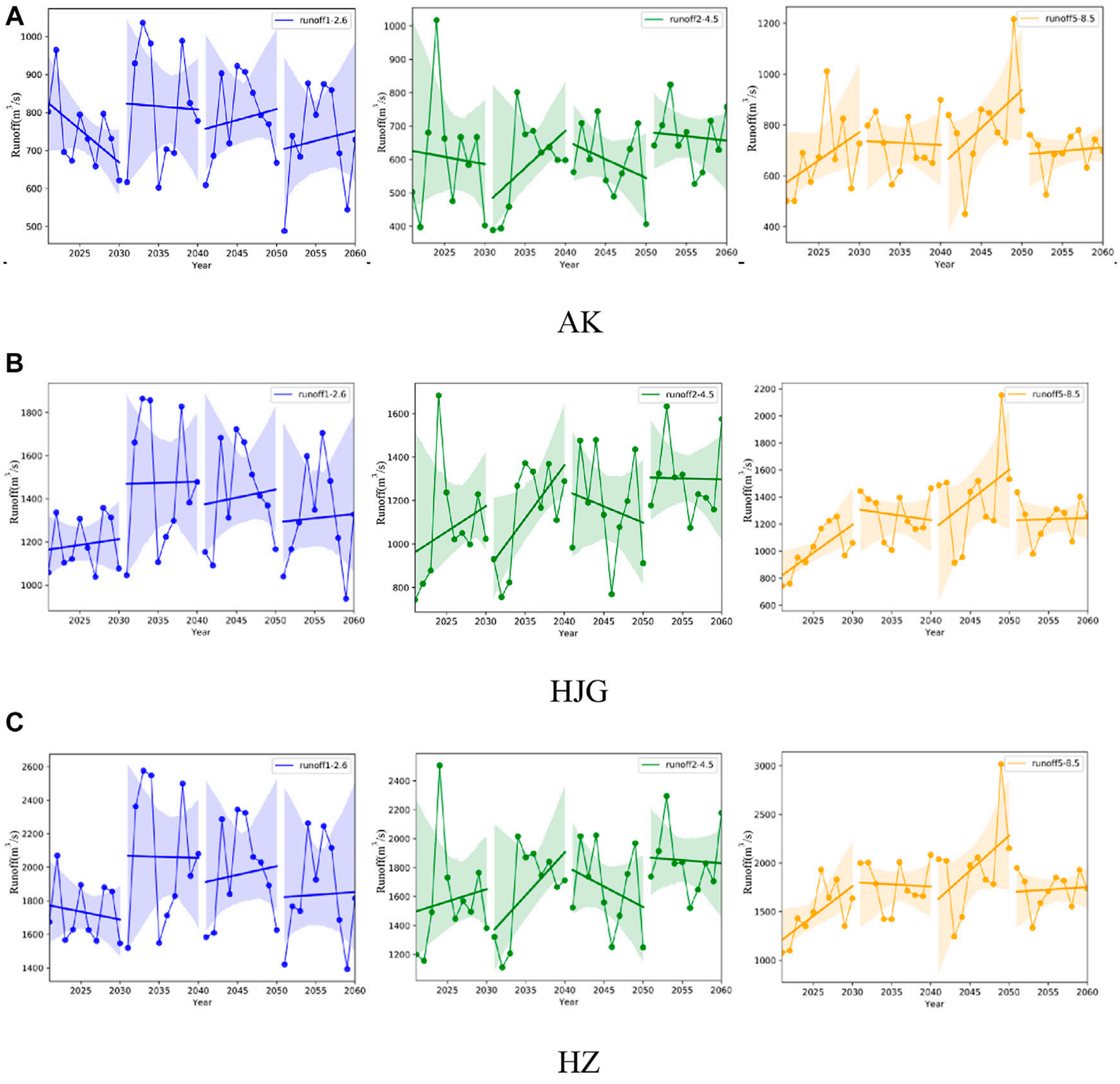

FIGURE 10
Change trend of the three sections with every 10 years as nodes under different scenarios. **(A–C)** are the inter-annual variation trends of runoff in AK, HJG and HZ under SSP1-2.6, SSP2-4.5 and SSP5-8.5 respectively.

Climate change has the most significant impact on Runoff in spring, autumn and winter.

The difference of the monthly runoff proportion of the three sections under different scenarios relative to the base period is shown in the figure below (Figure 13). Compared with the base period, the runoff proportion of AK and HJG sections shows an increasing trend from February to June, and increases most in May and June, and decreases from August to November, of which August and September decrease most. The changes in January, February and July are uncertain. Except for SSP2-4.5, the other two scenarios of AK section show an increasing trend, while the three scenarios of HJG section show a decreasing trend. Under the two scenarios of SSP1-2.6 and SSP2-4.5, the runoff proportion of HZ section increases from April to June, and increases the most in June. The runoff proportion of January to March and August to December decreases, while the runoff proportion of all months under SSP5-8.5 shows an increasing trend.

4 Discussion

(1) Temporal and spatial variation characteristics of runoff

In this paper, the improved Wetspa model is used to simulate the future runoff of the Hanjiang River Basin by selecting the

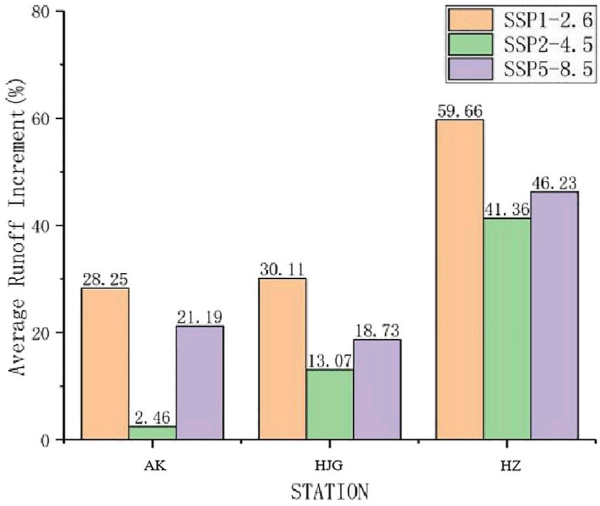

FIGURE 11
Differences between the average runoff of three sections from 2021 to 2060 and the reference period (%).

meteorological data of the CMIP6 model with the closest change trend to the historical measured data. By analyzing the rainfall data under this model and the simulated runoff data, it is found that the future runoff change trend of the upstream AK is basically the same as that of the future rainfall, indicating that for the AK section, the rainfall change is positively correlated with the increase or decrease of runoff, while the Runoff Trend of the middle HJG and the runoff law of the downstream HZ are significantly different from that of AK, regardless of the rainfall trend under the three scenarios. The runoff generally shows an upward trend, which is affected by the blocking river at the upstream of HJG and the Nanhe River and Tangbai river at the upstream of HZ. Under the two scenarios of SSP 2–4.5 and SSP 5–8.5, where the runoff trend of the three sections is upward, the runoff growth of HJG and HZ sections corresponding to the upstream and downstream sections is also larger than that of AK section. The main reason for the decrease of runoff in the upstream of Hanjiang River is the operation of reservoirs in the middle reaches and the influence of other human activities (Li et al., 2020). The influence of reservoir regulation on the downstream can not be ignored (Cong et al., 2013). When forecasting future runoff, the following conclusions can be drawn: It is very important to carry out reservoir simulation.

The correlation between the multi-year average runoff of the three sections and the multi-year average value of area rainfall is slightly different. The multi-year average runoff of each section simulated by the three scenarios is SSP1-2.6 > SSP5-8.5 > SSP2-4.5, while the multi-year average value of area rainfall is SSP1-2.6 > SSP2-4.5 > SSP5-8.5. The reason for this may be that the comparison of areal rainfall is the comparison of the whole basin, and the rainfall stations affecting the three sections are only a part of these data. Because the three sections selected are typical sections in the upper, middle and lower reaches of the Hanjiang River Basin, the three sections are far apart, and the rainfall stations do not overlap each other, and the size relationship is not consistent, which leads to the difference in the average rainfall of the three sections over the years (Table 4). The runoff of the Hanjiang River basin increases most in spring and winter, and reaches its peak value in May and June, which is consistent with the conclusions reached by Xiang et al. (2021). in Yarkant River Basin. Ji et al. (2021) found that the runoff in spring decreases while the runoff in winter increases. In April, May, June, July, October, Tang Naihai, Toudaoguan, Sanmenxia, and Lijin hydrological stations, the monthly

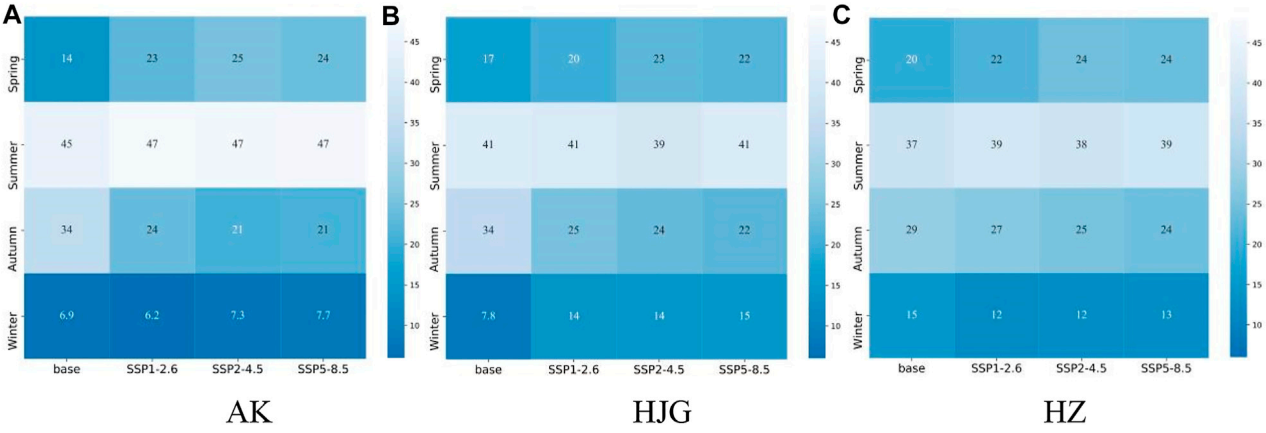

FIGURE 12
Difference of seasonal runoff proportion of three sections under NESM3 mode relative (%). **(A–C)** are the seasonal runoff distribution of AK, HJG and HZ under SSP1-2.6, SSP2-4.5 and SSP5-8.5 compared with the historical period.

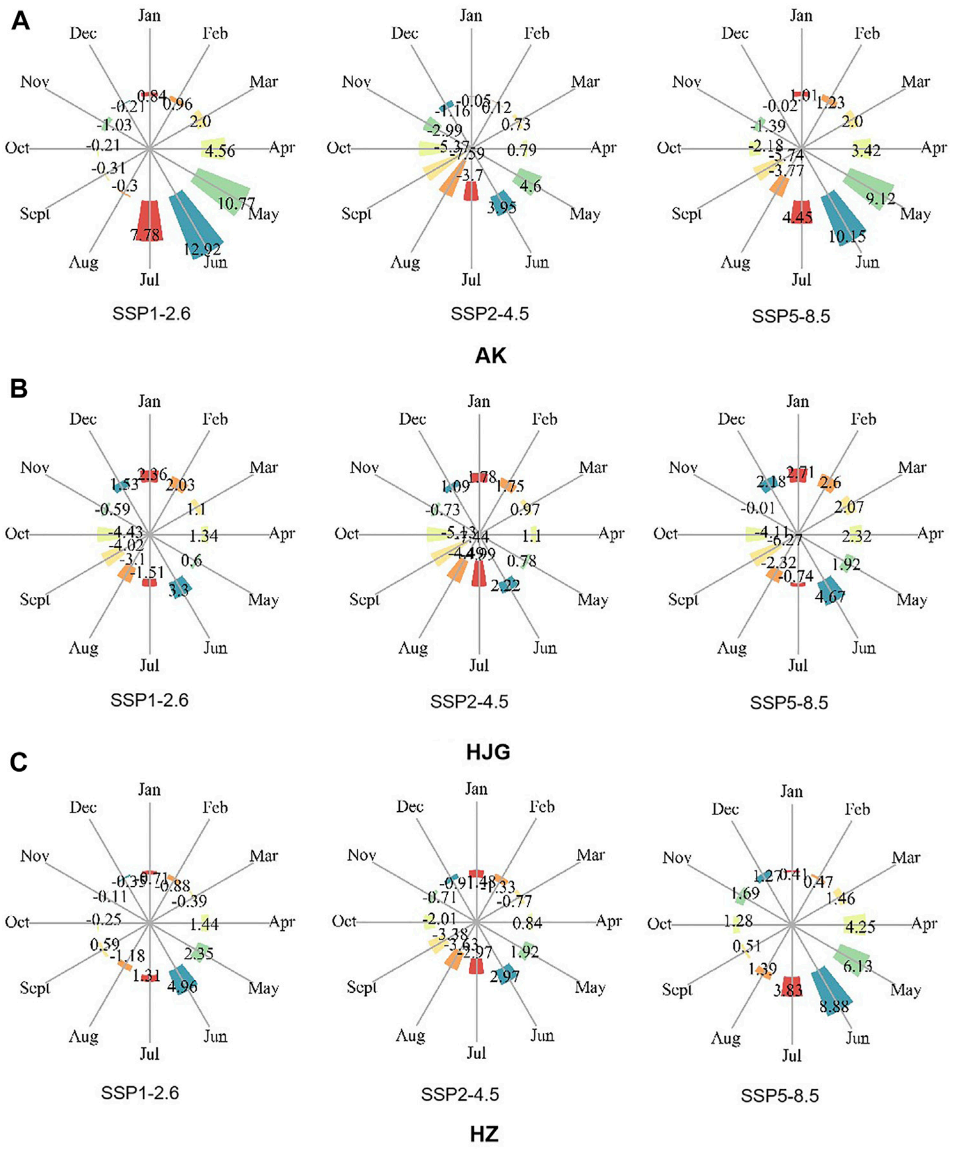

FIGURE 13
Difference of monthly runoff proportion of three sections under different scenarios relative to historical period (%). **(A–C)** are the monthly runoff distribution of AK, HJG and HZ under SSP1-2.6, SSP2-4.5 and SSP5-8.5 compared with the historical period.

TABLE 4 Average runoff and rainfall of three sections under three scenarios.

Station	Runoff (m^3/s)			Percipitation (mm/d)		
	SSP1-2.6	SSP2-4.5	SSP5-8.5	SSP1-2.6	SSP2-4.5	SSP5-8.5
AK	768.34	618.82	726.05	2.57	2.49	2.46
HJG	1345.89	1169.55	1228.18	2.45	2.28	2.27
HZ	1897.32	1679.85	1737.67	2.73	2.13	2.56

runoff ratio shows a downward trend. This gap may be caused by different impacts of human activities on Runoff in different watershed.

(2) Advantages and limitations of Wetspa model and uncertainty of simulation results of measured data

Based on the improved Wetspa model, this paper simulates the runoff change of the Hanjiang River basin in the future 2021–2060 years. The layered structure and grid calculation method of Wetspa model make it universal and portable, at the same time, the topological thinking of the model in modeling can well consider the impact of reservoir regulation and water access in the basin, and it can also produce good results for runoff simulation of Complex Watershed (De Smedt et al., 2004). The improved Wetspa model solves the difficult problem of reservoir inflow and outlet and reservoir capacity calculation when no measured data is available, so the role of reservoir storage can be considered in forecasting future runoff changes of Hanjiang River Basin. Through the research above, it can be found that when calibrating and validating the measured data of AK, HJG, and HZ sections in 2016–2020, although it can be proved that the Wetspa model is applicable used in the Hanjiang River Basin, there are still large errors between the simulated results and measured data in some time periods (Figure 7), and this is unavoidable, which is caused by the limitations of the model. It mainly includes the following aspects: 1) There is uncertainty in the description of runoff-runoff process by mathematical formula, which may lead to different simulation effects of different models (Jiang et al., 2007); 2) Considering the limitation of the length of measured water consumption data, only 4 years of historical data are used for model calibration verification, and the evaporation data in the model are calculated by Penman formula instead of measured data, which will also affect the forecast of future runoff. 3) Reservoir storage of large reservoir will affect regional climate change and result in hydrological change (Wu et al., 2006). Therefore, it is very important for reservoir treatment and forecasting runoff in the future. The improved model needs to analyze historical data when calculating future reservoir reserve conditions. If the length of historical data is too short, it may lead to abnormal values of the calculated results. 4) Like other physical models, Wetspa calculates from upstream to downstream in turn, so errors accumulate gradually, and simulation results using artificial intelligence and other methods may be better (Wu and Chau, 2011; Fotovatikhah et al., 2018). Therefore, in the follow-up study, it is necessary to further modify the model to make the simulation process more in line with the physical process of rainfall-runoff and remove the unreasonable values in the simulation results. In addition, more comprehensive data should be collected to carry out long-sequence data simulation during simulation to improve the simulation accuracy.

(3) Influence of future climate model data on simulation results

Future climate model data are highly uncertain (Xu et al., 2011; Teng et al., 2012). These uncertainties are highly related to the corresponding structure, parameters and spatial resolution of the global climate model (Yan et al., 2015). When forecasting the future, there is a significant gap between the future climate model data and historical measured data even though the trend is similar. Therefore, its replacement effect to historical data is not necessarily excellent. In addition, the choice of different climate models has a great influence on the simulation results. For example, Guo et al. found that the annual change trend is different between CGSM2 model and HadCM3 model, the runoff increase and decrease trend is uncertain in 2020s, there is no significant change in 2050s in CGCMS model and increase in HadCM3 model. However, the runoff increase and decrease in three sections simulated based on three scenarios of NESM3 model is uncertain in 2020s and 2050s. Besides that, different model data will affect the forecasting results As shown above, even the simulated runoff change trend and annual runoff distribution of the data in the same model under different scenarios are different. Therefore, the simulation results of any model in any basin may not reflect the true runoff change of the Hanjiang River basin in the next 40 years. Its main function is to provide reference for future planning and utilization of water resources in the Hanjiang River Basin. In addition to considering the meteorological data itself, meteorological elements, especially precipitation, have a great impact on land use and will also affect the future runoff simulation (Yu et al., 2022). In the follow-up study, we will also study other impacts of meteorological elements on runoff simulation, try more methods to modify future meteorological data or use more climate model data to estimate future runoff.

5 Conclusion

Based on the Wetspa model of the improved reservoir module, this paper verifies the applicability of the model in the Hanjiang River Basin, simulates the runoff change of the Hanjiang River Basin under the action of climate, and analyzes the overall change of the runoff trend, the change of each year, the average runoff and the annual distribution of the three typical sections of the Hanjiang River in the future. The research conclusions are as follows:

(1) The accuracy of reservoir simulation of the improved Wetspa model has been greatly improved, and the Nash coefficient of Danjiangkou reservoir simulation results has increased from 0.86 to 0.91. The determination coefficient and Nash efficiency coefficient of the improved Wetspa model in AKR, DJK, and HZ sections are greater than 0.7, and the model has good

accuracy and is suitable for the Hanjiang River Basin. By comparing the area rainfall of historical data and model data in Hanjiang River Basin, the percentage deviation of NESM3 model data relative to historical data is the smallest, so nesm3 model data is selected as the meteorological data for future runoff forecast.

(2) From 2021 to 2060, the runoff of AK section shows a downward trend, while the runoff of HJG section and HZ section shows an upward trend. Taking every decade as a node, except for individual time, the change trends of the three sections in the same period and under the same scenario are consistent. From 2041 to 2050, under the SSP5-8.5 scenario, the runoff of the three sections will have the maximum extreme value ratio and change range in the future prediction period, indicating that the runoff of each section will change dramatically during this period, and attention should be paid to the risk of flood disaster. From 2051 to 2060, the three sections have small extreme value ratio and change range under SSP2-4.5 and SSP5-8.5 scenarios, indicating that the runoff of each section is relatively stable during this period.

(3) Compared with the reference period (1981–2020), the average runoff of Hanjiang River Basin in the future (2021–2060) years shows an increasing trend. Accordingly, the possibility of flood disaster also shows an increasing trend. Under the influence of climate change, the runoff proportion of Hanjiang River Basin in spring and winter shows an increasing trend, and the increase is more obvious in spring. Attention should be paid to the risk of flood in spring. The proportion in autumn is decreasing. Attention also should be paid to the risk of drought in autumn to reduce the impact on crops.

Data availability statement

The original contributions presented in the study are included in the article/Supplementary Material, further inquiries can be directed to the corresponding author.

Author contributions

Conceptualization: SC and LS; Methodology: SC and QL; Writing-original draft preparation: SC; Writing-review and editing: SC and YJ; Guiding: HW. All authors read and approved the final manuscript.

Funding

This work was funded by the National Key Research and Development Program of China (2021YFC3000205), the National Nature Science Fund (42175178), the National Natural Science Fund (U20A20316), and the Hebei Natural Science Fund (E2020402074).

Acknowledgments

We are very grateful to the editors and reviewers for their critical comments and thoughtful suggestions.

Conflict of interest

The authors declare that the research was conducted in the absence of any commercial or financial relationships that could be construed as a potential conflict of interest.

Publisher's note

References

Al-Faraj, F. A. M., and Al-Dabbagh, B. N. S. (2015). Assessment of collective impact of upstream watershed development and basin-wide successive droughts on downstream flow regime: The Lesser Zab transboundary basin. *J. Hydrology* 530, 419–430. doi:10.1016/j.jhydrol.2015.09.074

Batelaan, O., Wang, Z. M., and De Smedt, F. (1996). "An adaptive GIS toolbox for hydrological modelling[J]," in *IAHS publications-series of proceedings and reports-intern assoc hydrological sciences*, 235, 3–10.

Cong, M. A., Chunxia, L. U., and Yiqiu, L. (2013). Runoff change in the lower reaches of Ankang Reservoir and the influence of Ankang Reservoir on its downstream[J]. *Resour. Environ. Yangtze Basin* 22 (11), 1433–1440.

De Smedt, F. H., Liu, Y. B., and Gebremeskel, S. (2004). "Application of GIS and remote sensing in flood [J]," in *GIS and remote sensing in hydrology, water resources and environment* (289), 23.

Ding, H., Trajcevski, G., Scheuermann, P., Wang, X., and Keogh, E. (2008). Querying and mining of time series data: Experimental comparison of representations and distance measures[J]. *Proc. VLDB Endow.* 1 (2), 1542–1552. doi:10.14778/1454159.1454226

Fotovatikhah, F., Herrera, M., Shamshirband, S., Chau, K. W., Faizollahzadeh Ardabili, S., and Piran, M. J. (2018). Survey of computational intelligence as basis to big flood management: Challenges, research directions and future work. *Eng. Appl. Comput. Fluid Mech.* 12 (1), 411–437. doi:10.1080/19942060.2018.1448896

Guo, J., Cheng, K. Y., Xiong, L. H., and Chen, H. (2012). Prediction of the future runoff of the upper Hanjiang Basin under the climate change conditions. *Adv. Mater. Res.* 518, 4194–4200. Trans Tech Publications Ltd. doi:10.4028/www.scientific.net/AMR.518-523.4194

Guo, S., Guo, J., Hou, Y., Xiong, L., and Hong, X. (2015). Prediction of future runoff change based on Budyko hypothesis in Yangtze Riverbasin[J]. *Adv. Water Sci.* 26 (2), 151–160. doi:10.14042/j.cnki.32.1309.2015.02.001

Hayal, D., Brook, L., and Ephrem, G. (2017). Identifying sustainability challenges on land and water uses: The case of lake ziway watershed, Ethiopia[J]. *Appl. Geogr.* 88, 130–143. doi:10.1016/j.apgeog.2017.09.005

Homa, E. S., Brown, C., Mcgarigal, K., Compton, B. W., and Jackson, S. D. (2013). Estimating hydrologic alteration from basin characteristics in Massachusetts. *J. Hydrology* 503, 196–208. doi:10.1016/j.jhydrol.2013.09.008

IPCC (2014). *Climate change 2014: Impacts, adaptation, and vulnerability[M].* Cambridge: Cambridge University Press.

Ji, G., Lai, Z., Xia, H., Liu, H., and Wang, Z. (2021). Future runoff variation and flood disaster prediction of the Yellow River Basin based on CA-markov and SWAT. *Land* 10 (4), 421. doi:10.3390/land10040421

Jiang, T., Chen, Y. D., Xu, C., Chen, X., Chen, X., and Singh, V. P. (2007). Comparison of hydrological impacts of climate change simulated by six hydrological models in the Dongjiang Basin, South China. *J. hydrology* 336 (3-4), 316–333. doi:10.1016/j.jhydrol.2007.01.010

Li, Q., Chi, Z., and Sun, R. C. (2004). A novel similar matching algorithm for time series data. *Control Decis.* 19, 915–919. doi:10.3321/j.issn:1001-0920.2004.08.017

Li, S., Zhang, L., Du, Y., Zhuang, Y., and Yan, C. (2020). Anthropogenic impacts on streamflow-compensated climate change effect in the Hanjiang River basin, China. *J. Hydrol. Eng.* 25 (1), 04019058. doi:10.1061/(asce)he.1943-5584.0001876

Liu, J., Zhang, Q., Singh, V. P., and Shi, P. (2017). Contribution of multiple climatic variables and human activities to streamflow changes across China. *J. Hydrology* 545, 145–162. doi:10.1016/j.jhydrol.2016.12.016

Liu, P., Deng, C., and Zhang, W.lizejun (2017). *A method for calculating the reservoir inflow process*. Hubei Province: State Intellectual Property Office of the People's Republic of China. cn104021307b.

Liu, Y. B., Batelaan, O., Smedt, F. D., Huong, N. T., and Tam, V. T. (2005). Test of a distributed modelling approach to predict flood flows in the karst Suoimuoi catchment in Vietnam. *Environ. Geol.* 48 (7), 931–940. doi:10.1007/s00254-005-0031-1

Liu, Y. B., and De Smedt, F. (2005). Flood modeling for Complex terrain using GIS and remote sensed information. *Water Resour. manage.* 19 (5), 605–624. doi:10.1007/s11269-005-6808-x

Liu, Y. B., and De Smedt, F. (2004). *Wetspa extension, a GIS-based hydrologic model for flood prediction and watershed management*, Belgium: Vrije Universiteit Brussel, 1, e108.

Liu, Y. B., Gebremeskel, S., De Smedt, F., Hoffmann, L., and Pfister, L. (2006). Predicting storm runoff from different land-use classes using a geographical information system-based distributed model. *Hydrol. Process.* 20 (3), 533–548. doi:10.1002/hyp.5920

Ma, D., Deng, H., Yin, Y., Wu, S., and Zheng, D. (2019). Sensitivity of arid/humid patterns in China to future climate change under a high-emissions scenario. *J. Geogr. Sci.* 29 (1), 29–48. doi:10.1007/s11442-019-1582-5

Nashwan, M. S., and Shahid, S. (2020). A novel framework for selecting general circulation models based on the spatial patterns of climate. *Int. J. Climatol.* 40 (10), 4422–4443. doi:10.1002/joc.6465

Teng, J., Vaze, J., Chiew, F. H. S., Wang, B., and Perraud, J. M. (2012). Estimating the relative uncertainties sourced from GCMs and hydrological models in modeling climate change impact on runoff. *J. Hydrometeorol.* 13 (1), 122–139. doi:10.1175/jhm-d-11-058.1

Wang, G. Q., Yan, X. L., Zhang, J. Y., Liu, C. S., Jin, J. L., Liu, Y. L., et al. (2013). Detecting evolution trends in the recorded runoffs from the major rivers in China during 1950–2010. *J. Water Clim. Change* 4 (3), 252–264. doi:10.2166/wcc.2013.021

Wang, G. Q., Zhang, J. Y., He, R. M., Liu, C., Ma, T., Bao, Z., et al. (2017). Runoff sensitivity to climate change for hydro-climatically different catchments in China. *Stoch. Environ. Res. Risk Assess.* 31 (4), 1011–1021. doi:10.1007/s00477-016-1218-6

Wang, Z. M., Batelaan, O., and DeSmedt, F. (1996). A distributed model for water and energy transfer between soil, plants and atmosphere (Wetspa) [J]. *Phys. Chem. Earth* 21, 189–193. doi:10.1016/S0079-1946(97)85583-8

Wei, J., Chang, J., and Chen, L. (2016). Runoff change in upper reach of Yellow River under future climate change based on VIC model[J]. *J. Eng.* 35, 65–74. doi:10.11660/slfdxb.20160508

Wu, C. L., and Chau, K. W. (2011). Rainfall–runoff modeling using artificial neural network coupled with singular spectrum analysis. *J. Hydrology* 399 (3-4), 394–409. doi:10.1016/j.jhydrol.2011.01.017

Wu, L., Zhang, Q., and Jiang, Z. (2006). Three Gorges Dam affects regional precipitation. *Geophys. Res. Lett.* 33 (13), L13806. doi:10.1029/2006gl026780

Xiang, Y., Wang, Y., Chen, Y., and Zhang, Q. (2021). Impact of climate change on the hydrological regime of the Yarkant River basin, China: An assessment using three SSP scenarios of CMIP6 GCMs. *Remote Sens.* 14 (1), 115. doi:10.3390/rs14010115

Xu, H., Taylor, R. G., and Xu, Y. (2011). Quantifying uncertainty in the impacts of climate change on river discharge in sub-catchments of the Yangtze and Yellow River Basins, China. *Hydrol. Earth Syst. Sci.* 15 (1), 333–344. doi:10.5194/hess-15-333-2011

Yaghmaei, H., Sadeghi, S. H., Moradi, H., and Gholamalifard, M. (2018). Effect of Dam operation on monthly and annual trends of flow discharge in the Qom Rood Watershed, Iran. *J. Hydrology* 557, 254–264. doi:10.1016/j.jhydrol.2017.12.039

Yan, D., Werners, S. E., Ludwig, F., and Huang, H. Q. (2015). Hydrological response to climate change: The Pearl River, China under different RCP scenarios. *J. Hydrology Regional Stud.* 4, 228–245. doi:10.1016/j.ejrh.2015.06.006

Yan, T., Bai, J., Lee Zhi Yi, A., and Shen, Z. (2018). SWAT-simulated streamflow responses to climate variability and human activities in the miyun reservoir Basin by considering streamflow components. *Sustainability* 10 (4), 941. doi:10.3390/su10040941

Yang, W., Andréasson, J., Graham, L. P., Olsson, J., Rosberg, J., and Wetterhall, F. (2010). Distribution-based scaling to improve usability of regional climate model projections for hydrological climate change impacts studies. *Hydrology Res.* 41 (3/4), 211–229. doi:10.2166/nh.2010.004

Yu, Y., Zhu, R., Ma, D., Liu, D., Liu, Y., Gao, Z., et al. (2022). Multiple surface runoff and soil loss responses by sandstone morphologies to land-use and precipitation regimes changes in the Loess Plateau, China. *CATENA* 217, 106477. doi:10.1016/j.catena.2022.106477

Zeinivand, H., De Smedt, F., and Bahremand, A. (2007). "Simulation of basin runoff due to rainfall and snowmelt," in *International congress on modelling and simulation* (Christchurch, New Zealand: Modelling and Simulation Society of Australia and New Zealand), 7.

Zhang, L., and Yang, X. (2018). Applying a multi-model ensemble method for long-term runoff prediction under climate change scenarios for the Yellow River basin, China. *Water* 10 (3), 301. doi:10.3390/w10030301

Zhao, J., Xia, H., Yue, Q., and Wang, Z. (2020). Spatiotemporal variation in reference evapotranspiration and its contributing climatic factors in China under future scenarios. *Int. J. Climatol.* 40 (8), 3813–3831. doi:10.1002/joc.6429

frontiers | Frontiers in Environmental Science

TYPE Original Research
PUBLISHED 12 September 2022
DOI 10.3389/fenvs.2022.996701

Check for updates

OPEN ACCESS

EDITED BY
Yang Yu,
Beijing Forestry University, China

REVIEWED BY
Dong An,
Lund University, Sweden
Xiaofan Zeng,
Huazhong University of Science and Technology, China

*CORRESPONDENCE
Qin Ju,
juqin@hhu.edu.cn

SPECIALTY SECTION
This article was submitted to Freshwater Science,
a section of the journal
Frontiers in Environmental Science

RECEIVED 18 July 2022
ACCEPTED 10 August 2022
PUBLISHED 12 September 2022

CITATION
Ju Q, Zhang R, Wang G, Hao W, Wang Q, Liu Y and Wang W (2022), Simulating the freezing-thawing processes based on MODIS data in the Three-River Souce Region, China.
Front. Environ. Sci. 10:996701.
doi: 10.3389/fenvs.2022.996701

Simulating the freezing-thawing processes based on MODIS data in the Three-River Souce Region, China

Qin Ju[1]*, Rongrong Zhang[1], Guoqing Wang[2], Wenlong Hao[1,3], Qin Wang[1], Yanli Liu[2] and Wei Wang[4]

[1]State Key Laboratory of Hydrology-Water Resources and Hydraulic Engineering, Hohai University, Nanjing, China, [2]Nanjing Hydraulic Research Institute, State Key Laboratory of Hydrology-Water Resources and Hydraulic Engineering, Nanjing, China, [3]College of Energy and Environmental Engineering, Hebei University of Engineering, Handan, China, [4]PowerChina Jiangxi Electric Power Design Institute Co., Nanchang, China

The processes of soil freezing-thawing lead to soil water and heat movement in cold regions, which significantly influences the hydrological and energy cycles in the soil-plant-atmosphere system. This study presents a soil water content coupled with heat transfer model based on physical processes of water and heat movement in frozen soil. The model was calibrated and validated using the measured data of soil temperature and frost and thaw depth at 19 stations in and around the Three-River Source Region of China. The results show that the frozen soil model could capture the processes of soil freezing-thawing processes well at this region. The relationship between model parameters and climate and vegetation factors was analyzed using the observation data and remote sensing data obtained from MODIS, and results showed that the parameter c which represents the soil properties has a good correlation with longitude and vegetation coverage. A multi-regression model was established to estimate the model parameters in regions without observation data and its determination coefficient R^2 was 0.82. The mean relative error between calibration and inversion parameters of 19 stations is 6.29%. Thus, the proposed method can be applied to cold regions without observation data to obtain the parameters and simulated the soil freezing-thawing processes.

KEYWORDS

frozen soil, soil freezing-thawing processes, soil temperature, active soil depth, cold regions

1 Introduction

The area of frozen soil accounts approximately 60% of the Northern Hemisphere in the winter (Zhang et al., 1999). Frozen soil processes play an important role in the land surface hydrological and energy cycles in cold regions by altering soil hydraulic and thermal characteristics. The processes of soil water freezing delay the winter cooling of the land surface, while the processes of soil water thawing delay the summer warming of the land surface (Poutou et al., 2004). The spatial distribution of frozen soil at early spring melt season exerts significant influences on spring runoff generation.

The presence of ice in the soil reduces the infiltration capacity, which leads to a higher percentage of snowmelt and spring precipitation being partitioned into surface runoff and thus influences the hydrological cycles (Cherkauer and Lettenmaier, 2003; Jiang et al., 2013; Orakoglu et al., 2016). It also influences the timing of spring runoff and the amount of soil moisture (Koren et al., 1999). In the late 1960s, researchers began to study the basic processes of soil freezing. According to the experimental study by Hoekstra (Hoekstra, 1966), water transferred from the unfrozen zone to the frozen zone when the soil temperature was below a freezing point and then the soil was frozen. The first coupled frozen soil model was developed by Harlan (1971), and most of the other frozen soil models were established on the basis of Harlan's theories (Sheppard et al., 1978; Taylor and Luthin, 1978; Fukuda, 1980; Fukuda et al., 1987). In recent years, more attention has been paid to the frozen soil processes and hydrological cycles in cold regions, especially on the Qinghai-Tibet Plateau. Due to its unique geographical location with high latitude, the frozen soil is more sensitive to climate change and surface conditions (Jiang et al., 2016; Sun et al., 2020; Sheng et al., 2021). In the past 30 years, global warming had led to a 0.2°C increase in the frozen soil temperature on the Qinghai-Tibet Plateau, and the thickness of frozen soil is projected to decrease in the next 100 years (Wang et al., 2001; Gao et al., 2003; Du et al., 2012). After analyzing the relationship between maximum frozen depth and accumulated negative temperatures, Hao. (2013) found a significant linear correlation between the maximum accumulated negative temperatures and the maximum frozen depth, and established an empirical relationship to estimate the maximum frozen depth in the Yellow River Source Region. Xia et al. (2011) simulated the soil freezing and thawing on the northeast Tibetan Plateau by using the land-surface model CLM3.0 and results showed that the trend of freezing and thawing processes could be simulated well, and the simulation of freezing was better than that of thawing in general. Yin et al. (2010) applied the SHAW model in alpine steppe on the Tibetan Plateau and showed that the model performed well. However, most of frozen soil models applied on the Qinghai-Tibet Plateau focus more on the freezing-thawing processes and consider less on the interactions between heat transfer and water movement.

Another development of frozen soil models is to optimize the frozen soil parameterization scheme in land surface models (LSMs). By introducing the super cooled soil water and a fractional permeable area, Niu and Yang (2006) modified the frozen soil scheme in Community Land Model version 2.0 (CLM2.0) and improved the monthly runoff and terrestrial water storage change in cold-region river basins. Using soil matric potential to define maximum liquid water content when the soil temperature was below the freezing point, Luo et al. (2009) improved a frozen soil parameterization scheme in CoLM and the simulated soil liquid water content and soil temperatures were significantly improved. Liu. (2015) optimized the frozen parameterization scheme of CoLM model and simulated the frozen soil processes in the Naqu area on the Qinghai-Tibet Plateau. The results showed that the modified models capture the characteristics of the soil freezing-thawing processes better.

The active layer of frozen ground is a rock and soil layer that is frozen in winter and thawed in summer in the crustal surface every year. And it is highly sensitive to climate and environmental change. The processes of frozen soil active layer freezing and thawing lead to the movement of soil water, which significantly influences hydrological processes, water resources, agriculture, and environment in cold regions. Understanding the water and heat transfer processes of active layer in these areas is highly important for a better understanding of the water and energy cycles.

However, due to the sparse meteorological station networks in the cold regions, previous studies mostly focused on the processes at point or local scale with observation data. In regions without observation data, model parameters could not be obtained. In this paper, we obtained frozen soil model parameters that calibrated by observation data of 19 stations in the Three-River Source Region. Based on analyzing the relationship between model parameters and climate and vegetation factors, we tried to establish a model to obtain the parameters in regions without observation data. The results of this work will provide a method to study coupling of the frozen soil water-heat and hydrological cycles in the cold regions without observation data.

2 Research area

The name of Three-River Source Region (TRSR) indicates that it is source region of three rivers including Yellow River, Yangtze River and Lancang River. It is located in central part of the Qinghai-Tibetan Plateau (Figure 1), which covers a territory about 297,000 km^2 and is well known as the "Roof of the World". The areas of the Yellow River Source Region (YeSR), the Yangtze River Source Region (YaSR), and the Lancang River Source Region (LcSR) are 116,000 km^2 (39%), 128,000 km^2 (43.2%), and 53,000 km^2 (17.8%), respectively (Liu et al., 2008; Zhang et al., 2012; Liang et al., 2013; Yuan et al., 2015). This region is also called 'water tower of China' as 49% of water in Yellow River, 15% of water in Lancang River and 25% of water in Yangtze River originate from here (Tang, 2003; Liu et al., 2012; Zhang et al., 2013).

The general climate in TRSR is cold and dry, and characterized by the typical plateau continental climate (Yi

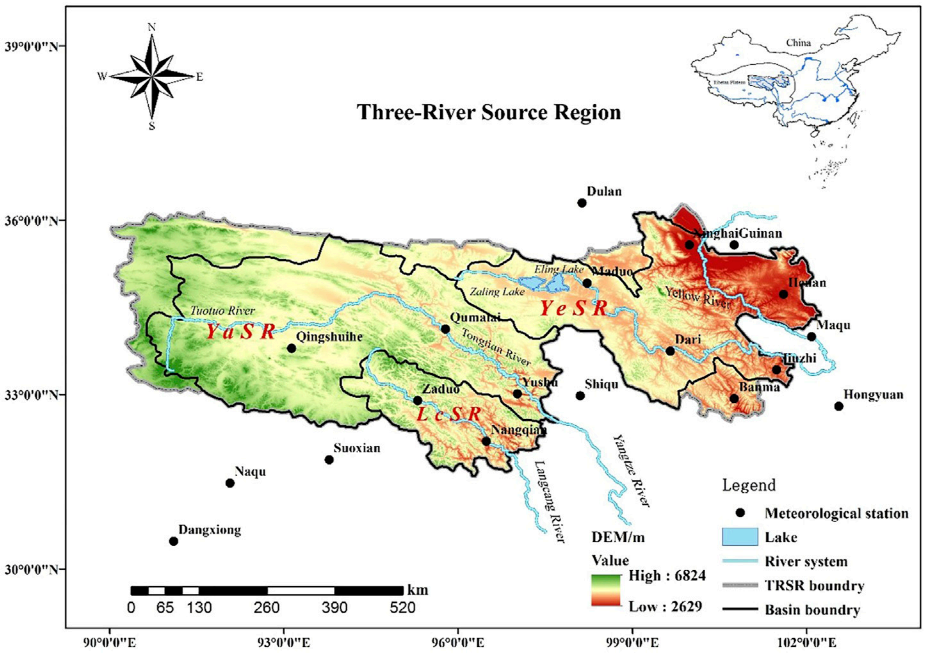

FIGURE 1
Geographical overview and spatial distribution of meteorological stations in the Three-River Source Region (TRSR) of Tibetan Plateau, China.

et al., 2011; Xiang et al., 2013). The average annual air temperature of TRSR ranges from −5.4 to 4.2°C (Xu et al., 2011; Luo et al., 2016; Yu et al., 2022). The maximum mean monthly temperature is in July with a range of 6.4°C–13.2°C in July, and the minimum mean monthly temperature is in January from −6.6°C to −13.8°C (Wang et al., 2005).

The average annual precipitation ranges from 770 mm in the southeast to 260 mm in the northwest, and approximately 75% of the total precipitation occurred during the rainy season (June to September) (Li et al., 2009; Xiang et al., 2013). The average annual sunlight hours and evaporation ranges from 2300 to 2900 h and 730–1700 mm, respectively. Cumulative annual solar radiation fluctuates from 5500 to 6800 MJ/m^2 (Liu, 2010).

TRSR has a special structure of the natural environment, diverse ecosystem types and species diversity of unique, in which some types of vegetation, such as coniferous forest, shrub, alpine meadow, alpine grassland, alpine sparse vegetation, distribute from southeast to northwest (Li et al., 2011). TRSR has the largest alpine wetland ecosystem in the world, and abundant rivers, lakes, mountain snow and glacier resources, therefore it plays an important role in providing water resources for industry, agriculture and domestic water use in downstream (Liu et al., 2014; Tong et al., 2014). The permafrost and seasonal frozen soil distributed in 75% area of this region (Jiang and Zhang, 2016). Due to the sensitivity of active layer to temperature, the ecosystem in this region is highly fragile. The global warming and the increasing of human activities in recent decades have contributed to glaciers retreat, the rising snow line, grassland degradation, and the decline in water conservation capacity, and further pose a serious threat to the ecosystem in TRSR (Shao et al., 2013; Yu et al., 2020).

3 Mathematical models

3.1 Model description

This study simulated the processes of soil freezing and thawing and coupled water-heat movement based on Harlan's model. Comparing water movement in frozen soil to that in unsaturated soil, Harlan firstly developed a coupled model to analyze water and heat movement in frozen soil under some hypotheses (Harlan, 1971; Harlan, 1973). Subsequently, a numerical model that adopted the finite difference method was derived by Kung and Steenhuis (1986) to simulate soil water and heat movement. This model overcame limitations in description of water flux for a partly frozen soil in Harlan's model. Based on Harlan's theories, Taylor, Sheppard, Fukuda, et al. (Sheppard et al., 1978; Taylor and Luthin, 1978; Fukuda, 1980; Fukuda et al., 1987) analyzed and improved Harlan's model or developed their own models.

3.2 The frozen soil water-heat movement model and parameters

Soil water movement for the processes of soil freezing and thawing was described by Richards equation as follows:

$$\frac{\partial\theta_u}{\partial t} = \frac{\partial}{\partial z}\left[D(\theta_u)\frac{\partial\theta_u}{\partial z} - K(\theta_u)\right] - \frac{\rho_{\mathrm{i}}}{\rho_w}\frac{\partial\theta_i}{\partial t}, \tag{1}$$

where θ_u is the volumetric liquid content ($m^3 \cdot m^{-3}$); θ_i is the ice content ($\mathrm{m}^3 \cdot \mathrm{m}^{-3}$); ρ_i is the density of ice ($900\mathrm{kg} \cdot \mathrm{m}^{-3}$); ρ_w is the density of water ($1000\mathrm{kg} \cdot \mathrm{m}^{-3}$); $\mathrm{K}(\theta_u)$ is the unsaturated hydraulic conductivity of soil ($\mathrm{m} \cdot \mathrm{s}^{-1}$); $\mathrm{D}(\theta_u)$ is the diffusivity of frozen soil ($\mathrm{m}^2 \cdot \mathrm{s}^{-1}$); t is time (s) and z is depth (m).

In this paper, due to lack of available soil data in TRSR, the unsaturated hydraulic conductivity and the diffusivity of frozen soil are given as the following empirical formulas respectively (Lei et al., 1988; Hao et al., 2009):

$$D(\theta_u) = D_1(\theta_u/\theta_s)^{D_2}, \tag{2}$$

$$K(\theta_u) = K_1(\theta_u/\theta_s)^{K_2}, \tag{3}$$

where $D1$, $D2$, $K1$ and $K2$ are parameters, $D1 = 226.4$, $D2 = 8.4$, $K1 = 0.9$, $K2 = 10.87$ (Lei et al., 1988; Hao et al., 2009); θs is saturated water content ($\mathrm{m}^3 \cdot \mathrm{m}^{-3}$).

For partially frozen soil, hydraulic conductivity and diffusivity are adjusted by the following formulas respectively (Taylor and Luthin, 1978; Lei et al., 1988):

$$D_i(\theta_u) = D(\theta_u)\big/10^{10\theta_i}, \tag{4}$$

$$K_i(\theta_u) = K(\theta_u)\big/10^{10\theta_i}, \tag{5}$$

where $\mathrm{D_i}(\theta_\mathrm{u})$ is the adjusted diffusivity for partially frozen soil ($\mathrm{m}^2 \cdot \mathrm{s}^{-1}$); $\mathrm{K_i}(\theta_\mathrm{u})$ is the adjusted hydraulic conductivity in the partially frozen soil ($\mathrm{m} \cdot \mathrm{s}^{-1}$).

The one-dimensional heat flux equation of frozen soil is given by:

$$C_{VS}\frac{\partial T}{\partial t} = \frac{\partial}{\partial z}\left[\lambda\frac{\partial T}{\partial z}\right] + L\rho_i\frac{\partial\theta_i}{\partial t}, \tag{6}$$

where $\mathrm{C_{vs}}$ is volumetric heat capacity of soil ($\mathrm{J} \cdot \mathrm{m}^{-3} \cdot \mathrm{K}^{-1}$); λ is thermal conductivity of soil ($\mathrm{W} \cdot \mathrm{m}^{-1} \cdot \mathrm{K}^{-1}$); L is latent heat of fusion ($\mathrm{J} \cdot \mathrm{kg}^{-1}$); T is soil temperature (°C); other symbols are the same as before.

Volumetric heat capacity, $\mathrm{C_{vs}}$, of soil is from De Vries (De Vries and Van Wijk, 1963):

$$C_{vs} = c_s(1 - \theta_{sat}) + \theta_{liq}c_{liq} + \theta_{ice}c_{ice}, \tag{7}$$

where θ_{liq}($\mathrm{m}^3 \cdot \mathrm{m}^{-3}$) and θ_{ice} ($\mathrm{m}^3 \cdot \mathrm{m}^{-3}$) are liquid water content and ice content, respectively; θ_{sat} is the saturated volumetric water content ($\mathrm{m}^3 \cdot \mathrm{m}^{-3}$); $\mathrm{C_s}$ is the volumetric heat capacity of the soil solids ($\mathrm{J} \cdot \mathrm{m}^{-3} \cdot \mathrm{K}^{-1}$); $\mathrm{c_{liq}}$ and $\mathrm{c_{ice}}$ are the specific heat capacities of liquid water and ice, respectively ($4.213\mathrm{J} \cdot \mathrm{m}^{-3} \cdot \mathrm{K}^{-1}$; $1.94\mathrm{J} \cdot \mathrm{m}^{-3} \cdot \mathrm{K}^{-1}$). So Equation 7 can be written as follows:

$$C_{vs} = c + 4.213 \times \theta_{liq} + 1.94 \times \theta_{ice}, \tag{8}$$

where c is a parameter about the soil properties and varies with the sand and clay content, which is mainly influenced by the regional climate including long term average temperature and precipitation and land cover. It also exhibits an obvious vertical distribution which could be characterized by latitude-longitude and elevation. As an important parameter in frozen soil water-heat movement model, this paper established a multiple regression model between c and factors that significantly correlated with it (i.e. climate characteristics, vegetation characteristics and geographical characteristics). After that, the multiple regression model was applied to calculate the spatial distribution of c in TRSR for simulating the processes of soil freezing and thawing. The calculation were conducted at a resolution of 1 km by 1 km to match the vegetation coverage and MODIS LST data.

Soil thermal conductivity is highly complex because it is not only related to the proportion of the components, but also related to the structure and shape of soil components and other factors. Considering this, in this paper, an empirical formula was used for estimation of soil thermal conductivity (Shi et al., 1998).

$$\lambda = \lambda_m - (\lambda_m - \lambda_T)\frac{\theta_u}{\theta_u + \frac{\rho_i}{\rho_w} \cdot \theta_i}, \tag{9}$$

where λ_m is thermal conductivity of frozen soil ($\mathrm{W} \cdot \mathrm{m}^{-1} \cdot \mathrm{K}^{-1}$); λ_T is thermal conductivity of unfrozen soil ($\mathrm{W} \cdot \mathrm{m}^{-1} \cdot \mathrm{K}^{-1}$). Based on the measured data, Pang et al. (2006) calculated the values of λ_m and λ_T in this region and $\lambda_m = 1.84\mathrm{W} \cdot \mathrm{m}^{-1} \cdot \mathrm{K}^{-1}$ and $\lambda_T = 1.57\mathrm{W} \cdot \mathrm{m}^{-1} \cdot \mathrm{K}^{-1}$.

In the processes of soil freezing and thawing, the connection between water and heat movement of frozen soil is mainly reflected in the dynamic equilibrium of water content and soil subzero temperature, namely a one-one correspondence exists between the soil subzero temperature and water content. Therefore, the connecting equation is written as (Shang et al., 1997):

$$\theta_u = \theta_{max}(T), \tag{10}$$

where $\theta_{\mathrm{max}}(\mathrm{T})$ is the largest unfrozen water content in the condition of the corresponding soil subzero temperature. Thus, the soil water content coupled with heat transfer model comprises Eqss. 1, 6, 10.

However, due to the different initial water content and the hysteresis effect of soil water retention characteristics, the relationship between water content and subzero temperature is not a one-to-one correspondence single value function. In this paper, the relationship is given as the following empirical formula (An et al., 1987):

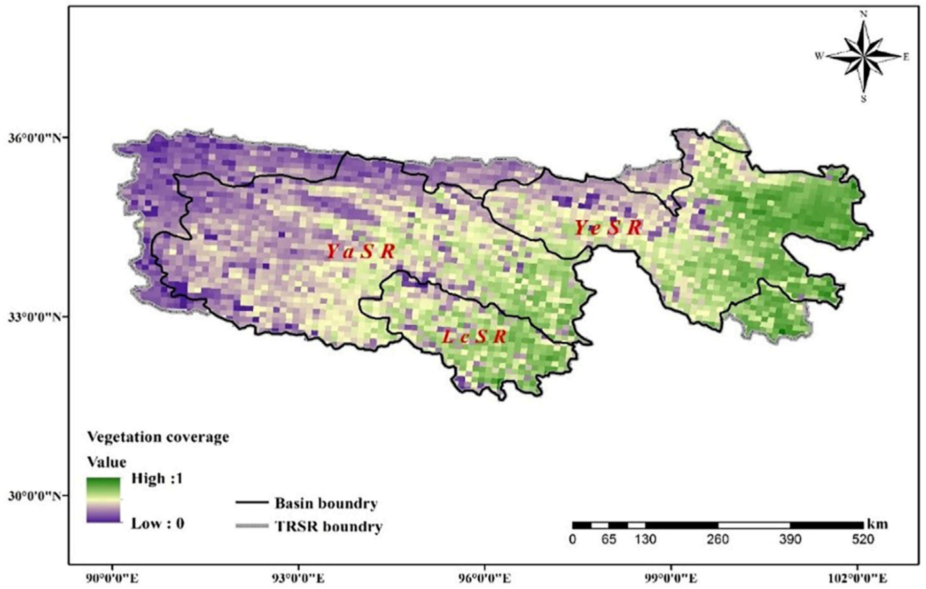

FIGURE 2
Spatial distribution of vegetation coverage in the TRSR of Tibetan Plateau, China.

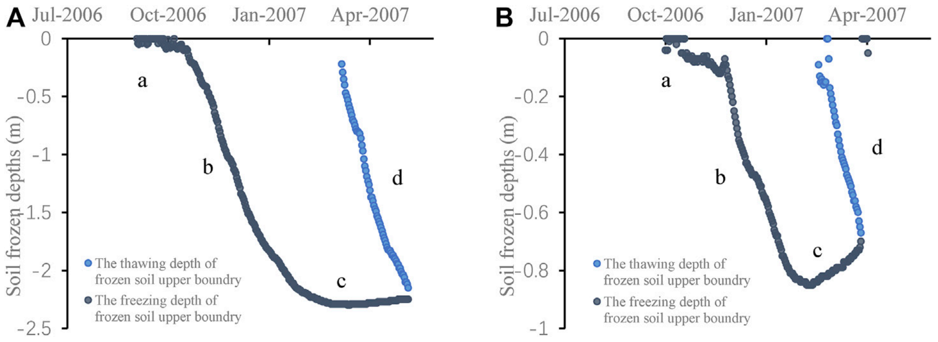

FIGURE 3
The processes of frozen soil freezing and thawing at Maduo station **(A)** and Jiuzhi station **(B)** from 1 July 2006 to 30 June 2007.

$$\begin{cases} \theta_u = 0.0644\,exp\,(0.0551T) \quad T < -0.75 \\ \theta_u = 0.3058 + 0.596\,(T + 0.30) \quad -0.75 \le T \le -0.30, \\ \theta_u = 0.3058 \quad T \ge -0.30 \end{cases} \tag{11}$$

Due to the nonlinearity of soil water-heat movement basic equations, the anisotropy of soils and the complexity of the initial and boundary conditions, a numerical simulation method instead of analytical methods was generally used to solve these equations. In this paper, the finite difference method was used to numerically simulate the water–heat coupled movements.

Using a central difference scheme, Equations 1, 6 can be transferred respectively as follows:

$$\alpha_i\,(\theta_u)_{i-1}^{k+1} + \beta_i\,(\theta_u)_i^{k+1} + \gamma_i\,(\theta_u)_{i+1}^{k+1} = h_i\,, \tag{12}$$

$$A_i T_{i-1}^{k+1} + B_i T_i^{k+1} + C_i T_{i+1}^{k+1} = D_i, \tag{13}$$

where subscript i is the ith soil layer, superscript k is the number of computation time intervals in a time step. The coefficients of α_i, β_i, γ_i, h_i, A_i, B_i, C_i and D_i can be calculated from initial conditions of soil temperature and water content.

Equations 12 and 13 are all in a set of tridiagonal equations, which can be solved by a chasing method. The time step was set as 1 day and the spatial step was 0.01 m. So, on the basis of certain initial and boundary conditions, the numerical solution of water and heat coupled movement in frozen soil can be obtained.

TABLE 1 The model parameters for calibration at 19 meteorological stations in and around TRSR.

Meteorological stations	c
Banma	3.90
Dari	3.30
Dangxiong	2.85
Dulan	2.85
Guinan	3.30
Henan	3.80
Hongyuan	4.40
Jiuzhi	4.30
Maduo	3.00
Maqu	3.90
Naqu	2.50
Nangqian	3.20
Qingshuihe	3.00
Qumalai	3.25
Shiqu	4.00
Suoxian	3.20
Xinghai	3.30
Yushu	3.80
Zaduo	2.95

TABLE 2 Correlation coefficient r, Nash-Sutcliffe efficiency coefficient NSE and RMSE between simulated and observed freezing depths during the verification period.

Meteorological stations	r	NSE	RMSE/m
Banma	0.91	0.80	0.11
Dari	0.86	0.71	0.39
Dangxiong	0.95	0.88	0.07
Dulan	0.94	0.87	0.21
Guinan	0.90	0.79	0.27
Henan	0.87	0.73	0.27
Hongyuan	0.84	0.69	0.09
Jiuzhi	0.88	0.76	0.14
Maduo	0.73	0.40	0.69
Maqu	0.85	0.68	0.17
Naqu	0.90	0.79	0.27
Nangqian	0.95	0.86	0.06
Qingshuihe	0.76	0.48	0.60
Qumalai	0.97	0.93	0.21
Shiqu	0.82	0.61	0.28
Suoxian	0.92	0.81	0.10
Xinghai	0.96	0.92	0.18
Yushu	0.97	0.92	0.07
Zaduo	0.97	0.94	0.11

4 Data and method

4.1 Meteorological data

The data were collected from 19 meteorological stations in and around TRSR. The station information is presented in S1, and the geographical location of the stations is shown in Figure 1. The data includes daily air temperature, precipitation, frozen depth, thawed depth, surface temperature and soil temperatures at 5, 10, 15, 20 and 40 cm depth from 1 January 2006 to 31 December 2008, and the missing data were obtained by linear interpolation.

4.2 Vegetation coverage

The index of vegetation coverage was used to analyze the geographical law of parameters c in TRSR. The parameter c in the coupled model relates to the soil properties, and experiments showed that Normalized Difference Vegetation Index (NDVI) is sensitive to the change of soil properties (Baret and Guyot, 1991; Fang and Tian, 1998). NDVI is a comprehensive reflection of the vegetation types, form and growth status in the unit pixel and its value depends on vegetation coverage and leaf area index (LAI) and other factors, thus providing a measure of vegetation coverage (Carlson and Ripley, 1997). The NDVI data were acquired from NASA (https://ladsweb.nascom.nasa.gov).

A dimidiate pixel model, which is a simplified linear spectral unmixing method, was used to calculate fractional vegetation coverage (FVC) due to its simplicity in principle and form (Ivits et al., 2013). Many studies examined this model by theoretical method and applied research (Leprieur et al., 1994; QI et al., 2000; Zribi et al., 2003). An assumption of the model is that a pixel contains only two elements of vegetation and soil, which can be represented as follows:

$$FVC = (NDVI - NDVI_{soil}) / (NDVI_{veg} - NDVI_{soil}), \quad (14)$$

where NDVI used in this study was organized at 1 km by 1 km spatial resolution with a 16-days time interval from Moderate-resolution Imaging Spectroradiometer (MODIS). $NDVI_{soil}$ and $NDVI_{soil}$ are two key input parameters that represent the NDVI values of pure pixels of bare soil and vegetation, respectively. For more detailed processes of FVC estimation, readers can refer to Zeng et al. (2000) for further information.

Figure 2 shows the spatial distribution of FVC that used in this study, i.e. the mean value of 12 months from July 2006 to June 2007 in the TRSR, with the vegetation coverage gradually deteriorating from southeast to northwest. The cover in the east of YeSR represent the highest (60%–90%) in TRSR. The vegetation coverage in the LcSR, southeast YaSR and southwest YeSR are relatively high (40%–60%). However, the vegetation coverage was relatively low and generally below 40% in the northwestern YeSR and west of YaSR.

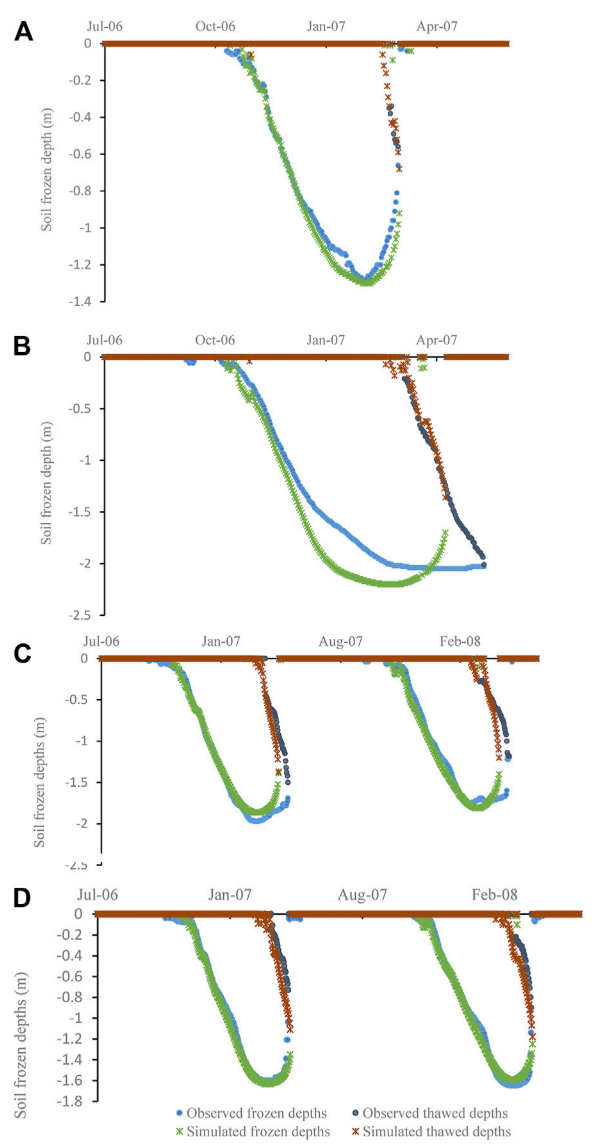

FIGURE 4
The simulated and observed frozen and thawed depths at Zaduo station **(A)** and Maduo station **(B)** from 1 July 2007 to 30 June 2008, Dari station **(C)** and Xinghai station **(D)** from 1 July 2006 to 30 June 2008.

4.3 MODIS LST

Land surface temperature (LST) from MODIS were used as the input data in the frozen soil water-heat model in this study. It plays an important role in material exchange and energy balance between the surface and the atmosphere, and it is a key variable in the study of land surface physical processes at regional and global scale (Wang et al., 2012). Due to the large area of missing pixels of daily MODIS LST product in TRSR, we used the MYD11A2 product with 1 km spatial resolution. This product provides 8-days LST data recovered by the spilt-window algorithm. The empty pixels of MYD11A2 product were filtered from its neighbors by using the spline interpolation. Then we used the liner interpolation method to obtain the daily LST data in TRSR.

The MODIS/AQUA LST products provide two instantaneous observations every day, and the overpass times are in 1:30a.m. and 1:30p.m. In this paper, the daily land surface temperature was estimated by the average of daytime LST and nighttime LST that are respectively closed to the minimum and maximum temperature in a day (Geerts, 2003).

4.4 Statistical analysis of simulation results

The model performance is evaluated by correlation coefficient r, Nash-Sutcliffe efficiency coefficient NSE and the root mean square error RMSE. The methods of calculating r, NSE and RMSE are shown as follows:

$$r = \frac{\sum_{i=1}^{N} (x_i - \bar{x})(y_i - \bar{y})}{\sqrt{\sum_{i=1}^{N} (x_i - \bar{x})^2 \sum_{i=1}^{N} (y_i - \bar{y})^2}}, \tag{15}$$

$$NSE = 1 - \frac{\sum_{i=1}^{N} (x_i - y_i)^2}{\sum_{i=1}^{N} (y_i - \bar{y})^2}, \tag{16}$$

$$RMSE = \sqrt{\frac{\sum_{i=1}^{N} (x_i - y_i)^2}{N}}, \tag{17}$$

Where N is the number of sample; x_i and y_i is the simulation value and observation value respectively; $\bar{x}$ and $\bar{y}$ are mean of x_i and y_i respectively.

5 Results and discussion

5.1 Analyze on the processes of frozen soil freezing and thawing

In TRSR, Jiuzhi and Maduo are the typical stations in the processes of soil freezing and thawing. Figure 3 shows that the processes can be divided into four stages.

1) Unstable freezing phase. In this phase, the soil temperatures periodically decrease to less than 0°C with the air temperatures fluctuate around 0°C, which makes the shallow-layer soil periodically experience freezing and thawing. When the negative accumulated temperature is higher than 0°C and the shallow-layer soil is always frozen in the daytime.
2) Freezing phase. In this phase, the air temperatures are always below 0°C. As the air temperatures drop, the freezing depth increases continuously. When the

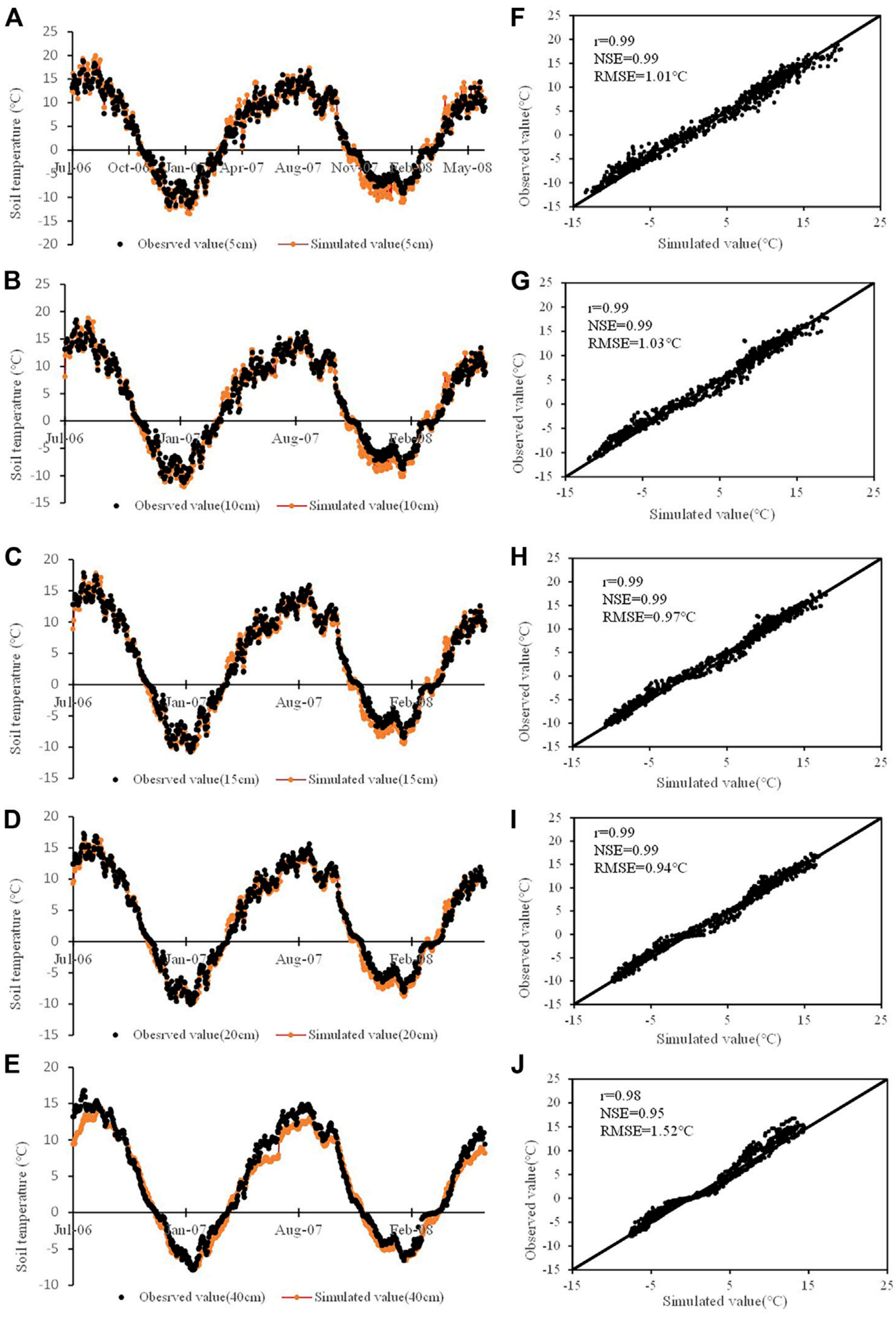

FIGURE 5
At Dari from 1 July 2006 to 30 June 2008: **(A–E)** daily soil temperatures at 5, 10, 15, 20 and 40cm, **(F–J)** correlation between the simulation and observation daily soil temperatures at 5, 10, 15, 20 and 40 cm.

freezing layer temperature reaches the lowest temperature during the freezing period, this phase ends and enters the stable freezing phase.

3) Stable freezing phase. In this phase, the temperatures will stay above 0°C in the daytime, but the nighttime temperatures are still below 0°C. The soil freezing depth has reached the maximum and then remains stable.
4) Thawing phase. As the air temperature continues to rise, the thawing layer thickens gradually. However, because the nighttime temperatures are still below 0°C, the shallow-layer soil is still

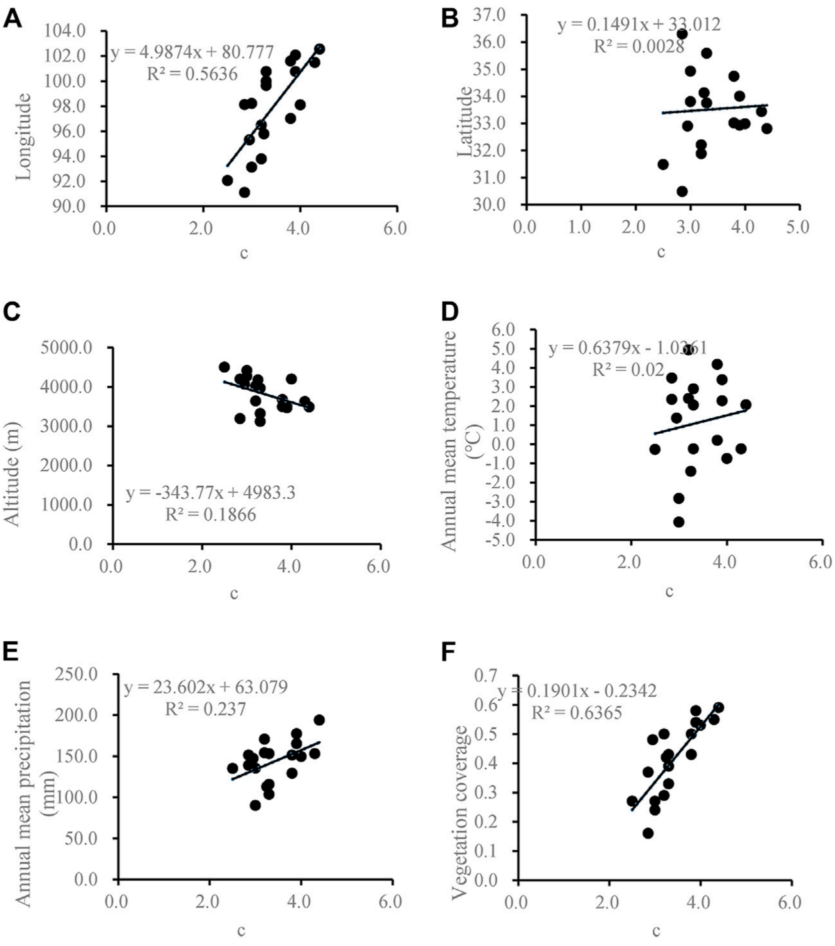

FIGURE 6
Correlation between model parameter and **(A)** longitude, **(B)** latitude, **(C)** altitude, **(D)** annual mean temperature, **(E)** annual mean precipitation, **(F)** vegetation coverage.

frozen in the nighttime. Due to the solar radiation and geothermal, the frozen soil begins to thaw bidirectionally until it disappears.

5.2 Model calibration and verification

Model calibration and verification were carried out at 19 stations in and around TRSR by comparing simulated and observed freezing depths and soil temperatures. The observation data were separated into two periods, 1 July 2006-30 June 2007 and 1 July 2007-30 June 2008, for model calibration and verification, respectively. The calibration results are shown in Table 1.

Taking Xinghai and Dari stations for examples, NSE values for the soil freezing depths were 0.92 and 0.75 during the calibration period, respectively. The NSE for the daily soil temperatures at the Xinghai station for 5, 10, 15, 20, 40 cm were 0.98, 0.98, 0.98, 0.97 and 0.94, respectively. The NSE for the daily soil temperatures at the Dari station for 5, 10, 15, 20, 40 cm were 0.98, 0.99, 0.99, 0.99 and 0.95, respectively.

During the verification period, the r, NSE and RMSE values for simulation of freezing depths of 19 meteorological stations are presented in Table 2. Table 2 shows that the lowest Nash-Sutcliffe efficiency coefficient NSE and correlation coefficient r in simulated freezing depths at Maduo station (Figure 4B) are 0.4 and 0.73, respectively. The highest NSE and r at Zaduo station (Figure 4A) are 0.94 and 0.97, respectively. The average values of NSE and r are 0.89 and 0.77, respectively. It is proved that the model can capture the characteristics of the soil freezing-thawing processes well.

The simulated and observed frozen depths at Dari and Xinghai stations during the period from 1 July 2006 to

TABLE 3 Parameters, inversion parameters and relative error of 19 stations in and around TRSR. Inversion parameters are calculated by regression Eq. 17.

Meteorological stations	C	Inversion c	Relative error (%)
Banma	3.90	4.00	2.52
Dangxiong	2.85	2.91	2.12
Dulan	2.85	2.88	1.05
Guinan	3.30	3.63	9.95
Henan	3.80	3.96	4.17
Hongyuan	4.40	4.24	−3.50
Jiuzhi	4.30	4.07	−5.27
Maduo	3.00	3.16	5.25
Maqu	3.90	4.19	7.41
Naqu	2.50	2.73	9.33
Nangqian	3.20	3.09	−3.53
Qingshuihe	3.00	2.73	−8.92
Qumalai	3.25	3.36	3.37
Shiqu	4.00	3.79	−5.23
Xinghai	3.30	3.43	3.85
Yushu	3.80	3.47	-8.70
Zaduo	2.95	3.47	17.77
Suoxian	3.20	3.42	6.84
Dari	3.30	3.65	10.64

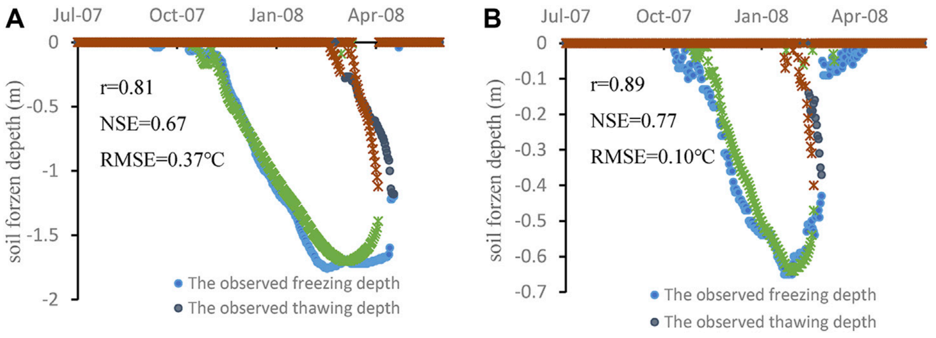

FIGURE 7
The simulated by using the inversion parameters and observed freezing and thawing processes at Dari station **(A)** and Suoxian station **(B)** from 1 July 2007 to 30 June 2008. At Dari, r, NSE and RMSE are 0.81, 0.67 and 0.37°C, respectively. At Suoxian, r, NSE and RMSE are 0.89, 0.77 and 0.10°C, respectively.

30 June 2008 are shown in Figure 4. The simulation of frozen depths is more accurate than the thawed depths. The simulated and observed daily soil temperatures at Dari station for 5, 10, 15, 20 and 40 cm are shown in Figures 5A–E. The r and NSE values between observed and simulated soil temperatures at Dari station for 5, 10, 15, 20 and 40 cm are all above 0.98 and 0.95, respectively (Figures 5F–J). The RMSE for the five layers is less than 1.52°C (Figures 5F–J). Therefore, the simulated values agreed well with the observed values.

5.3 The analysis of geographical law of parameters

5.3.1 Correlation analysis

Model parameter c is an important factor affecting water movement and solutes transport. Hence, correlation analysis using stepwise regression was performed between parameter c and the climate characteristics (annual mean air temperature and annual mean precipitation), vegetation

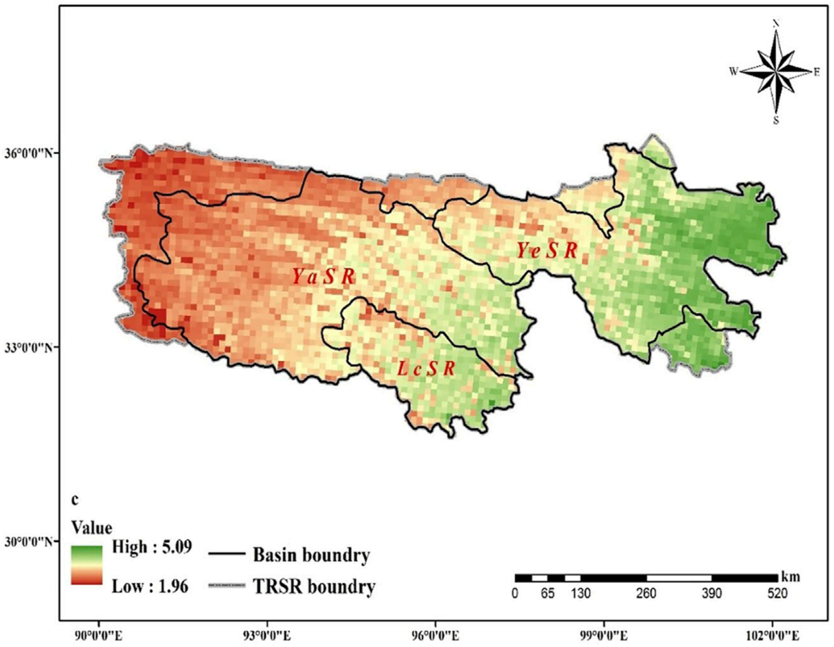

FIGURE 8
Spatial distribution of model parameter c in the TRSR of Tibetan Plateau, China.

characteristics (vegetation coverage), geographical characteristics (longitude, latitude and altitude) and model parameters.

Figure 6 shows that model parameter c has a positive correlation with longitude, annual mean precipitation, and vegetation coverage. The model parameter c has a better correlation with longitude (Figure 6A, r = 0.75) and vegetation coverage (Figure 6F, r = 0.80) than annual mean precipitation. This is because the longitudinal zonality of soil and the status of vegetation comprehensively reflect soil texture, organic content, and soil moisture content.

Apart from Suoxian and Dari, a multi-regression equation is established and its determination coefficients R^2 is 0.82 under 99% significance test.

$$c = -4.286 + 0.069 \times Lon + 2.468 \times FVC, \qquad (18)$$

where Lon is longitude, FVC is vegetation coverage.

The reliability of the equation was verified before applying the inversion parameters obtained from the above equation to the model in regions. Parameters, inversion parameters and relative error at 19 meteorological stations are shown in Table 3. The highest relative error at Zaduo is 17.77%, the lowest relative error at Dulan is 1.05% and the mean relative error of 19 stations is 6.29%. For examples, the relative errors of Suoxian and Dari are 6.84% and 10.64%, respectively (Table 3). During 1 July 2007 to 30 June 2008, the processes of the soil freezing and thawing simulated by using the inversion parameters are compared with the actual freezing and thawing processes (Figure 7). The correlation coefficient r, Nash-Sutcliffe efficiency coefficient NSE and root mean square error RMSE at Dari are 0.81, 0.67 and 0.37°C, respectively (Figure 7A). At Suoxian, the r, NSE and RMSE values are 0.89, 0.77 and 0.10°C, respectively (Figure 7B). By comparison, the simulation results by using the inversion parameters agree with observed values. Therefore, the method proposed is reliable and can be applied to other regions. The spatial distribution map of c in TRSR is shown in Figure 8.

5.3.2 The simulation of the processes of soil freezing and thawing in TRSR

The soil freezing and thawing are simulated using the inversion parameters calculated by Equation 14 and MODIS daily land surface temperature data from 1 July 2006 to 30 June 2007 in TRSR. Figure 9A, Figure 9B and Figure 9C show the frozen depths in TRSR in January1st 2007, 1 February 2007 and 1 March 2007, respectively. The frozen depths increase from southeast to northwest generally (Figure 9). On January1st 2007 and 1 February 2007, the frozen depths range from 1.13 to 4.10 m (Figure 9A) and 1.21–4.89 m (Figure 9B), respectively. In the east of YeSR and south of LcSR, the frozen depths are below 2 m. In 1 March 2007, the frozen depths range from 0 to 3.12 m and there is almost no frozen soil in the south of LcSR (Figure 9C).

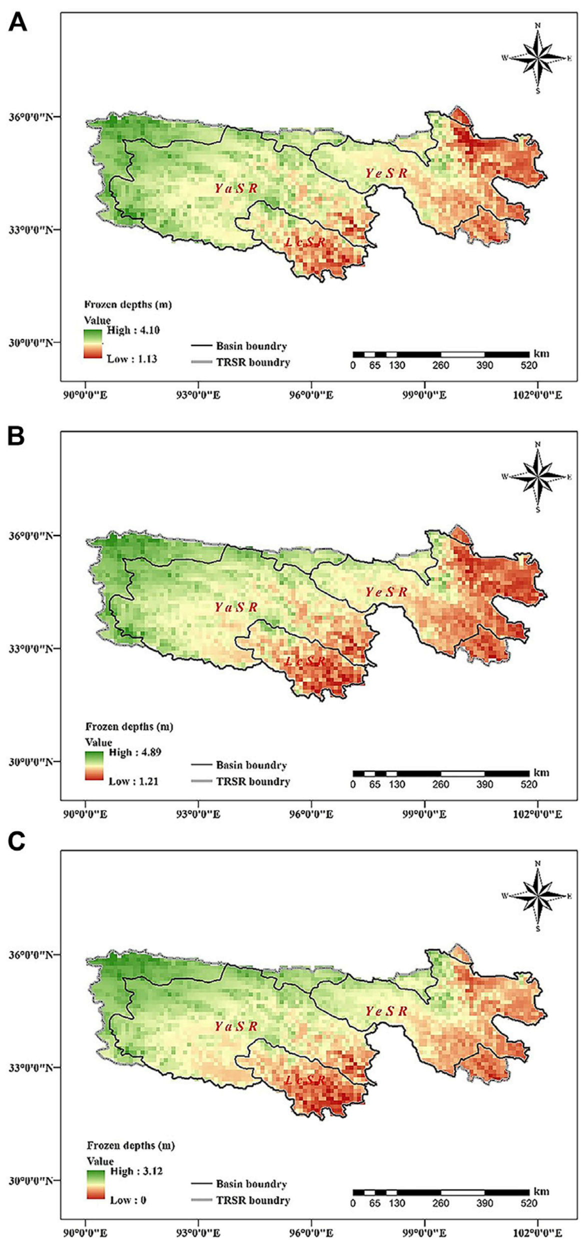

FIGURE 9
Spatial distribution of frozen depths in the TRSR in **(A)** 1 January 2007, **(B)** 1 February 2007 and **(C)** 1 March 2007.

6 Conclusion

In the cold region, water resources, hydrology and ecosystem are significantly influenced by climate change. The simulation of active soil depths and soil temperatures can help us better understand the soil freezing and thawing processes. Based on Harlan's model, a soil water content coupled with heat transfer model was presented in this paper. Measured data of soil temperature and active soil depths at 19 stations in and around the Three-River Source Region of China were collected for model calibration (1 July 2006-30 June 2007) and verification (1 July 2007 to 30 June 2008). The results showed that the simulated freezing depths and soil temperatures agreed well with the observed values. However, the other factors, e.g. solar radiation, humidity, ground water et al. are not considered in this model, which is the reason that the simulation of thawing processes are not better than freezing processes (Figure 4). During the verification period, the average Nash-Sutcliffe efficiency coefficient NSE and correlation coefficient r in simulated freezing depths at 19 stations are 0.89 and 0.77, respectively. The r and NSE values between observed and simulated soil temperatures at Dari station for 5, 10, 15, 20 and 40 cm are all above 0.98 and 0.95, respectively.

After the correlation analysis between model parameters and the climate characteristics (annual mean air temperature and annual mean precipitation), vegetation characteristics (vegetation coverage) and geographical characteristics (longitude, latitude and altitude), a multi-regression model was established to estimate the model parameters in regions without observation data and its determination coefficient R^2 was 0.82. The model parameter c has a better correlation with longitude (r = 0.75) and vegetation coverage (r = 0.80). The mean relative error of 19 stations between calibration and inversion parameters are 6.29%. The simulation results by using the inversion parameters are in good agreement with observed values. However, more geographical parameters should be considered to do correlation analysis to find significant factors. The results showed that the method proposed in this paper can be applied to cold regions without observation data to obtain the parameters and simulated the soil freezing-thawing processes.

Data availability statement

The raw data supporting the conclusions of this article will be made available by the authors, without undue reservation.

Author contributions

The authors' individual contributions to the paper are listing as follows: QJ: Conceptualization, Software, Writing—Original Draft, Project administration, Funding acquisition RZ: Writing—Review and Editing GW: Supervision WH: Methodology, Formal analysis, QW: Writing—Original Draft, Visualization YL: Visualization WW: Data Curation.

Funding

This work was supported by the National Key R&D Program of China (Grant No. 2021YFC3201104); National

Natural Science Foundation of China (Grant No. 52179013, U2240217, and 92047301); the Belt and Road Special Foundation of the State Key Laboratory of Hydrology-Water Resources and Hydraulic Engineering (Grant No. 2020491111).

Conflict of interest

Author WW was employed by the company PowerChina Jiangxi Electric Power Design Institute Co.

The remaining author declares that the research was conducted in the absence of any commercial or financial relationships that could be construed as a potential conflict of interest.

Publisher's note

Supplementary material

The Supplementary Material for this article can be found online at: https://www.frontiersin.org/articles/10.3389/fenvs.2022.996701/full#supplementary-material

References

An, W. D., Chen, X. B., and Wu, Z. W. (1987). Numerical simulation analysis of heat and mass transfer under a cannel in freezing. *J. Glaciol. Geocryol.* 9 (1), 35–46.

Baret, F., and Guyot, G. (1991). Potentials and limits of vegetation indices for LAI and APAR assessment. *Remote Sens. Environ.* 35 (2-3), 161–173. doi:10.1016/0034-4257(91)90009-u

Carlson, T. N., and Ripley, D. A. (1997). On the relation between NDVI, fractional vegetation cover, and leaf area index. *Remote Sens. Environ.* 62 (3), 241–252. doi:10.1016/s0034-4257(97)00104-1

Cherkauer, K. A., and Lettenmaier, D. P. (2003). Simulation of spatial variability in snow and frozen soil. *J. Geophys. Res.* 108 (D22), 2003JD003575–1675. doi:10.1029/2003jd003575

De Vries, D. A., and Van Wijk, W. R. (1963). Physics of plant environment. *Environmental control of plant growth* 5, 69.

Du, J., Jian, J., Hong, J. C., Lu, H. Y., and Chen, D. M. (2012). Response of seasonal frozen soil to climate change on Tibet Region from 1961 to 2010. *J. Glaciol. Geocryol.* 34 (3), 512–521.

Fang, H. L., and Tian, Q. J. (1998). A review of hyperspectral remote sensing in vegetation monitoring. *Remote Sens. Technol. Appl.* 13 (1), 62–69.

Fukuda, M., Kinosita, S., and Nakagawa, S. (1987). Numerical analysis of frost heaving based upon the coupled heat and water flow model. *Low Temp. Sci. ser. a Phys. Sci.* 45, 83–97.

Fukuda, M., Orhun, A., and Luthin, J. N. (1980). Experimental studies of coupled heat and moisture transfer in soils during freezing. *Cold Regions Sci. Technol.* 3 (2-3), 223–232. doi:10.1016/0165-232x(80)90028-2

Gao, R., Wei, Z. G., and Dong, W. J. (2003). International variation of the beginning data and the ending data of soil freezing in the Tibetan Plateau. *J. Glaciol. Geocryol.* 25 (1), 49–54.

Geerts, B. (2003). Empirical estimation of the monthly-mean daily temperature range. *Theor. Appl. Climatol.* 74, 145–165. doi:10.1007/s00704-002-0715-3

Hao, Z. C. (2013). Estimation method for maximum frozen depth of seasonal frozen soil in Source Region of the Yellow River. *Water Resour. Power* 31 (5), 73–76.

Hao, Z. C., Zhang, X. P., Zhang, L. L., Wang, L., and Shi, X. L. (2009). Numerical simulation of the change of frozen soil in source regions of the Yellow River under climate warming. *J. Heilongjiang Hydraulic Eng.* 36 (3), 100–104.

Harlan, R. L. (1973). Analysis of coupled heat-fluid transport in partially frozen soil. *Water Resour. Res.* 9 (5), 1314–1323. doi:10.1029/wr009i005p01314

Harlan, R. L. (1971). Water transport in frozen and partially frozen porous media. *Proc. Can. Hydrol. Symp.* 1 (8), 109–129.

Hoekstra, P. (1966). Moisture movement in soils under temperature gradients with the cold-side temperature below freezing. *Water Resour. Res.* 2, 241–250. doi:10.1029/wr002i002p00241

Ivits, E., Cherlet, M., Sommer, S., and Mehl, W. (2013). Addressing the complexity in nonlinear evolution of vegetation phenological change with time-series of remote sensing images. *Ecol. Indic.* 26, 49–60. doi:10.1016/j.ecolind.2012.10.012

Jiang, C., and Zhang, L. B. (2016). Ecosystem change assessment in the Three-River headwater region, China: Patterns, causes, and implications. *Ecol. Eng.* 93, 24–36. doi:10.1016/j.ecoleng.2016.05.011

Jiang, P., Gautam, M. R., Zhu, J., and Yu, Z. (2013). How well do the GCMs/RCMs capture the multi-scale temporal variability of precipitation in the Southwestern United States?. *J. Hydrol.* 479, 75–85.

Jiang, P., Yu, Z., Gautam, M. R., Yuan, F., and Acharya, K. (2016). Changes of storm properties in the United States: Observations and multimodel ensemble projections. *Glob Planet Change* 142, 41–52.

Koren, V., Schaake, J., Mitchell, K., Duan, Q. Y., Chen, F., and Baker, J. M. (1999). A parameterization of snowpack and frozen ground intended for NCEP weather and climate models. *J. Geophys. Res.* 104 (D16), 19569–19585. doi:10.1029/1999jd900232

Kung, S. K. J., and Steenhuis, T. S. (1986). Heat and moisture transfer in a partly frozen nonheaving soil. *Soil Sci. Soc. Am. J.* 50, 1114–1122. doi:10.2136/sssaj1986.03615995005000050005x

Lei, Z. D., Shang, S. H., and Yang, S. X. (1988). *Soil hydrodynamics*. Beijing, China: Tsinghua University Press.

Leprieur, C., Verstraete, M. M., and Pinty, B. (1994). Evaluation of the performance of various vegetation indices to retrieve vegetation cover from AVHRR data. *Remote Sens. Rev.* 10 (4), 265–284. doi:10.1080/02757259409532250

Li, H. X., Liu, G. H., and Fu, B. J. (2011). Response of vegetation to climate change and human activity based on NDVI in the Three-River Headwaters region. *Acta Ecol. Sin.* 31 (19), 5495–5504.

Li, S. C., Li, D. L., Zhao, P., and Zhang, G. Q. (2009). The climatic characteristics of vapor transportation in rainy season of the origin area of three rivers in Qinhai-Xizang Plateau. *Acta Meteorol. Sin.* 67 (4), 591–598.

Liang, L. Q., Li, L. J., Liu, C. M., and Cuo, L. (2013). Climate change in the Tibetan plateau three rivers source region: 1960-2009. *Int. J. Climatol.* 33, 2900–2916. doi:10.1002/joc.3642

Liu, G. S., Wang, G. X., and Zhang, W. (2012). Research on climate and runoff variation characteristics in the Three-River Headwater Region. *Resour. Environ. Yangtze Basin* 21 (3), 302–309.

Liu, H. (2015). Simulation of the freezing-thawing processes at nagqu area over qinghai-xizang plateau. *Plateau Meteorol.* 34 (3), 676–683.

Liu, J. Y., Xu, X. L., and Shao, Q. Q. (2008). Grassland degradation in the "Three-River headwaters" region, Qinghai province. *J. Geogr. Sci.* 18, 259–273. doi:10.1007/s11442-008-0259-2

Liu, X. D. (2010). Study on information extraction and the dynamic monitoring of grassland coverage in three river source area. *Acta Agrestia Sin.* 18 (2), 154–159.

Liu, X., Zhang, J., Zhu, X., Pan, Y., Liu, Y., Zhang, D., et al. (2014). Spatiotemporal changes in vegetation coverage and its driving factors in the Three-River Headwaters Region during 2000-2011. *J. Geogr. Sci.* 24, 288–302. doi:10.1007/s11442-014-1088-0

Luo, S. Q., Fang, X., Lyu, S., Ma, D., Chang, Y., Song, M., et al. (2016). Frozen ground temperature trends associated with climate change in the Tibetan Plateau Three River Source Region from 1980 to 2014. *Clim. Res.* 67, 241–255. doi:10.3354/cr01371

Luo, S. Q., Lv, S. H., and Zhang, Y. (2009). Development and validation of the frozen soil parameterization scheme in Common Land Model. *Cold Regions Sci. Technol.* 55, 130–140. doi:10.1016/j.coldregions.2008.07.009

Niu, G. Y., and Yang, Z. L. (2006). Effects of frozen soil on snowmelt runoff and soil water storage at a continental scale. *J. Hydrometeorol.* 7, 937–952. doi:10.1175/jhm538.1

Orakoglu, M. E., Liu, J. K., and Tutumluer, E. (2016). Frost depth prediction for seasonal freezing area in Eastern Turkey. *Cold Regions Sci. Technol.* 124, 118–126. doi:10.1016/j.coldregions.2015.12.012

Pang, Q. Q., Li, S. X., Wu, T. H., and Zhang, W. G. (2006). Simulated distribution of active layer depths in the frozen ground regions of Tibetan plateau. *J. Glaciol. Geocryol.* 28 (3), 390–395.

Poutou, E., Krinner, G., Genthon, C., and Noblet-Ducoudré, N. D. (2004). Role of soil freezing in future boreal climate change. *Clim. Dyn.* 23 (6), 621–639. doi:10.1007/s00382-004-0459-0

Qi, J., Marsett, R. C., Moran, M. S., and Goodrich, D. C. (2000). Spatial and temporal dynamics of vegetation in the San Pedro River basin area. *Agric. For. Meteorology* 105 (1-3), 55–68. doi:10.1016/s0168-1923(00)00195-7

Shang, S. H., Lei, Z. D., and Yang, S. X. (1997). Numerical simulation improvement of coupled moisture and heat transfer during soil freezing. *J. Tsinghua Univ. (Sci Tech)* 37, 62–64.

Shao, Q. Q., Jiyuan, L., Lin, H., Jiangwen, F., Xinliang, X., and Junbang, W. (2013). Integrated assessment on the effectiveness of ecological conservation in sanjiangyuan national nature reserve. *Geogr. Res.* 32, 1945–1956.

Sheng, N. N., Ju, Q., and Dun, Z. J. C. (2021). Permafrost variation characteristics and its relationship with temperature in Yellow River. *South-to-North Water Transfers Water Sci. Technol.* 19 (5), 843–852. (in Chinese).

Sheppard, M. W., Key, B., and Loch, J. (1978). Development and testing of a computer model for heat and mass flow in freezing soils. *Proc. 3rd Int. Conf. Permafr.* 1, 76–81.

Shi, C. L., Yu, J. M., and Jin, Z. Q. (1998). Numerical simulation of water and heat transfer during soil freezing and thawing in the situation of saturated soil. *Chin. J. Agrometeorology* 19 (4), 21–26.

Sun, A., Yu, Z., Zhou, J., Acharya, K., Ju, Q., Xing, R., et al. (2020). Quantified hydrological responses to permafrost degradation in the headwaters of the Yellow River (HWYR) in High Asia. *Sci. Total Environ.* 712, 135632. doi:10.1016/j.scitotenv.2019.135632

Tang, X. P. (2003). Basic ecological characteristics of the three-rivers' source area and design of the nature reserve. *For. Resour. Manag.* 1, 38–44.

Taylor, G. S., and Luthin, J. N. (1978). A model for coupled heat and moisture transfer during soil freezing. *Can. Geotech. J.* 18, 548–555. doi:10.1139/t78-058

Tong, L. G., Xu, X. L., Fu, Y., and Li, S. (2014). Wetland changes and their responses to climate change in the "Three-River headwaters" region of China since the 1990s. *Energies* 7, 2515–2534. doi:10.3390/en7042515

Wang, B. B., Ma, Y. M., and Ma, W. Q. (2012). Estimation of land surface temperature retrieved from EOS/MODIS in Naqu area over Tibetan Plateau. *J. Remote Sens.* 16 (6), 1289–1298.

Wang, C. H., Dong, W. J., and Wei, Z. G. (2001). The feature of seasonal frozen soil in Qinghai-Tibet Plateau. *Acta Geogr. Sin.* 56 (5), 523–531.

Wang, Q. J., Lai, D. Z., Jing, Z. C., Shi-Xiong, L. I., and Shi, H. L. (2005). The resources, ecological environment and sustainable development in the source regions of the Yangtze, Huanghe and Yalu Tsangpo Rivers. *J. Lanzhou Univ. Nat. Sci.* 41 (4), 50–55.

Xia, K., Luo, Y., and Li, W. P. (2011). Simulation of freezing and melting of soil on the northeast Tibetan Plateau. *Chin. Sci. Bull.* 43 (20), 2145–2155. doi:10.1007/s11434-011-4542-8

Xiang, X. H., Wu, X. L., Wang, C. H., Chen, X., and Shao, Q. X. (2013). Influences of climate variation on thawing-freezing processes in the northeast of Three-River Source Region China. *Cold Regions Sci. Technol.* 86, 86–97. doi:10.1016/j.coldregions.2012.10.006

Xu, W. X., Gu, S., Zhao, X., Xiao, J., Tang, Y., Fang, J., et al. (2011). High positive correlation between soil temperature and NDVI from 1982 to 2006 in alpine meadow of the Three-River Source Region on the Qinghai-Tibetan Plateau. *Int. J. Appl. Earth Observation Geoinformation* 13, 528–535. doi:10.1016/j.jag.2011.02.001

Yi, X. S., Yin, Y. Y., Li, G. S., and Peng, J. T. (2011). Temperature variation in recent 50 Years in the Three-River headwaters region of Qinghai province. *Acta Agrestia Sin.* 66 (11), 1451–1465.

Yin, Z. F., Ouyang, H., and Chen, X. (2010). Simulating soil freezing and thawing of temperate desert ecosystem on the Qinghai-Tibet Plateau. *Procedia Environ. Sci.* 2 (9), 476–485. doi:10.1016/j.proenv.2010.10.052

Yu, Y., Zhao, W., Martinez-Murillo, J. F., and Pereira, P. (2020). Loess Plateau: From degradation to restoration. *Sci. Total Environ.* 738, 140206.

Yu, Y., Zhu, R., Ma, D., Liu, D., Liu, Y., Gao, Z., et al. (2022). Multiple surface runoff and soil loss responses by sandstone morphologies to land-use and precipitation regimes changes in the Loess Plateau, China. *CATENA* 217, 106477.

Yuan, F. F., Berndtsson, R., Zhang, L., Uvo, C. B., Hao, Z., Wang, X., et al. (2015). Hydro climatic trend and periodicity for the source region of the Yellow River. *J. Hydrol. Eng.* 20 (10), 05015003. doi:10.1061/(asce)he.1943-5584.0001182

Zeng, X. B., Dickinson, R. E., Walker, A., Shaikh, M., DeFries, R. S., and Qi, J. (2000). Derivation and evaluation of global 1-km fractional vegetation cover data for land modeling. *J. Appl. Meteor.* 39 (6), 826–839. doi:10.1175/1520-0450(2000)039<0826:daeogk>2.0.co;2

Zhang, T., Barry, R. G., Knowles, K., Heginbottom, J. A., and Brown, J. (1999). Statistics and characteristics of permafrost and ground ice distribution in the Northern Hemisphere. *Polar Geogr. Palm. Beach.* 23 (2), 147–168. doi:10.1080/10889370802175895

Zhang, Y. Y., Zhang, S. F., Xia, J., and Hua, D. (2013). Temporal and spatial variation of the main water balance components in the three rivers source region, China from 1960 to 2000. *Environ. Earth Sci.* 68, 973–983. doi:10.1007/s12665-012-1800-2

Zhang, Y. Y., Zhang, S. F., Zhai, X. Y., and Xia, J. (2012). Runoff variation and its response to climate change in the three rivers source region. *J. Geogr. Sci.* 22 (5), 781–794. doi:10.1007/s11442-012-0963-9

Zribi, M., Le Hegarat-Mascle, S., Taconet, O., Ciarletti, V., Vidal-Madjar, D., and Boussema, M. R. (2003). Derivation of wild vegetation cover density in semi-arid regions: ERS2/SAR evaluation. *Int. J. Remote Sens.* 24 (6), 1335–1352. doi:10.1080/01431160210146668

frontiers | Frontiers in Environmental Science

TYPE Original Research
PUBLISHED 24 November 2022
DOI 10.3389/fenvs.2022.1067318

EDITED BY
Yang Yu,
Beijing Forestry University, China

REVIEWED BY
Batsuren Dorjsuren,
National University of Mongolia,
Mongolia
Hong Wang,
Institute of Geographic Sciences and
Natural Resources Research, China
Henian Wang,
Chinese Academy of Forestry, China

*CORRESPONDENCE
Tianling Qin,
qintl@iwhr.com

SPECIALTY SECTION
This article was submitted to
Freshwater Science,
a section of the journal
Frontiers in Environmental Science

RECEIVED 11 October 2022
ACCEPTED 07 November 2022
PUBLISHED 24 November 2022

CITATION
Hou J, Yan D, Qin T, Liu S, Yan S, Li J, Abebe SA and Cao X (2022), Evolution and attribution of the water yield coefficient in the Yiluo river basin.
Front. Environ. Sci. 10:1067318.
doi: 10.3389/fenvs.2022.1067318

Evolution and attribution of the water yield coefficient in the Yiluo river basin

Jun Hou[1,2], Denghua Yan[1], Tianling Qin[1]*, Shanshan Liu[1], Sheng Yan[1,2], Jian Li[1,3], Sintayehu A. Abebe[1,4] and Xuchao Cao[5]

[1]State Key Laboratory of Simulation and Regulation of Water Cycle in River Basin, China Institute of Water Resources and Hydropower Research, Beijing, China, [2]School of Water Conservancy and Engineering, Zhengzhou University, Zhengzhou, China, [3]School of Environment, Liaoning University, Shenyang, China, [4]Hydraulic and Water Resources Engineering Department, Debre Markos University Institute of Technology, Debre Markos, Ethiopia, [5]Baoding Water Conservancy and Hydropower Surveying and Designing Institute, Baoding, China

Our aim in this research was to detect historical and future water yield coefficient evolution and attribution. Based on the calibrated and validated water yield coefficient model in the Yiluo River Basin, the coefficient for the years 2000–2020 was simulated, along with the future projection for 2030–2050 under four Shared Socioeconomic Pathways (SSP126, SSP245, SSP370, and SSP585). The spatio-temporal evolution of historical and future water yield coefficients was then analyzed. Moreover, the geographical detector model was used to detect the impacts of climate, land use, and terrain factors on the water yield coefficient. The results showed that the water yield coefficient increased by 8.53% from 2000 to 2020, with the coefficient of farmland increasing by 10.47% and that of forestland decreasing by 8.93%. The coefficient was highest under the SSP370 scenario and the lowest under the SSP585 scenario in projections for 2030–2050. Compared to 2000–2020, the coefficients of the two scenarios increased by 12.2% and 2.0%, respectively. Consequently, under the SSP370 and SSP585 scenarios, the coefficient of farmland increased by 13.2% and 2.7%, and that of the forestland decreased by 0.9% and 14.6%, respectively. Driving factors detection indicated that land use types had the strongest explanatory power affecting the water yield coefficient; the explanatory value reached 26.5% in 2000–2020 and will exceed 29.5% in 2030–2050. In addition, the interaction between any two factors was stronger than a single factor. This research provides scientific support for the precise management of watershed and water-land resources.

KEYWORDS

InVEST, geographical detector, SSPs, water yield coefficient, Yiluo river basin

1 Introduction

The water yield coefficient is an indicator of the capacity of regional water yield, which refers to the proportion of water yield to precipitation. The water yield coefficient has changed under the dual impacts of climatic variation and human activity, profoundly influencing the development and utilization of available water resources (Liu et al., 2016; Schwärzel et al., 2020; Gbohoui et al., 2021). Climate variation, accompanied by temperature increments and extreme precipitation, have fundamentally affected the state of water resources (Capo et al., 2018; Li and Wang, 2021; Ouyang, 2021). Additionally, human activity has greatly changed the properties of water yield and consumption through underlying surface construction (Hu et al., 2021; Li et al., 2022a; Xu et al., 2022). In the context of climate warming and intensified human activity, it is critical to analyze the spatio-temporal evolution of the water yield coefficient and identify driving factors in development of watershed and water-land resources.

Scholars worldwide have conducted extensive studies assessing historical water yield capacity (Li H. et al., 2021; Guo et al., 2021; Li et al., 2022b; Zhou et al., 2022). Hydrological modeling is the principal approach in quantitative simulation of regional water yield. Hydrological models, such as the Soil and Water Assessment Tool (SWAT) (Ayivi and Jha, 2018; Chiang et al., 2019), MIKE European Hydrological System (MIKE SHE) (Wang et al., 2013; Zheng et al., 2020), and the Integrated Valuation of Ecosystem Services and Tradeoffs (InVEST) model (Yang X. et al., 2021; Jin et al., 2022), have been used for this purpose. Yang et al. (2019) evaluated water yield based on the SWAT model and pointed out that the annual water yield decreased by 38.48% in the Yanhe Basin due to the implementation of the Grain for Green Project. Pei et al. (2022)adopted the InVEST model and noted that the annual water yield had an increasing trend of 1.96 mm/a ($p < 0.1$) in the Agro-pastoral ecotone of Northern China from 2000 to 2019. Moreover, historical water yield coefficient evaluation has been conducted in recent years. Shi et al. (2018)analyzed spatio-temporal variation of the water yield coefficient based on gross water resources and reported that the coefficient was between 0.03 and 0.58 in the Huang-Huai-Hai River Basin from 1961 to 2011. Li et al. (2017) employed the Budyko framework and proposed that vegetation restoration significantly reduced the water yield coefficient during the growing season in the Yangtze River source region, with a decrease from 0.37 ± 0.07 in 1982–1999 to 0.24 ± 0.07 in 2000–2012.

For identification of attributes related to water yield capacity, common methods include scenario analysis (Yang J. et al., 2021; Shao and Yang, 2021), model analysis (Sun et al., 2019; Wang X. et al., 2022), and statistical analysis (Rizzo et al., 2020; Deng et al., 2022). Dai and Wang (2020) studied the influence of climate factors and land use factors on water yield using the geographic detector model and reported that precipitation and evapotranspiration were the primary driving factors in the Hengduan Mountain region. Zhang et al. (2021) used the automatic linear and geographically weighted regression models to evaluate the interactive effects of diverse driving factors on water yield and observed that annual precipitation and urban expansion were the dominant factors in the Yangtze River Basin during 2000–2015. However, the evolution and attribution of the future water yield coefficient remain unclear.

The Yiluo River Basin is the largest tributary below the Sanmenxia Dam of the Yellow River Basin, which is mainly composed of the Yi River and the Luo River. The study area plays an important role in flood control, water resource allocation, and water-sediment regulation in the lower reaches of the Yellow River Basin (Wang et al., 2019; Hou et al., 2021). To prevent soil erosion and improve the ecological environment, large-scale water and soil conservation work has been carried out in the basin. Along with climate variation and urban expansion, water yield and consumption properties have been altered, which has greatly impacted the watershed water yield coefficient. Our aim was to analyze the spatio-temporal variation of historical and future water yield coefficients and identify driving factors affecting water yield in the Yiluo River Basin.

2 Data and methods

2.1 Study area

The Yiluo River Basin (109°43′-113°10′ E and 33°39′-34°54′ N) flows through more than 20 counties of the Henan and Shaanxi provinces; it covers an area of 18.9 thousand km^2 (Figure 1). The Yiluo River is a typical “twins river,” where the north bank is the Luo River and the south bank is the Yi River; the Yiluo River results from the convergence of the two rivers. The trunk stream (Luo River) originates in the Shaanxi Province and has a total length of 446.9 km and an area of 11.9 thousand km^2. The main tributary (Yi River) originates in Henan and has a total length of 264.8 km and an area of 6.1 thousand km^2. The Yiluo River Basin is in the continental monsoon climate zone. The climate is hot and rainy in summer due to the warm and humid flow of the Pacific Ocean and cold and rainless in winter due to cold air from the north. The annual average temperature is 13.1°C, and the annual average precipitation is 688.1 mm. The precipitation occurs mainly from May to October, accounting for more than 80% of the annual precipitation. During 2000–2020, the watershed land use categories primarily consisted of cultivated land and woodland, with proportions exceeding 38.2% and 48.3%, respectively, while grassland, urban land, and bodies of water accounted for a relatively small proportion.

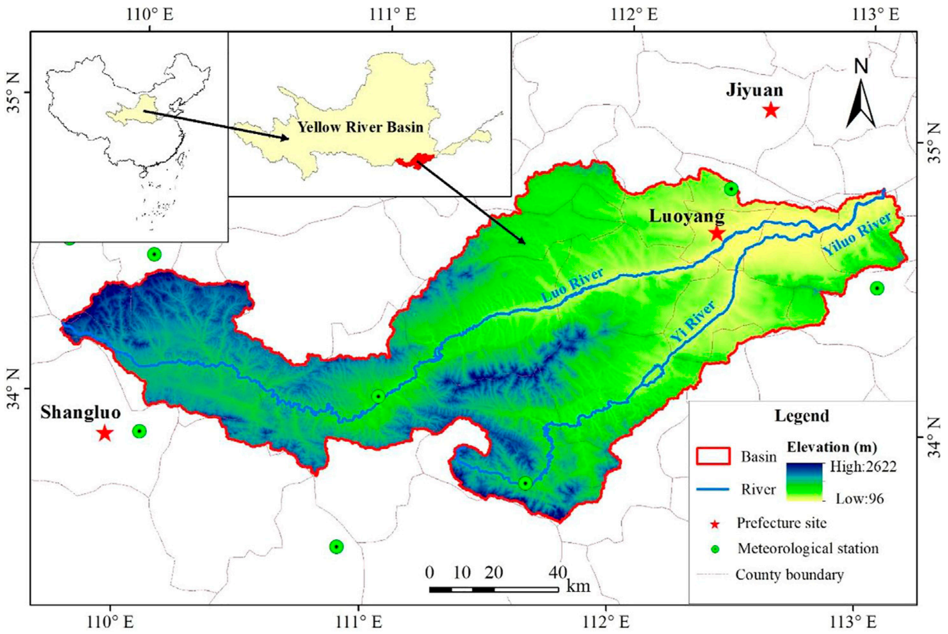

FIGURE 1
Location, main cities, meteorological stations, major rivers, basin boundary, and elevation of the Yiluo River Basin.

TABLE 1 Study data description and sources.

Category	Name	Year	Data source	Description
Historical climate	Precipitation Temperature	1961–2020	China Meteorological Data Service Center (http://data.cma.cn/)	Daily data from 10 meteorological stations
Underlying surface	Land use	2000, 2010, 2020	National Geomatics Center of China (http://www.ngcc.cn/)	With a resolution of 30 m
	DEM	2000	Geospatial Data Cloud (http://www.gscloud.cn/)	With a resolution of 90 m
	Slope Aspect		Generated by DEM	
	Soil	2009	National Cryosphere Desert Data Center (http://www.ncdc.ac.cn)	Chinese soil data set based on world soil database
	Depth to bedrock	2018	Scientific Data (http://globalchange.bnu.edu.cn/research/cdtb.jsp)	With a resolution of 100 m
Water resources	Water resources	1990–2020	Water Resources Bulletin	Provincial and municipal
	Soil water		United States Geological Survey (https://www.usgs.gov/)	With a resolution of 1,000 m
Future climate	Precipitation Temperature	2021–2050	Coupled Model Intercomparison Project Phase 6 (https://esgf-node.llnl.gov/projects/cmip6/)	With a resolution of 0.1°m

2.2 Data

The data collected in this research included historical climate data, underlying surface data, water resource data, and future climate data (Table 1). Historical climate data were obtained from the China Meteorological Data Service Center. Underlying surface data included land use, the digital elevation model (DEM), and soil and bedrock depth. Land use data were derived from the National Geomatics Center of China. The DEM was obtained from the Geospatial Data Cloud, and the slope and aspect were generated from the DEM. Soil data was obtained from the National Cryosphere Desert Data Center; bedrock depth was obtained from an article in Scientific Data (Yan et al., 2020). Water resource data included soil water content and the amount of

TABLE 2 Global climate models selected for this study.

Number	Mode	Institutions	Resolution
1	ACCESS-CM2	CSIRO-ARCCSS, Australia	1.2° × 1.8°
2	ACCESS-ESM1-5	CSIRO, Australia	1.2° × 1.8°
3	BCC-CSM2-MR	BCC, China	1.12° × 1.12°
4	CanESM5	CCCma, Canada	2.8° × 2.8°
5	CESM2-WACCM	NCAR, United States	0.94° × 1.25°
6	CMCC-CM2-SR5	CMCC, Italy	1.0° × 1.0°
7	FGOALS-g3	CAS, China	2.25° × 2°
8	IITM-ESM	CCCR-IITM, India	2° × 2°
9	MIROC6	MIROC, Japan	1.4° × 1.4°
10	MPI-ESM1-2-HR	MRI-M DWD DKRZ, Germany	0.9° × 0.9°
11	MPI-ESM1-2-LR	MRI-M AWI DKRZ, Germany	1.9° × 1.9°
12	MRI-ESM2-0	MRI, Japan	1.125° × 1.125°
13	NorESM2-LM	NCC, Norway	1.9° × 2.5°
14	NorESM2-MM	NCC, Norway	0.9° × 1.3°
15	TaiESM1	RCEC-AS, Taiwan, China	1.3° × 0.9°

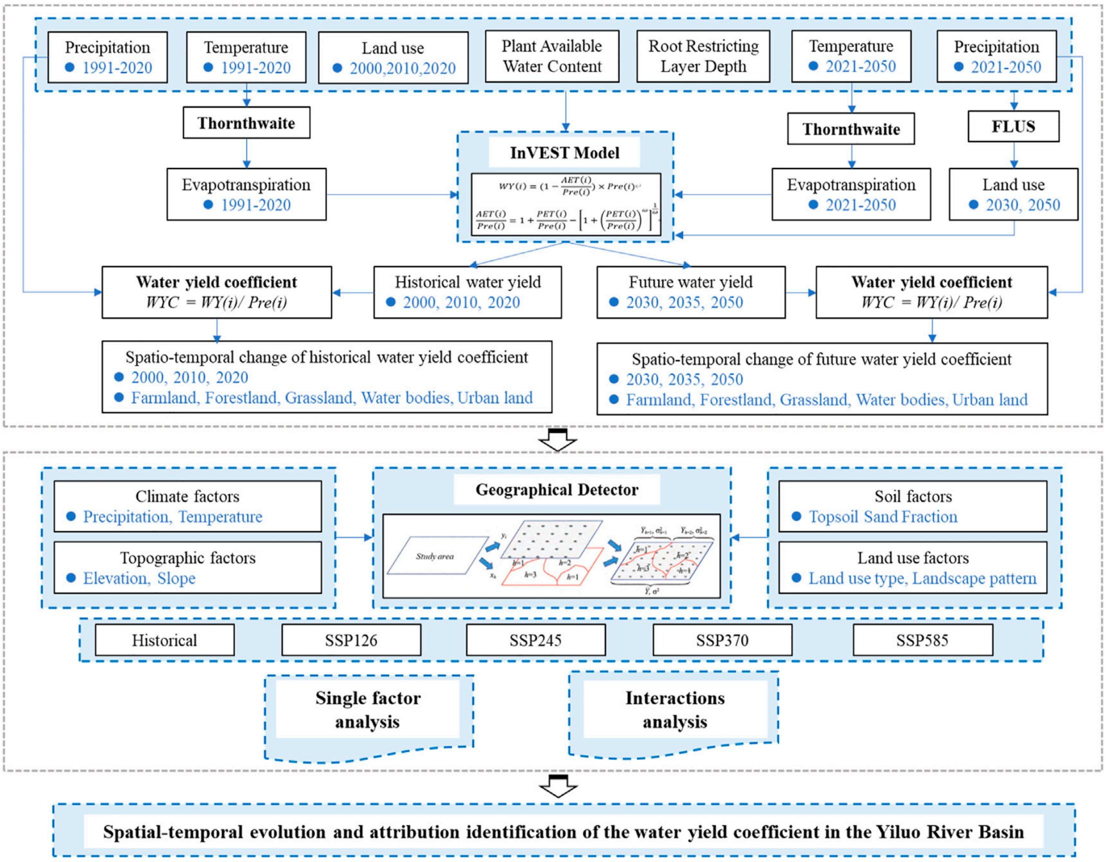

FIGURE 2
Research workflow.

gross water resources; soil water content was derived from the United States Geological Survey. The data on gross water resources were obtained from the Water Resources Bulletin.

Future precipitation and temperature data used in the future climate model was provided by Coupled Model Intercomparison Project Phase 6 (CMIP6). The authentic data considered the Representative Concentration Pathways (RCPs) and the Shared Socioeconomic Pathways (SSPs), which confront the challenges of future climate variation more comprehensively. Fifteen models of CMIP6 (Table 2) were selected to decrease uncertainty in the future climate model data. The scenarios SSP126, SSP245, SSP370, and SSP585 were considered in this study. The equidistant cumulative distribution function (EDCDF) method was used for downscaling correction (Li et al., 2010; Piao et al., 2021), and historical climate data were used for correction and verification of the CMIP6 data.

2.3 Methods

The research workflow of this study included model simulation, trend analysis, and attribution identification (Figure 2). First, based on the water yield coefficient calculation model, the watershed water yield coefficients for 2000–2020 and 2030–2050 were simulated. Next, the temporal and spatial variations of the historical and future water yield coefficients in the basin were analyzed. Finally, the impacts of different driving factors on the basin's historical and future water yield coefficients were identified based on the geographical detector model.

2.3.1 Calculation of the water yield coefficient

The water yield coefficient refers to the proportion of regional water yield to precipitation. The methods are described as follows:

$$WYC(i) = \frac{WY(i)}{Pre(i)}$$

where $WYC(i)$, $WY(i)$ (mm), and $Pre(i)$ (mm) refer to the annual average water yield coefficient, water yield, and precipitation of grid cell i, respectively. The water yield was calculated using the water yield module of the InVEST model. Based on the water balance, the water yield was obtained by subtracting the actual evapotranspiration from the precipitation of each grid cell. The formulae are as follows (Redhead et al., 2016; Wang H. et al., 2022):

$$WY(i) = \left(1 - \frac{AET(i)}{Pre(i)}\right) \times Pre(i)$$

$$\frac{AET(i)}{Pre(i)} = 1 + \frac{PET(i)}{Pre(i)} - \left[1 + \left(\frac{PET(i)}{Pre(i)}\right)^{\omega}\right]^{1/\omega}$$

where: $AET(i)$ (mm) and $PET(i)$ (mm) represent the annual average actual evapotranspiration and potential evapotranspiration of grid cell i, respectively, and ω represents the non-physical parameters of natural climate-soil properties. The calculation method is as follows:

$$\omega(i) = Z \times \frac{AWC(i)}{Pre(i)} + 1.25$$

$$PET(i) = K_c(\iota_x) \times ET_0(i)$$

where $AWC(i)$ refers to the soil water content available to vegetation on grid cell i, the Z value reflects the local climate patterns and hydrogeological properties, and the value of Z for this calculation was set as 6. $K_c(\iota_x)$ denotes the evapotranspiration coefficient of a particular land use type in raster cell i, and $ET_0(i)$ (mm) represents the reference evapotranspiration of raster cell i. The Thornthwaite method was applied to simulate the reference evapotranspiration considering data availability, which is an empirical formula based on the monthly temperature. The formula is as follows:

$$ET_0 = \begin{cases} 0, & T_i < 0^{\circ}\mathrm{C} \\ 1.6 \times L_D \times \left(\frac{10T_i}{I}\right)^{\alpha}, & 0 \le T_i \le 26.5^{\circ}\mathrm{C} \\ L_d \times (-415.85 + 32.24T_i - 0.43T_i^2), & T_i > 26.5^{\circ}\mathrm{C} \end{cases}$$

$$I = \sum_{i=1}^{12} \left(\frac{T_i}{5}\right)^{1.514}$$

$$\alpha = 0.49 + 1.79 \times 10^{-2} \times I - 7.71 \times 10^{-5} \times I^2 + 6.75 \times 10^{-7} \times I^3$$

where T_i (°C) is the monthly average temperature, I is the coefficient of temperature efficiency, α is the function of the heat index, and L_d is the adjustment coefficient related to day length and latitude.

2.3.2 Future land use simulation

In this study, the future land use simulation (FLUS) model was applied to simulate the future land use distribution in 2030 and 2050. First, the model employed the neural network algorithm to obtain the suitability probability between the land use types and their driving factors. Second, the Markov model was used to calculate the pixel number of each land use type in the prediction year. Last, the land use types were allocated to each pixel on the strength of a roulette selection method (Liu X. et al., 2017; Liang et al., 2018). Based on the land use data in 2010, the land use in 2020 was simulated. Then, the actual data in 2020 was used to verify the simulation result. On this basis, the calibrated and verified model was used to simulate future land use in 2030 and 2050 by adjusting the input parameters.

2.3.3 Geographical detector

A geographical detector is a new statistical method to detect spatial differentiation and reveal its driving factors. The model includes single-factor detection, interaction detection, risk detection, and ecological detection (Wang et al., 2016; Wang and Xu, 2017). This study used primarily single-factor and interaction detection. Single-factor detection is used to determine the

TABLE 3 Water yield results verification.

Period	Actual water resources (billion m^3)	Simulated water yield (billion m^3)	Relative error (%)
1990–2000	2.52	2.43	−3.53
2001–2010	3.24	3.40	4.85
2011–2020	2.66	2.72	2.01

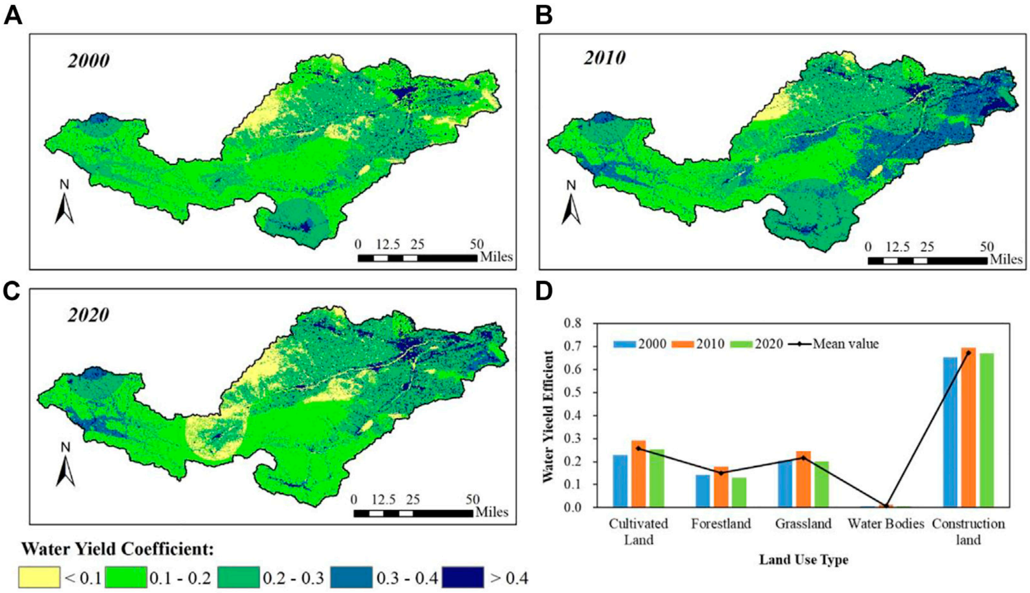

FIGURE 3
Water yield coefficient of the Yiluo River Basin during 2000–2020. **(A–C)** Water yield coefficients of 2000, 2010, and 2020, respectively. **(D)** Water yield coefficients of different land use types.

explanatory power of the driving factor X on the variable Y. The q value measures the explanatory power, and a higher q value indicates a better explanatory power of X on Y. Interaction detection determines the explanatory power of the combined effect of two driving factors, X, on the variable Y. In this study, the geographical detector method was applied to identify the impacts of precipitation (X1), temperature (X2), elevation (X3), slope (X4), land use types (X5), Shannon's diversity index (SHDI) of landscape pattern (X6), and topsoil sand fraction (X7) on water yield coefficient (Y).

3 Results

3.1 Spatio-temporal evolution of the historical water yield coefficient

The relative error between the volume of simulated water yield and the amount of gross water resources was within 5% in the Yiluo River Basin during 2000–2020 (Table 3), indicating that the model has good simulation capability and is useful for subsequent simulation and prediction. Further, the model for water yield coefficient calculation was used to obtain the water yield coefficient of the basin for 2000–2020 (Figure 3). We found an annual average water yield coefficient of 0.23 in 2000–2020, with spatial distribution higher in the east and lower in the west. The water yield coefficient in the most recent 20 years has shown an increase of 8.53%. Within this time span, the coefficient increased by 26.75% in 2000–2010 and decreased by 14.38% in 2010–2020 (Figure 3A–C). In terms of different land use types, the water yield coefficient of urban land was the highest (0.67), followed by farmland (0.26), grassland (0.20), and woodland (0.15). Bodies of water had the lowest water yield coefficient. During the study period, the water yield coefficients of woodland and grassland decreased by 8.93% and 1.12%, respectively. The coefficients of cultivated land, urban land, and bodies of water increased by 10.47%, 3.24%, and 2.85%, respectively (Figure 3D).

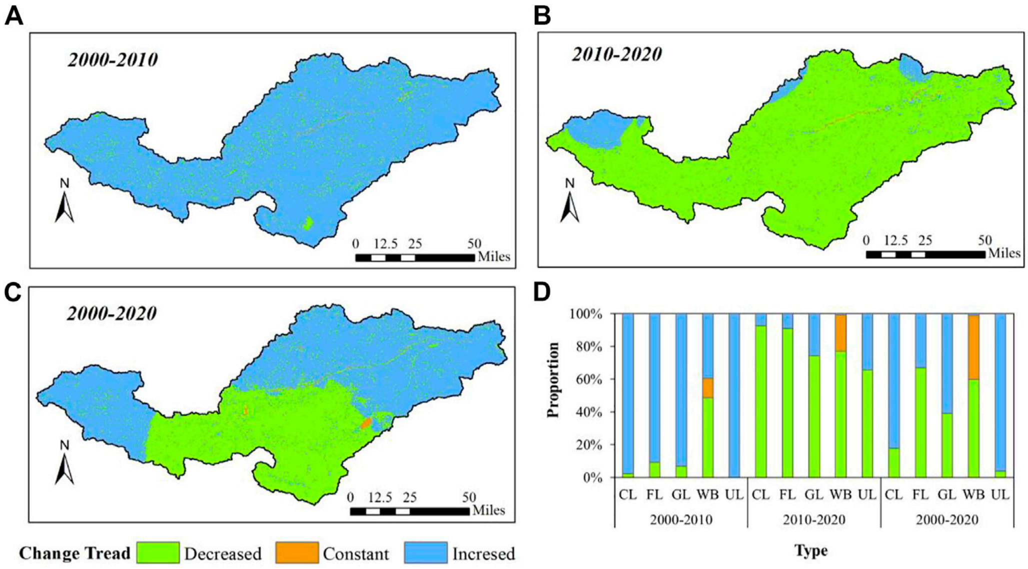

FIGURE 4
Spatio-temporal variation of the water yield coefficient in the Yiluo River Basin during 2000–2020. **(A–C)** Trends in change of the water yield coefficient in 2000–2010, 2010–2020, and 2000–2020, respectively. **(D)** Area proportion of the water yield coefficient variation in different land use types. CL, FL, GL, WB, and UL indicate cultivated land, forestland, grassland, water body, and urban land, respectively.

Spatially, the trend in variation of the water yield coefficient in the Yiluo River Basin showed obvious spatial heterogeneity (Figure 4). During 2000–2020, the water yield coefficients in 57.93% of the regions were increasing. Approximately 41.7% of the regions showed decreasing trends. The trends were distributed mainly in the middle reaches of the Yiluo River Basin (Figure 4C). During the 20-year span, the water coefficients were mostly increasing in 2000–2010 (Figure 4A), and then decreasing in 2010–2020 (Figure 4B). In addition, the area proportion of water yield coefficient variation in different land types was calculated. During 2000–2020, the coefficients of cultivated land, grassland, and bodies of water had increasing trends that accounted for 82.4%, 60.8%, and 96.2% of those land types, respectively; in contrast, the coefficients of woodland and urban land showed primarily decreasing trends that occurred in 66.8% and 59.9% of those land types, respectively (Figure 4D).

3.2 Spatio-temporal evolution of the future water yield coefficient

The Kappa coefficient was 0.87 between the simulated and actual land use in 2020, which indicated that the FLUS model provided a reliable simulation of the spatial distribution of land use in the Yiluo River Basin. The land use in 2030 and 2050 was then simulated. By using predicted future climate data, the water yield coefficient model was applied to simulate the spatial distribution of the water yield coefficient during 2030–2050. We used the SSP126, SSP245, SSP370, and SSP585 scenarios (Figure 5). The results indicated that the water yield coefficient of the Yiluo River Basin in 2030–2050 had spatial distribution that was higher in the east and lower in the west, therefore similar to that of the historical period. The multi-year average water yield coefficient was highest under the SSP370 scenario (Figure 5G–I) and lowest under the SSP585 scenario (Figure 5J–L). Compared with the historical periods, the coefficients of the two scenarios increased by 12.2% and 2.0%, respectively. In 2030–2050, the water yield coefficient increased by 4.9% under the SSP126 scenario (Figure 5A–C). The water yield coefficient decreased by 0.4% and 3.2% under the SSP245 (Figure 5D–F) and SSP585 scenarios and continuously increased by 8.1% under the SSP370 scenario.

Considering different land use types, the multi-year average water yield coefficient was highest under the SSP370 scenario and lowest under the SSP585 scenario in 2030–2050 (Figure 6). Compared with 2000–2020, the water yield coefficients of cultivated land and forestland changed the most. Under the SSP370 and SSP585 scenarios, the coefficients of cultivated land increased by 13.2% and 2.7%, respectively. Similarly, the coefficients of forestland decreased by 0.9% and 14.6%, respectively. The coefficients of grassland, urban land, and bodies of water changed slightly. During the study period, the water yield coefficients of different land use types showed a primarily increasing trend under the SSP126 and SSP370 scenarios. The coefficient of forestland showed the greatest change under the SSP126 scenario, with an increase

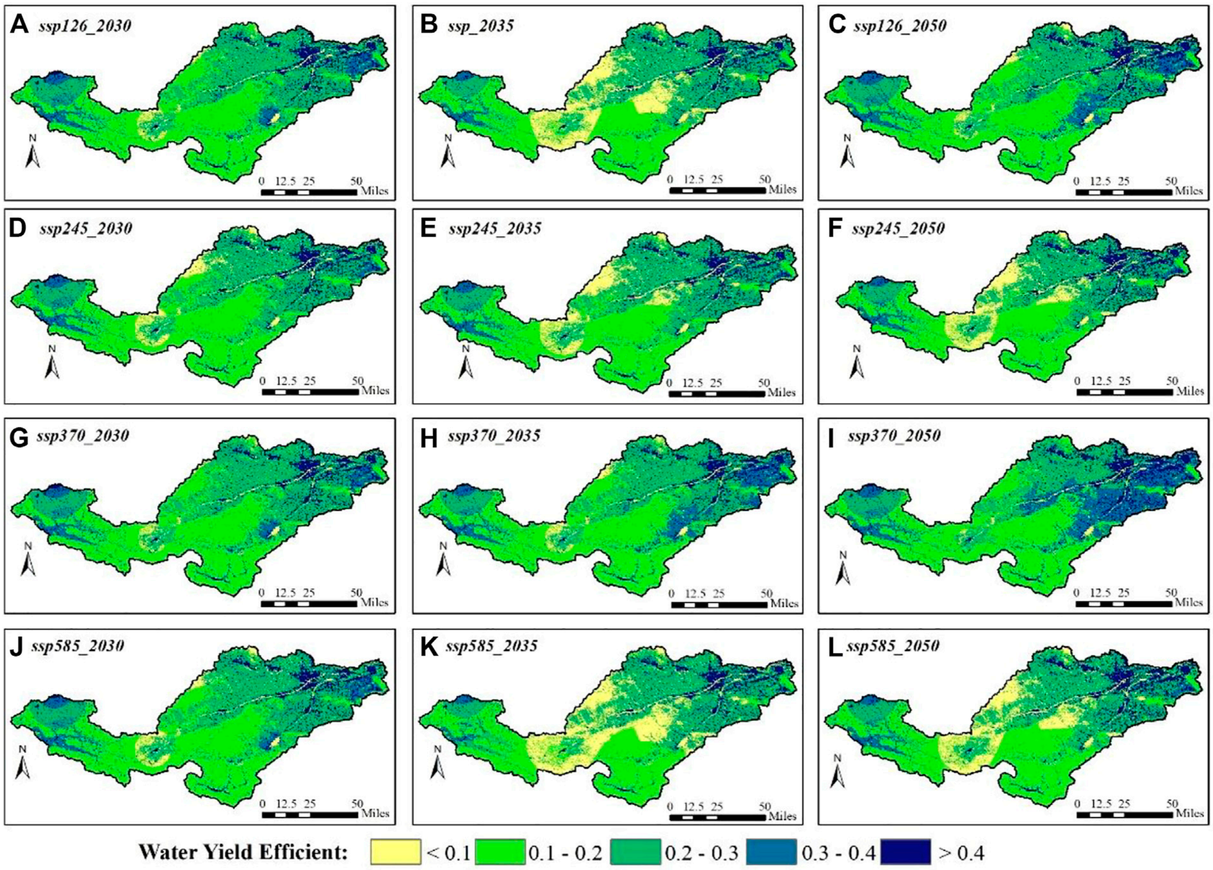

FIGURE 5
Water yield coefficient of the Yiluo River Basin in 2030–2050. **(A–L)** Coefficients for 2030, 2035, and 2050 under the SSP126, SSP245, SSP370, and SSP585 scenarios, respectively.

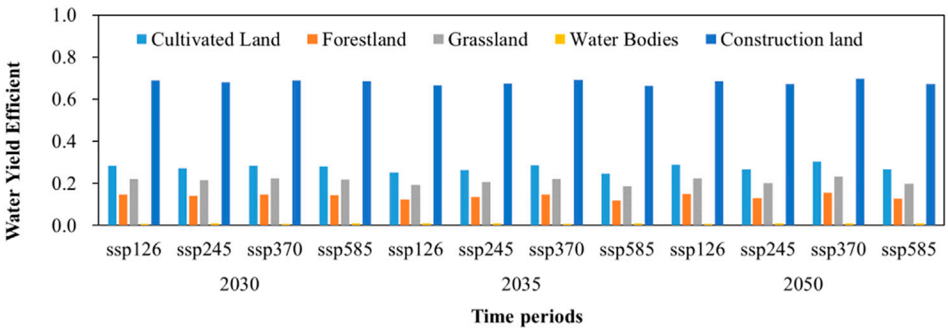

FIGURE 6
Water yield coefficients of different land use types in 2030, 2035, and 2050 under the SSP126, SSP245, SSP370, and SSP585 scenarios.

of 2.6%. Similarly, cultivated land showed the greatest change under the SSP370 scenario, with an increase of 7.1%. The water yield coefficients of different land use types showed primarily decreasing trends under the SSP245 and SSP585 scenarios, and the coefficients of forestland with the greatest change showed decreases of 11.1% and 8.2%, respectively.

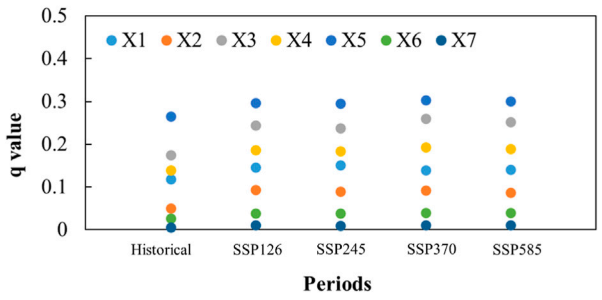

FIGURE 7
Summary of q values for each driving factor assessed for effects on water yield coefficients. X1, X2, X3, X4, X5, X6, and X7 indicate precipitation, temperature, elevation, slope, land use type, Shannon's diversity index, and topsoil sand fraction, respectively.

3.3 Detection of driving factors of the water yield coefficient

The impacts of precipitation, temperature, elevation, slope, land use, SHDI, and topsoil sand fraction on the water yield coefficient in the Yiluo River Basin were analyzed based on the geographical detector model. Single-factor detection results showed that the land use types in the Yiluo River Basin had the strongest explanatory power on the water yield coefficient (Figure 7). The q value reached 26.5% in 2000–2020 and is projected to exceed 29.5% in 2030–2050. After land use type, the factors with greatest impact were elevation, slope, precipitation, and temperature, which had q values between 5% and 25% in the historical and future periods. The q values of the topsoil sand fraction and the SHDI were less than 5%.

Based on the interactive detection module of the geographical detector model, the interaction of each driving factor with the water yield coefficient in the Yiluo River Basin was analyzed (Figure 8). The results show that the interaction between different driving factors presented mainly bilinear and nonlinear enhancements. These enhancements indicate that the interaction between any two factors was stronger than a single-factor effect on the water yield coefficient. The interactions of the land use types with other driving factors were the strongest. Explanatory values of 27%–35% in 2000–2020 (Figure 8A) and 30–44% in 2030–2050 were obtained under the SSP126 (Figure 8B), SSP245 (Figure 8C), SSP370 (Figure 8D), and SSP585 (Figure 8E) scenarios. The results indicated that interaction between land use and other driving factors had enhanced influence on the spatial variation of the water yield coefficient in the Yiluo River Basin. Precipitation, temperature, elevation, slope, and the interaction between these driving factors with other factors had additional impact, with explanatory value of more than 8%.

4 Discussion

4.1 Influence of climate factors on the water yield coefficient

The explanatory values of the precipitation and temperature factors on the water yield coefficient were 11.9% and 5.1%, respectively, in 2000–2020, and accounted for 14.0%–15.1% and 8.7%–9.4%, respectively, in projections for 2030–2050. Moreover, the effects of interaction between climate factors on the water yield coefficient were stronger than the effects of a single factor. These results were consistent with previous studies (Fang et al., 2021; Wang X. et al., 2022). According to the definition of the water yield coefficient, precipitation intensity affects the water yield coefficient directly. The watershed precipitation increased by 3.4% in 2000–2020, and is projected to increase by 5.8%–8.5% in 2030–2050 compared with the historical period. The precipitation variation tendency was consistent with the trend in change of the water yield coefficient. Simultaneously, rising temperature resulted in precipitation being increasingly allocated to evapotranspiration rather than water yield (Liu L. et al., 2017; Ouyang, 2021). From 2000 to 2020, the average annual temperature of the basin increased by 3.2%, and the actual evapotranspiration increased by 1.3%. Compared with the historical period, the temperature is projected to increase by 4.4%–8.6%, and the evapotranspiration to increase by 4.7%–5.8% in 2030–2050. In addition, climate warming has led to an increased frequency of extreme weather events in the Yiluo River Basin, and changed the precipitation regimes, which further exacerbated the trend in change of the water yield coefficient (Tian et al., 2018; Xu et al., 2020; Yu et al., 2022).

4.2 Influence of land use factors on the water yield coefficient

Land use types had the strongest explanatory power affecting the water yield coefficient in the Yiluo River Basin; the q value reached 26.5% in 2000–2020 and the value is projected to exceed 29.5% in 2030–2050. Moreover, the interaction between land use types and other driving factors resulted in enhanced influence on water yield coefficient spatial variation. The results were consistent with previous studies (Gao et al., 2020; Yu et al., 2020; Liu et al., 2022). In the historical period, the population and Gross Domestic Product (GDP) of the basin increased by 76% and 269%, respectively. With economic development and population growth, urban land area increased by 86%. In the future, the urban land area will continue to expand, with a projected increase of 41% between 2020 and 2050. The expansion of urban land will primarily involve conversion from cultivated land. In the lower reaches of the Luo River, the expansion of urban land was associated with a large amount

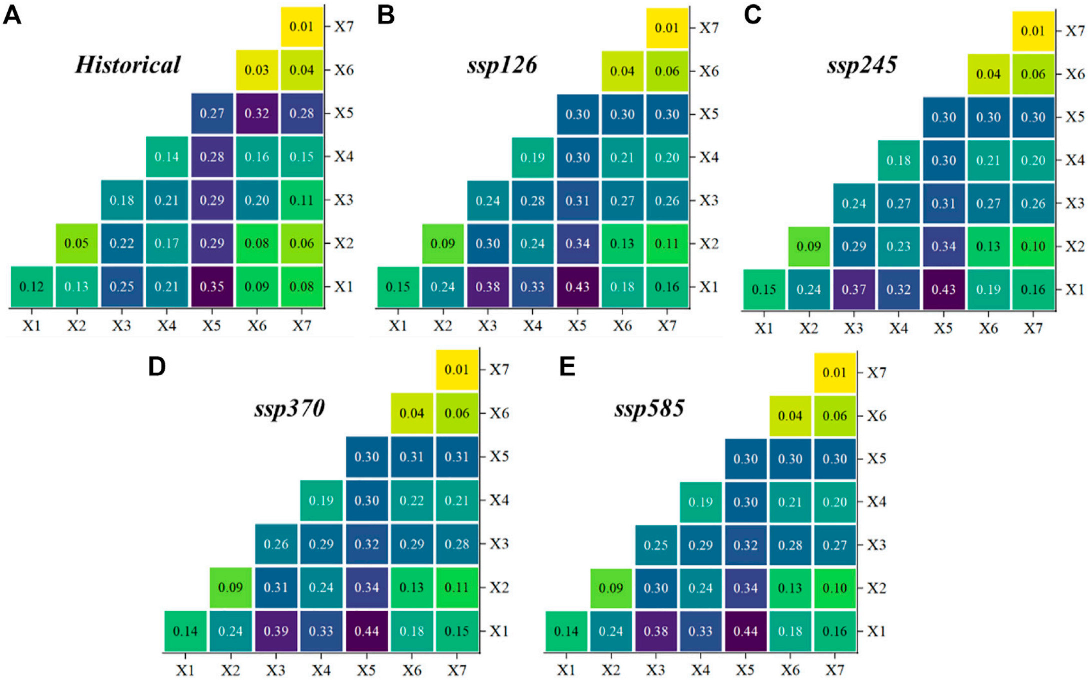

FIGURE 8
Detection of interaction among different driving factors. X1, X2, X3, X4, X5, X6, and X7 indicate precipitation, temperature, elevation, slope, land use type, Shannon's diversity index, and topsoil sand fraction, respectively. **(A–E)** Historical and future periods under the SSP126, SSP245, SSP370, and SSP585 scenarios, respectively.

of impervious area, resulting in a decrease in infiltration and an increase in water yield (Zang et al., 2019; Yang Y. et al., 2021). The Grain for Green Project implementation in 1999 and increasing public awareness of the need to protect forest resources led to an increase of 0.39% in woodland area from 2000 to 2020. Compared with 2020, further increase in forestland area is projected, with a forecast of approximately 1% increase in 2050. Forestland area has increased mainly in the middle reaches of the Yi River. With the increase of forest area, canopy interception of moisture and evapotranspiration has increased, resulting in decreased water yield. In this study, the landscape pattern index SHDI had weak explanatory power in affecting the water yield coefficient (the q value was less than 5%), which may be due to the large size of the calculated raster (Xu et al., 2019; Zong et al., 2020).

4.3 Effects of topography and soil factors on the water yield coefficient

The q value of the elevation and slope factors on the water yield coefficient in the historical and future periods was 15%–30%, and the q value of the topsoil sand fraction factor was less than 5%. The regional elevation and slope jointly determined the land use and vegetation types, which are closely related to the capacity for water yield and consumption (Gao et al., 2021; He et al., 2022). The upper reaches of the Yiluo River Basin are mountainous, with large slopes, and the primary land utilization type is woodland. The lower reaches are plains with gentle terrain, and the main land use types are cultivated and urban. The spatial distribution of elevation and slope was consistent with the water yield coefficient. The topsoil sand fraction determined the soil category and texture, which affects infiltration rate. In this study, the topsoil sand fraction factor had a weak explanatory power in affecting the water yield coefficient, which may be due to the extended time scale (Qi et al., 2020; Li J. et al., 2021).

5 Conclusion

Our research focused on the Yiluo River Basin and trends in spatial and temporal variation of the historical and future water yield coefficients were analyzed. We also assessed the influence of climate, topography, land use, and soil composition on the water yield coefficient. Our main conclusions are:

(1) The annual average water yield coefficient of the Yiluo River Basin is 0.23, which has increased by 8.53% in the last

20 years. Compared with the historical period, the coefficient is projected to increase by 2.0–12.2% from 2030 to 2050.

(2) During the study period, the water yield coefficients of farmland and forestland changed the most. The coefficient of farmland increased by 10.47% and that of the forestland decreased by 8.93% from 2000 to 2020. Compared with the historical period, the water yield coefficient of farmland is projected to increase by 2.7–13.2% and that of the forestland projected to decrease by 0.9%–14.6% in 2030–2050.

(3) Based on our model, increasing precipitation (10.6%–13.4%) and urban expansion (163%) from 2000 to 2050, are, and will continue to be, the immediate causes of increased water yield coefficients in the Yiluo River Basin. At the same time, the rate of increase of the water yield coefficient will be inhibited by rising temperature (5.6%–9.9%). Increased water consumption caused by forest construction (4.1%) was one of the main reasons for decrease in water yield capacity in the upper reaches of the Yi River.

(4) Future studies are needed to analyze dynamic mutual feeding mechanisms of water and land resources in greater depth.

Data availability statement

The raw data supporting the conclusion of this article will be made available by the authors, without undue reservation.

Author contributions

All the authors contributed to the completion of this article. JH conducted the original draft preparation. DY and TQ reviewed and edited the article. SL designed the structure of the manuscript. SY, JL, and SA edited and polished the manuscript. XC provided assistance in model building and data processing. All authors have read and agreed to the published version of the manuscript.

Funding

This research was supported by the National Science Fund Project (52130907 and 51725905) and Five Major Excellent Talent Programs of IWHR (WR0199A012021).

Acknowledgments

We acknowledge the China Meteorological Data Service Center for providing the basic meteorological data. Moreover, we would like to thank the reviewers for their constructive and detailed comments.

Conflict of interest

The authors declare that the research was conducted in the absence of any commercial or financial relationships that could be construed as a potential conflict of interest.

Publisher's note

References

Ayivi, F., and Jha, M. K. (2018). Estimation of water balance and water yield in the Reedy Fork-Buffalo Creek Watershed in North Carolina using SWAT. *Int. Soil Water Conservation Res.* 6, 203–213. doi:10.1016/j.iswcr.2018.03.007

Capon, S. J., Leigh, C., Hadwen, W. L., George, A., McMahon, J. M., Linke, S., et al. (2018). Transforming environmental water management to adapt to a changing climate. *Front. Environ. Sci.* 6, 80. doi:10.3389/fenvs.2018.00080

Chiang, L. C., Chuang, Y. T., and Han, C. C. (2019). Integrating landscape metrics and hydrologic modeling to assess the impact of natural disturbances on ecohydrological processes in the chenyulan watershed, taiwan. *Int. J. Environ. Res. Public Health* 16, 266. doi:10.3390/ijerph16020266

Dai, E., and Wang, Y. (2020). Attribution analysis for water yield service based on the geographical detector method: A case study of the hengduan mountain region. *J. Geogr. Sci.* 30, 1005–1020. doi:10.1007/s11442-020-1767-y

Deng, L., Li, Y., Cao, Z., Hao, R., Wang, Z., Zou, J., et al. (2022). Revealing impacts of human activities and natural factors on dynamic changes of relationships among ecosystem services: A case study in the huang-huai-hai plain, China. *Int. J. Environ. Res. Public Health* 19, 10230. doi:10.3390/ijerph191610230

Fang, L., Wang, L., Chen, W., Sun, J., Cao, Q., Wang, S., et al. (2021). Identifying the impacts of natural and human factors on ecosystem service in the Yangtze and Yellow River Basins. *J. Clean. Prod.* 314, 127995. doi:10.1016/j.jclepro.2021.127995

Gao, J., Jiang, Y., and Anker, Y. (2021). Contribution analysis on spatial tradeoff/synergy of Karst soil conservation and water retention for various geomorphological types: Geographical detector application. *Ecol. Indic.* 125, 107470. doi:10.1016/j.ecolind.2021.107470

Gao, J., Jiang, Y., Wang, H., and Zuo, L. (2020). Identification of dominant factors affecting soil erosion and water yield within ecological red line areas. *Remote Sens. (Basel).* 12, 399. doi:10.3390/rs12030399

Gbohoui, Y. P., Paturel, J. E., Fowe, T., Mounirou, L. A., Yonaba, R., Karambiri, H., et al. (2021). Impacts of climate and environmental changes on water resources: A multi-scale study based on nakanbé nested watersheds in west african sahel. *J. Hydrology Regional Stud.* 35, 100828. doi:10.1016/j.ejrh.2021.100828

Guo, M., Ma, S., Wang, L., and Lin, C. (2021). Impacts of future climate change and different management scenarios on water-related ecosystem services: A case study in the jianghuai ecological economic zone, China. *Ecol. Indic.* 127, 107732. doi:10.1016/j.ecolind.2021.107732

He, J., Zhao, Y., and Wen, C. (2022). Spatiotemporal variation and driving factors of water supply services in the three gorges reservoir area of China based on supply-demand balance. *Water* 14, 2271. doi:10.3390/w14142271

Hou, J., Qin, T., Liu, S., Wang, J., Dong, B., Yan, S., et al. (2021). Analysis and prediction of ecosystem service values based on land use/cover change in the Yiluo river basin. *Sustainability* 13, 6432. doi:10.3390/su13116432

Hu, J., Wu, Y., Wang, L., Sun, P., Zhao, F., Jin, Z., et al. (2021). Impacts of land-use conversions on the water cycle in a typical watershed in the southern Chinese Loess Plateau. *J. Hydrol. X.* 593, 125741. doi:10.1016/j.jhydrol.2020.125741

Jin, T., Yan, L., Wang, S., and Gong, J. (2022). Spatiotemporal variation in ecological risk on water yield service via land-use and climate change simulations: A case study of the ziwuling mountainous region, China. *Front. Environ. Sci.* 10, 908057. doi:10.3389/fenvs.2022.908057

Li, H., Liu, L., Koppa, A., Shan, B., Liu, X., Li, X., et al. (2021a). Vegetation greening concurs with increases in dry season water yield over the Upper Brahmaputra River basin. *J. Hydrol. X.* 603, 126981. doi:10.1016/j.jhydrol.2021.126981

Li, H., Sheffield, J., and Wood, E. F. (2010). Bias correction of monthly precipitation and temperature fields from Intergovernmental Panel on Climate Change AR4 models using equidistant quantile matching. *J. Geophys. Res.* 115, D10101. doi:10.1029/2009jd012882

Li, J., Chen, X., Kurban, A., Van de Voorde, T., De Maeyer, P., and Zhang, C. (2021b). Coupled SSPs-RCPs scenarios to project the future dynamic variations of water-soil-carbon-biodiversity services in Central Asia. *Ecol. Indic.* 129, 107936. doi:10.1016/j.ecolind.2021.107936

Li, J., Liu, D., Wang, T., Li, Y., Wang, S., Yang, Y., et al. (2017). Grassland restoration reduces water yield in the headstream region of Yangtze River. *Sci. Rep.* 7, 2162. doi:10.1038/s41598-017-02413-9

Li, Y., Chen, P., Niu, Y., Liang, Y., and Wei, T. (2022b). Dynamics and attributions of ecosystem water yields in China from 2001 to 2020. *Ecol. Indic.* 143, 109373. doi:10.1016/j.ecolind.2022.109373

Li, Y., Deng, J., Zang, C., Kong, M., and Zhao, J. (2022a). Spatial and temporal evolution characteristics of water resources in the Hanjiang River Basin of China over 50 years under a changing environment. *Front. Environ. Sci.* 10, 968693. doi:10.3389/fenvs.2022.968693

Li, Z., and Wang, S. (2021). Water yield variability and response to climate change across Canada. *Hydrological Sci. J.* 66, 1–16. doi:10.1080/02626667.2021.1925122

Liang, X., Liu, X., Li, X., Chen, Y., Tian, H., and Yao, Y. (2018). Delineating multi-scenario urban growth boundaries with a CA-based FLUS model and morphological method. *Landsc. Urban Plan.* 177, 47–63. doi:10.1016/j.landurbplan.2018.04.016

Liu, H., Xiao, W., Li, Q., Tian, Y., and Zhu, J. (2022). Spatio-temporal change of multiple ecosystem services and their driving factors: A case study in beijing, China. *Forests* 13, 260. doi:10.3390/f13020260

Liu, L., Xu, H., Wang, Y., and Jiang, T. (2017b). Impacts of 1.5 and 2 °C global warming on water availability and extreme hydrological events in Yiluo and Beijiang River catchments in China. *Clim. Change* 145, 145–158. doi:10.1007/s10584-017-2072-3

Liu, X., Liang, X., Li, X., Xu, X., Ou, J., Chen, Y., et al. (2017a). A future land use simulation model (FLUS) for simulating multiple land use scenarios by coupling human and natural effects. *Landsc. Urban Plan.* 168, 94–116. doi:10.1016/j.landurbplan.2017.09.019

Liu, Y., Xiao, J., Ju, W., Xu, K., Zhou, Y., and Zhao, Y. (2016). Recent trends in vegetation greenness in China significantly altered annual evapotranspiration and water yield. *Environ. Res. Lett.* 11, 094010. doi:10.1088/1748-9326/11/9/094010

Ouyang, Y. (2021). New insights on evapotranspiration and water yield in crop and forest lands under changing climate. *J. Hydrol. X.* 603, 127192. doi:10.1016/j.jhydrol.2021.127192

Pei, H., Liu, M., Shen, Y., Xu, K., Zhang, H., Li, Y., et al. (2022). Quantifying impacts of climate dynamics and land-use changes on water yield service in the agro-pastoral ecotone of northern China. *Sci. Total Environ.* 809, 151153. doi:10.1016/j.scitotenv.2021.151153

Piao, J., Chen, W., Wang, L., and Chen, S. (2021). Future projections of precipitation, surface temperatures and drought events over the monsoon transitional zone in China from bias-corrected CMIP6 models. *Int. J. Climatol.* 42 (2), 1203–1219. doi:10.1002/joc.7297

Qi, Y., Lian, X., Wang, H., Zhang, J., and Yang, R. (2020). Dynamic mechanism between human activities and ecosystem services: A case study of qinghai lake watershed, China. *Ecol. Indic.* 117, 106528. doi:10.1016/j.ecolind.2020.106528

Redhead, J. W., Stratford, C., Sharps, K., Jones, L., Ziv, G., Clarke, D., et al. (2016). Empirical validation of the InVEST water yield ecosystem service model at a national scale. *Sci. Total Environ.* 569-570, 1418–1426. doi:10.1016/j.scitotenv.2016.06.227

Rizzo, R., Garcia, A. S., Vilela, V. M. d. F. N., Ballester, M. V. R., Neill, C., Victoria, D. C., et al. (2020). Land use changes in Southeastern Amazon and trends in rainfall and water yield of the Xingu River during 1976–2015. *Clim. Change* 162 (3), 1419–1436. doi:10.1007/s10584-020-02736-z

Schwarzel, K., Zhang, L., Montanarella, L., Wang, Y., and Sun, G. (2020). How afforestation affects the water cycle in drylands: A process-based comparative analysis. *Glob. Chang. Biol.* 26 (2), 944–959. doi:10.1111/gcb.14875

Shao, S., and Yang, Y. (2021). Effects of precipitation and land use/cover changes on the spatio-temporal distribution of the water yield in the Huang-Huai-Hai basin, China. *Environ. Earth Sci.* 80, 812. doi:10.1007/s12665-021-10119-5

Shi, X., Qin, T., Yan, D., Sun, R., Cao, S., Jing, L., et al. (2018). Analysis of the changes in the water yield coefficient over the past 50 Years in the huang-huai-Hai River basin, China. *Adv. Meteorology* 2018, 1–20. doi:10.1155/2018/6302853

Sun, F., Mejia, A., and Che, Y. (2019). Disentangling the contributions of climate and basin characteristics to water yield across spatial and temporal scales in the Yangtze river basin: A combined hydrological model and boosted regression approach. *Water Resour. manage.* 33 (10), 3449–3468. doi:10.1007/s11269-019-02310-y

Tian, W., Liu, X., Liu, C., and Bai, P. (2018). Investigation and simulations of changes in the relationship of precipitation-runoff in drought years. *J. Hydrol. X.* 565, 95–105. doi:10.1016/j.jhydrol.2018.08.015

Wang, H., Wang, W. J., Wang, L., Ma, S., Liu, Z., Zhang, W., et al. (2022b). Impacts of future climate and land use/cover changes on water-related ecosystem services in changbai mountains, northeast China. *Front. Ecol. Evol.* 10, 854497. doi:10.3389/fevo.2022.854497

Wang, J., and Xu, C. (2017). Geodetector: Principle and prospective. *Acta Geogr. Sin.* 72, 19. doi:10.11821/dlxb201701010

Wang, J., Zhang, T., and Fu, B.-J. (2016). A measure of spatial stratified heterogeneity. *Ecol. Indic.* 67, 250–256. doi:10.1016/j.ecolind.2016.02.052

Wang, S., Zhang, Z., Mc Vicar, R. T., Guo, J., Tang, Y., et al. (2013). Isolating the impacts of climate change and land use change on decadal streamflow variation: Assessing three complementary approaches. *J. Hydrol. X.* 507, 63–74. doi:10.1016/j.jhydrol.2013.10.018

Wang, X., Wu, J., Liu, Y., Hai, X., Shanguan, Z., and Deng, L. (2022a). Driving factors of ecosystem services and their spatiotemporal change assessment based on land use types in the Loess Plateau. *J. Environ. Manage.* 311, 114835. doi:10.1016/j.jenvman.2022.114835

Wang, X., Zhang, P., Liu, L., Li, D., and Wang, Y. (2019). Effects of human activities on hydrological components in the Yiluo river basin in middle Yellow River. *Water* 11, 689. doi:10.3390/w11040689

Xu, C., Duan, Z., Wu, S., Li, R., Zhang, X., Zhang, X., et al. (2020). Detection and attribution of flood responses to precipitation change and urbanization: A case study in qinhuai river basin, southeast China. *Hydrol. Res.* 51, 351–365. doi:10.2166/nh.2020.063

Xu, C., Jiang, Y., Su, Z., Liu, Y., and Lyu, J. (2022). Assessing the impacts of grain-for-green programme on ecosystem services in jinghe river Basin, China. *Ecol. Indic.* 137, 108757. doi:10.1016/j.ecolind.2022.108757

Xu, J., Liu, S., Zhao, S., Wu, X., Hou, X., An, Y., et al. (2019). Spatiotemporal dynamics of water yield service and its response to urbanisation in the beiyun river basin, beijing. *Sustainability* 11, 4361. doi:10.3390/su11164361

Yan, F., Shangguan, W., Zhang, J., and Hu, B. (2020). Depth-to-bedrock map of China at a spatial resolution of 100 meters. *Sci. Data* 7, 2. doi:10.1038/s41597-019-0345-6

Yang, X., Sun, W., Li, P., Mu, X., Gao, P., and Zhao, G. (2019). Integrating agricultural land, water yield and soil conservation trade-offs into spatial land use planning. *Ecol. Indic.* 104, 219–228. doi:10.1016/j.ecolind.2019.04.082

Yang, X., Chen, R., Ji, G., Wang, C., Yang, Y., and Xu, J. (2021a). Assessment of future water yield and water purification services in data scarce region of northwest China. *Int. J. Environ. Res. Public Health* 18, 8960. doi:10.3390/ijerph18178960

Yang, J., Xie, B., Zhang, D., and Tao, W. (2021b). Climate and land use change impacts on water yield ecosystem service in the Yellow River Basin, China. *Environ. Earth Sci.* 80, 72. doi:10.1007/s12665-020-09277-9

Yang, Y., Li, M., Feng, X., Yan, H., Su, M., and Wu, M. (2021c). Spatiotemporal variation of essential ecosystem services and their trade-off/synergy along with rapid urbanization in the Lower Pearl River Basin, China. *Ecol. Indic.* 133, 108439. doi:10.1016/j.ecolind.2021.108439

Yu, Y., Zhao, W., Martinez-Murillo, J. F., and Pereira, P. (2020). Loess plateau: From degradation to restoration. *Sci. Total Environ.* 738, 140206. doi:10.1016/j.scitotenv.2020.140206

Yu, Y., Zhu, R., Ma, D., Liu, D., Liu, Y., and Gao, Z. (2022). Multiple surface runoff and soil loss responses by sandstone morphologies to land-use and precipitation regimes changes in the Loess Plateau, China. *Catena* 217, 106477. doi:10.1016/j.catena.2022.106477

Zang, W., Liu, S., Huang, S., Li, J., Fu, Y., Sun, Y., et al. (2019). Impact of urbanization on hydrological processes under different precipitation scenarios. *Nat. Hazards* 99, 1233–1257. doi:10.1007/s11069-018-3534-2

Zhang, X., Zhang, G., Long, X., Zhang, Q., Liu, D., Wu, H., et al. (2021). Identifying the drivers of water yield ecosystem service: A case study in the Yangtze River basin, China. *Ecol. Indic.* 132, 108304. doi:10.1016/j.ecolind.2021.108304

Zheng, Q., Hao, L., Huang, X., Sun, L., and Sun, G. (2020). Effects of urbanization on watershed evapotranspiration and its components in southern China. *Water* 12, 645. doi:10.3390/w12030645

Zhou, Y., Zhao, L., Cao, J., and Wang, Y. (2022). Using an improved SWAT model to simulate karst sinkholes: A case study in southwest China. *Front. Environ. Sci.* 10, 950098. doi:10.3389/fenvs.2022.950098

Zong, M., Hu, Y., Liu, M., Li, C., Wang, C., and Ping, X. (2020). Effects of landscape pattern change on water yield and nonpoint source pollution in the hun-taizi river watershed, China. *Int. J. Environ. Res. Public Health* 17, 3060. doi:10.3390/ijerph17093060

Frontiers in Environmental Science

TYPE Original Research
PUBLISHED 10 January 2023
DOI 10.3389/fenvs.2022.1108631

OPEN ACCESS

EDITED BY
Yang Yu,
Beijing Forestry University, China

REVIEWED BY
Wenyi Dong,
Chinese Academy of Agricultural Sciences (CAAS), China
Peogui Liu,
Hefei University of Technology, China

*CORRESPONDENCE
Jing Qin,
✉ qinjing@iwhr.com

SPECIALTY SECTION
This article was submitted to Freshwater Science, a section of the journal Frontiers in Environmental Science

RECEIVED 26 November 2022
ACCEPTED 27 December 2022
PUBLISHED 10 January 2023

CITATION
Qin J, Niu J and Niu W (2023), Research on water resource carrying capacity of capital water conservation functional zone.
Front. Environ. Sci. 10:1108631.
doi: 10.3389/fenvs.2022.1108631

Research on water resource carrying capacity of capital water conservation functional zone

Jing Qin[1]*, Jie Niu[2] and Wenlong Niu[2]

[1]China Institute of Water Resources and Hydropower Research, Beijing, China, [2]Engineering Design and Research Center, Beijing IWHR Corporation, Beijing, China

Water resources are important for supporting regional economic development. A scientific and reasonable evaluation of the carrying capacity of water resources is of high significance to regional sustainable development. Zhangjiakou City is China's first capital water conservation functional area, which plays a role in ensuring the safety of water resources and ecological environment in the capital. Considering Chicheng County, Zhangjiakou City, as a typical area, its water resource carrying capacity in the current year (2018) and the plan year (2025) is evaluated by constructing a water resource carrying capacity evaluation index system for the county, determining the threshold of the bearing capacity evaluation index, and using the single-factor evaluation method and cloud theory method. In addition, the main factors affecting the water resource carrying capacity of Chicheng County are analyzed. The results show that: Based on the single factor evaluation results, the critical state of water resources carrying capacity was evaluated comprehensively, and the factor carrying capacity of total water consumption in the predicted planning level year (38.0603 in normal water year and 41.3403 in dry water year) does not exceed the total water consumption index (51.14). Furthermore, The water resources carrying capacity level of the present level year (.45) and the planned level year (.46) belong to the third level of the evaluation index system. There is further scope for the carrying capacity of water resources in Chicheng County to satisfy its economic and social development. However, it is urgent to solve the problems affecting the water quality elements of rivers, such as heavy river water pollution, low sewage treatment capacity, and weak pollution monitoring and supervision. It is necessary to optimize the industrial economic structure of Chicheng County, accelerate the improvement of water resources management system and mechanism, and ensure the long-term safety of water resources and ecological environment in the capital.

KEYWORDS

capital water conservation functional zone, water carrying capacity, single-factor evaluation, cloud theory, Chicheng County

1 Introduction

As the most basic natural resource, water resources not only provide the necessary material basis for the socio-economic development of the region and the virtuous cycle of ecological environment, but also one of the places with the most serious pollution (Yang et al., 2016; Jin et al., 2018; Zhang, 2019). China confronts water shortages. The study of the carrying capacity of water resources is of high significance to the sustainable development of its social economy (Wang et al., 2021). A reasonable and complete evaluation index system for the carrying capacity of water resources can improve the accuracy of the evaluation results and provide guidance for decision makers to make more scientific decisions (Wan, 2015).

At present, the evaluation methods for water resource carrying capacity mainly include the fuzzy comprehensive evaluation method, gray correlation analysis method, principal component analysis method, and set pair analysis method. Zhou Yanmei used the fuzzy comprehensive evaluation model to predict the carrying capacity of water resources in Heze City from 2020 to 2030 (ZHOU et al., 2021). Tong Changfu used the grey correlation degree analysis method to evaluate the bearing capacity of water resources in Ordos City and each sub-district (Tong et al., 2009). Lumin used the principal component analysis method to comprehensively evaluate the bearing capacity of water resources in Linyi City (Lu et al., 2016). Tang Aizhu used the set pair analysis method to diagnose and identify the evolution characteristics and vulnerability indicators of the water resource carrying capacity in Guiyang City from 2005 to 2017 (Tang and He, 2021). The single factor evaluation method is rarely used in the evaluation of water resources carrying capacity. Li, (2006) used the fuzzy single factor evaluation method to carry out a case study on the current situation of water resources carrying capacity of Linjiang River basin and analyzed the water resources carrying capacity of the basin. According to the single factor evaluation standard, Zhang, (2018) evaluated the total surface water carrying capacity and the total groundwater extraction carrying capacity respectively in Jimusi City, and the comprehensive evaluation result was serious overload. The number of single factor evaluation indicators has a significant impact on the evaluation results. The more the number, the more reliable the comprehensive evaluation results. Cloud model can reveal the randomness and fuzziness of objective events and realize the quantitative expression and objective evaluation of indicators. With the deepening of research, cloud model has been widely applied. Su Yangyue (Su et al., 2017) took the fuzzy comprehensive evaluation method as the main framework of evaluation, used the cloud model to grasp the uncertainty of the index quantity, built the improved evaluation model based on the cloud model and the fuzzy comprehensive evaluation method, and evaluated the water resources management of Huizhou City. Yang Lizhi (Yang et al., 2014) introduced the research idea of "cloud model" and carried on the quantitative expression and objective evaluation of the potential risks of water resource disputes between our country and 4 countries on the southwest border.

Ji Feng used the fuzzy comprehensive evaluation model to evaluate the carrying capacity of water resources in Zhangjiakou City considering the relevant research (Ji et al., 2012). Liu Yijiang combined the entropy right method with the multi-level comprehensive fuzzy evaluation method to study and analyze the current situation of water resource carrying capacity and the development and transformation of water resources in Zhangjiakou City (Liu et al., 2020). Ma Zhengang et al. used the comprehensive index method to calculate the variations in the water resource carrying capacity of Zhangjiakou City in the past 5 years and analyzed the main influencing factors (Ma et al., 2018). The above research focused on the definition of water resource carrying capacity in Zhangjiakou City, construction of the water resource carrying capacity index system, and evaluation model for water resource carrying capacity. In January 2017, General Secretary Xi Jinping proposed that Zhangjiakou City would construct a capital water conservation functional area and an ecological environment support area (Wu and Fu, 2017). At present, with the capital water conservation functional area as the research object, no additional research is being conducted on the comparative analysis of water resources carrying capacity in Zhangjiakou City using multiple methods.

The National Development and Reform Commission and the People's Government of Hebei Province jointly issued the "Construction Plan for the Zhangjiakou Capital Water Conservation Functional Zone and the Ecological Environment Support Area (2019–2035)" (July 2019). It clarifies the functional positioning of the capital water conservation functional area; capital ecological environment support area; and development positioning, construction goals, spatial layout, and construction priorities of the "two districts" in the capital (People's Government of Hebei Province, 2019). The capital water conservation functional area is based on the water systems of important river basins such as the Yongding River and Chaobai River in Beijing as the starting point. It improves the carrying capacity of water resources through a series of water conservation projects such as hydrological regulation, comprehensive treatment of river basins, and reclaimed water utilization (Liu and Chen, 2018). Based on this, this study considers Chicheng County, Zhangjiakou City, as the research area, and analyzes and evaluates its water resource carrying capacity in the current year (2018) and plan year (2025) by constructing the water resources carrying capacity evaluation index system of the county and determining the threshold of the bearing capacity evaluation index. The single-factor evaluation method is used to analyze the water quantity elements and water quality elements of Chicheng County. The "driving force-pressure-state-response" assessment model of the county is constructed using the cloud theory method. The twelve evaluation indicators of Chicheng County are analyzed to determine its water resource carrying capacity level in the current year and plan year. This is to provide 1) technical support for utilizing and protecting water resources in the county's "14th Five-Year Plan" and 2) reference for the subsequent implementation of the sustainable development of the capital water conservation functional area and the water resources security capacity building in the coordinated development of Beijing–Tianjin–Hebei.

2 Overview of study area

Located in the north of Hebei Province and southwest of Beijing, Zhangjiakou City belongs to the same natural ecosystem as Beijing. It plays an essential role in ensuring the safety of the capital's water resources and ecological environment (Su et al., 2017). Chicheng County is located in the southwest of Beijing, and the county's center is at a distance of 180 km from Beijing, with a straight-line distance of 110 km. Chicheng County is 95 km long from north to south, and 88.75 km wide from east to west. It has a total area of 5287 km^2. Its jurisdiction area is the fourth in Hebei Province. Chicheng County is one of the 14 ring capital counties in Hebei Province. It has four townships bordering Beijing, with a bordering mileage of 153 km. The geographical location of Chicheng County is shown in Figure 1.

Chicheng County is located in the western branch of Yanshan. It is surrounded by high mountains. The medium and low mountainous areas account for approximately 90% of the county area, and the mountain valley area and basin area account for approximately 10% of the county area. The entire terrain slopes from northwest to southeast, with an average altitude of 1000 m. The landform types of Chicheng County can be divided into tectonic and ablative landforms, and river

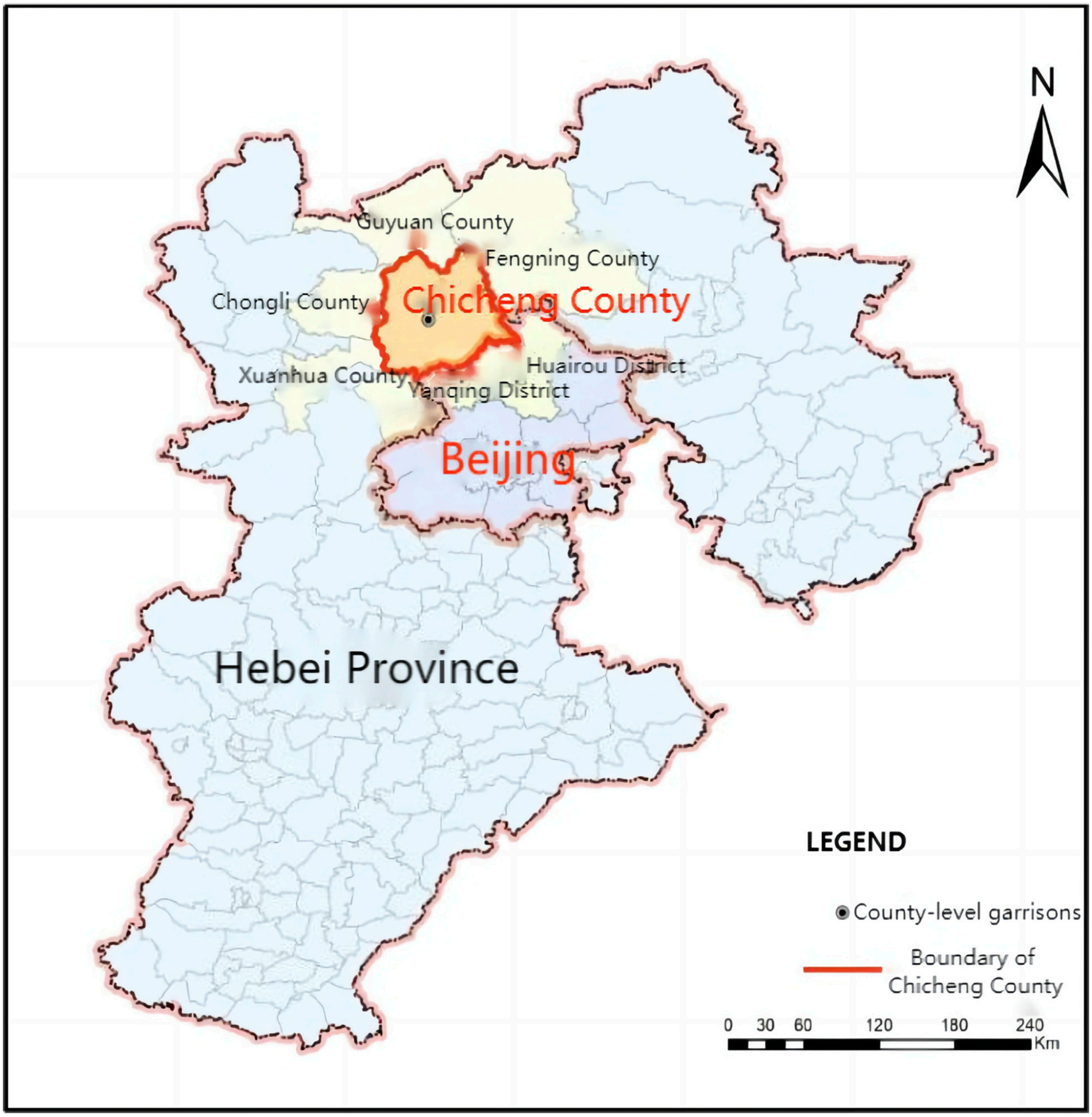

FIGURE 1
Geographical map of Chicheng county.

erosion and accumulation landforms according to the genesis. It can be divided into three forms according to the morphology: Zhongshan area, low mountainous area, and river valley area. Chicheng County mainly has the Heihe River, and the Bai River and its tributaries (the Three Rivers of the Red River). All these belong to the Bai River basin of the Chaobai River system. Of this, the Red River flows into the White River in the territory. Furthermore, the two main rivers Heihe River and White River run through the county from north to south, and flow into the Miyun Reservoir in Beijing. Approximately 200 million m^3 of water enters the reservoir annually. This accounts for 53% of the annual amount of water, which is an important source of drinking water in Beijing.

The annual average total water resources of Chicheng County amount to 247 million m^3. Of this, the total surface water resources amount to 241 million m^3, the total groundwater resources amount to 122 million m^3 (mineralization ≤ 2 g/L), and the amount of double calculation is 116 million m^3. The water quality of rivers throughout the year belongs to Class III. water quality, and the water quality is in Category II throughout the year, and the non-flood season is Class III. Water resources vary considerably during the year and between years, the spatial distribution is non-uniform, there is a contradiction between supply and demand, the total amount of water resources in the county is inadequate, and the amount of water resources *per capita* is highly insufficient. The total annual average water resources

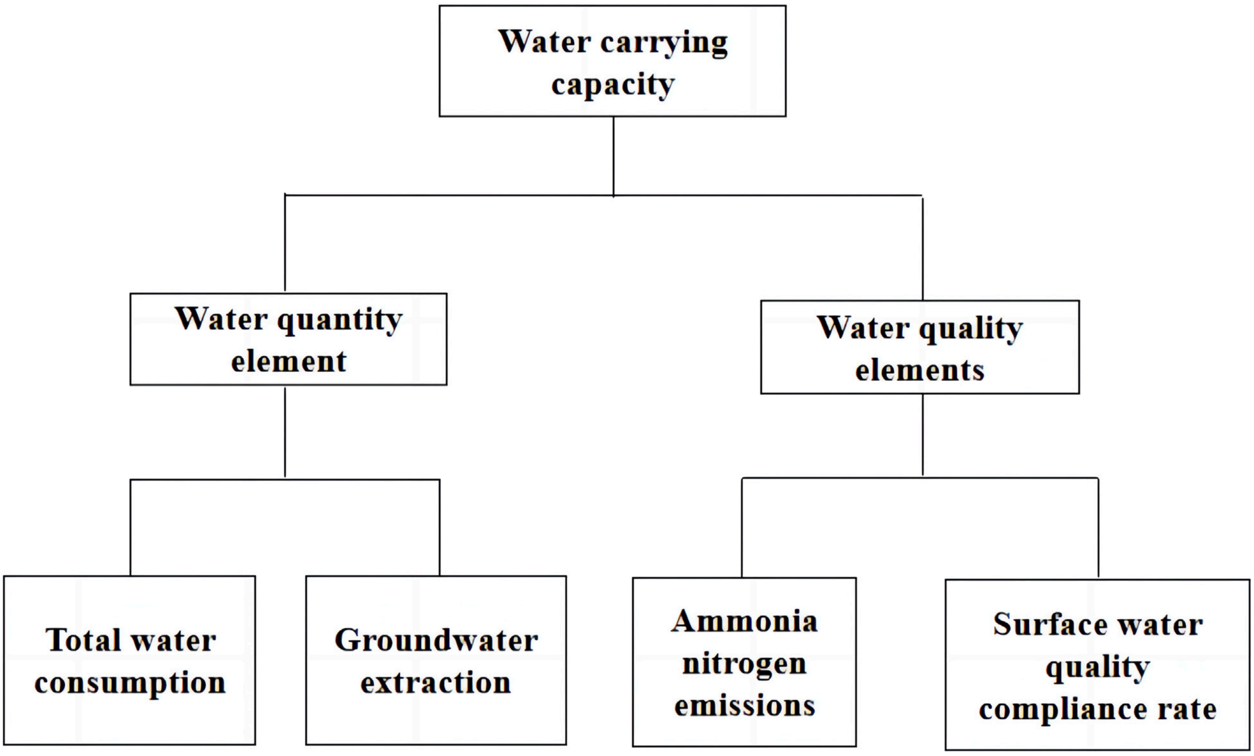

FIGURE 2
One-factor evaluation method index system.

of Chicheng County amount to 247 million m^3. The *per capita* water resources in 2018 amount to 839.28 m^3, which is less than half of the national *per capita* water resources of 2007.57 m^3 in that year.

3 Evaluation of the carrying capacity of water resources

The carrying capacity of water resources refers to the maximum level of sustainable development that a certain area of water ecosystems can carry when water management and social economy are optimized under a certain time period and technology level (Wang and Dan, 2012). The establishment of an appropriate evaluation model for the carrying capacity of regional water resources has important theoretical and practical significance for regional economic development, ecological environmental protection, and sustainable utilization of water resources (Zheng and Li, 2021).

In this study, the water resources carrying capacity of Chicheng County in 2018 (current year) and 2025 (plan year) are analyzed and evaluated by constructing its water carrying capacity evaluation index system, determining the threshold of the bearing capacity evaluation index, and using the one-factor evaluation method and cloud theory method.

3.1 One-factor evaluation method

3.1.1 Introduction to univariate evaluation

The single-factor evaluation method refers to the analysis and evaluation of a single index separately. Furthermore, the bearing status of each index is assessed directly according to the measurement standard of each index (Wu et al., 2015).

Combined with the actual situation of Chicheng County and the analysis requirements of single-factor evaluation methods, an evaluation index system is constructed as shown in Figure 2. The evaluation of water quantity elements is carried out according to the current total annual water consumption W and groundwater extraction amount G. In addition, the regional scope of severe overload, overload, critical state, and non-overload is divided. The pollutant discharge emission P and surface water quality compliance rate Q are evaluated according to the water quality element evaluation standards. In addition, the water quality elements are delineated as severe overload, critical state, and non-overload.

The evaluation index level threshold table is established as shown in Table 1 according to the “Technical Guidelines for the Work of the National Population Development Functional Zone” and the actual situation of Chicheng County.

The criteria for assessing the bearing status of resources according to the evaluation results of water quantity and water quality elements are as follows:

(1) Severe overload: any of the water quantity and water quality elements is overloaded severely;
(2) Overload: any of the water quantity and water quality elements is overloaded;
(3) Critical state: any of the water quantity and water quality elements is in a critical state;
(4) No overloading: Water quantity and water quality elements are not overloaded.

TABLE 1 Evaluation level threshold of one-factor evaluation method for water resource carrying capacity in Chicheng County.

Evaluation indicators	Evaluation of carrying status			
	Severe overload	Overload	Critical	No overloading
Total water consumption W	$W \geq 1.2\times W_0$	$W_0\leq W \leq 1.2\times W_0$	$.9\times W_0\leq W \leq W_0$	$W < .9\times W_0$
Amount of groundwater used G	$G \geq 1.2\times G_0$ or The over-exploitation coefficient of shallow groundwater in the over-exploitation area ≥.3 or there is a deep pressure water extraction or there is excessive groundwater exploitation in mountainous areas	$G_0\leq G \leq 1.2\times G_0$ or Shallow groundwater overexement coefficient in over-exploitation areas is between (0,0.3] or there is over-exploitation of groundwater in hilly areas	$.9\times G_0\leq G \leq G_0$	$G < .9\times G_0$
Pollutant emissions P	$p \geq 3\times P_0$	$1.2\times P_0\leq p < 3\times P_0$	$1.1\times P_0\leq p < 1.2\times P_0$	$p < 1.1\times P_0$
Surface water quality compliance rate Q	$Q \leq .4\times Q_0$	$.4\times Q_0<Q \leq .6\times Q_0$	$.6\times Q_0<Q \leq .8\times Q_0$	$.8\times Q_0\leq Q$

TABLE 2 Data acquisition and sources.

Serial number	Index	Numerical and categorical	Data sources
1	total annual water consumption of Chicheng County (million m^3)	33.8074	the results of the 2018 Chicheng County Water Resources Bulletin
2	groundwater extraction volume (million m^3)	23.6074	
3	red line index of total water use control in Chicheng County in the current year (million m^3)	51.14	Zhangjiakou City Implementation of the Strictest Water Resources Management System 2016–2020 Control Target Decomposition Plan
4	groundwater exploitation control index in Chicheng County in the current year (million m^3)	26.29	
5	water quality targets in important water functional areas	Class II	
6	Water quality compliance rate	100%	In 2016, 8 of the provincial water function area compliance evaluation results participated in the evaluation results
7	Water quality compliance rate control indicators	100%	
8	COD limit the amount of discharge into the river (t/a)	177.7	Adopt the 2015 COD and ammonia nitrogen emission limits in Chicheng Prefecture
9	COD emissions (t/a)	28.1	
10	Limits of ammonia nitrogen into the river (t/a)	5.9	
11	Ammonia nitrogen emissions (t/a)	6.6	

The water resources carrying status of Chicheng County are analyzed sequentially according to the above evaluation method. Furthermore, the rationality of the evaluation results is analyzed in combination with the regional water resource conditions, development and utilization conditions, and economic and social development and trends.

3.1.2 Results of the single-factor evaluation method

3.1.2.1 Data acquisition

According to the results of the 2018 Chicheng County Water Resources Bulletin, the total annual water consumption of Chicheng County is 33.8074 million m^3. Of this, the groundwater extraction volume is 23.6074 million m^3. According to the “Zhangjiakou City Implementation of the Strictest Water Resources Management System 2016–2020 Control Target Decomposition Plan”, the red line index of total water use control in Chicheng County in the current year is 51.14 million m^3, the groundwater exploitation control index in Chicheng County in the current year is 26.29 million m^3, and the water quality targets in important water functional areas are Class II.

According to the results of the 2016 provincial water function zone standard evaluation, eight water function areas in Chicheng County participated in the water quality compliance rate of 100%. Furthermore, Water quality compliance rate control indicators was 100%.

The 2015 COD and ammonia nitrogen emission limits of Chicheng County were used rather than the current annual pollutant discharge limits. Among these, the COD emission limit, river entry, ammonia nitrogen emission limit, and river entry are 177.7 t/a, 28.1 t/a, 5.9 t/a, and 6.6 t/a, respectively.

The above results are summarized in the following Table2.

3.1.2.2 The carrying capacity of water resources

First, the single-factor evaluation of water quantity factors and water quality elements is carried out. Furthermore, the four evaluation

TABLE 3 Evaluation table of the total water consumption capacity of the current year (2018).

Administrative	Evaluation indicators	Metrics	The carrying capacity of the water quantity element	
	Total water consumption (Ten thousand m^3)	Total water consumption target (Ten thousand m^3)	W/W_0	Load level
Chicheng County	3380.74	5114	.66	No overloading

TABLE 4 Groundwater carrying status evaluation table for the current year (2018).

Administrative	Evaluation indicators	Metrics	The carrying capacity of the water quantity element	
	Groundwater extraction (Ten thousand m^3)	Groundwater extraction indicators (Ten thousand m^3)	G/G_0	Load level
Chicheng County	2360.74	2629	.89	No overloading

TABLE 5 Status quo year (2018) water quality compliance rate element evaluation results table.

Administrative	Evaluate the number of water functional areas	Evaluation indicators	Metrics	The carrying capacity of the water quantity element	
		Water quality compliance rate Q (%)	Water quality compliance rate control indicators Q_0 (%)	Q/Q_0	Load level
Chicheng County	8	100	100	1	No overloading

levels of severe overload, overload, critical state, and non-overload are delineated and then, evaluated comprehensively according to the evaluation results of water quantity factors and water quality elements. The evaluation table of the total water consumption capacity of the current year (2018) and Groundwater Carrying Status Evaluation Table for the current year (2018) are presented in Tables 3, 4.

As is evident from Table 2, the current annual total water consumption in Chicheng County is not overloaded.

As is evident from Table 3, the current annual groundwater bearing status of Chicheng County is not overloaded.

The water quality elements are evaluated according to the current annual water quality compliance rate of the water functional area, the amount of pollutants entering the river, etc. The annual compliance rate of Chicheng County from the evaluation of the water function area is 87.5%, Q/Q0 is one, and the water quality compliance rate element of the water function area is not overloaded. The evaluation results of the water quality compliance rate element of the water function area are detailed in Table 5.

The average emission degree of COD and ammonia nitrogen in the water functional area of Chicheng County is calculated according to the current annual discharge of major pollutants and the limit of pollutants entering the river in Chicheng County, respectively (see Table 6).

A comprehensive evaluation of the current annual water resources carrying status is carried out based on the above water quantity and water quality analysis results (see Table 7). The comprehensive evaluation results are critical.

3.1.2.3 Forecast of the bearing capacity of the total annual water consumption element at the planning level

The total amount of water used includes five categories: domestic water; industrial water; agricultural water; forestry, animal husbandry, fishing, and livestock water demand; and ecological water demand. It is predicted separately by means of quota forecasting, and trend analysis and prediction.

The county’s urban population is predicted to attain 102,100 in 2025, and the rural population would attain 189,600. The comprehensive water consumption index of urban residents is taken from 120 L/personday. The quota method is used to predict that the domestic water consumption of urban residents would be 4.472 million m^3 in 2025. The comprehensive water consumption index of rural residents would be 65 L/personday. The quota method is used

TABLE 6 Results of the evaluation of the elements of the river into the river in the current year (2018).

Administrative	Evaluation indicators	Metrics	Bearing conditions of water quality elements				
	COD emissions P_1 (t/a)	Ammonia nitrogen emissions P_2 (t/a)	COD limit the amount of discharge into the river P_{10} (t/a)	Limits of ammonia nitrogen into the river P_{20} (t/a)	P_1/P_{10}	P_1/P_{20}	Load level
Chicheng County	28.1	6.6	177.7	5.9	.158	1.12	Critical

TABLE 7 Current status year (2018) water carrying capacity evaluation table.

Administrative	The bearing status of the water quantity element			Bearing status of water quality elements			Comprehensive evaluation
	Elements of total water consumption	Groundwater Mining elements	Evaluation results of water quantity elements	Water quality compliance rate elements	Contaminant River entry features	Evaluation results of water quality elements	
Chicheng County	No overloading	No overloading	No overloading	No overloading	Critical	Critical	Critical

to predict the water consumption of rural residents in 2025 to be 4.4983 million m^3.

According to the average annual growth rate of industrial added value above the designated size in Zhangjiakou City during the "13th Five-Year Plan" period, it is predicted that the industrial added value of Chicheng County in 2025 would be CNY 2.53 billion. The water consumption of industrial added value of CNY 10,000 is 10 m^3, and the total industrial water demand of Chicheng County in 2025 is predicted to be 2.53 million m^3.

According to the "Five-year Implementation Plan for the Comprehensive Treatment of Groundwater Over-exploitation in Hebei Province (2018–2022)" and the "Opinions on the Guarantee of Surface Water Supply in Zhangjiakou City" (Zhang Zhengcheng [2019] No. 115), the effective irrigation area of the county would continue to maintain 192,800 mu in 2025. The irrigation water demand of farmland is predicted by the irrigation quota method. The analysis shows that the irrigation water demand of farmland in Chicheng County would be 22.43 million m^3 (50% flat water year) and 25.71 million m^3 (75% dry water year).

After calculating the current quotas for irrigation of forest fruit fields, the water demand for grassland, and the water replenishment of fish ponds, the water demand for forestry, animal husbandry, and fishery would be 650,000 m^3 in 2025, and that for livestock would be 1.9 million m^3.

Combined with the requirements of the Zhangjiakou Surface Water Allocation and Utilization Plan (2020), the ecological water demand forecast predicts that the ecological water demand of Chicheng County would be 1.58 million m^3 by 2025.

According to the above analysis, the total water demand in Chicheng County in 2025 would 38.0603 million m^3 (50% flat water year) and 41.3403 million m^3 (75% dry water year). The results are shown in Table 8.

The bearing capacity of the total water consumption elements of Chicheng County in 2025 (plan year) of the flat water year and dry water year is predicted based on the total water consumption control index of Chicheng County in the current year (2018). The results are shown in Table 9.

As is evident from Tables 3–8, the bearing conditions of the total water consumption elements under the conditions of the plan year (2025) for Chicheng County are predicted to be non-overloaded.

3.2 Evaluation method of water carrying capacity based on cloud theory

3.2.1 Cloud model theory

Cloud models can scientifically and effectively describe the ambiguity and randomness of things, quantitatively characterize the qualitative language that exists in life, and strengthen the quantitative analysis and data operability of uncertain things (Hu, 2008). In this study, a comprehensive evaluation model based on the cloud theory is established, and the carrying capacity of water resources in Chicheng County is analyzed and evaluated.

3.2.1.1 The digital characteristics of the cloud are determined.

Let U be a domain of the theory for the formation of an exact set of numbers, A be a qualitative concept on U, and x be a qualitative language value on U. x corresponds to the membership degree of A, y ($0 \le y \le 1$), is a random number with a stable trend, the distribution of y on U is called the subordinate cloud (referred to as the cloud), and each group (x, y) becomes a cloud droplet. Clouds are mappings from the domain U to the interval [0,1] (Wang et al., 2021).

The cloud is a mapping from the domain U to the interval [0,1] using numerical features such as expectation (Ex), entropy (En), and superentropy (He) to represent its concept of uncertainty.

Ex is a numerical value of a qualitative concept that determines the center of gravity of the cloud:

$$\mathbf{E_x = (B_{min} + B_{max})/2}$$

TABLE 8 Forecast results of water demand for chicheng county in the planning level year (2025).

Domestic water consumption		Industrial water demand	Agricultural irrigation Water requirements		Water requirements for forestry, herding, fishing and livestock	Ecology Water requirements	Total water demand	
Domestic water for urban residents	Rural residents use water comprehensively		50% Flat water year	75% Dry years			50% Flat water year	75% Dry years
447.20	449.83	253	2243	2571	255	158	3806.03	4134.03

TABLE 9 Evaluation table of the total water consumption capacity of Chicheng County in the planning level year (2025).

Domestic water consumption	Evaluation indicators	Metrics	The carrying capacity of the water quantity element	
	Total water consumption (Ten thousand m^3)	Total water consumption target (Ten thousand m^3)	W/W_0	Load level
Chicheng County (50% Flat water year)	3806.03	5114	.69	No overloading
Chicheng County (75% Dry years)	4134.03	5114	.81	No overloading

Entropy En is a measure of uncertainty in qualitative concepts:

$$\exp\left|-\frac{(B_{\max}-B_{\min})^2}{8E_n^{\,2}}\right| \approx 0.5$$

$$E_n = \frac{|B_{\max}-B_{\min}|}{2.355}$$

Superentropy (He) is a measure of ambiguity of entropy that determines the thickness of the cloud.

Here, the minimum and maximum boundaries of an evaluation level are represented with k as the constant.

3.2.1.2 Forward normal cloud generator

A normal random number is generated with En as the expectation and He2 as the variance. Second, a normal random number xi is generated with Ex as the expectation and variance. Finally, the corresponding membership value yi, (xi, yi) is calculated to form any cloud drop in the number field. The above process is repeated until n cloud droplets are generated. The yi calculation formula is as follows:

$$y_i = \exp\left[\frac{-(x_i - E_x)^2}{2(E_{ni})^2}\right]$$

3.2.1.3 Membership matrix

The corresponding membership R of each evaluation index is calculated by the above steps related to the forward cloud generator.

$$R = \begin{pmatrix} r_{11} & \cdots & r_{1m} \\ \vdots & \ldots & \vdots \\ r_{n1} & \cdots & r_{nm} \end{pmatrix}$$

3.2.1.4 The evaluation grade value of the carrying capacity of water resources

The evaluation grade value of the carrying capacity of water resources is calculated as follows:

$$P = W^T \times R$$

where W is the weight of each metric.

3.2.2 Evaluation index system

An evaluation model of “driving force-pressure-state-response” is established. Furthermore, an evaluation index system for the carrying capacity of water resources in Chicheng County is constructed (see Figure 3).

According to the actual scenario of the existing indicators, the evaluation threshold is divided into five levels with reference to the average status of various indicator systems worldwide. Among these, the first level indicates that the bearing capacity in the state is exceptionally strong, and that the potential for development and utilization is high. The second level indicates that the bearing capacity in the state is relatively strong, and that the potential for development and utilization is high. The third level indicates that the carrying capacity in the state matches the economic development. The fourth level indicates that the bearing capacity in the state is relatively weak, and that there is a marginal overload of water resources. The fifth level indicates that the bearing capacity in the state is exceptionally weak, and that the overload of water resources is severe. The thresholds for the specific grade division are shown in Table 10:

The values of the annual evaluation indexes of the current year and plan year for Chicheng County are shown in Table 11:

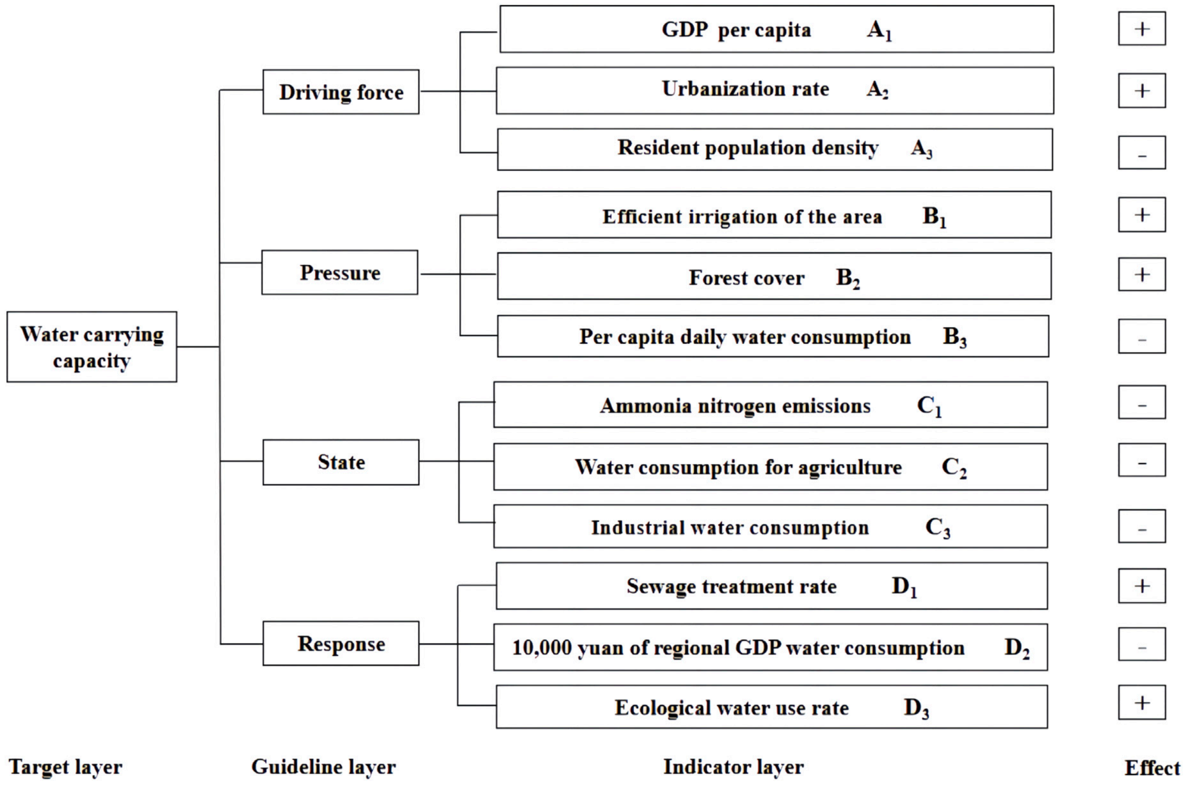

FIGURE 3
Evaluation index system of water resource carrying capacity in Chicheng County.

TABLE 10 The threshold of water resource carrying capacity evaluation level based on cloud theory in Chicheng County.

Grade			Class I	Class II	Class III	Class IV	Class V
Driving force A	GDP per capita A_1	Million yuan/person	5–10	2.5–5	1.5–2.5	.5–1.5	0–0.5
	Urbanization rate A_2	%	80–100	60–80	40–60	20–40	0–20
	Resident population density A_3	person/km^2	100–300	300–500	500–800	800–1200	1200–1400
Pressure B	Efficient irrigation of the area B_1	10,000 acres	50–100	30–50	20–30	10–20	0–10
	Forest cover B_2	%	60–100	50–60	40–50	30–40	8–30
	Per capita daily water consumption B_3	L/(person*year)	40–80	80–140	140–180	180–200	200–220
State C	Ammonia nitrogen emissions C_1	Tons/year	0–20	20–60	60–120	120–200	200–500
	Water consumption for agriculture C_2	%	0–20	20–30	30–50	50–70	70–100
	Industrial water consumption C_3	%	0–15	15–20	20–30	30–40	40–60
Response	Sewage treatment rate D_1	%	95–100	90–95	85–90	60–85	0–60
D	10,000 yuan of regional GDP water consumption D_2	m^3/10,000 yuan	10–50	50–150	150–250	250–300	300–400
	Ecological water use rate D_3	%	45–100	30–45	15–30	5–15	0–5

3.2.3 Evaluation and analysis results of water resource carrying capacity of cloud theory

The numerical characteristics of the cloud are obtained by calculating and analyzing the bearing capacity of water resources in Chicheng County according to the cloud theoretical algorithm based on the “driving force-pressure-state-response” indicator model. The results are shown in Table 12.

According to the corresponding index values, weights, and numerical characteristics, the membership matrix of the positive cloud generator algorithm is generated, the randomness and uncertainty in the cloud model membership calculation are considered, the mean value of the 1000 program operation results is used as the final membership degree in this study,

TABLE 11 The annual evaluation index values of the current situation and planning level of Chicheng County.

Evaluation indicators	unit	2018(Status quo year)	2025(Planning level year)
GDP per capita A_1	Million yuan/person	3.8	4.5
Urbanization rate A_2	%	33.2	35
Resident population density A_3	person/km^2	48	55
Efficient irrigation of the area B_1	10,000 acres	19.28	19.28
Forest cover B_2	%	54.37	59
Per capita daily water consumption B_3	L/(person*year)	47450	41975
Ammonia nitrogen emissions C_1	Tons/year	5.9	5.9
Water consumption for agriculture C_2	%	71	58.9
Industrial water consumption C_3	%	8	6.6
Sewage treatment rate D_1	%	90	95
10,000 yuan of regional GDP water consumption D_2	m^3/10,000 yuan	11.8	10
Ecological water use rate D_3	%	3	4.2

TABLE 12 The digital characteristics of the cloud.

Index	Grade	A_1	A_2	A_3	B_1	B_2	B_3	C_1	C_2	C_3	D_1	D_2	D_3
Ex	I	7.5	90	200	75	80	60	10	10	7.5	97.5	30	72.5
	II	3.75	70	400	40	55	110	40	25	17.5	92.5	100	37.5
	III	2	50	650	25	45	160	90	40	25	87.5	200	22.5
	IV	1	30	1000	15	35	190	160	60	35	72.5	300	10
	V	.25	10	1300	5	19	210	350	85	50	30	375	2.5
En	I	2.12	8.49	84.93	21.23	16.99	16.99	8.49	8.49	6.37	2.12	16.99	23.35
	II	1.06	8.49	84.93	8.49	4.25	25.48	16.99	4.25	2.12	2.12	42.46	6.37
	III	.42	8.49	127.39	4.25	4.25	16.99	25.48	8.49	4.25	2.12	42.46	6.37
	IV	.42	8.49	169.85	4.25	4.25	8.49	33.97	8.49	4.25	10.62	21.23	4.25
	V	.21	8.49	84.93	4.25	9.34	8.49	127.39	12.74	8.49	25.48	42.46	2.12

TABLE 13 Evaluation results of cloud model of water resource carrying capacity game.

Year of evaluation	Evaluation values of water resource carrying capacity in different grades					Final rating
	I	II	III	IV	V	
Status quo year (2018)	.12	.03	.45	.29	.14	III
Planning level year (2025)	.09	.07	.46	.27	.11	III

and the membership matrix R1–R12 of 12 evaluation indicators is constructed. It is illustrated using R1 as an example:

$$R_1 = \begin{array}{c} \text{year} \\ 2018 \\ 2025 \end{array} \left[\begin{array}{ccccc} \text{I} & \text{II} & \text{III} & \text{IV} & \text{V} \\ 0 & 0.134 & 0.750 & 0.116 & 0 \\ 0 & 0.012 & 0.685 & 0.279 & 0 \end{array} \right]$$

The entropy weight method is used to calculate the weights of the 12 evaluation indicators. The maximum eigenvectors and eigenvalues of the matrix are calculated with the help of MATLAB software and by normalizing the formula : $\mathbf{W_i} = \frac{M_i}{\sum_{i=1}^{n} M_i}$, i = 1,2, ... 12. The characteristic vector components of each evaluation index (i.e., the weights W) are calculated.

$$\mathbf{Wi} = (\mathbf{.039}, \mathbf{0.044}, \mathbf{0.066}, \mathbf{0.105}, \mathbf{0.028}, \mathbf{0.078}, \mathbf{0.029}, \mathbf{0.044}, \mathbf{0.066}, \mathbf{0.029}, \mathbf{0.037}, \mathbf{0.025}).$$

The evaluation value of the carrying capacity of water resources under different grades is calculated by the affiliation matrix R and weight W. The water resource carrying capacity levels of Chicheng County in 2018 (*status quo* year) and 2025 (plan year) are determined by the principle of maximum affiliation (see Table 13).

The above table shows that the carrying capacity level of water resources in Chicheng County in 2018 belongs to the third level in the evaluation index system. The water resource carrying capacity level of the county in 2025 based on the predicted values of the indicators also belongs to the third level in the evaluation index system.

4 Analysis of influencing factors of water carrying capacity

The above two analysis and evaluation results show that the water resource carrying capacity of Chicheng County in the current year (2018) and plan year (2025) matches the economic development. Furthermore, in the future period, the water resource carrying capacity of Chicheng County would have more scope for satisfying its economic and social development.

The implementation of documents such as the “Hebei Provincial Water Resources Protection Plan” and “Zhangjiakou City Implementation of the Strictest Water Resources Management System 2016–2020 Control Target Decomposition Plan” has further strengthened the water resources protection of Chicheng County. The county has steadily promoted water resources protection and treatment projects and the efficient operation of sewage treatment and reclaimed water utilization, continuously strengthened the protection management of water resources, improved the construction of water conservancy informatization, and implemented policies such as total water withdrawal control. This has substantially improved the water security capacity for Chicheng County’s economic and social development, and promoted the adaptation of economic and social development to the carrying capacity of water resources and water environment.

Meanwhile, the single-factor evaluation method shows that the water quality factors in Chicheng County are in a critical state, and that the problems of water resource utilization and protection are prominent. This is owing to the low water quality of certain rivers in the county. The capacity to absorb pollution is low. A large amount of sewage such as urban domestic sewage, rural livestock and poultry manure, and agricultural fertilizers is discharged directly into the river. This causes surface water pollution. Coupled with the deficiency of water in small and medium-sized rivers, the task of river water ecological restoration and governance is highly challenging. To a certain extent, it lags behind the improvement of the carrying capacity of water resources in Chicheng County.

4.1 Analysis of influencing factors

According to the analysis, the main factors affecting the carrying capacity of water resources in Chicheng County are as follows.

4.1.1 The total amount of water resources and the degree of development and utilization

The total amount of water resources is the fundamental data for the study of the carrying capacity of water resources. It is also one of the key factors that determine the carrying capacity of water resources in the basin. In addition, the carrying capacity of water resources is based on a certain level of development and utilization of water resources. The current development and utilization of water resources is also one of the main factors affecting the carrying capacity of water resources. Therefore, the amount of groundwater resources, average annual total amount of water resources, irrigation rate of cultivated land, and amount of groundwater extraction in Chicheng County are important indicators affecting the carrying capacity of water resources in it.

4.1.2 The state of economic and social development

Economic development factors are the main drivers of the variation in the water resource carrying capacity in Chicheng County. These also impose the highest demands on the carrying capacity of water resources. The proportion of industrial and agricultural water consumption, per capita water consumption, and ecological environment water consumption has increased continuously with the rapid development of the economy and the population increase. This places significant demands on the carrying capacity of water resources. The urbanization rate of Chicheng County, proportion of tertiary industry in the GDP, and reuse rate of industrial water are the most important sensitive factors for the dynamic transformation of water resources.

4.1.3 Degree of water pollution and ecological damage

Water pollution is the main factor influencing the decrease in carrying capacity of water resources. Insufficient attention is paid to the treatment of water used in the industry, agriculture, and daily production. This aggravates the degree of water pollution, results in the continuous deterioration of water quality, and makes the limited water resources more scarce. To a certain extent, water pollution would accelerate the process of ecological destruction, result in the shrinkage of drinking water sources, and restrict the development of water resource carrying capacity in Chicheng County to a certain extent.

4.1.4 Construction of water-saving management system

The construction of a water-saving management system can effectively improve the carrying capacity of regional water resources. With the gradual implementation of relevant plans, the protection of water resources in Chicheng County has been developed further, the construction of a water-saving society has been promoted vigorously, the protection and management of water resources have been strengthened, the rational development and conservation and utilization of water resources have been improved considerably, and the carrying capacity of water resources in Chicheng County has been improved to a certain extent.

4.2 Suggestions and measures

At this stage, the overall carrying capacity level of water resources in Chicheng County is optimistic. This indicates that the management and protection of water resources in Chicheng County have achieved remarkable results. However, there is a substantial scope for improvement. At present, the significant problems of river water pollution, low sewage treatment capacity, weak pollution monitoring and supervision, etc., severely affect the carrying capacity of water resources in Chicheng County. Therefore, this study puts forward the following four recommendations:

4.2.1 Implement documentation requirements

Stringently execute the Opinions of the State Council on implementing the Strictest Water Resources Management System. Chicheng County should clarify the "three red lines" of water resources management, and stringently implement the "four systems" of total water-use control, water-use efficiency control, water function area restriction, and water resource management responsibility and assessment according to the requirements of the document.

4.2.2 Optimize the industrial structure

Optimize the industrial economic structure of Chicheng County. Stringently limit industries with high water consumption and high pollution, and reduce the consumption of water resources and sewage discharge. Relevant departments should formulate development and reform policies for the above industries. These should be clarified in documents such as medium- and long-term development plans to improve the utilization rate of water resources.

4.2.3 Improve wastewater treatment capacity

Improve the sewage treatment capacity of Chicheng County. The industrial wastewater, agricultural wastewater, and domestic wastewater in Chicheng County would be rectified effectively by improving the construction of urban sewage pipe network and the daily treatment capacity of existing sewage treatment plants, or adding an appropriate number of new sewage treatment plants. Furthermore, "100% sewage treatment" would be realized, and the carrying capacity of water resources would no longer be restricted.

4.2.4 Improve relevant systems

Accelerate the improvement of water resources management systems and mechanisms, and strengthen the supervision of water resources. Install equipment for monitoring water quality and water quantity in the main sections of reservoirs and rivers, the control sections of rivers in townships and towns, water function areas, drinking water sources, groundwater intake points, medium and large irrigation areas, groundwater over-exploitation areas, etc. Ensure real-time monitoring and supervision. Strengthen the formulation, implementation, and publicity of relevant laws, regulations, and policies.

5 Conclusion

This study considered Chicheng County, Zhangjiakou City, Hebei Province, as the research object and constructed the water resource carrying capacity evaluation index system of the county, determined the threshold of the bearing capacity evaluation index, and used the one-factor evaluation method and cloud theory method to analyze and evaluate the water resource carrying capacity of the county in the current year (2018) and plan year (2025). The main conclusions are as follows:

(1) The carrying capacity of water resources in Chicheng County was analyzed using the one-factor evaluation method. The total annual water consumption and groundwater bearing status of Chicheng County are not overloaded. The evaluation result of the water quantity element is not overloaded, the water quality compliance rate element is not overloaded, and the pollutant entry factor is critical. Thus, the water quality element evaluation result and the comprehensive evaluation status of Chicheng County water resources carrying capacity level are in critical states. According to the current annual total water consumption control index, the bearing situation of the total water consumption element of Chicheng County's planning level in the year is not overloaded.

(2) The evaluation and analysis of the carrying capacity of water resources in Chicheng County based on the cloud theory algorithm of the "driving force-pressure-state-response" index model revealed that the water resource carrying capacity of Chicheng County in both current year and plan year belongs to the third level in the evaluation index system.

(3) The results of both analyses and evaluations show that the water resource carrying capacity of Chicheng County in the current year matches the economic development. These also show that the water resource carrying capacity of the plan year of Chicheng County would match the economic development. Furthermore, in the next time period, the water resources carrying capacity of Akagi County would have more scope for satisfying its economic and social development.

(4) The water security capacity of Chicheng County's economic and social development has been improved considerably. However, there are still problems of low river-water quality and pollution absorption capacity. Chicheng County should speed up the improvement of the water resources management system and mechanism, improve the capacity of sewage treatment, and provide a long-term sustainable assurance for the security of the capital's water resources and ecological environment.

Data availability statement

The original contributions presented in the study are included in the article/supplementary material, further inquiries can be directed to the corresponding author.

Author contributions

All authors listed have made a substantial, direct, and intellectual contribution to the work and approved it for publication.

Conflict of interest

JN and WN were employed by Engineering Design and Research Center, Beijing IWHR Corporation

The remaining author declares that the research was conducted in the absence of any commercial or financial relationships that could be construed as a potential conflict of interest.

Publisher's note

References

Hu, J. (2008). *Evaluation of bearing capacity of water resources in coastal areas*. Dalian, China: Dalian University of Technology.

Ji, F., Deng, D., and Ma, L., (2012). Research on carrying capacity of water resources in Zhangjiakou City and analysis on rational utilization of water resources. *Journal of Hebei Institute of Architecture and Civil Engineering*. 30 (02), 25–28. doi:10.3969/j.issn.1008-4185.2012.02.008

Jin, J., Dong, T., Li, J., Zhang, L., and Li, H., (2018). Evaluation of water resources carrying capacity under different bearing standards. *Advances in Water Science* 29 (01), 31–39. doi:10.14042/j.cnki.32.1309.2018.01.004

Li, Z. (2006). *Research on comprehensive evaluation and software development of regional water resources carrying capacity*. Chongqing, China: Chongqing University.

Liu, Y., and Chen, Y. G. (2018). 2D- and 3D-based intestinal stem cell cultures for personalized medicine. *Foreign Entrepreneurs in China*. 7 (26), 225–226. doi:10.3390/cells7120225

Liu, Y., Lu, C., and Huang, S. (2020). Comprehensive evaluation of water resources carrying capacity in the northwest agricultural and pastoral staggered area of beijing-tianjin-hebei: A case study of Zhangjiakou. *Pratacultural Science*. 37 (07), 1302–1312.doi:10.3390/w13030249

Lu, M., Zhou, T., and Yang, Z. (2016). Application of principal component analysis method in the evaluation of bearing capacity of water resources. *Science Technologies Wind* 2016 (21), 149. doi:10.19392/j.cnki.1671-7341.201621136

Ma, Z., Li, L., Zhang, J., and Xu, Y., (2018). Spatio-temporal analysis of carrying capacity of water resources in Zhangjiakou. *Journal of Hebei North University(Natural Science Edition)*. 34 (05), 51–57. doi:10.3969/j.issn.1673-1492.2018.05.011

People's Government of Hebei Province (2019). Notice of the general office of the People's government of Hebei Province on printing and distributing the > implementation Opinions on the construction plan of the water conservation functional zone and the ecological environment support area of the capital of Zhangjiakou < (2019-2035). *Gazette People's Government Hebei Province*. (12), 53–72.

Su, Y., Ji, C., Zhang, J., and Li, R., (2017). Comprehensive evaluation method of water resources management based on cloud model: A case study of Huizhou city. *China Rural Water Resource Hydropower* (12), 53–58. doi:10.3969/j.issn.1007-2284.2017.12.011

Tang, A., and He, S. (2021). Set pair analysis and diagnostic identification of the evolution of water resources carrying capacity in Guiyang. *China Rural Water Resour. Hydropower* 2021 (01), 76–83. doi:10.3969/j.issn.1007-2284.2021.01.015

Tong, C., Shi, H., Li, H., Li, Y., and Wang, J., (2009). Evaluation of water carrying capacity of water resources in Ordos City based on grey correlation analysis. *Water-saving Irrigation*. (11), 43–49. doi:10.3969/j.issn.1007-4929.2009.11.014

Wan, G. (2015). *Evaluation and application of groundwater resource carrying capacity in typical areas of northern Henan*. Henan Province, China: Bureau of Hydrological and Water Resources Survey of Anyang.

Wang, B., and Dan, D. (2012). A new understanding of the connotation of water resources carrying capacity. *Heilongjiang Water Conservancy Science Technology*. 40 (07), 1–2. doi:10.14122/j.cnki.hskj.2012.07.010

Wang, W., Yang, L., Zheng, Y., and Xu, D., (2021). Evaluation of water resource carrying capacity in Shiyang River Basin based on game theory and cloud model. *Water Conservancy Hydropower Technology China Engl*. 52 (10), 35–45. doi:10.13928/j.cnki.wrahe.2021.10.004

Wu, Y., Wang, Y., and Cheng, F. (2015). Evaluation of the current situation of groundwater quality in mining areas and surrounding areas based on index method: A case study of jieshou serpenite mine in jinan, shandong Province. *Water-saving Irrigation* 2015 (06), 50–54. doi:10.3969/j.issn.1007-4929.2015.06.013

Wu, Y., and Fu, D. (2017). In-depth implementation of the "three solid" work requirements - study the spirit of General Secretary Xi Jinping's important speech on inspecting Zhangjiakou. *Friends Leaders* 2017 (12), 16–18. doi:10.16321/j.cnki.ldzy.2017.12.007

Yang, L., Zhang, R., Hong, M., Liu, J., and Song, C., (2014). Risk assessment of water resources security in southwest China based on cloud model. *Resources and Environment in the Yangtze Basin*. 23 (1), 1–5. doi:10.11870/cjlyzyyhj2014Z1001

Yang, Q., Zhang, F., Jiang, Z., Yuan, D., and Jiang, Y., (2016). Assessment of water resource carrying capacity in karst area of Southwest China. *Environmental Earth Sciences*. 75 (1), 37. doi:10.1007/s12665-015-4816-6

Zhang, F. (2018). *Analysis of water resources carrying capacity in jiamusi city*. Heilongjiang, China: Heilongjiang University.

Zhang, X. (2019). *Dynamic carrying capacity of water resources under climate change*. Henan Province, China: North China University of Water Resources and Electric Power.

Zheng, J., and Li, X. (2021). Assessment model of regional water carrying capacity based on coordination. *Water Source Protection*. 37 (05), 30–35.

Zhou, Y., Ding, M., Gao, S., Yu-Strzelczyk, J., Krischke, M., Duan, X., et al. (2021). Optogenetic control of plant growth by a microbial rhodopsin. *Hydraulic Science Cold Zone Engineering*. 4 (05), 144–151. doi:10.1038/s41477-021-00853-w

frontiers | Frontiers in Environmental Science

TYPE Original Research
PUBLISHED 16 January 2023
DOI 10.3389/fenvs.2023.1082619

Free and underfit-scavenger river dynamics dominate the large Amazonian Pacaya-Samiria wetland structure

Tania V. Rojas[1,2], Jorge D. Abad[2]*, Wendy R. Roque[2], Edgardo M. Latrubesse[3] and Jingfu Shan[4]

[1]Aquatic Ecology and Fisheries Laboratory, Department of Natural and Applied Sciences, University of Wisconsin-Green Bay, Green Bay, WI, United States, [2]Department of Research, Education and Development, RED YAKU, Lima, Peru, [3]Programa de Pós-Graduação em Ciências Ambientais—CIAMB, Universidade Federal de Goiás, Goiás, Brazil, [4]School of Geosciences, Yangtze University, Wuhan, China

Check for updates

OPEN ACCESS

EDITED BY
Omer Yetemen,
Istanbul Technical University, Türkiye

REVIEWED BY
Richard George Pearson,
James Cook University, Australia
Steven Sandi,
The University of Newcastle, Australia

*CORRESPONDENCE
Jorge D. Abad,
✉ jabad@redyaku.com

SPECIALTY SECTION
This article was submitted to Freshwater Science, a section of the journal Frontiers in Environmental Science

RECEIVED 28 October 2022
ACCEPTED 02 January 2023
PUBLISHED 16 January 2023

CITATION
Rojas TV, Abad JD, Roque WR, Latrubesse EM and Shan J (2023), Free and underfit-scavenger river dynamics dominate the large Amazonian Pacaya-Samiria wetland structure.
Front. Environ. Sci. 11:1082619.
doi: 10.3389/fenvs.2023.1082619

The Peruvian Amazon is known for harboring the greatest biodiversity on the planet, with a world record for biodiversity per unit area. Previous studies suggested that the high ecological value depends on correlations between ecosystem functionality and seasonal inundation control vegetation patches. However, the knowledge on how river morphodynamics and its complex erosion-depositional processes influence the aquatic mosaic and fishing activity in the region is still incipient. This study examines the hydrogeomorphology of the Peruvian tropical wetland of Pacaya Samiria, located in Western Amazonia, and its role in the distribution of aquatic habitats. By using remote sensing techniques, the hydrogeomorphological connectivity that bounds the Pacaya Samiria National Reserve is characterized by ancient to modern river processes. Additionally, river signatures developed by the Ucayali, Marañon, Huallaga, Pacaya, and Samiria Rivers overlap with fish extraction and dominant vegetation to describe how geomorphology is associated with the spatial distribution of fishing zones. Results indicated that paleochannels regulate wetland drainage within the Ucamara Depression, supporting stational water stagnation, vegetation cover, and formation of carbon rich detritus, relevant aspects to understand fish traits. Moreover, the Ucayali River dominates river dynamics in the Pacaya Samiria wetland, thus playing a pivotal role in shaping the complexity of streams and lakes. Furthermore, underfit-scavenger meandering rivers are observed in areas where paleochannels from large rivers are found. A geomorphological characterization of drainage patterns in freshwater environments, such as Amazonian wetlands, is crucial to develop sound management strategies. This methodological approach is expected to support decision-making in conservation actions in Amazonian environments based on understanding wetland connectivity and hydrogeomorphological behavior and their influence on commercial fisheries.

KEYWORDS

wetlands, paleo-channels, Amazon basin, Pacaya-Samiria, meandering rivers, anabranching rivers, hydrologic connectivity, underfit-scavenger rivers

1 Introduction

The Amazon Basin is composed of a mosaic of interconnected freshwater and terrestrial ecosystems. The complexity of these connections depends not only on the hydrological patterns but also on the geomorphic features in the floodplain, creating a heterogeneous network of wetlands, lakes, channels, and alluvial deposits that varies in space and time (Alsdorf, 2003; Park and Latrubesse, 2017). Seasonally based flooding patterns of both hydrological and hydraulic regimes also create a diverse mosaic of vegetation and habitats, supporting the functioning of ecosystems. As a result of the constant development of the floodplains caused by seasonal alluvial flows, previous studies suggest that the diversity of the vegetation from different ages generated the high biological diversity in the Amazon rainforest (Salo et al., 1986). Therefore, dynamic flow regimes establish critical interactions between the main channel and adjacent floodplain habitats, such as “tipishcas” or oxbow lakes, thereby providing fish and other aquatic species access to shelter, food, and spawning grounds (Junk et al., 1989; Couto et al., 2017; Virgilio et al., 2020). According to Castello et al. (2013), this dynamic interaction explains the high ecological value of the Amazonian ecosystems but also makes them more sensitive to anthropogenic pressures. Flood frequency and duration of inundation are relevant to characterize the hydrological connectivity and the ecological features of Amazonian ecosystems (Wilson et al., 2007; Castello et al., 2013; Reis et al., 2019). Reis et al. (2019) also indicate that the predominance of local rainfall in flooding patterns of complex wetlands makes them more sensitive to climate change and external pressures at a regional scale but less vulnerable to alterations in the local hydrology of the river. However, this is the opposite for systems dominated by floodplain inundation that depend on the overflow from large rivers and lateral connectivity. Moreover, Arantes et al. (2019) demonstrated that the biomass distribution of fish functional diversity in floodplains is associated with the vegetation cover, resulting that biomass being most significant in areas of the flooded forest when compared to other habitats.

The Peruvian Amazon is one of the regions that harbor the largest biodiversity on the planet, with a world record for biodiversity per unit area (OTCA, 2009). Some theories explain that this biological value depends on the correlations of ecosystems with the dynamics of rivers because it is related to flooding patterns (Ferreira and Stohlgren, 1999), the geomorphology of the riverbed, the altitudinal climatic changes, and the influence of the upper part on the river channel (Naiman et al., 1993). A dynamic fluvial system helps to modify the flora, unlike a more stable environment where the time scale of these processes is much longer. Kalliola et al. (1992); Kalliola et al. (1993a); Kalliola et al. (1993b) and Puhakka et al. (1992) explained that the vegetation patterns and the diversity of the species are usually controlled by other environmental factors, such as 1) the dynamics of the river that defines the type of vegetation and habitats; 2) the influence of the change of season in the plain alluvial that generates regions of different elevations, age, and soil properties (deposition processes along the point bars, ridges, depressions, flooded basins, and abandoned channels); and 3) the alluvial processes that create new habitats, modify existing ones and produce a diversity of vegetation. Additionally, the seasonal intermittency of discharge into rivers produces variations in water cycles, which are associated with the frequency of floods, erosion of riverbanks, changes in fishing activity, and changes in the planimetric and altimetric patterns of rivers (Salonen et al., 2012; Abad et al., 2013).

The primary objective of this study was to explore the ancient and modern river geomorphology across the Pacaya-Samiria wetland system (the second largest protected area in Peru), considering the high geomorphological complexity observed in this region (Dumont, 1991; Dumont, 1992). Based on it, the second objective was to relate the landscape dynamism to water fluxes, peat vegetation, and fish extraction. This study hypothesizes that the characterization of wetland landscapes will help understand the gradients in habitats and support decision-making in conservation and planning strategies for Amazonian wetlands.

2 Study area

The Pacaya Samiria National Reserve (PSNR) is in the west portion of the Amazon basin (Figure 1A), a region where the Amazon River is born due to the confluence of the Ucayali (meandering) and Marañon (anabranching) rivers (Garcia et al., 2022; Guerrero et al., 2022), as illustrated in Figure 1A. The PSNR is a protected Ramsar Site of 20,800 km^2 (one of the largest flooded forests within the Amazon basin) composed of a tropical seasonally flooded forest dominated by rainfall and upland run-off (Castello et al., 2013), where biodiversity indicators (e.g., terrestrial mammal richness, tree a-diversity) are higher compared to other regions in the Amazon basin (Hoorn et al., 2010).

From the geological point of view, the Pacaya-Samiria (P-S) wetland develops in the subsiding Ucamara depression of the Marañon Basin in the Peruvian Andean forelands. It is a very flat subsiding area of 330,000 km^2, consisting of a complex network of rivers and permanent and semi-permanent swamps and lakes, and paleochannels. The depression is approximately delimited on the north by the Marañon River and to the southern and eastern borders by morphostructural boundaries and the Ucayali River. The Ucamara depression was an active sediment sink that was filled up by with sediment sourced from the Andes by avulsed alluvial belts of the Ucayali and Marañon (Dumont, 1992; Latrubesse, 2015). The thickness of the Quaternary deposits is unknown, but more than 15 m are exposed in bank outcrops of Quaternary terraces in the Ucayali River. Figure 1B shows that the P-S wetland overlies with the Chambira (continental) formation in the Ucayali Basin of Peru, to later overlap with the Solimões (previously known as Pebas) formation in the confluence between the Ucayali and Marañon Rivers (da Silva-Caminha et al., 2020; Guerrero et al., 2022).

Figure 1C shows that the P-S wetland has a low-water stage from October to November, whereas flooding (high-water stage) occurs between May and July (Hess et al., 2015; Reis et al., 2019). In this ecosystem, bordering rivers are narrow (Reis et al., 2019) and there is a direct correlation between flooded area percentage (open water, inundated non-forest, and inundated forest) (Jensen et al., 2018) and river level measurements. As illustrated in Figures 1C, D, the P-S wetland cover is composed of late-successional vegetation, such as forests and woodlands, that are inundated most of the year. During the high-water stage, areas along the streams (bare soil) inundate, allowing early successional vegetation, such as aquatic macrophytes, to grow.

Figure 1E shows that the P-S wetland includes different river systems: self-formed meandering (Ucayali, Huallaga, Tigre, Tapiche, Puinahua), underfit-scavenger-formed meandering (Yanayacu,

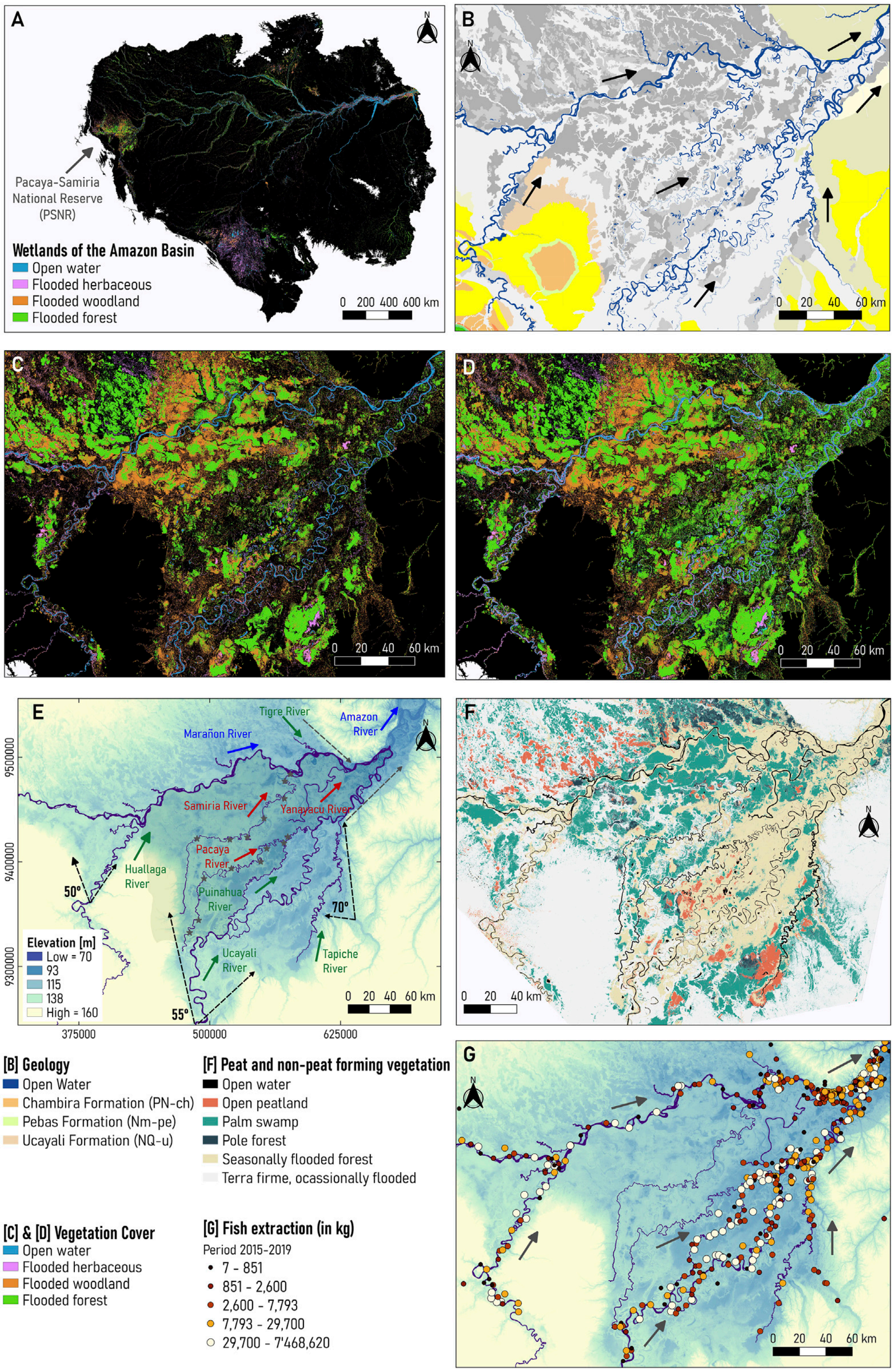

FIGURE 1
(A) Location of the Pacaya-Samiria (P–S) wetland in the Amazon Basin, **(B)** Geology (dataset obtained from the Geological Mining and Metallurgical Institute (INGEMMET) of Peru, **(C)** Low-water stage in 1995, **(D)** high-water stage 1996 (datasets obtained from Hess et al., 2015), **(E)** Main rivers and tributaries with DEM, **(F)** Peat and non-peat forming vegetation (dataset obtained from Draper et al., 2014), **(G)** Fish extraction from 2015–2017 (dataset provided by Wildlife Conservation Society, 2022).

Pacaya, Samiria), and anabranching (Marañon, Amazonas). The Huallaga, Ucayali, and Tapiche Rivers enter the P-S wetland with an increase in the valley angle—50, 55, and 70°, respectively, thus avulsion processes and meandering migration rates are enhanced (Abad et al., 2022a; Abad et al., 2022b). As observed in Figure 1E, there is a reduction in valley angle, promoting the birthplace of the

Amazon River as the confluence of the Marañon and Ucayali Rivers (Garcia et al., 2022; Guerrero et al., 2022).

Previous studies have described the complex geomorphology within the P-S wetland, composed of interconnected rivers and swamps (Dumont and Garcia, 1991; Kalliola et al., 1992). The Marañon, the Ucayali, and the Tapiche are white-water rivers (high concentrations of solutes and sediment) that flow from west to east and south to north, respectively, while the Pacaya, Yanayacu and the Samiria are black-water rivers (high concentration of dissolved organic carbon) with similar geomorphic patterns that resulted from the accumulation of rainfall and flooding on fossil fluvial landforms (Dumont 1991; Duncan and Fernandes, 2010). Dumont. (1991) described that the composition of fluvial landforms along the Pacaya River is similar to those Ucayali River present, thus suggesting that the Ucayali River has flowed northward forming the Pacaya River valley to shift southeastward later. Likewise, the Samiria River presents similar fluvial landforms to the Ucayali River, but that are more preserved than Pacaya's. These landforms are also surrounded by the Marañon River, indicating that Samiria was formerly connected to the Marañon River. Dumont. (1991) and Räsänen et al. (1992) indicated that the Samiria, Pacaya, and Tapiche are then underfit-scavenger rivers that rely on relic belts left by the Ucayali River. Additionally, Dumont. (1991) suggested that the Ucayali and Marañon Rivers have been joined on the western side of the P-S wetland and later the junction migrated eastward due to avulsion shifting dynamics.

Puhakka et al. (1992) described that sediment deposited in adjacent bars in meandering rivers tends to inundate during the high-flow season then allowing plant colonization in the following months. Herein, long-term aggradation and deposition of meandering river sediments result in alternated vegetation mosaics (Kalliola et al., 1992). Likewise, other colonized areas include poorly drained swales between the ridges. In meandering systems, such as the Ucayali and Huallaga Rivers, banks in chute islands (result from chute cutoff) are prone to erosion thus limiting vegetation succession, whereas river margin areas are more stable and can extend many kilometers downstream allowing vegetation grows in aged zones. Studies of vegetational successions in tropical and subtropical anabranching rivers are less known (Wittman et al., 2006; Peixoto et al., 2009; Montero and Latrubesse, 2013; Stevaux et al., 2013; Marchetti et al., 2013; Marchetti et al., 2020; among others). In anabranching systems, such as the Marañon River, braided channels are constantly dividing and rejoining; thereby, developing an unstable system composed of young successional vegetation. Additionally, Draper et al. (2014), Lähteenoja et al. (2012), and Lähteenoja and Page. (2011) suggested linkages between vegetation history with carbon stocks in peatland environments across the P-S wetland in the Pastaza-Marañon foreland. Figure 1F shows larger open peatland areas across the Ucayali River, and pole forests and palm swamps along the Marañon River. High carbon density has been found in below-ground pole forests, followed by palm swamps and pole forests (Draper et al., 2014), which suggests that the Marañon valley has greater carbon stocks than the Ucayali.

Gradients in land cover, because of inundation timing and consequent vegetation succession, are often associated with animal functional diversity and biomass in Amazonian floodplains (Arantes et al., 2019). The interconnected system between the Marañon and Ucayali Rivers combined with the exchange of water and sediment (Anderson et al., 2018) supports a high alpha and beta diversity of a myriad of fish species due to the habitat specialization and geographic isolation conditions (Albert et al., 2011; Aldea-Guevara et al., 2013). In the Marañon and Ucayali basins, more than 1,300 fish species have been estimated (Anderson et al., 2018; Latrubesse et al., 2021). The Ucayali basin encompasses more than 650 species of fish, 90 to 110 species of floodplain trees and more than 80 species of floodplain birds, whilst the Marañon basin sustains around 700 species of fish, the highest tree diversity among Amazon sub-basins, and more than 50% of flooded-habitat birds identified in the Amazon (Latrubesse et al., 2021). In addition, the Amazon basin reaches the highest diversity in the Marañon basin and Andean-foreland rivers have the highest tree diversity compared to any floodplain forests on Earth, including up to 30% endemic tree species (Wittmann et al., 2013).

Figure 1G shows about 1,112 fish extraction zones georeferenced across the Loreto region, of which 28% are in the PSNR along the Marañon, Huallaga, and Ucayali rivers (Wildlife Conservation Society, 2022). More than 60 billion kilograms were extracted in a 5-year period (from 2015 to 2017) in Loreto, and only 40% of the total fish extraction was extracted from the Ucayali River. Moreover, Figure 1F indicates a higher concentration of fishing areas near the San Lorenzo community (Marañon) but a lower fish extraction capacity. In contrast, locations near the Requena community (Ucayali) show a higher fish extraction capacity but a lower concentration of fishing zones. Note that this information was derived from the landings of commercial fishing registered in the main ports. Although the Regional Directorate of Production of Loreto (Dirección Regional de la Producción de Loreto, in Spanish) collected all data, there may be underestimates of the total fish volume of landings because not all ports have enough personnel to collect that information (Wildlife Conservation Society, 2022).

3 Materials and methods

3.1 Modern river dynamics

Modern meandering and anabranching river dynamics of the Ucayali and Marañon rivers were previously characterized by Gutierrez and Abad. (2014), Gutierrez et al. (2014), Frias et al. (2015), Mendoza et al. (2016) and Abad et al. (2022a). Figure 2 shows the planform configuration for upstream- (A1) and downstream-skewed (A2) meandering channels (Abad and Garcia, 2009a; Abad and Garcia, 2009b). The main metrics for rivers include W (channel width), A (amplitude), R (radius of curvature), L (wavelength, straight line between inflection points), λ (arc-wavelength), and sinuosity S ($S = \lambda/L$). Figure 2B shows the planform configuration of anabranching rivers (based on Garcia et al., 2022) which is composed of the main channel and several secondary channels, as well as islands and distinct size angles of bifurcation and confluence of channels.

This study covered satellite imagery processing every 5 years between 1985 and 2021 (the last time interval was 6 years from 2015 to 2021) due to the dynamism of meandering (Ucayali and Huallaga) and anabranching (Marañon) rivers (Salo et al., 1986; Frias et al., 2015; Abad et al., 2022a), reporting a total of 36 years of analysis. Landsat imagery was downloaded from the USGS Earth Explorer data portal (https://earthexplorer.usgs.gov/) considering a cloud percentage of less than 10% during the

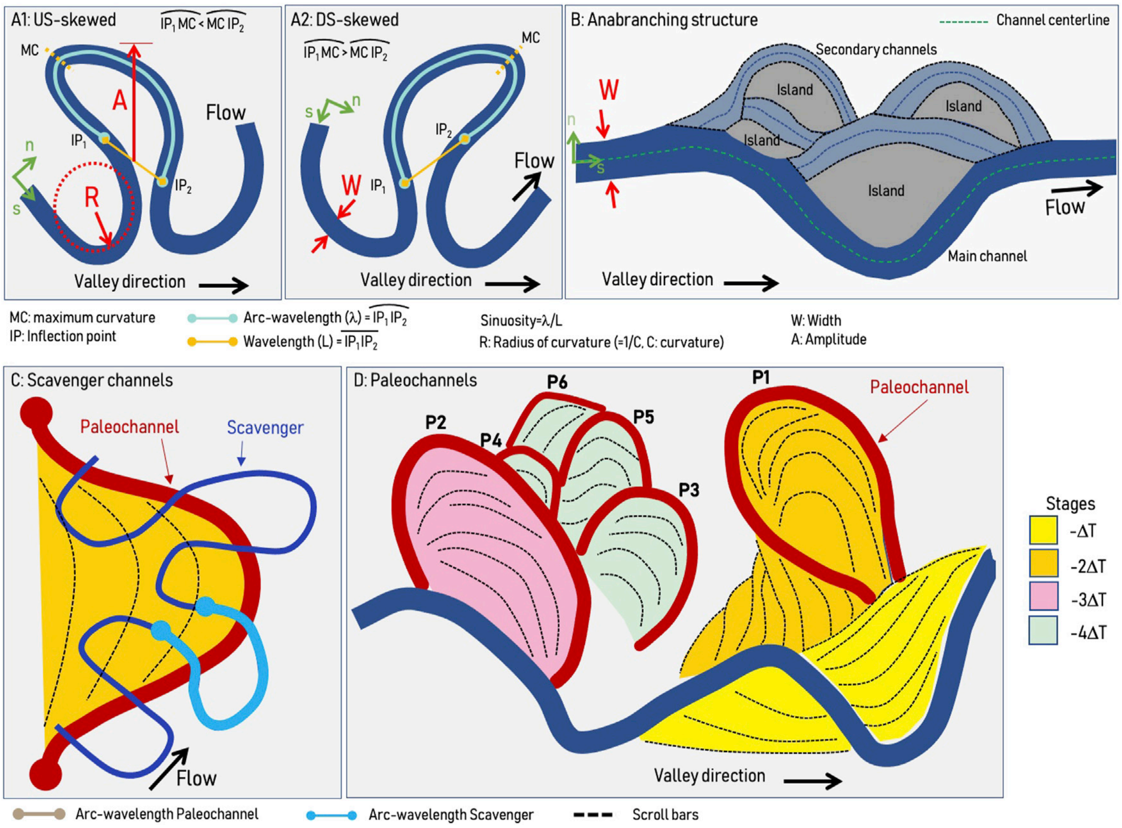

FIGURE 2
(A) meandering river (A1: US-skewed, A2: DS-skewed), **(B)** Anabranching structure, **(C)** Underfit-scavenger channels, **(D)** Paleochannels in different stages (ages).

dry season in the area—from July to December. Landsat bands were then combined to determine the NDVI (Normalized Difference Vegetation Index) and later filtered to discretize "water" and "not water" areas (Frias et al., 2015; Marchetti et al., 2020). Using the polygonization tool, raster data were converted into vectors and removed clouds, disconnected streams, and ponds were to only determine the main river channels. For more details on imagery analysis, see the supplemental material.

After obtaining the channel GIS features (especially the channel centerline and curvature), planform metrics can be obtained. Catano et al. (2009), Gutierrez and Abad. (2014), and Gutierrez et al. (2014) developed the first studies to characterize river meandering dynamics using continuous wavelet transform (CWT). Later on, Ruben-Dominguez et al. (2021) developed the MStaT toolbox to extract river planform metrics (using CWT) and migration rates (from two centerlines at different time intervals). Rivers are composed of a wide spectrum of bends, thus, Vermeulen et al. (2016) also has used the CWT and described that river meandering planforms are multiscale, non-stationary features. By using the continuous wavelet transform and the curvature signal of the river centerline, Vermeulen et al. (2016) analyzed the wavelet spectrum in a hierarchically ordered tree. This approach aimed to describe how small-scale meanders are connected to large-scale meanders as in a train of meanders. As suggested by Vermeulen et al. (2016), in this study, the Gaussian wavelet of order 2 (Mexican-hat) was used.

3.2 Ancient river dynamics

River migration patterns can be identified by mapping the fluvial landforms on the terrain. Geomorphology is a key tool to interpret the temporal channel-floodplain changes and migrations, the soils mosaic and the morpho-hydrological patterns that control vegetational units in fluvial wetlands (Abad et al., 2013; Abad and Garcia, 2009b; Motta et al., 2012a; Motta et al., 2012b; Latrubesse and Suizu, 2022). These characteristics can be mapped from high-resolution Google Earth imagery and digital elevation models (DEM) (Ghinassi et al., 2014; Rojas et al., 2021). In this study, ancient planform architecture was determined using the methodology described by Lin et al. (2017) and Shan et al. (2018) to characterize past river dynamics and geomorphic features in meandering (Ucayali, Huallaga, Tapiche, Pacaya, Samiria, Yanayacu) and anabranching (Marañon) rivers.

River signatures were traced using both satellite and radar imagery. Satellite imagery consisted of a 30-m resolution DEM derived from the Aster Global Digital Elevation Model (ASTER GDEM) globe map data sets from the Peruvian Ministry of Environment and 90-m resolution data from the Shuttle Radar Topography Mission (SRTM) (Jarvis et al., 2008). In addition, radar imagery combined SAR mosaics from the Advanced Land Observing Satellite 2 (ALOS2) Phased Array L-band Synthetic Aperture Radar 2 (PALSAR-2) and the Uninhabited Aerial Vehicle Synthetic Aperture Radar (UAVSAR), of 12.50 m and 1.80 m resolution, respectively. SAR (Satellite Aperture Radar) imagery was

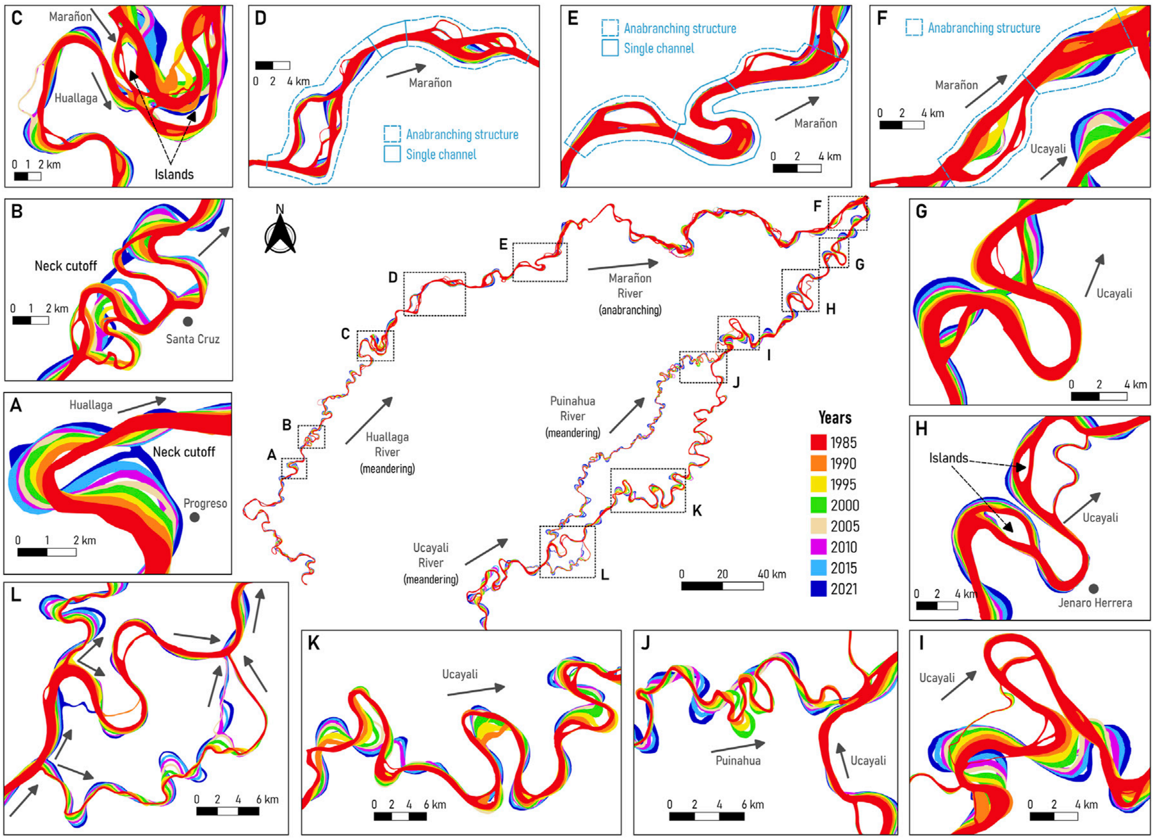

FIGURE 3
Modern River dynamics (from 1985 to 2021) in the P-S wetland. **(A)**] Huallaga River (near Progreso), **(B)** Huallaga River (near Santa Cruz), **(C)** Confluence of the Huallaga and Marañon Rivers, **(D,E)** Marañon River, **(F)** Confluence of the Marañon and Ucayali Rivers, **(G–I)** Lower Ucayali River, **(J)** Confluence of the Ucayali and Puinahua Rivers, **(K)** Ucayali River, **(L)** Bifurcation of the Ucayali and Puinahua Rivers.

acquired from the Advanced Land Observing Satellite 2 (ALOS2) Phased Array L-band Synthetic Aperture Radar 2 (PALSAR-2) mission available at the Alaska Satellite Facility (https://search.asf.alaska.edu/) while UAVSAR data were downloaded from the Jet Propulsion Laboratory at the California Institute of Technology (https://uavsar.jpl.nasa.gov/cgi-bin/data.pl). Radar mosaics have been previously processed by applying radiometric calibration and terrain correction to reveal surface characteristics.

Combining DEM, satellite, and radar imagery, paleochannels were reconstructed by tracing river signatures in erosion and deposition areas along streams. Ancient channels revealed river migration patterns and bend apex orientation observable on Google Earth based on the abandoned direction of the river (Shan et al., 2018). Depending on flow and sediment discharges, rivers tend to use the paleochannels structures usually formed by larger rivers, thus paleochannels dimensions are larger than those of underfit-scavenger rivers and try to develop their own planform configuration. Figure 2C shows a typical underfit-scavenger meandering channel being developed over paleochannels that were created by larger rivers. Likewise, Figure 2D shows paleochannels along a river including their scroll bars. Notice that paleochannels are classified into stages (depending on age), and depending on planform river dynamics, not all paleochannels are properly preserved.

4 Results

4.1 Modern and ancient river dynamics

Figure 3 shows the modern multitemporal analysis from 1985 to 2021 of large meandering (Huallaga, Ucayali, Puinahua) and anabranching (Marañon and Amazon) rivers surrounding the P-S wetland. Figures 3A, B show the Progreso and Santa Cruz, respectively, recent neck cutoffs along the Huallaga River (Valverde et al., 2019). The Santa Cruz cutoff occurred in 2018 producing an upstream erosional wave (Abad et al., 2012) that accelerated the Progresso cutoff in 2021. Figures 3G, I show two recent cutoffs along the Ucayali River (Abad et al., 2022a), unveiling a potential cutoff near Jenaro Herrera town (see Figure 3H).

Figures 3D, E show the planform configuration for the Marañon River, evidencing typical anabranching structures formed by islands and channels (main and secondary channels) which are most of the time connected with single channels. Indeed, Garcia et al. (2022) found a periodicity of 22.40 km for the occurrence of anabranching structures for the Peruvian Amazon River from Nauta to Santa Rosa (border with Colombia and Brazil). The anabranching structures have low migration rates compared to meandering channels (see Figure 3F), thus the confluence location of the Marañon and Ucayali Rivers (birthplace of the Amazon River) is dominated by the planform

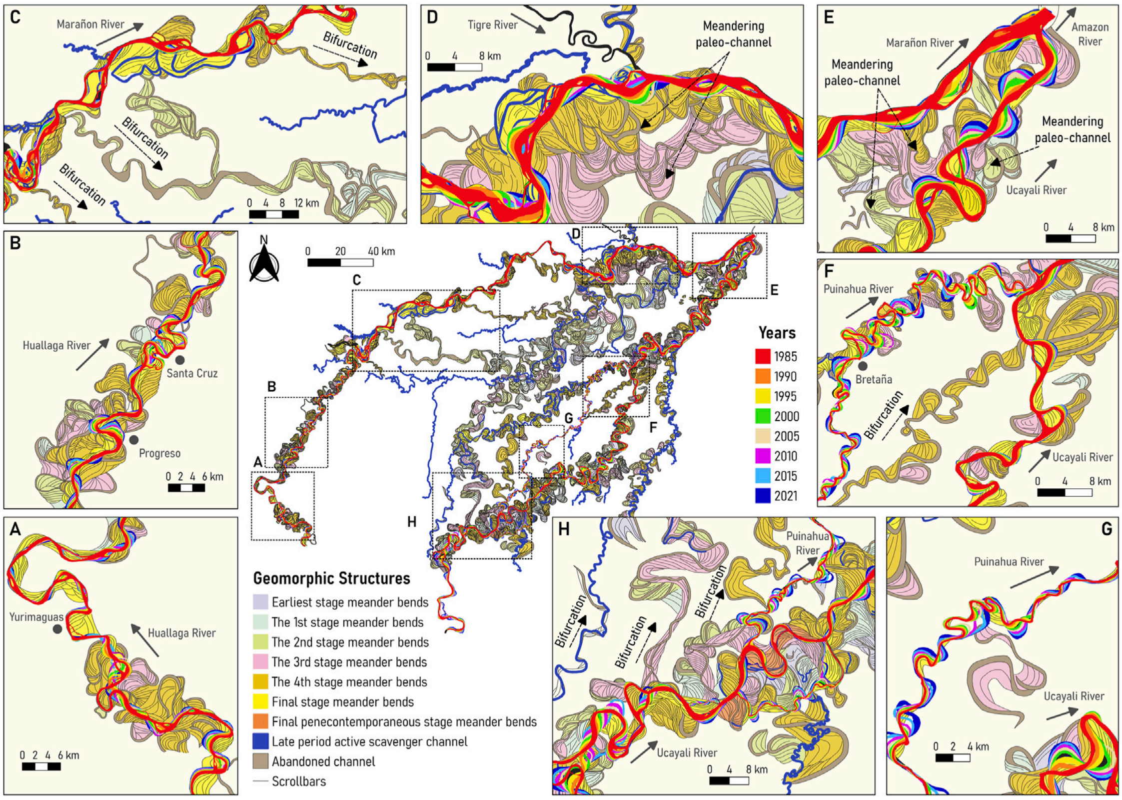

FIGURE 4
Ancient and modern river dynamics of the buffer zone in the P-S wetland. **(A)** Huallaga River near Yurimaguas city, **(B)** Huallaga River near Progreso and Santa Cruz cutoffs, **(C)** Birfurcated channels along the Marañon River, **(D)** Confluence of the Tigre and Marañon Rivers, **(E)** Confluence of the Marañon and Ucayali Rivers, **(F)** Confluence of the Puinahua and Ucayali Rivers, **(G)** Puinahua River, **(H)** Bifurcation of the Puinahua and Ucayali Rivers.

dynamics of the meandering Ucayali River (Garcia et al., 2022; Guerrero et al., 2022).

Abad et al. (2022a) described that bends along the lower Ucayali River transition from purely meandering to anabranching rivers, observing islands and multichannel structures. Figure 3K shows the planform dynamics of bends along the Ucayali River in the region where the Ucayali and Puinahua rivers share water flow. Figure 3L shows the bifurcation of the Ucayali River to form the Puinahua River and Figure 3J shows the confluence of the Puinahua and Ucayali Rivers. Notice that the bifurcation produces bends of varied sizes based on the trapping efficiency of water and sediment. In general, the planform migration rates of meandering rivers are higher than in anabranching rivers and cutoff occurrence happens in meandering rivers rather than in anabranching ones (Abad et al., 2013).

Figure 4 shows the reconstruction of paleochannels and oxbow lakes along the large meandering (Huallaga, Ucayali, Puinahua, and Tapiche) and anabranching (Marañon) rivers surrounding the P-S wetland, as well as those rivers (Samiria, Pacaya, and Yanayacu) located inside of the P-S wetland. The Huallaga, Ucayali, and Marañon rivers transport water and sediments originating in the Andes, the main source of sediments of the entire Amazon basin whereas the Tapiche River carries water and sediment from a watershed originated in the lowlands, indicating a lower sediment concentration than the Andean rivers. The Pacaya, Samiria, and Yanayacu Rivers have their origin in the P-S wetland, thus the water they conduct derives from multiple sources such as yearly flooding and springs from large rivers (Marañon, Ucayali, and Huallaga), and local rainfall (water table saturation-surface exposure, groundwater connectivity). These rivers present low sediment concentrations since they are not connected to the Andes region.

As discussed by Abad et al. (2013) and Marin-Diaz et al. (2020), planform dynamics show that Peruvian Amazon meandering rivers are more morphologically active than anabranching rivers. CITA (2021) described that lateral migration rates for meandering rivers are: 25.16 m/year (Huallaga), 50.47 m/year (Ucayali). Figures 4A, B illustrate paleochannels with comparable size as those of modern channels along the Huallaga River. Figure 4C shows several bifurcated paleochannels along the Marañon River that describe meander-type characteristics. Likewise, Figure 4D shows that the Marañon Rivers present high-sinuosity and high-amplitude paleochannels, contrary to those of modern dynamics. Depending on the occurrence of these bifurcated channels, the Marañon River has changed from purely anabranching—as today—to transition to a meandering configuration, thus presenting meander-type paleochannels. As described by Abad et al., 2013; Marin-Diaz et al. (2020), meandering rivers transition into anabranching rivers occur when water and sediment discharge are added (confluences), thus these river signatures suggested that the opposite could be also possible (bifurcations).

Figure 4E show the paleochannels in the confluence of the Marañon and Ucayali Rivers where meander-type paleochannels

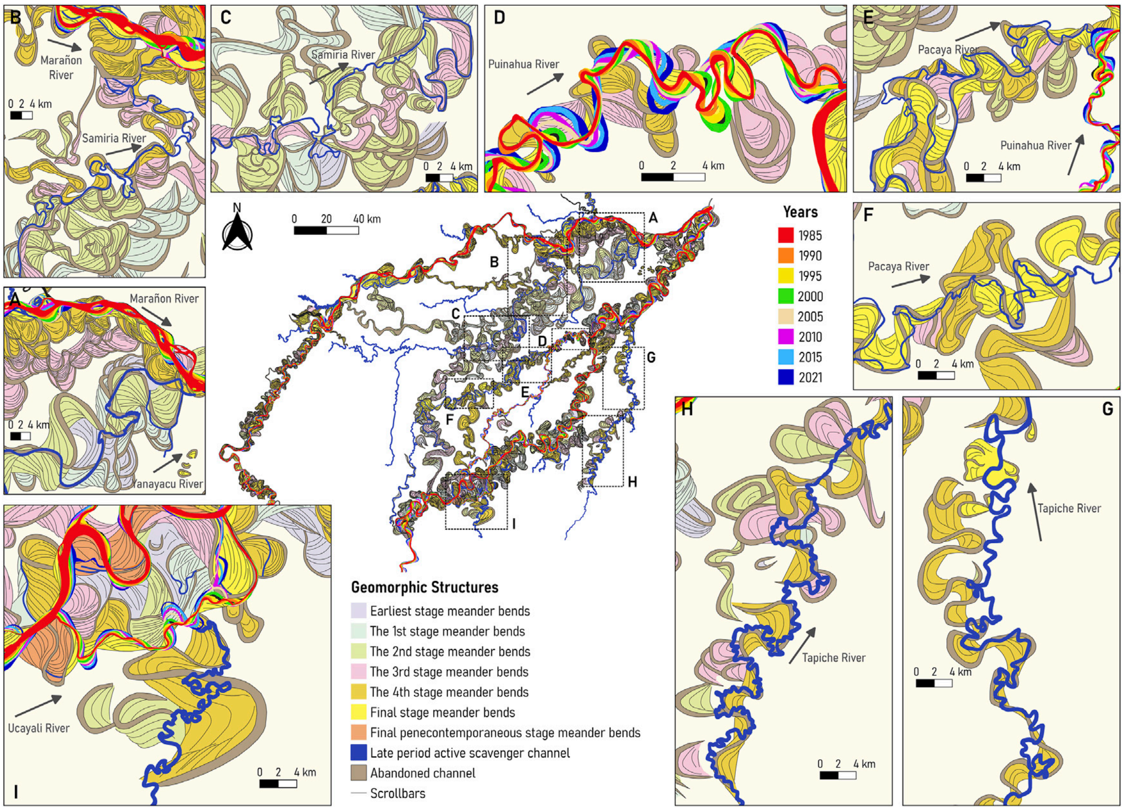

FIGURE 5
Free and underfit-scavenger river dynamics in the P-S wetland: **(A)**] Yanayacu River, **(B,C)** Samiria River, **(D)** Puinahua River, **(E)** confluence between the Pacaya and Puinahua Rivers, **(F)** Pacaya River, **(G,H)** Tapiche River, and **(I)** Sungaro River.

clearly dominated the floodplain whereas those paleochannels derived from the Ucayali River dominated the confluence location. Due to the geology and digital terrain model, the confluence valley is narrowed (see Figure 1B), thus allowing the Amazon River to shape (Guerrero et al., 2022).

Figure 4F shows the confluence of the Puinahua and Ucayali Rivers. As illustrated in Figure 4G, the Puinahua shows a mixture of paleochannels generated by the Puinahua itself together with paleochannels that were formed by the Ucayali River (large-size channels). The confluence between the Puinahua and Ucayali Rivers appears to have been placed in distinct locations depending on the bifurcated channels or the drainage system of the area. Figure 4H shows the bifurcated channels along the Ucayali River, describing that several rivers with similar characteristics as the Puinahua River have coexisted in the region. These paleochannels have similar patterns to those of the modern Ucayali River. In this study, the paleochannels were classified in different stages (Figure 4), describing what is older or younger, however, there is still a need for dating the sediments along the paleochannels and describing their age.

4.2 Underfit-scavenger rivers: Pacaya, Samiria, Yanayacu, Tapiche, and Sungaro

In Figure 5, underfit-scavenger rivers have used paleochannels to build up their planform dynamics. Figure 5A shows the Yanayacu River's centerline that follows the Ucayali's paleochannel except in regions where 1) connects different paleochannels, and 2) develops its own meanders, which are smaller size compared to the Ucayali's paleochannel. Figures 5B, C show that Samiria's planform configuration follows Ucayali's paleochannel configuration but there is a region where significant reworking of the floodplain is observed. It suggests that the Samiria River produces its own meanders but still uses the paleochannels as its main alignment. Figure 5D shows that the Puinahua River is developing its own meanders slightly smaller than those of the Ucayali River but in certain regions, it uses the Ucayali's paleochannels as the main alignment. As observed in Figure 3, the Puinahua modern migration has increased in the last years (from 1985 to 2021) and capturing more water and sediments; it suggests that the Puinahua River might become the new Ucayali River configuration in the upcoming years. Figures 5E, F show the Pacaya's planform configuration and, similarly to the Samiria River, it follows the Ucayali's paleochannel as the main alignment and develops smaller meanders. The Samiria, Yanayacu, and Pacaya rivers are underfit-scavenger meanders that are still developing their own size of meanders but most of the time they use the Ucayali's paleochannel configuration. Figures 5G, H show that the Tapiche River has developed small-size meanders but clearly above the Ucayali's paleochannel. This is a good example of how a underfit-scavenger river can modify significantly the paleochannel environment. Similar processes occur with the Sungaro River as shown in Figure 5I.

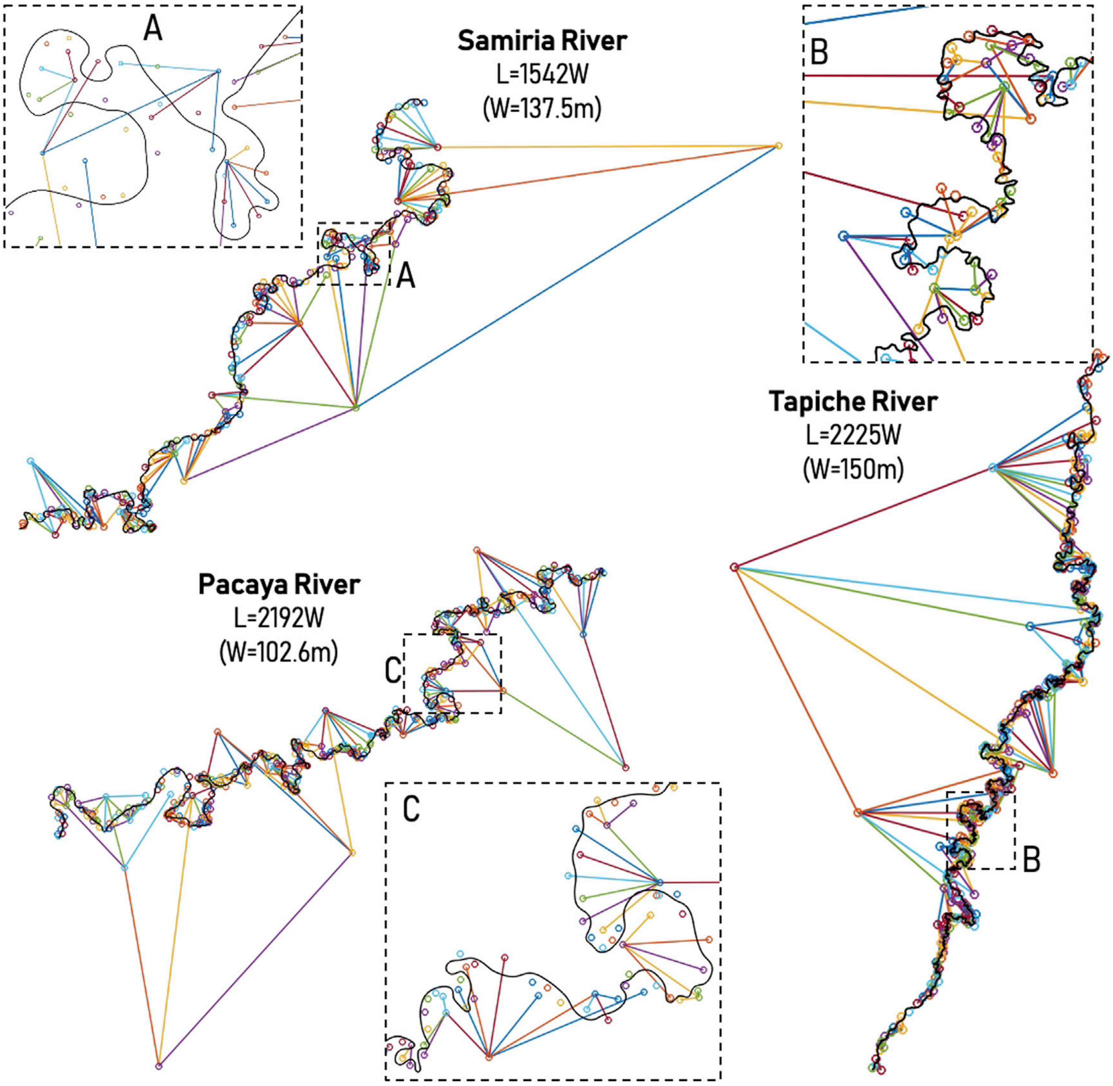

FIGURE 6
Hierarchically ordered in a tree using the methodology by Vermeulen et al. (2016). L is the longitudinal scale, and W is the channel width. **(A–C)** show examples of tree-based scales for the underfit-scavenger rivers Samiria, Tapiche and Pacaya, respectively.

4.3 Morphometrics of free and underfit-scavenger rivers, and paleochannels

The goal is to analyze the planform behavior of the rivers that interact with large-scale paleochannels, thus the planform curvature for the Samiria (L = 1542W), Pacaya (L = 2192W), and Tapiche (L = 2225W) Rivers were extracted. Following Vermeulen et al. (2016)'s methodology, several regions with small-scale meanders are observed in Figure 6, those that are being reworked by the river itself (see Figure 5), that later connect to large-scale meanders, those of the size of the large-scale paleochannels from the ancient dynamics of the Ucayali River. The Samiria and Pacaya Rivers shape some smaller meanders on top of large-scale meanders (paleochannels from the Ucayali River), however for the case of the Tapiche River, the shaping of smaller meanders is more abundant, since the Tapiche River carries out more water and sediments from its own upstream watershed, in contrast to the Samiria and Pacaya Rivers that don´t have a clear watershed, they are interconnected, especially at high flows.

By using the MStaT toolbox (Ruben-Dominguez et al., 2021), for the case of modern rivers, the skewness (see Figure 2) of meandering channels shows that more DS than US oriented bends are found along the Ucayali (59% vs. 15%), Puinahua (66% vs. 23%), Huallaga (46% vs. 29%), Tapiche (61% vs. 21%), Pacaya (56% vs. 24%) and Samiria (59% vs. 19%) Rivers. Along these rivers, a range between 11% and 26% are described as compound or symmetric bends. Besides, the averaged channel width for the modern rivers (using 2021 imagery) are: 602.44 m (Ucayali). 454.10 m (Puinahua), 370.71 m (Huallaga), 150.92 m (Tapiche), 102.57 m (Pacaya), 137.45 m (Samiria).

For the case of ancient rivers, paleochannels are usually reconstructed individually and not necessarily the alignment of the original river (just before the bend was abandoned) is accurate, thus, the assessment of US and DS bends becomes more challenging. Similarly, the averaged channel width and the arc-wavelength of the paleochannels are reduced from the original ones, since water does not flow constantly (temporal connectivity) and some portions are covered by vegetation.

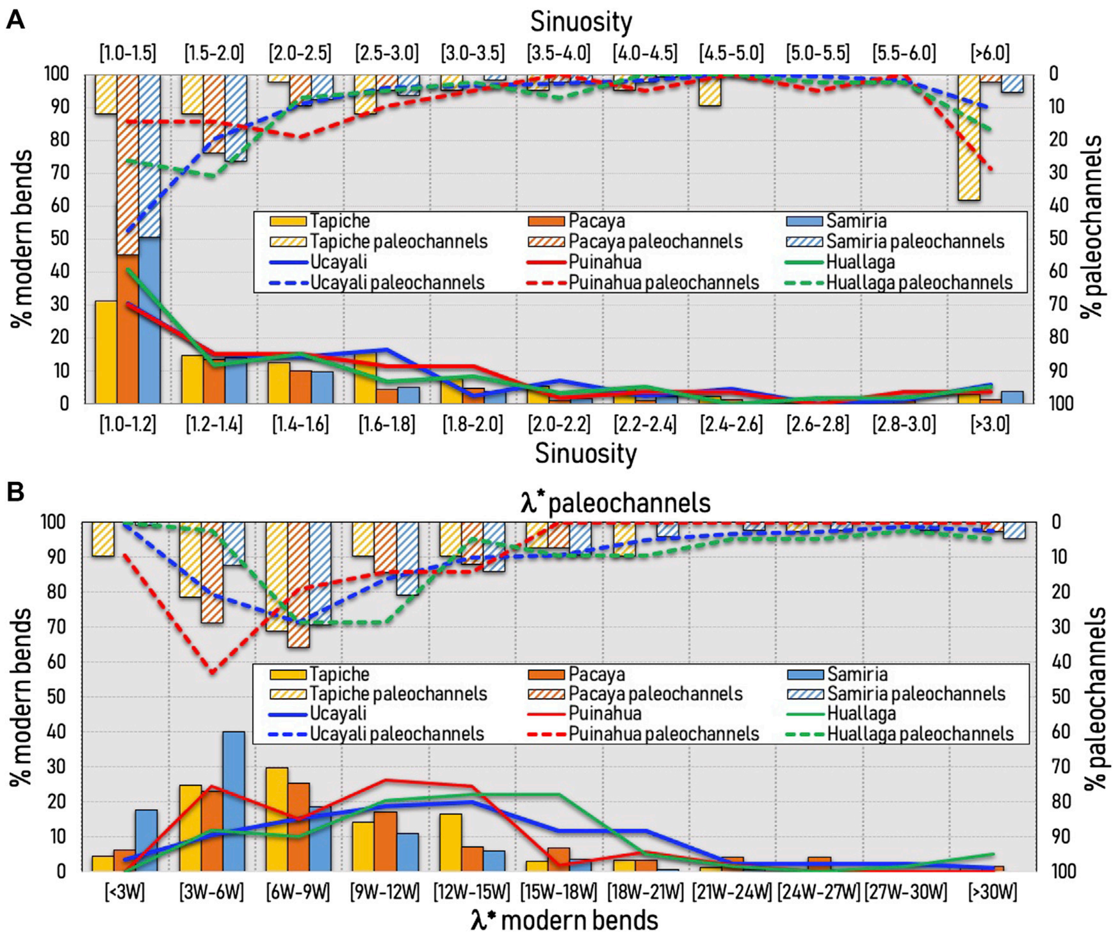

FIGURE 7
(A) Sinuosity and **(B)** arc-wavelength of the rivers in the P-S wetland (modern and paleochannels). The percentage plots are normalized using the total amount of bends for each river. The dimensionless arc-wavelength for the modern bends is obtained using the river width for each river; however, the dimensionless arc-wavelength for the paleochannels is obtained using the Ucayali's width (except for the Huallaga River).

By using the channel centerline of all rivers except the Marañon River (anabranching), the sinuosity and arc-wavelength are described in Figures 7A, B, respectively. The sinuosity for the modern bends (as those in Figure 3) shows that the highest percentage (between 30 and 50%) of bends is between 1.0 and 1.2 (being the $Sinuosity_{[Samiria]}$> $Sinuosity_{[Pacaya]}$ > $Sinuosity_{[Tapiche]}$). Similarly for the Ucayali, Puinahua, and Huallaga, most of the modern bends are between 1.0 and 1.2 sinuosity. Fewer bends reach 2.0 sinuosity and are rarely larger than 3.0. For the case of paleochannel's sinuosity, for the case of the Pacaya and Samiria, more than 50% of the bends are in the range of 1.0–1.2 sinuosity, which does not happen to the Tapiche River. The Ucayali River also has close to 50% of the paleochannels around the 1.0 to 1.2 sinuosity, similar to the ones found near the Pacaya and Samiria Rivers. A decaying behavior of the sinuosity occurs for all rivers, similar to the modern bends; however, when the sinuosity is higher than 6.0 (40% of the paleochannels near the Pacaya River), there is evidence of high-amplitude bends that are preserved after cutoff occurred. A similar trend is also observed for the Ucayali, Puinahua, and Huallaga paleochannels, suggesting that paleochannel signature preserves sinuosities near cutoff events.

Figure 7B shows the normalized arc-wavelength (λ* = λ/W) of all rivers except the Marañon River. The λ* for the majority of modern bends of the Pacaya, Tapiche and Samiria Rivers are 3W–18W, 3W–15W, and 3W–15W, respectively. However, for the modern bends along the Ucayali, Puinahua, and Huallaga Rivers, the λ* are 3W–21W, 3W–18W, and 3W–21W, respectively; showing that the self-meandering rivers tend to have slightly larger meanders. The normalization of the arc-wavelength was performed for all paleochannels within the P-S wetland (except those from the Huallaga River) using the Ucayali's current width since there is evidence that the Ucayali's paleochannels are the main alignment for the development of the planform configuration for the Pacaya, Samiria, Yanayacu, Puinahua, and Tapiche Rivers. The peak of paleochannels for the Pacaya, Samiria and Tapiche rivers has moved towards having larger paleochannels, while for the case of the Ucayali and Huallaga Rivers the peak has moved towards having smaller paleochannels. Notice also that the river signatures shown in Figures 4, 5 does not fully reconstruct the entire paleochannel bend at cutoff (vegetation cover or partial or full loss of connectivity to the main river), thus a tendency for smaller bends was incorporated into the analysis. Moreover, more than 40% of paleochannels along the Puinahua River have λ* between three and six channel widths (similar peak behavior for the modern bends), showing that the Puinahua River developed paleochannels by itself that interact with paleochannels from the Ucayali River.

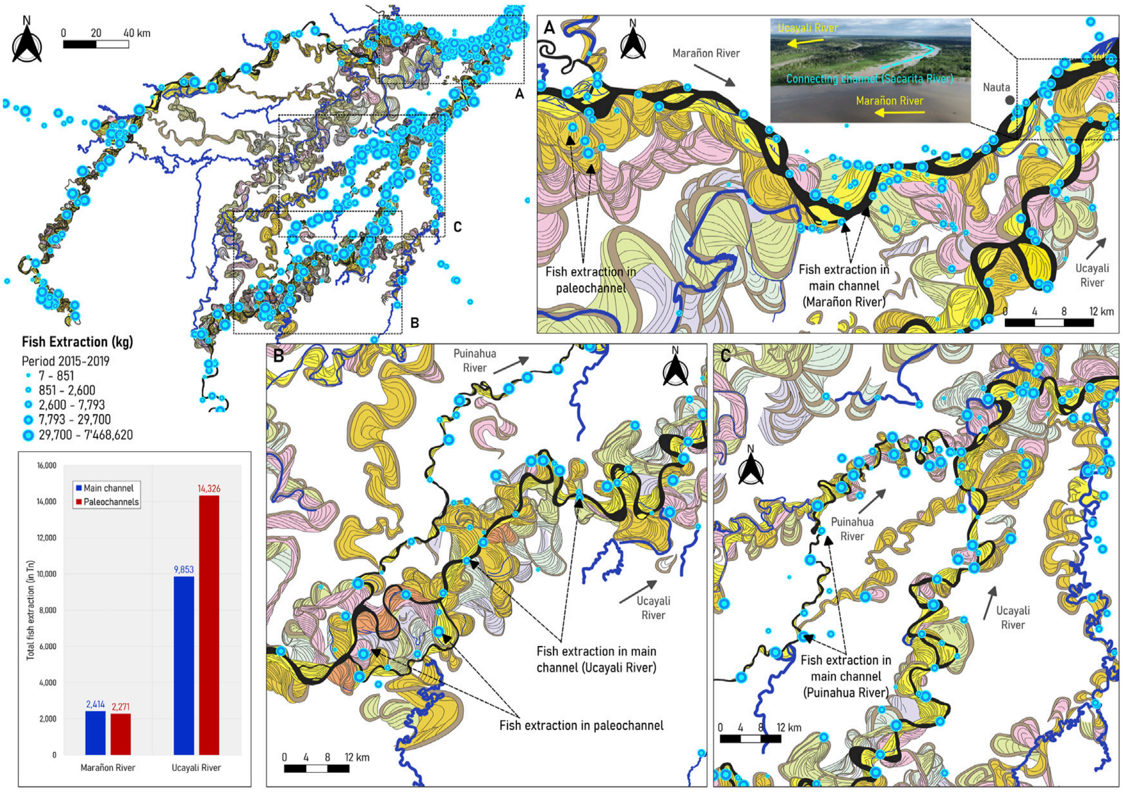

FIGURE 8
Modern and ancient river dynamics and fish production (photo courtesy of Senamhi-Loreto) **(A)** in the P-S wetland (reported by GOREL and WCS), **(B)** near the confluence of the Marañon and Ucayali Rivers, and **(C)** around the confluence of the Puinahua and Tapiche rivers with the Ucayali River. In **(B)**, the picture shows the connecting channel (sacarita), a connecting channel that is well-observed during the peak of the high-flow season (around May 2022). Fisheries data provided by Wildlife Conservation Society, 2022.

4.4 Relationship between modern and ancient river dynamics and fisheries

Figure 8 shows the overlap between the commercial fish extraction between 2015 and 2019 with the modern and ancient river dynamics in the P-S wetland. Notice that the fish extraction dataset corresponds to annual catch (Wildlife Conservation Society, 2022; Wildlife Conservation Society, 2020). Therefore, the following analysis does not provide conclusive evidence of a relationship between hydrology and fish biomass but indirect evidence that river dynamics impacts on fisheries of the PSNR.

As observed in Figure 8A, fishing occurs along the main channel and several paleochannels of the Marañon River, especially in the connecting channels (known as "sacaritas") near Nauta city. These connecting channels become active and more visible during high flows (from March to June). Most of them were left by the Ucayali River dynamics, as indicated by Dumont. (1991). Along the Marañon River, fish extraction was similar in the main channel and paleochannels. On the other hand, in the Ucayali River, there are more zones for commercial fishing than in the Marañon River, located along the main channel (see Figures 8B, C). However, more fish are extracted from paleochannels than from the main channel (14,326 Tn in paleochannels compared to 9,853 Tn along the main channel of the Ucayali River).

Arantes et al. (2019) suggested that fish biomass was strongly associated with forest cover during the low-water season, suggesting that aquatic macrophyte cover plays a key role in maintaining functional richness and dispersion. Along the Marañon and Ucayali Rivers (Figure 9), the most representative and most abundant fish species include the black prochilodus or boquichico (*Prochilodus nigricans*), Pinecone Pleco or carachama (*Pseudorinelepis genibarbis*), llambina (*Potamorhina altamazonica*), tiger fish or fasaco (*Hoplias malabaricus*), among others. In particular, the *Prochilodus nigricans* is an important fishery species in the Andean-Amazon region, a detritus feeder that lives in floodplains and channels during the low-water season to later migrate to tributaries (McClain and Naiman, 2008). The *Pseudorinelepis genibarbis* is an omnivorous armored catfish that live in low-oxygen waters that can be found in floating meadows and oxbow lakes (Virgilio et al., 2020). As shown in Figure 9, fishing zones of *Prochilodus nigricans* include paleochannels within the Marañon and Ucayali floodplains; these areas are composed of palm swamps (Figure 10B) that contain detritus rich in amino acids with a greater nutritional value (Bowen, 1983). By contrast, *Pseudorinelepis genibarbis* is extracted from the riverbanks and ancient channels, corresponding to stagnated water zones.

In the last decade, trends indicated a decline in fish population and richness due to socio-economic and unsustainable practices, such as overharvesting and dams construction (Gerstner et al., 2006; Anderson et al., 2018; Kirkland et al., 2020), leading to the threatening of certain fish species, such as the paiche (*Arapaima gigas*) (Bodmer and Puertas, 2007) and the aruana (*Osteoglossum bicirrhosum*). Since tropical forests support fishery as the main source of protein and income for Indigenous

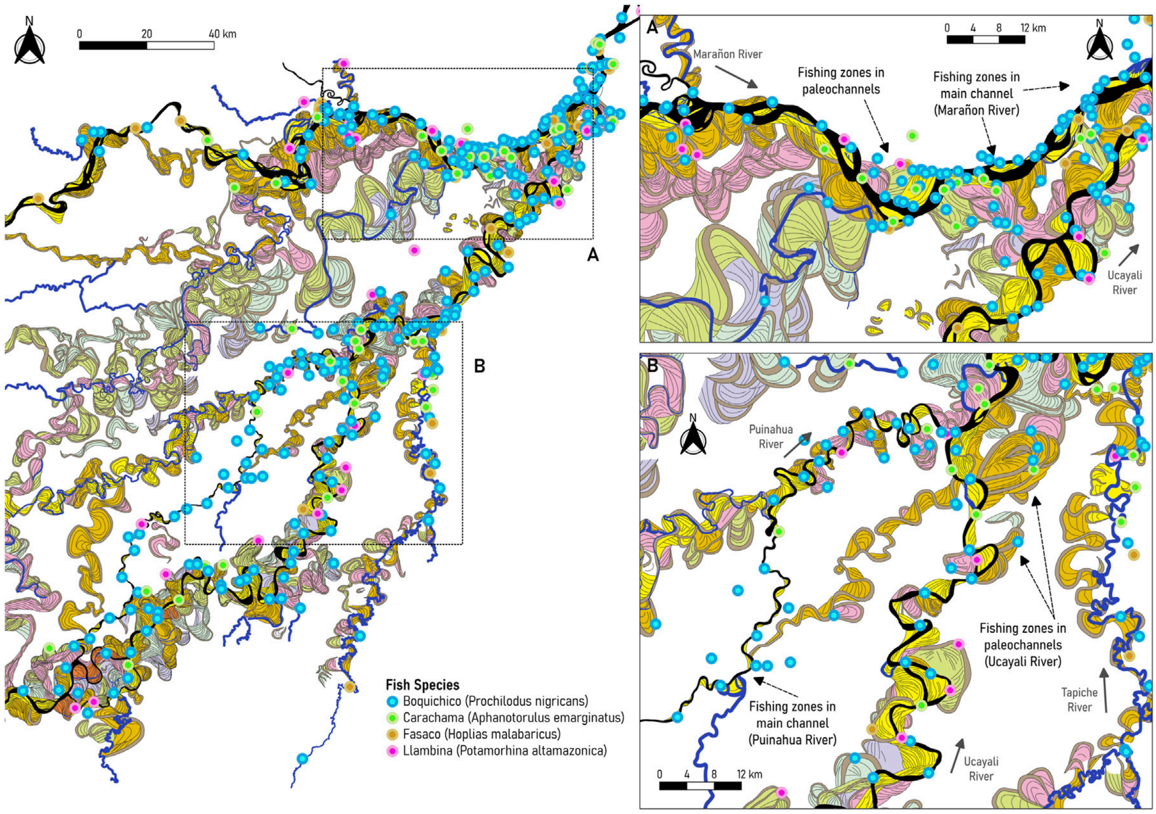

FIGURE 9
Most representative and abundant fish species for local commercial fishing in the PSNR **(A)** along the Marañon River, and **(B)** along the Ucayali and Puinahua rivers. Fisheries data provided by Wildlife Conservation Society, 2022.

communities (East et al., 2005), understanding river and floodplain connectivity is vital to improve the management of fisheries and aquatic life yield. Likewise, quantifying river planform dynamics in terms of flooding, sediment transport, and ecological processes will help understand the origin of species diversity and abundance.

5 Discussion

The Science Panel for the Amazon. (2021) described that the biodiversity of terrestrial and freshwater ecosystems is under the constant pressure from socioeconomic activities, such as deforestation for agricultural development and mining (Volckhausen, 2020), pollution (especially from constant oil spills; Sierra, 2020), climate change and the development of river-related infrastructure (dams, roads, waterways; Gonzales, 2019; Sierra, 2019), affecting indigenous lands and protected areas as well. Human-induced disturbances are generally associated with habitat degradation, loss of species, and, consequently, loss of ecosystem services. For instance, sedimentation (excessive deposition of fine particles) may cause impacts on community composition and species losses, thus affecting energy flow and trophic diversity (Osmundson et al., 2002; Burdon et al., 2013; Burdon et al., 2020). In the Amazon region, little is known about how ecosystem components (e.g., plant-animal interactions, habitat distribution) might respond to these pressures. The lack of adequate management strategies is affecting the management of not only aquatic habitats but also carbon-rich ecosystems and terrestrial biodiversity (Castello et al., 2013).

Previous studies indicates that fisheries productivity in the Amazon is linked to seasonal water level changes which conditions feeding and spawning opportunities (Junk et al., 1989; Isaac et al., 2016). Currently, population declines are driven by habitat fragmentation, overharvesting, barriers to migration, and climate change (Duponchelle et al., 2021). In general, Anderson et al. (2018), Gerstner et al. (2006) and Kirkland et al. (2020) have discussed how pressures (e.g., infrastructure) on rivers can affect aquatic diversity (fish richness and population; Wildlife Conservation Society, 2020). Thus, it is very relevant to incorporate the link between river geomorphology (from water to sediments to erosion/depositional patterns) and biodiversity, not only for baseline studies but for predicting future impacts, thus the science and information can be of support for better decision-making.

A major concern in the Amazon are the impacts produced by the existing dams and the potential impact of tens of planned dams. River disturbance by dams may affect sediment supplies river channel and floodplain dynamics and can decrease or even suppress ecological connectivity among populations of aquatic organisms and organisms that depend on flood seasonality (Finer and Jenkins, 2012; Flecker et al., 2022). Latrubesse et al. (2017) provided an analysis of the potential irreparable consequences for Amazon rivers that can be expected at different scales and sub-basins by more than 400 dam that exist already or

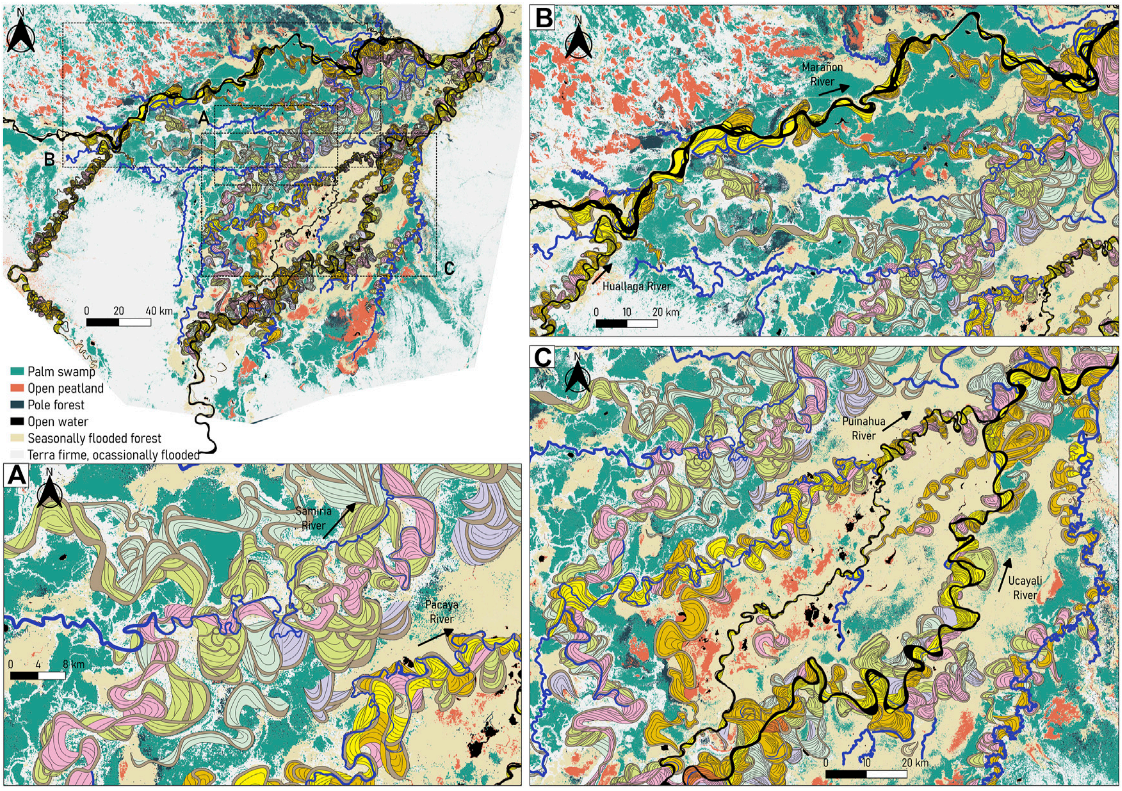

FIGURE 10
Modern and ancient river dynamics superposed to the vegetation cover map developed by Draper et al. (2014). **(A)** Section within the PSNR, showing the vegetation mosaic between the Samiria and Pacaya Rivers. **(B)** Section along the Marañon River surrounded by larger areas of palm swamps. **(C)** Section of the Ucayali River, covered by seasonally flooded forests and several areas of open peatlands. Land cover data provided by Draper et al. (2014).

are under consideration for construction, especially along the upper Marañón river (Flecker et al., 2022). The analysis to vulnerability by dams by using the Dam Environmental Vulnerability Index (DEVI) points that the Marañon and Ucayali are the most vulnerable Andean Rivers. Regarding flow regulation and decrease of sediment load, the Ucayali River, the most active river flowing through the P-S wetland, is the most sensitive Andean River to dam building (Latrubesse et al., 2017). Reductions of these factors by dam construction pose threats to wetland creation and maintenance. As discussed above, the anabranching Marañon River is less dynamic in terms of sediment regime and changing morphology but is critically threatened by a large number of planned and built dams in mountainous reaches of its main channel and it can decrease both the sediment supplies and inundation potential which maintain floodplain and the peripheral wetlands environments of PSNR. Furthermore, if sediment and water is reduced in an anabranching system, a transitional (from anabranching to meandering) condition could be triggered, therefore, promoting significant lateral migration of rivers (similar to the bifurcated channels in Figure 4C). The assessment of the potential impacts on the P-S wetlands by hydrophysical modifications of the Ucayali and Marañon by dams would need a priority. Both the Ucayali and Marañón rivers interact with the P-S wetland in terms of hydrology and geomorphology, proving the wetland with sediment and nutrient fluxes every year (hydrology dominated) and when there are bifurcations or significant planform modifications like the Puinahua River (geomorphology dominated), thus, the lateral connectivity of both systems is important for the sustainability of the biodiversity of the P-S wetland.

Likewise, this study provides indirect evidence that incorporating river dynamics is central to determine the distribution and to characterize the hydrophysical genesis and behavior of river wetlands and related peatland-type ecosystems. Figure 10 shows the overlap between the peat and non-peat-forming vegetation with the modern and ancient river dynamics in the P-S wetland unveiling vegetation patterns, composed of large areas of palm swamps. Palm swamps are nutrient-rich peatlands that resulted from a higher frequency of river avulsions and river dynamism (Draper et al., 2014), allowing oligotrophic conditions (low levels of nutrients) for certain aquatic species to spawn and feed (Lähteenoja and Page, 2011). Moreover, the current and past dynamics of the Ucayali River, evidenced by the complex network of paleochannels, support the development of early-successional vegetation.

As observed in Figure 10A, the recent low dynamism of the Marañon River (ancient and modern conditions) suggested appropriate conditions for pole forest and late-successional vegetation to develop, also allowing peat to accumulate and ombrotrophic condition (i.e., rainfall fed) to remain (Draper et al., 2014). On the other hand, in the bifurcation of the Ucayali River with the Puinahua River there are patches of open peatlands that are prone to frequent fluvial activity due to their high dynamics, as shown in Figures 10A, C. Large and dynamic rivers, such as the Ucayali River, then help maintain higher nutrient inputs to these areas, impeding to ombrotophic conditions and late-successional vegetation to develop (Dumont, 1991; Draper et al., 2014).

6 Conclusion

The hydrologic cycles in the Marañon and Ucayali Rivers are dominated by the precipitation patterns of the eastern Peruvian Mountains. Every year, these two rivers flood during the rainy season depositing nutrient-rich sediment into the flooded forests. Furthermore, the planform complex geomorphology between the Marañon and Ucayali rivers, showing numerous islands, oxbow lakes, and cutoffs within floodplains, has resulted in the creation of underfit-scavenger streams like Pacaya, Samiria and Tapiche rivers. In this research, modern and ancient signatures unveiled high river dynamics and shifting by the Ucayali River, evidencing frequent avulsions and erosional/depositional processes. The resultant environmental mosaic of the P-S wetland is the consequence of a palimpsest of relict geomorphological fluvial features that imprint spatial control to the hydrosedimentological routing and flooding processes in the wetlands. This investigation provides an integrative characterization of how fluvial shifting in the PSNR created suitable conditions and hydro-connectivity process to sustain both nutrient-poor and nutrient-rich environments, allowing different fish assemblages to spawn. The identification and characterization of present and paleo-fluvial landforms are then crucial for fishery management and carbon stock estimations.

During the high flow season, a considerable number of fluvial networks traverse the watershed between the Ucayali and Marañon rivers following ancient fluvial landforms (paleochannels). Annually, the flooded forests in the PSNR are enriched with nutrient-dense sediments generated by erosional processes upstream of the Marañon and Ucayali Rivers, which are later transported downstream and over the lowlands by the floods. Algae growth in the Amazon relies on the phosphorus and nitrogen conducted from the main rivers to the floodplains, and so the magnitude of the flood determines the number of algae produced and thus the number of fish that feed on these algae (Goulding, 1980). Additionally, these floods enable the lateral migration of fish and other aquatic life and the movement of nutrients from these rivers to one another or nearby streams. Therefore, the river dynamics associated with hydrogeomorphological events could favor the fragmentation, isolation, and dispersion of populations through changes in river courses (avulsions and captures phenomena) and disconnection and recapture of oxbow lakes from the main channel. The hydrogeomorphological events would favor allopatric speciation and then, during reconnections or course changes, it would lead to colonization of the sub-basins by neo-species.

Data availability statement

The raw data supporting the conclusion of this article will be made available by the authors, without undue reservation.

Author contributions

Conceptualization, JA; methods and materials, JA, TR, WR, and JS; formal analysis, TR, JA, and WR; data curation, TR, WR, and JS; interpretation and discussion, JA, TR, EL, and JS; writing—original draft preparation, TR and JA; review and editing, TR, JA, EL, and JS; visualization, TR, WR, and JS; supervision, JA; project administration, JA and TR; funding acquisition, JA. All authors have read and agreed to the published version of the manuscript.

Funding

This manuscript was started during JS visit to JA research group (based on visiting grant: National Natural Science Foundation of China, No. 41972098) and finalized based on RED YAKU's seeding funding.

Acknowledgments

The authors thank the staff from the Peru Program of the Wildlife Conservation Society—WCS and Tim Baker (University of Leeds and IIAP) for providing the fisheries and vegetation cover map dataset, respectively. Thanks to the Peruvian institutions (Directorate of Hydrography and Navigation from the Peruvian Navy, the National Service of Natural Areas Protected by the State-SERNANP and the National Meteorology and Hydrology Service of Peru-SENAMHI) for providing insightful discussion related to P-S wetland. UAVSAR data courtesy NASA/JPL-Caltech. The authors also thank the reviewers and editors for their constructive comments on the manuscript.

Conflict of interest

The authors declare that the research was conducted in the absence of any commercial or financial relationships that could be construed as a potential conflict of interest.

Publisher's note

Supplementary material

The Supplementary Material for this article can be found online at: https://www.frontiersin.org/articles/10.3389/fenvs.2023.1082619/full#supplementary-material

References

Abad, J. D., and Garcia, M. H. (2009a). Experiments in a high-amplitude kinoshita meandering channel: 1. Implications of bend orientation on mean and turbulent flow structure. *Water Resour. Res.* 45, 2. doi:10.1029/2008wr007016

Abad, J. D., and Garcia, M. H. (2009b). Experiments in a high-amplitude kinoshita meandering channel: 2. Implications of bend orientation on bed morphodynamics. *Water Resour. Res.* 45, W02402. doi:10.1029/2008wr007017

Abad, J. D., Mendoza, A., Arceo, K., Torres, Z., Valverde, H., Medina, G., et al. (2022a). Planform dynamics and cut-off processes in the lower Ucayali River, Peruvian Amazon. *Water* 14 (19), 3059. doi:10.3390/w14193059

Abad, J. D., Motta, D., Guerrero, L., Paredes, M., Kuroiwa, J., and Garcia, M. H. (2022b). *Hydrogeomorphology of asymmetric meandering channels: Experiments and field evidence*. Water Resources Research.

Abad, J. D., Peralta, B., Paredes, J., Frias, C., Gutierrez, R., and Montoro, H. (2012). *The meandering Ucayali River, a cyclic adaptation of cutoff and planform migration*. San Jose, Costa Rica: River Flow.

Abad, J. D., Vizcarra, J., Paredes, J., Montoro, H., Frias, C., and Holguin, C. (2013). Morphodynamics of the upper peruvian amazonian rivers, implications into fluvial transportation EUT Edizioni Università di Trieste. Avaliable at: http://hdl.handle.net/10077/8822.

Albert, J. S., Carvalho, T. P., Petry, P., Holder, M. A., Maxime, E. L., Espino, J., et al. (2011). Aquatic biodiversity in the Amazon: Habitat specialization and geographic isolation promote species richness. *Animals* 1 (2), 205–241. doi:10.3390/ani1020205

Aldea-Guevara, M. I., Hargrove, J., and Austin, J. D. (2013). Diversity and geneflow in a migratory frugivorous fish: Implications for amazonian habitat connectivity. *Conserv. Genet.* 14 (5), 935–942. doi:10.1007/s10592-012-0442-y

Alsdorf, D. E. (2003). Water storage of the central Amazon floodplain measured with GIS and remote sensing imagery. *Ann. Assoc. Am. Geogr.* 93 (1), 55–66. doi:10.1111/1467-8306.93105

Anderson, E. P., Jenkins, C. N., Heilpern, S., Maldonado-Ocampo, J. A., Carvajal-Vallejos, F. M., Encalada, A. C., et al. (2018). Fragmentation of Andes-to-Amazon connectivity by hydropower dams. *Sci. Adv.* 4 (1), eaao1642. doi:10.1126/sciadv.aao1642

Arantes, C. C., Winemiller, K. O., Asher, A., Castello, L., Hess, L. L., Petrere, M., et al. (2019). Floodplain land cover affects biomass distribution of fish functional diversity in the Amazon River. *Sci. Rep.* 9 (1), 16684–16713. doi:10.1038/s41598-019-52243-0

Bodmer, R. E., and Puertas, P. E. (2007). "Impacts of displacement in the pacaya-samiria national Reserve, Peru," in *Protected areas and human displacement: A conservation perspective (Wildlife C, pp. 29–33)*. Editors E. Redford and K. H. Fearn (New York, USA: Wildlife Conservation Society). Avaliable at: http://indiaenvironmentportal.org.in/files/Protected Areas and human displacement.pdf.

Bowen, S. H. (1983). Detritivory in neotropical fish communities. *Environ. Biol. Fishes* 9 (2), 137–144. doi:10.1007/BF00690858

Burdon, F. J., McIntosh, A. R., and Harding, J. S. (2013). Habitat loss drives threshold response of benthic invertebrate communities to deposited sediment in agricultural streams. *Ecol. Appl.* 23 (5), 1036–1047. doi:10.1890/12-1190.1

Burdon, F. J., McIntosh, A. R., and Harding, J. S. (2020). Mechanisms of trophic niche compression: Evidence from landscape disturbance. *J. Animal Ecol.* 89 (3), 730–744. doi:10.1111/1365-2656.13142

Castello, L., Mcgrath, D. G., Hess, L. L., Coe, M. T., Lefebvre, P. A., Petry, P., et al. (2013). The vulnerability of Amazon freshwater ecosystems. *Conserv. Lett.* 6 (4), 217–229. doi:10.1111/conl.12008

Catano, Y., Abad, J. D., and Garcia, M. H. (2009). Characterization of bedform morphology generated under combined flows and currents using wavelet analysis. *Ocean. Eng.* 36, 617–632. doi:10.1016/j.oceaneng.2009.01.014

CITA (2021). *Guías metodológicas para el Desarrollo de la línea base física de los ríos en Andes-Amazonía. Centro de Investigación y Tecnología del Agua CITA-UTEC*. Lima, Perú: Universidad de Ingeniería y Tecnología.

Couto, T. B., Zuanon, J., Olden, J. D., and Ferraz, G. (2017). Longitudinal variability in lateral hydrologic connectivity shapes fish occurrence in temporary floodplain ponds. *Can. J. Fish. Aquatic Sci.* 75 (2), 319–328. doi:10.1139/cjfas-2016-0388

da Silva-Caminha, S. A. F., D'Apolito, C., Jaramillo, C., Espinosa, B. S., and Rueda, M. (2020). Palynostratigraphy of the ramon and Solimões formations in the acre basin, Brazil. *J. S. Am. Earth Sci.* 103, 102720. doi:10.1016/j.jsames.2020.102720

Draper, F. C., Roucoux, K. H., Lawson, I. T., Mitchard, E. T. A., Honorio Coronado, E. N., Lähteenoja, O., et al. (2014). The distribution and amount of carbon in the largest peatland complex in Amazonia. *Environ. Res. Lett.* 9 (12), 124017. doi:10.1088/1748-9326/9/12/124017

Dumont, J. F. (1991). Fluvial shifting in the Ucamara Depression as related to the neotectonics of the Andean foreland Brazilian craton border (Peru). *Geodynamique* 6 (1), 9–20.

Dumont, J. F., and Garcia, F. (1991). Active subsidence controlled by basement structures in the Marañon Basin of northeastern Peru. *IAHS Fourth Int. Symposium Land Subsidence* 200, 343–350.

Dumont, J. F. (1992). Rasgos morfoestructurales de la llanura amazónica del perú: Efecto de la neotectónica sobre los cambios fluviales y la delimitación de las provincias morfológicas. *Bull. l'Institut Français d'études Andin.* 21 (3), 801–833. doi:10.3406/bifea.1992.1089

Duncan, W. P., and Fernandes, M. N. (2010). Physicochemical characterization of the white, black, and clearwater rivers of the Amazon Basin and its implications on the distribution of freshwater stingrays (Chondrichthyes, Potamotrygonidae). *Pan-American J. Aquatic Sci.* 5 (3), 454–464.

Duponchelle, F., Isaac, V. J., Rodrigues Da Costa Doria, C., Van Damme, P., Herrera-R, G., Anderson, E. P., et al. (2013). Conservation of migratory fishes in the Amazon basin. *Aquatic Conservation: Marine and Freshwater Ecosystems* 31 1087–1105. doi:10.1002/aqc.3550

East, T., Kümpel, N. F., Milner-Gulland, E. J., and Rowcliffe, J. M. (2005). Determinants of urban bushmeat consumption in Río Muni, Equatorial Guinea. *Biol. Conserv.* 126 (2), 206–215. doi:10.1016/j.biocon.2005.05.012

Ferreira, L. V., and Stohlgren, T. J. (1999). Effects of river level fluctuation on plant species richness, diversity, and distribution in a floodplain forest in Central Amazonia. *Oecologia* 120 (4), 582–587. doi:10.1007/s004420050893

Finer, M., and Jenkins, C. N. (2012). Proliferation of hydroelectric dams in the Andean Amazon and implications for Andes-Amazon connectivity. *PLoS One* 7 (4), e35126. doi:10.1371/journal.pone.0035126

Flecker, A. S., Shi, Q., Almeida, R. M., Angarita, H., Gomes-Selman, J. M., García-Villacorta, R., et al. (2022). Reducing adverse impacts of Amazon hydropower expansion. *Science* 375 (6582), 753–760. doi:10.1126/science.abj4017

Frias, C. E., Abad, J. D., Mendoza, A., Paredes, J., Ortals, C., and Montoro, H. (2015). Planform evolution of two anabranching structures in the Upper Peruvian Amazon River. *Water Resour. Res.*, 51 (4), 2742–2759. doi:10.1002/2014WR015836

Garcia, A. P., Marin-Diaz, J., Escobar, C., Ortals, C., and Abad, J. D. (2022). The Peruvian upper Amazon River: A planform morphologic characterization of single and compound anabranching structures. *Under review*.

Gerstner, C. L., Ortega, H., Sanchez, H., and Graham, D. L. (2006). Effects of the freshwater aquarium trade on wild fish populations in differentially-fished areas of the Peruvian Amazon. *J. Fish Biol.* 68 (3), 862–875. doi:10.1111/j.0022-1112.2006.00978.x

Ghinassi, M., Nemec, W., Aldinucci, M., Nehyba, S., Özaksoy, V., and Fidolini, F. (2014). Plan-form evolution of ancient meandering rivers reconstructed from longitudinal outcrop sections. *Sedimentology* 61 (4), 952–977. doi:10.1111/sed.12081

Gonzales, J. (2019). Amazon infrastructure puts 68% of indigenous lands/protected areas at risk: Report. Mongabay: News & inspiration from Nature´s frontline. Avaliable at: https://news.mongabay.com/2019/06/amazon-infrastructure-puts-68-of-indigenous-lands-protected-areas-at-risk-report/.

Goulding, M. (1980). *The fishes and the forest: Explorations in amazonian natural history*. USA: Univ of California Press.

Guerrero, L., Abad, J., Ortals, C., Naito, K., Valverde, H., Estrada, Y., et al. (2022). *The birthplace of the Amazon River, a confluence of anabranching and meandering rivers*. Water Resources Research.

Gutierrez, R. R., Abad, J. D., Choi, M., and Montoro, H. (2014). Characterization of confluences in free meandering rivers of the Amazon basin. *Geomorphology* 220, 1–14. doi:10.1016/j.geomorph.2014.05.011

Gutierrez, R. R., and Abad, J. D. (2014). On the analysis of the medium term planform dynamics of meandering rivers. *Water Resour. Res.* 50, 3714–3733. doi:10.1002/2012WR013358

Hess, L. L., Melack, J. M., Affonso, A. G., Barbosa, C. C. F., Gastil-Buhl, M., and Novo, E. M. L. M. (2015). *LBA-ECO LC-07 wetland extent, vegetation, and inundation: Lowland Amazon Basin*. Oak Ridge, TN: Oak Ridge National Laboratory, Distributed Active Archive Center for Biogeochemical Dynamics.

Hoorn, C., Wesselingh, F. P., ter Steege, H., Bermudez, M. A., Mora, A., Sevink, J., et al. (2010). Amazonia through time: Andean uplift, climate change, landscape evolution, and biodiversity. *Science* 330 (6006), 927–931. doi:10.1126/science.1194585

Isaac, V. J., Castello, L., Santos, P. R. B., and Ruffino, M. L. (2016). Seasonal and interannual dynamics of river-floodplain multispecies fisheries in relation to flood pulses in the Lower Amazon. *Fish. Res.* 183, 352–359. doi:10.1016/j.fishres.2016.06.017

Jarvis, A., Reuter, H. I., Nelson, A., and Guevara, E. (2008). Hole-filled SRTM for the globe version 4, available from the CGIARCSI SRTM 90 m database. Avaliable at: http://srtm.csi.cgiar.org.

Jensen, K., McDonald, K., Podest, E., Rodriguez-Alvarez, N., Horna, V., and Steiner, N. (2018). Assessing L-Band GNSS-reflectometry and imaging radar for detecting sub-canopy inundation dynamics in a tropical wetlands complex. *Remote Sens.* 10 (9), 1431–1529. doi:10.3390/rs10091431

Junk, W. J., Bayley, P. B., and Sparks, R. (1989). The flood pulse concept in river-floodplain systems. *Can. J. Fish. Aquatic Sci.* 106 (1), 110–127.

Kalliola, R., Puhakka, M., and Danjoy, W. (1993a). *Amazonia Peruana: Vegetacion Humeda Tropical en el Llano Subandino*. Finland: Proyecto Amazonia, University of Tunku.

Kalliola, R., Puhakka, M., Salo, J., Linna, A., and Räsänen, M. (1993b). Mineral nutrients in fluvial sediments from the Peruvian Amazon. *Catena* 20 (3), 333–349. doi:10.1016/0341-8162(93)90009-E

Kalliola, R., Salo, J., Puhakka, M., Rajasilta, M., Hame, T., Neller, R. J., et al. (1992). Upper Amazon channel migration: Implications for vegetation perturbance and succession using bitemporal landsat MSS images. *Naturwissenschaften* 79, 75–79. doi:10.1007/BF01131806

Kirkland, M., Eisenberg, C., Bicerra, A., Bodmer, R. E., Mayor, P., and Axmacher, J. C. (2020). Sustainable wildlife extraction and the impacts of socio-economic change among the Kukama-Kukamilla people of the Pacaya-Samiria National Reserve, Peru. *Oryx* 54 (2), 260–269. doi:10.1017/S0030605317001922

Lähteenoja, O., and Page, S. (2011). High diversity of tropical peatland ecosystem types in the Pastaza-Marañón basin, Peruvian Amazonia. *J. Geophys. Res. Biogeosciences* 116 (G2), G02025. doi:10.1029/2010JG001508

Lähteenoja, O., Reátegui, Y. R., Räsänen, M., Torres, D. D. C., Oinonen, M., and Page, S. (2012). The large Amazonian peatland carbon sink in the subsiding Pastaza-Marañón foreland basin, Peru. *Glob. Change Biol.* 18 (1), 164–178. doi:10.1111/j.1365-2486.2011.02504.x

Latrubesse, E. M., Arima, E. Y., Dunne, T., Park, E., Baker, V. R., d'Horta, F. M., et al. (2017). Damming the rivers of the Amazon basin. *Nature* 546 (7658), 363–369. doi:10.1038/nature22333

Latrubesse, E. M., d'Horta, F. M., Ribas, C. C., Wittmann, F., Zuanon, J., Park, E., et al. (2021). Vulnerability of the biota in riverine and seasonally flooded habitats to damming of Amazonian rivers. *Aquatic Conservation Mar. Freshw. Ecosyst.* 31 (5), 1136–1149. doi:10.1002/aqc.3424

Latrubesse, E. M. (2015). Large rivers, megafans and other quaternary avulsive fluvial systems: A potential "who's who" in the geological record. *Earth-Science Rev.* 146, 1–30. doi:10.1016/j.earscirev.2015.03.004

Latrubesse, E. M., and Suizu, T. M. (2022). "The geomorphology of river wetlands," in *Encyclopedia of inland waters*. Editors T. Mehner and K. Tockner (Oxford: Elsevier), pp33–50.

Lin, Z., Shan, J., and Chen, L. (2017). Geomorphology processes of channel planform migration on meandering rivers. *Acta Geol. Sin.* 91, 134–135. doi:10.1111/1755-6724.13223

Marchetti, Z., Latrubesse, E., Pereira, M., and Ramonell, C. (2013). Vegetation and its relationship with geomorphologic units in the Parana River floodplain, Argentina. *J. S. Am. Earth Sci.* 46, 122–136. doi:10.1016/j.jsames.2013.03.010

Marchetti, Z. Y., Villalba, A. B., Ramonell, C., Brumnich, F., and Pereira, M. S. (2020). Biogeomorphic succession in a fluvial-lacustrine delta of the Middle Paraná River (Argentina): Feedbacks between vegetation and morphodynamics. *Sci. Total Environ.* 739, 139799. doi:10.1016/j.scitotenv.2020.139799

Marin-Diaz, J., Flores, G., and Abad, J. D. (2020). *Similarities and differences between meandering and anabranching rivers. AGU Fall Meeting Abstracts*. San Francisco, United States: American Geophysical Union.

McClain, M. E., and Naiman, R. J. (2008). Andean influences on the biogeochemistry and ecology of the Amazon River. *BioScience* 58 (4), 325–338. doi:10.1641/B580408

Mendoza, A., Abad, J. D., Frias, C. E., Ortals, C. J., Paredes, J., Montoro, H., et al. (2016). Planform dynamics of the Iquitos anabranching structure in the Peruvian upper Amazon River. *Earth Surf. Process. Landforms* 41, 961–970. doi:10.1002/esp.3911

Montero, J. C., and Latrubesse, E. M. (2013). The igapo of the negro River in central Amazonia: Linking late-successional inundation forest with fluvial geomorphology. *J. S. Am. Earth Sci.* 46, 137–149. doi:10.1016/j.jsames.2013.05.009

Motta, D., Abad, J. D., Langendoen, E. J., and Garcia, M. H. (2012a). A simplified 2D model for meander migration with physically-based bank evolution. *Geomorphology* 163–164, 10–25. doi:10.1016/j.geomorph.2011.06.036

Motta, D., Abad, J. D., Langendoen, E. J., and Garcia, M. H. (2012b). The effects of floodplain soil heterogeneity on meander planform shape. *Water Resour. Res.* 48 (9), 2011WR011601. doi:10.1029/2011WR011601

Naiman, R. J., Decamps, H., and Pollock, M. (1993). The role of riparian corridors in maintaining regional biodiversity. *Ecol. Appl.* 3 (2), 209–212. doi:10.2307/1941822

Science Panel for the AmazonNobre, C., Encalada, A., Anderson, E., Roca Alcazar, F. H., Bustamante, M., Mena, C., et al. (2021). *Executive summary of the Amazon assessment report 2021*. New York, USA: United Nations Sustainable Development Solutions Network.

Organizacion de Tratado de Cooperacion Amazonica (OTCA) (2009). Perspectivas del Medio Ambiente en la Amazonía. Avaliable at: https://sinia.minam.gob.pe/documentos/geo-amazonia-perspectivas-medio-ambiente-amazonia.

Osmundson, D. B., Ryel, R. J., Lamarra, V. L., and Pitlick, J. (2002). Flow-sediment-biota relations: Implications for river regulation effects on native fish abundance. *Ecol. Appl.* 12 (6), 1719–1739. doi:10.1890/1051-0761(2002)012[1719:FSBRIF]2.0.CO;2

Park, E., and Latrubesse, E. M. (2017). The hydro-geomorphologic complexity of the lower Amazon River floodplain and hydrological connectivity assessed by remote sensing and field control. *Remote Sens. Environ.* 198, 321–332. doi:10.1016/j.rse.2017.06.021

Peixoto, J. M. A., Nelson, B. W., and Wittmann, F. (2009). Spatial and temporal dynamics of river channel migration and vegetation in central Amazonian white-water floodplains by remote-sensing techniques. *Remote Sens. Environ.* 113 (10), 2258–2266. doi:10.1016/j.rse.2009.06.015

Puhakka, M., Kalliola, R., Rajasilta, M., and Salo, J. (1992). River types, site evolution and successional vegetation patterns in Peruvian Amazonia. *J. Biogeogr.* 19 (6), 651–665. doi:10.2307/2845707

Räsänen, M., Neller, R., Salo, J., and Jungner, H. (1992). Recent and ancient fluvial deposition systems in the Amazonian foreland basin, Peru. *Geol. Mag.* 129 (3), 293–306. doi:10.1017/S0016756800019233

Reis, V., Hermoso, V., Hamilton, S. K., Bunn, S. E., Fluet-Chouinard, E., Venables, B., et al. (2019). Characterizing seasonal dynamics of Amazonian wetlands for conservation and decision making. *Aquatic Conservation Mar. Freshw. Ecosyst.* 29 (7), 1073–1082. doi:10.1002/aqc.3051

Rojas, T. V., Bartl, K., and Abad, J. D. (2021). Assessment of the potential responses of ecosystem services to anthropogenic threats in the Eten wetland, Peru. *Ecosyst. Health Sustain.* 7 (1), 1942224. doi:10.1080/20964129.2021.1942224

Ruben-Dominguez, L. D., Naito, K., Gutierrez, R. R., Szupiany, R., and Abad, J. D. (2021). Meander statistics toolbox (MStaT): A toolbox for geometry characterization of bends in large meandering channels. *SoftwareX* 14, 100674. doi:10.1016/j.softx.2021.100674

Salo, J., Kalliola, R., Häkkinen, I., Mäkinen, Y., Niemelä, P., Puhakka, M., et al. (1986). River dynamics and the diversity of Amazon lowland forest. *Nature* 322 (6076), 254–258. doi:10.1038/322254a0

Salonen, M., Toivonen, T., Cohalan, J. M., and Coomes, O. T. (2012). Critical distances: Comparing measures of spatial accessibility in the riverine landscapes of Peruvian Amazonia. *Appl. Geogr.* 32 (2), 501–513. doi:10.1016/j.apgeog.2011.06.017

Shan, J. F., Lin, Z. P., Chen, L., Zhang, B., Fang, S. X., Yan, X., et al. (2018). Reconstruction of meandering paleo-channels using dense well data, Daqing Oil Field, Songliao Basin, China. *Petroleum Sci.* 15 (4), 722–743. doi:10.1007/s12182-018-0270-x

Sierra, Y. (2019). Jorge Abad: "Me preocupa que la Hidrovía amazónica se haga mal". Mongabay: News & inspiration from Nature´s frontline. Avaliable at: https://es.mongabay.com/2019/05/peru-hidrovia-amazonica-jorge-abad/.

Sierra, Y. (2020). More than 470 oil spills in the Peruvian Amazon since 2000: Report. Mongabay: News & inspiration from Nature´s frontline. Avaliable at: https://news.mongabay.com/2020/10/more-than-470-oil-spills-in-the-peruvian-amazon-since-2000-report/.

Stevaux, J. C., Corradini, F. A., and Aquino, S. (2013). Connectivity processes and riparian vegetation of the upper Paraná River, Brazil. *J. S. Am. Earth Sci.* 46, 113–121. doi:10.1016/j.jsames.2011.12.007

Valverde, H., Estrada, Y., Naito, K., Guerrero, L., Canas, C., and Abad, J. D. (2019). *Geomorphological characteristics of the Huallaga River*. Peru: AGU Fall Meeting.

Vermeulen, B., Hoitink, A. J. F., Zolezzi, G., Abad, J. D., and Aalto, R. (2016). Multiscale structure of meanders. *Geophys. Res. Lett.* 43 (7), 3288–3297. doi:10.1002/2016GL068238

Virgilio, L. R., Silva, A. L. C., Saldanha, R. F., Suçuarana, M. da S., Fernandes, E. C., and Vieira, L. J. S. (2020). Fish fauna in oxbow lakes of the middle purus River in the neotropical region of the Amazon rainforest. *Braz. J. Dev.* 6 (8), 55545–55564. doi:10.34117/bjdv6n8-108

Volckhausen, T. (2020). As habitat degradation threatens Amazon species, one region offers hope. Mongabay: News & Inspiration from Nature´s frontline. Avaliable at: https://news.mongabay.com/2020/05/habitat-degradation-threatens-amazon-species-one-region-offers-hope-studies/.

Wildlife Conservation Society (WCS) (2020). Pesquerías en Loreto, amenazas emergentes y presiones prevalentes. Avaliable at: https://global.wcs.org.

Wildlife Conservation Society (WCS) (2022). Atlas de humedales y pesquerías en Loreto. Avaliable at: https://arcg.is/1OaanT.

Wilson, M. D., Bates, P., Alsdorf, D., Forsberg, B., Horritt, M., Melack, J., et al. (2007). Modeling large-scale inundation of Amazonian seasonally flooded wetlands. *Geophys. Res. Lett.* 34 (15), 4–9. doi:10.1029/2007GL030156

Wittman, F., Junk, W. J., and Piedade, M. T. (2006). The várzea forests in Amazonia: Flooding and the highly dynamic geomorphology interact with natural forest succession. *For. Ecol. Manag.* 196 (2-3), 199–212. doi:10.1016/j.foreco.2004.02.060

Wittmann, F., Householder, E., Piedade, M. T., de Assis, R. L., Schöngart, J., Parolin, P., et al. (2013). Habitat specifity, endemism and the neotropical distribution of Amazonian white-water floodplain trees. *Ecography* 36 (6), 690–707. doi:10.1111/j.1600-0587.2012.07723.x

frontiers | Frontiers in Environmental Science

TYPE Original Research
PUBLISHED 24 January 2023
DOI 10.3389/fenvs.2022.1090604

EDITED BY
Omer Yetemen,
Istanbul Technical University, Türkiye

REVIEWED BY
Daoyuan Wang,
Shanghai University, China
Noppol Arunrat,
Mahidol University, Thailand

*CORRESPONDENCE
Tianling Qin,
✉ qintl@iwhr.com

SPECIALTY SECTION
This article was submitted to Drylands, a section of the journal Frontiers in Environmental Science

RECEIVED 05 November 2022
ACCEPTED 29 December 2022
PUBLISHED 24 January 2023

CITATION
Li W, Liu S, Wang Y, Qin T, Zhang X, Li C and Feng J (2023), Experimental study of rock wool on the farmland soil erosion and crop growth of winter wheat and its comprehensive evaluation.
Front. Environ. Sci. 10:1090604.
doi: 10.3389/fenvs.2022.1090604

Experimental study of rock wool on the farmland soil erosion and crop growth of winter wheat and its comprehensive evaluation

Wei Li[1], Shanshan Liu[1], Yicheng Wang[1], Tianling Qin[1]*, Xin Zhang[1], Chenhao Li[1,2] and Jianming Feng[1]

[1]State Key Laboratory of Simulation and Regulation of Water Cycle in River Basin, China Institute of Water Resources and Hydropower Research, Beijing, China, [2]College of Resource Environment and Tourism, Capital Normal University, Beijing, China

Introduction: Droughts and flooding occur frequently due to climate change and human activities, which have significantly affected the ecological environment of farmland and crop production. Rock wool (RW) has some properties like high porosity and water retention capacity, and it is widely used in green roofing and agricultural production to reduce flood and drought disaster.

Methods: We set 24 artificial rainfall experiments to analyze the impact of RW on the farmland runoff, soil water storage capacity (SWSC), nitrogen and phosphorus loss and crop growth. Finally, the Critic-Entropy comprehensive evaluation method was used to select the best solution for RW embedding.

Results: The result shows that RW could reduce the runoff by 49.6%–93.3%, and it made the SWSC increase by .2%–11% Vol in the 10–70 cm depth. During the runoff process, the concentration of nitrogen and phosphorus decreased with the increase of the RW volume, while the nitrogen and phosphorus loss reduced by 51.9%–96.6% and 72.4%–96.4% respectively when RW was buried in the farmland, so RW could effectively promote soil and water conservation. Finally, RW increased the plant biomass and yield by a maximum of 12.1% and 20.4% respectively due to the large retention of water and nutrients. Therefore, combined with the above experimental result, this study indicates that RW could obtain the best comprehensive benefit in the embedding volume of 536.73 m^3/ha.

Discussion: When the volume of RW embedding was too large, RW easily caused insufficient water storage in short-duration rainfall or irrigation, which made the RW unable to release water to alleviate the soil water deficit during the critical growth period, which may result in drought events being aggravated and crop yield reduced. Overall, this study is conducive to clarifying the comprehensive application effect of RW in agricultural production, pollution control, and urban landscape, and it provides an important basis for expanding its application field and promoting the stability of farmland ecosystems.

KEYWORDS

rock wool, runoff, soil water storage capacity, nitrogen and phosphorus loss, crop growth

1 Introduction

Climate change and human activities result in the frequent occurrence of extreme hydrological events such as droughts and floods in farmland (Swain et al., 2018; Arunrat et al., 2021; Meresa et al., 2022), which makes the extreme hydrological events gradually increase in frequency, intensity, timing, and duration, while the extensive use of pesticides and fertilizers has caused serious agricultural non-point source pollution, both of them have seriously damaged the farmland ecological environment and the food production system (Dai et al., 2018; Li et al., 2018). For example, Li concluded that the future precipitation and temperature increase in Thailand under different climate models will lead to some negative effects on crops such as rice, and it also presents the same characteristics of high risk in Northeast, North, Central, and Southwest China (Du et al., 2022; Li J. N. et al., 2022). Therefore, how to alleviate the risk of drought and flood disasters without threatening the environment and natural resources, and promote the stability of farmland ecosystems and sustainable development has become a difficult problem that needs to be solved urgently (Liu et al., 2020).

Rock wool (RW) is composed of natural mineral rocks, which are melted at 1,600°C, centrifuged at a high speed, and sprayed with a special reagent (Lv et al., 2020). After the hydrophilic rock wool was found in 1969, people found RW have properties similar to biochar, including high porosity, and water retention capacity, and Choi studied indicating that rock wool could rapidly absorb and drain water, so RW is widely used in green roofing and agricultural production to reduce flood and drought disaster (Choi and Shin., 2019; Gu et al., 2020). The above-mentioned structural properties of rock wool show better benefits in soil and water conservation. Some studies show that: RW increases soil infiltration by 5.1%–79.2%, improves the wetting front advance rate by 0.5%–4.5%, and reduces runoff by 11.2%–62.5%, which can improve soil water holding capacity and reduce the risk of drought and flooding on farmland (Lv et al., 2020; Lv et al., 2021). Moreover, RW acts as a water storage module in the green roof, and it reduces the risk of urban flooding and the concentration of nitrogen and phosphorus in the runoff due to its stronger adsorption for nitrogen and phosphorus elements, so it has a wide range of applications in pollution prevention and urban landscape (Vijayaraghavan and Raja, 2014; Choi and Shin, 2019). In addition, RW alters water and nutrient cycling processes in farmland, it indirectly changes the composition and structure of soil microbial communities and key processes such as carbon and nutrient conversion, and then enhances the microbial activity and crop root growth in the root environment, thus supporting photosynthesis and crop growth in the upper part of the plant (Li S. P. et al., 2021; Hawrot-Paw et al., 2022). Therefore, RW may play an excellent role in soil and water conservation, soil remediation and agricultural production, etc (He et al., 2019; Yu et al., 2019). However, most of the above studies are simulations of a single element and a single process in a short time, while there is only a little attention has been paid to the comprehensive effect of RW on farmland soil erosion and crop growth (Pu et al., 2019; Cai et al., 2020; Libutti et al., 2021), which needs to be urgently explored and expand its application. To solve the above problem, we assume that rock wool (RW) can improve the soil structure, adjust the distribution of soil moisture, and then change the law of farmland runoff and nutrients migration, and ultimately affect the growth of crops, thereby maintaining the stability of the farmland ecosystem.

TABLE 1 The parameter of RW.

Parameter	Ranges
Porosity	94%–96%
Permeability coefficient	5–8.5 mm/s
Compressive strength	5,000–7,400 kg/m^3
Years of use	>30 years
Density	73–114 kg/m^3

The Huaibei Plain is the largest distribution area of lime concretion black soil in China. The poor soil structure and the high groundwater level cause the soil to be easily saturated and waterlogging, while the ability of capillary water upward is weak, which is very prone to drought (Zhang et al., 2001). Therefore, we explore the effect of RW on soil improvement through artificial rainfall experiments. The main research purposes are: 1) to evaluate the effect of RW embedding on soil moisture, nitrogen and phosphorus loss, and crop growth; 2) to explore the best multi-objective RW deployment scheme.

2 Experiment and method

2.1 Study area

The experiment was conducted at the Wudaogou Experimental Station (117°21′E, 33°09′N) in Anhui Province, which is located in the Huai River Basin. This area experiences the northern subtropical and warm temperate semi-humid monsoon climate zones. The climate is rainy and hot in summer and cold and dry in winter. The local average annual rainfall and temperature are 890 mm and 14°C, respectively, and the average yearly rainfall-runoff depth is 240.2 mm (Li W. et al., 2022). In this area, the average soil bulk density is 1.5 g/cm^3, and the average soil saturated water content, field capacity, and wilting point are about 45%, 34%, and 15%Vol, respectively, and the soil porosity is about 49.7%. The above data show that there is poor soil structure, soil bulk density varies from 1.41 g/cm^3 to 1.53 g/cm^3, and organic matter content from 5 g/kg to 15 g/kg, which easily aggravates the risk of droughts and floods disaster, resulting in crop reduction (Liu et al., 2017; Bi et al., 2020; Lv et al., 2020).

2.2 Rock wool

RW, an advanced product for rainfall regulation and storage, is made of natural mineral rocks as raw material, which is melted at 1,600°C, centrifuged at a high speed, and sprayed with a special reagent (www.hydrorock.com). Because of its stability, high porosity, and strong water retention, RW is widely used in sponge cities and green roofs (Table 1). More specifically, rainfall water will quickly enter the interior of the RW during rainfall due to RW with the strong water absorption capability. After the rain, RW will continuously release water to alleviate the soil water deficit, which is conducive to the consumption of rainwater and surface water (Figure 1.) (Lv et al., 2020; Li J. N. et al., 2022).

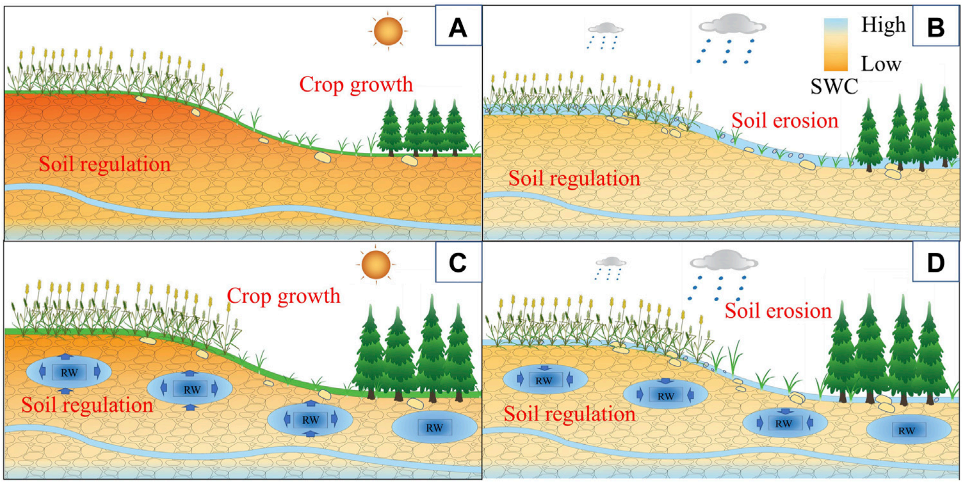

FIGURE 1
RW embedding in the farmland increases soil porosity, which benefits from reducing runoff, thereby improving soil water and nutrient distribution, and ultimately promoting crop production. Pictures **(B, D)** represent RW can absorb the rainwater and reduce the runoff owing to its high porosity. Pictures **(A, C)** represent the soil water will be infiltrated, evaporated, or absorbed by the vegetation, and the water in the RW will be released to the surrounding soil and alleviate the soil moisture deficit, which makes the wheat grow well during a drought.

TABLE 2 Experiment design.

Experimental plot	RW volume (m^3)	Rainfall intensity (mm/h)	Rainfall duration (min)
A1	0	100	90
A2	1.08	100	
A3	2.16	100	
A4	3.24	100	
B1	0	50	180
B2	1.08	50	
B3	2.16	50	
B4	3.24	50	

2.3 Experiment design

2.3.1 Variables

This study set three variables including the rainfall intensity, RW volume, and growth period, with a total of eight experiment plots and 24 rainfall experiments (Table 2) (Li W. et al., 2022). The RW volume was set to increase the soil porosity of the experimental plot by 0%, 5%, 10%, and 15%. The rainfall intensity was set according to the rainfall event records of the typical dry, normal, and wet years of the experimental station, their return periods were 100 and 30 years in the Huaibei plain and all represented a grade of heavy rain (the historical maximum rainfall intensity was 92 mm/h), and the single rainfall amount was set at averagely 150 mm based on the total rainfall during the growth period of winter wheat (Lv et al., 2020).

2.3.2 Experimental plot design

This study includes eight experimental plots in the greenhouse, the size of each plot is 5.3 × 3.8 m with a north-south slope with a slope of 3° (Figure 2). The effective depth of the local soil is 100 mm, so the RW is embedded in a depth of 30–70 cm. The devices in every plot includes artificial rainfall devices (Figure 3A): four conical nozzles are evenly distributed over each experimental plot; Wind dodger Figure 3B: polyethylene curtain is installed in the east-west direction of the experimental plots, which aims to reduce the influence of wind; Water-stop sheep Figure 3C: each experimental cell is isolated by a 1 m deep steel plate to mitigate the horizontal soil moisture exchange within the effective depth; Rain trap Figure 3D: it is mainly used to prevent rainfall splash into the experimental plot; Runoff canal Figure 3E: a baffle with a certain inclination is laid flat at the bottom of the slope to make the runoff flow to the outlet section; Water tank Figure 3F: we set up the exit section of the experimental plot to collect the runoff; Moisture sensor Figure 3G: FDR sensors are buried at 0.2, 0.4, and 0.6 m in the center of each experimental plot respectively, which is to monitor the variation of soil moisture (Lv et al., 2020; Li J. N. et al., 2022).

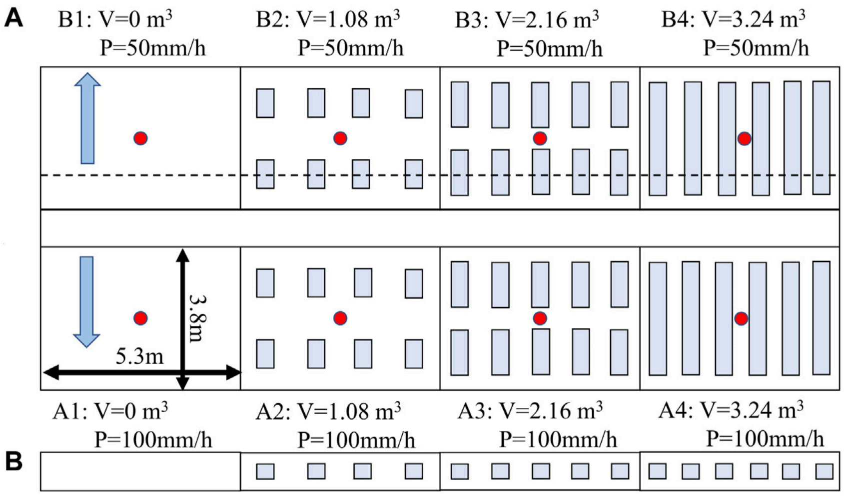

FIGURE 2
Picture **(A)** and **(B)** represent the plane and sectional figure of RW embedding, respectively. Red circles indicate soil moisture sensors in the center of every experiment plot, A1–A4 and B1–B4 represent the number of the experimental groups, V represents the volume of RW embedding in the soil, P represents the rainfall intensity.

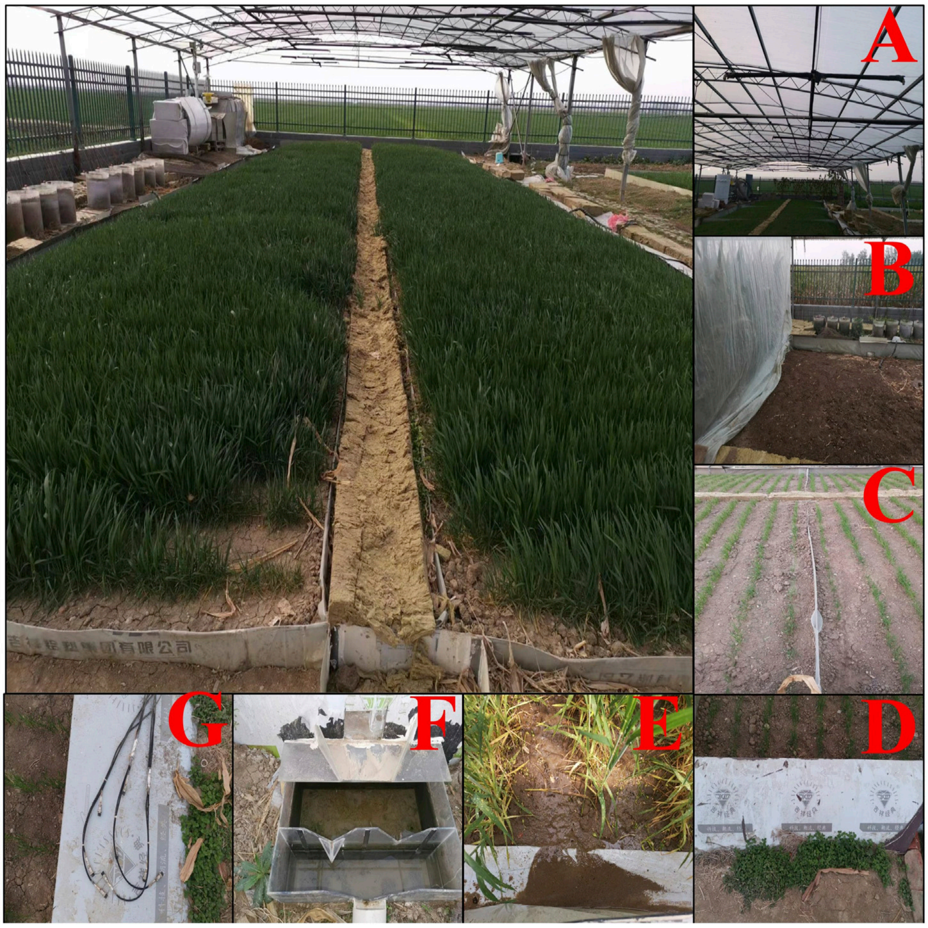

FIGURE 3
The experimental plot and its composition. [Figure **(A–G)** represent the composition of the whole experimental group, it includes artificial rainfall devices **(A)**, wind dodge **(B)**, water-stop sheep **(C)**, rain trap **(D)**, runoff canal **(E)**, water tank **(F)** and moisture sensor **(G)**].

2.3.3 Field management

We reference to local planting experience, winter wheat was sown at 675 kg/ha, sown in rows with a spacing of about 28 cm per row, and winter wheat sown on 1 November 2020. Fertilizer was applied a few days before sowing, with 750 kg/ha of compound fertilizer (24%N, 15%P_2O_5, and 6%K_2O) and 150 kg/ha (46%N) of urea, while fertilizer was chased at 75 kg/ha of urea during the regreening period. In detail, fertilizer was fully mixed with the soil in the tillage layer by manual plowing before crop planting. The soil water was rehydrated before the re-greening period according to the average daily rainfall, and then rainfall experiments were conducted at the heading stage (3.25), flowering stage (4.15), and grain-filling stage (5.10). The winter wheat was harvested on 31 May 2021, and the yield indicators (plant biomass, plant density, grain number per spike, thousand-grain weight, etc.) were measured at the time of harvest.

2.3.4 Data measuring

2.3.4.1 Soil water

We monitored the soil moisture at 8 a.m. and 8 p.m. The artificial rainfall was performed when the surface soil moisture content (0.2 m) reached 23% ± 2% Vol, which can satisfy the need of wheat in the whole growth period based on the local agricultural observations.

2.3.4.2 Runoff process

During the rainfall, the runoff process was recorded according to a fixed time interval (5 min), and the indicators included the stream flow and time. The total runoff is as follows:

$$R = \sum_{i=1}^{n} \frac{(r_i + r_{i+1}) \times T}{2F} \times 10^{-3} \tag{1}$$

Where R represents the total runoff, mm; n represents the total number of periods; r_i represents the value of stream flow at the time i, cm^3/s; T represents the time interval, s; F represents the area value of the experimental plot, m^2.

2.3.4.3 Nitrogen and phosphorus loss

During rainfall, we collected the sample of runoff water at regular intervals (10 or 30 min), which aimed to measure the concentrations of nitrogen and phosphorus. Total nitrogen was determined by the alkaline potassium persulfate digestion method, while total phosphorus and soluble phosphorus were determined by ammonium molybdate spectrophotometry (Wu et al., 2021; Yan et al., 2021; Wang et al., 2022). The total loss of nitrogen and phosphorus is as follows:

$$Q = \sum_{i=1}^{n} \frac{(r_i + r_{i+1}) \times (q_i + q_{i+1})}{4} \times T \times 10^{-3} \tag{2}$$

Where Q represents the total loss of nitrogen and phosphorus elements in a rainfall-runoff process, mg; q_i represents the concentration of nitrogen and phosphorus at the time i, mg/L;

2.3.4.4. Crop growth

We observed the variety of the plant morphological characteristics and divided the growth period of winter wheat. The indicators included plant biomass, number of plants, grains number per spike, and grain weight. Plants from eight rows in each experimental group (.5 m long peer line) were harvested at maturity (early June) for grain yield determination. In this process, the yield components, plant biomass, plant density (PD), grain number per spike (SGN), thousand-grain weight (TGW), were determined by sampling randomly 50 plants from each plot (excluding those in border plants) (Wu et al., 2015; Fan et al., 2015; Zhao et al., 2019). The formula of theoretical yield is as follows:

$$TY = (SGN \times TGW \times PD)/1000 \tag{3}$$

Where TY represents the theoretical yield, kg/m^2; SGN represents grain number peer ear; TGW represents the thousand-grain weight, g; PD represents the plant density, $plant/m^2$.

2.4 Data processing

2.4.1 Date analysis

In this study, data were analyzed by SPSS, Excel, and Origin. The statistical significance was set at $p < .05$ (Zhang et al., 2021). We evaluated the impact of RW on the farmland's ecosystem, the content of which mainly included the difference between the soil runoff process, nitrogen and phosphorus loss, and crop growth in different external environmental conditions. Based on the experiment data, we analyzed RW's mechanism of action. Finally, we selected the best RW embedding plan by the entropy-critic comprehensive evaluation method.

2.4.2 Evaluation method

To reduce human subjective factors and enhance the relative importance of indicators, we used the Critic-Entropy weight method (CEWM) to empower the evaluation index, it could analyze the internal and related relationship between the evaluation indexes, and at the same time, it considered the discrete degree of every evaluation index (Lu et al., 2022). We took the runoff, water storage capacity, the concentration of the TN and TP, the loss of the TN and TP, plant biomass, and yield as the evaluation indicators, which formed the evaluation eigenvalue matrix $X=(x_{ij})$, and calculated the relative membership degree. The formula is as follows (Lu et al., 2022):

$$\text{Positive target:} \quad r_{ij} = \left(x_{ij} - x_{i\,min}\right) / \left(x_{i\,max} - x_{i\,min}\right) \tag{4}$$

$$\text{Negative target:} \quad r_{ij} = \left(x_{i\,max} - x_{ij}\right) / \left(x_{i\,max} - x_{i\,min}\right) \tag{5}$$

Where r_{ij} represents the relative membership degree of the index i in the scheme j; x_i max represents the maximum value of the index i in the scheme; x_i min represents the minimum value of the index i in the scheme; x_{ij} represents the value corresponding to the index i in the scheme j.

2.4.2.1 Entropy weight method

We normalized the matrix of the evaluation index to obtain matrix $R=(r_{ij})$ by applying Eqs 4, 5). The entropy value H_i of the evaluation index i is (Xia et al., 2021):

$$H_i = -k\sum_{j=1}^{m} f_{ij} \ln f_{ij}, i = 1, 2, 3..., n \tag{6}$$

Where $f_{ij} = r_{ij}/\sum r_{ij}$, $k = 1/\ln m$. If $f_{ij} = 0$, and $\ln f_{ij} = 0$.

TABLE 3 Assignment scale.

The relative membership degree	Degree	Score (s_{li})
$0 \le r_{ij} < 0.2$	Very bad	1
$0.2 \le r_{ij} < 0.4$	Bad	2
$0.4 \le r_{ij} < 0.6$	General	3
$0.6 \le r_{ij} < 0.8$	Good	4
$0.8 \le r_{ij} < 1$	Excellent	5

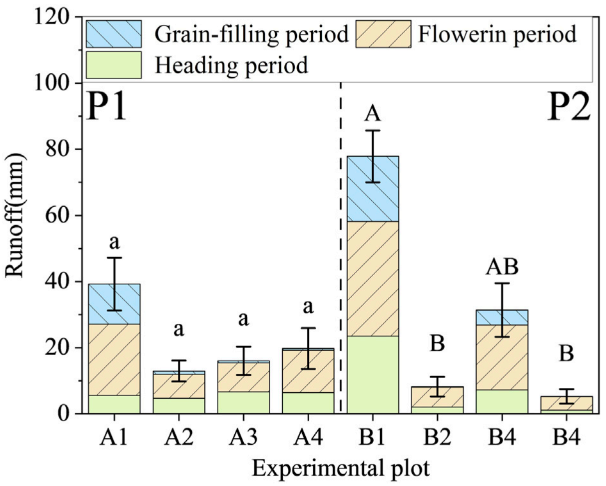

FIGURE 4
Observed runoff in different plots and growth periods under 100 mm/h (left) and 50 mm/h (right) rainfall intensities. P1 represents the experimental plots under 100 mm/h rainfall intensity; P2 represents the experimental plots under 50 mm/h rainfall intensity, a–d and A–D indicate the significant difference between the different groups at 0.05 in 100 and 50 mm/h, respectively.

$$w_{ei} = \frac{1 - H_i}{\sum_{i=1}^{m} (1 - H_i)} \tag{7}$$

Where w_{ei} represents the entropy weight of the evaluation index i; H_i represents the entropy value of the evaluation index i.

2.4.2.2 Critic weighting method

The degree of contrast was measured by the correlation between indicators, while the conflict was measured by the standard deviation within the indicators. The calculation formula is shown (Lu et al., 2022).

$$w_{ci} = \frac{C_i}{\sum_{i=1}^{n} C_i} \tag{8}$$

$$C_i = S_i \times \sum_{j=1}^{p} \left(1 - R_{ij}\right) = S_i \times R_i \tag{9}$$

$$S_i = \sqrt{\frac{\sum_{j=1}^{n} \left(r_{ij} - \overline{r_j}\right)^2}{n - 1}} \tag{10}$$

$$\overline{r_i} = \frac{1}{n} \times \sum_{j=1}^{m} r_{ij} \tag{11}$$

Where w_{ci} represents the objective weight of index i determined by CWM; C_i represents the amount of information contained in indicator I; R_{ij} represents the correlation coefficient between indicators i and j; S_i represents the standard deviation of the relative affiliation of indicator i.

2.4.2.3 Comprehensive weight and evaluation

The formula for calculating the comprehensive weight is shown below:

$$w_i = \frac{w_{ei} \times w_{ci}}{\sum_{i=1}^{m} (w_{ei} \times w_{ci})} \tag{12}$$

Where w_i represents the comprehensive weight, while w_{ei} and w_{ci} represent the objective weight determined by the EWM and CWM, respectively.

The comprehensive effect scores for each experimental group are:

$$Z_l = \sum_{i=1}^{6} w_{li} \times s_{li} \tag{13}$$

Where Z_l represents the total score for the farmland ecology when RW is embedded in the soil, l is the number of experiment groups, and w_{li} and s_{li} are the local weight and score data for the lth experiment groups, and ith. In this process, we classified the relative membership degree of every indicator into five levels and assign the appropriate score, the detail is as follows (Table 3) (Zhu, 2020):

3 Results

3.1 Runoff process

During the growth period of winter wheat, the A2–A4 experimental groups decreased runoff by 67.1%, 59.2%, and 49.6% respectively, compared with the control group (Figure 4). But in the 50 mm/h, the runoff of the B2–B4 experimental groups decreased by 89.4%, 59.7%, and 93.3% respectively. Therefore, the RW embedding can effectively reduce the runoff water, but the runoff water is incompletely decreased with the increase of the volume of RW embedding.

3.2 Soil water storage capacity

RW adjusts the distribution of soil moisture and increases the water storage capacity. In this study, the soil moisture decreased rapidly within 0–6 h after the rain, and the maximum reduction in the control group could reach 6.4% Vol (Figure 5). In addition, when the RW was embedded in the soil, the soil water storage capacity of the A2–A4 and B2–B4 groups decreased by 2.5%–6.3% Vol and 0.3%–2.6% Vol in 10–30 cm, compared with the control group, respectively. But in the depth of 30–50 and 30–50 cm, the water storage capacity of RW groups increased by 1.6%–16.3% Vol and −0.7%–17% Vol. To sum up, RW embedding made the water-storage capacity higher than the control groups by 0.2%–11% Vol in the depth of 10–70 cm (except

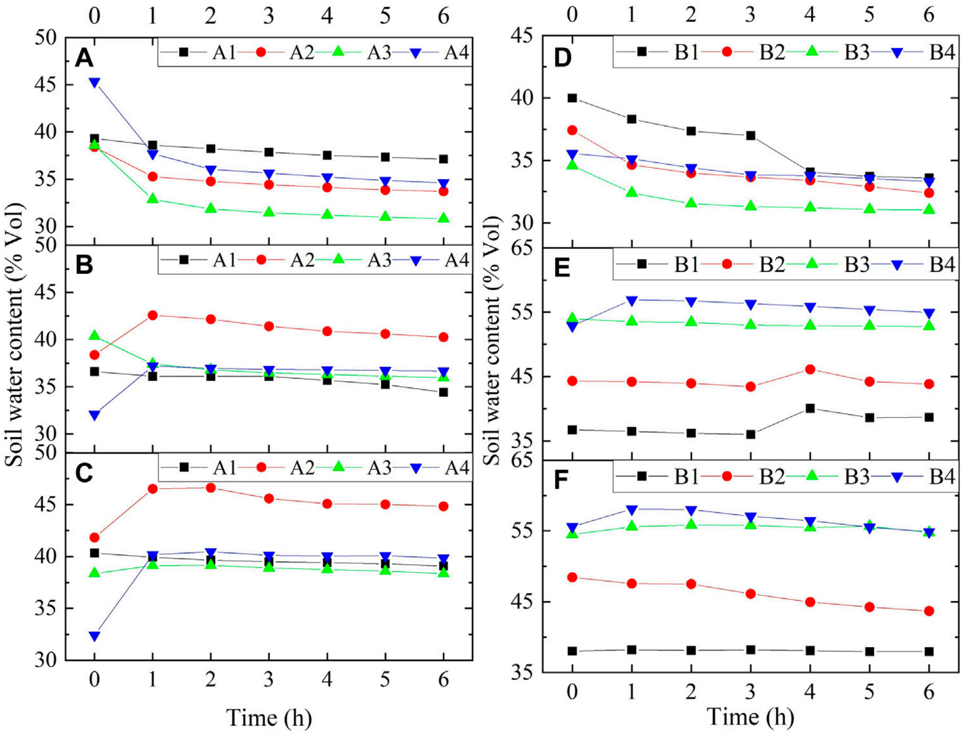

FIGURE 5
Redistributions of soil water content in experimental plots at 10–70 cm depth from 1 to 6 h after rainfall ended [**(A–C)** indict the SWC in the 10–30, 30–50, and 50–70 cm soil under 100 mm/h rainfall intensity, respectively, while **(D–F)** indict the SWC under 50 mm/h rainfall intensity].

for the A3 group reduced by 1.8%Vol). Therefore, RW embedding can effectively improve the water storage capacity.

3.3 Nitrogen and phosphorus loss

RW could reduce the nitrogen and phosphorus concentration of runoff water. In general, under the 100 mm/h rainfall event, RW embedding decreased the average concentrations of TN, TP, and DTP by 7.1%–18.1%, 32.9%–45.2%, and 3.1%–55.1%, respectively. While under the 50 mm/h rainfall event, the average concentration of RW groups reduced by 35.2%–56%, 14.5%–35.5%, and 34.4%–46.7%, similarly (Figure 6). The average concentration of nitrogen and phosphorus in the runoff water was negatively correlated with the volume of RW ($R^2 > .81$).

RW embedding effectively reduced the total loss of nitrogen and phosphorus. In general, under 100 mm/h, the RW embedding reduced the total loss of TN, TP, and DTP by 51.9%–70.3%, 72.4%–77.9%, and 68.1%–77.4%, compared with the control groups, respectively. The total loss of TN and TP in different experimental groups was A1>A4>A3>A2. Non-etheless, RW embedding made the total loss of TN, TP, and DTP decrease by 92.3%–96.6%, 73.6%–96.4%, and 73.6%–96.4% in the 50 mm/h, respectively. The loss of TN and TP was incompletely decreased with the RW volume increase. In addition, RW embedding had a higher reduction ratio of nitrogen and phosphorus loss under long-duration rainfall.

3.4 Crop growth

3.4.1 Plant biomass

RW promotes the accumulation of plant biomass. The biomass of winter wheat in the mature period was 3.21–3.51 g/plant (Figure 7), and RW made the biomass per plant of winter wheat higher than the control groups by 1.6%–7.7%. On the whole, the biomass of the RW groups increased by 0.3%–12.1%, compared with the control groups. Therefore, the biomass of winter wheat increased first and then decreased with the increase of RW embedding volume. To sum up, RW embedding can effectively prompt dry matter accumulation.

3.4.2 Yield components

3.4.2.1 Plant density

RW embedding prompts the proliferation and tiller of winter wheat. In the jointing period, the plant density (PD) of winter wheat increased with the increase of the RW embedding volume (R^2 = .43 and 0.97, Figure 8). The number of tillers in RW experimental groups increased by 0.5%–15.3%, compared with the control group. Therefore, RW embedding was conducive to the proliferation and tillering of winter wheat.

In the mature period, the PD increased first and then decreased with the increase of the RW embedding volume. The PD of the A2–A4 and B2–B4 groups increased by (3.8%, −3.2%, −4.1%) and (4.5%, 4.1%, and 0.6%), respectively. This was that PD increased first and then decreased with the increase of RW embedding volume ($p > 0.05$). To sum up, RW embedding can increase PD,

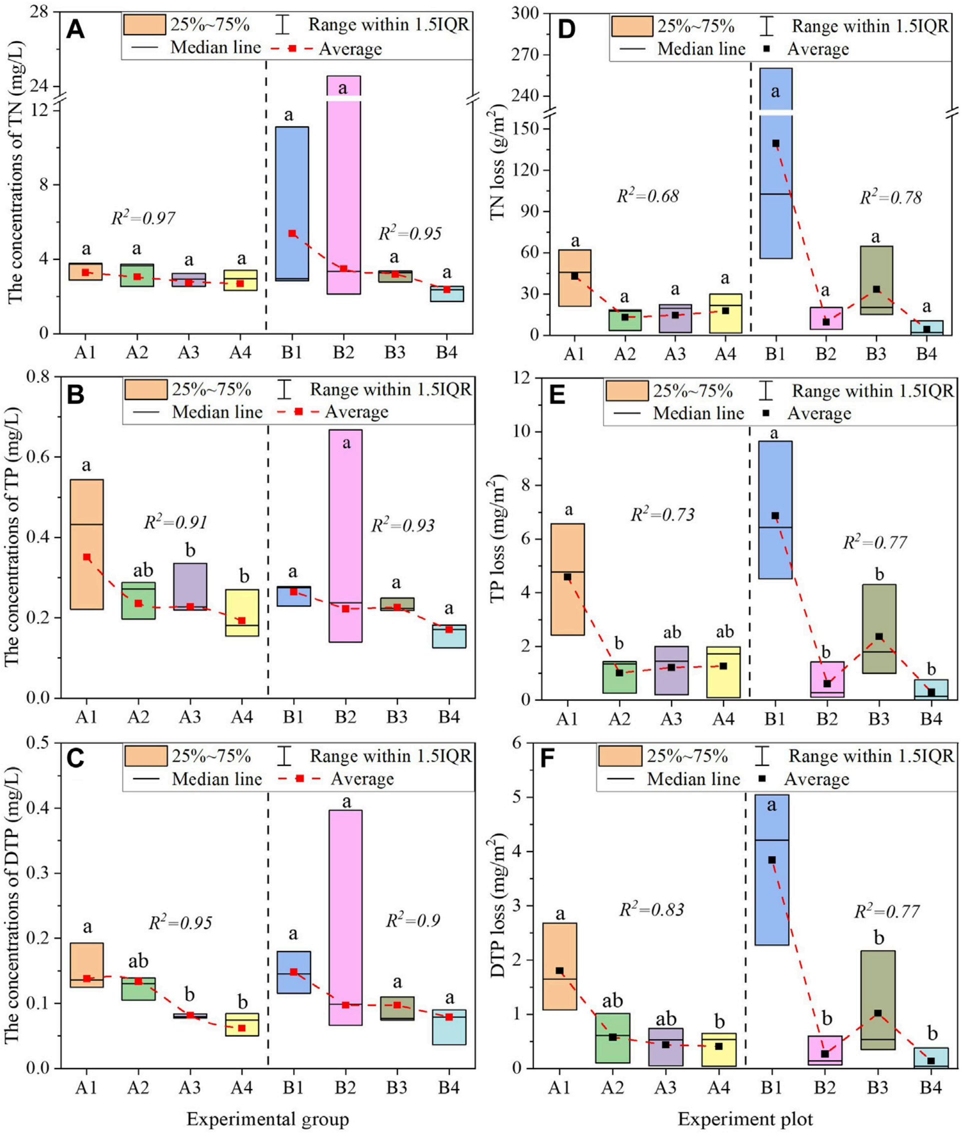

FIGURE 6
Nitrogen and phosphorus loss [**(A–C)** represent the average concentrations of TN, TP, and DTP during the rainfall in the growth period of winter wheat, respectively. While **(D–F)** represent the loss of TN, TP, and DTP, respectively. a–d indicates the significant difference between the different groups at 0.05.

but it may cause negative effects in high-intensity and short-duration irrigation events.

3.4.2.2 Grain number

RW increases the spike grain number (SGN) of winter wheat. In the mature period, the SGN of the A2-A4 and B2–B4 groups increased by (7.1%, −0.4%, 3.5%) and (5.4%, 5.8%, 9.2%), compared with the control group, respectively (Figure 9). The overall trend was increasing, and the SGN had a positive correlation with the volume of RW embedding (R^2 = .9) in the long-duration irrigation events (It only had a significant difference between the B1 and B4 group, $p < .05$).

3.4.2.3 Thousand-grain weight

The irrigation deeply affects the thousand-grain weight (TGW) of the winter wheat in the grain-filling period. In the 100 mm/h irrigation event, the TGW of the A2 and A4 groups decreased by 1.6% and 6%, compared with the A1 control groups, respectively, but the A3 group increased by 1.8% in turn (Figure 9). RW may inhabit the grain filling under short-duration irrigation. On the contrary, in the 50 mm/h irrigation event, RW embedding prompted the growth of winter wheat grain biomass. The TGW of B2 - B4 groups increased by 2.2%–9.6%, compared with the B1 group, and the TGW had a positive correlation with the different volumes of RW embedding (R^2 = .93). Overall, RW has a better appliance for grain filling in low rainfall intensity and long-duration irrigation events.

3.4.2.4 Theoretical yield

There is an interaction between RW embedding volume and irrigation method, which jointly affects the yield of winter wheat. In short-duration irrigation, the theoretical yield (TY)of winter wheat

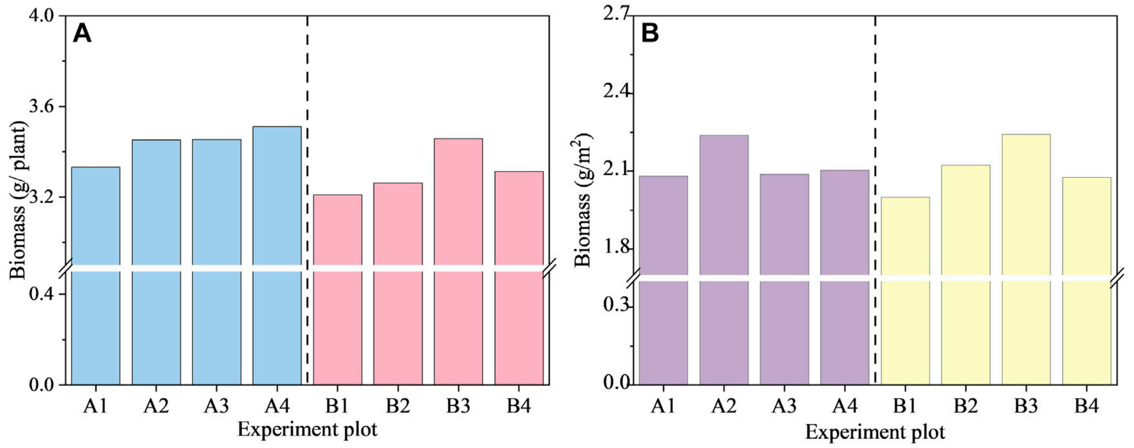

FIGURE 7
Variation of plant biomass [**(A)** represents the biomass in a plant, and **(B)** represents the biomass in the unit area].

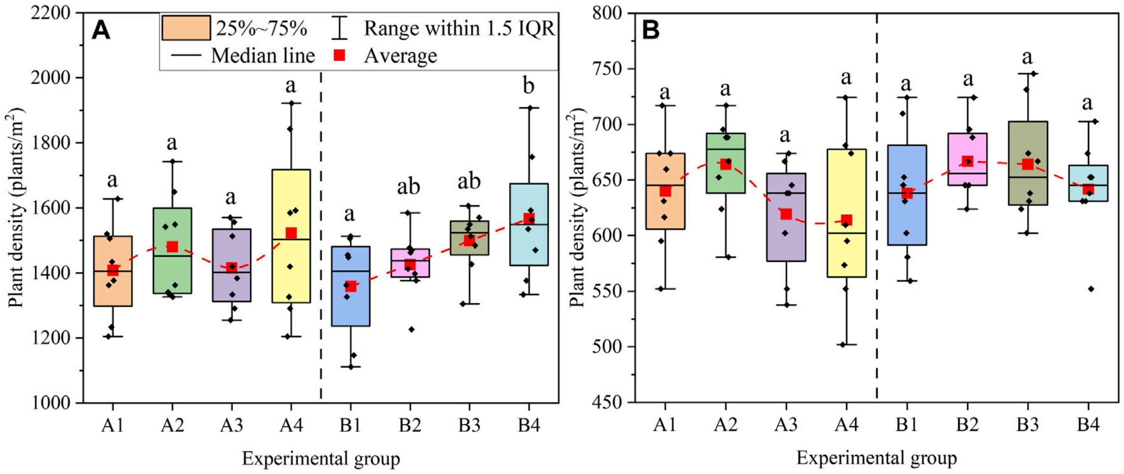

FIGURE 8
Plant density [**(A, B)** represent the jointing periods and mature periods, respectively, and a and b indicate the significant difference between different RW volumes].

increased first and then decreased with the increase of RW volume. The change rate of TY at the A2–A4 experimental plot was 9.4%, −1.9%, and −6.7%, compared with the control group, respectively (Figure 10). It would hold back the growth of yield when the RW is buried in the soil excessively. On the contrary, it had a positive correlation between the volume of RW embedding and TY in long-duration irrigation events ($R^2 = .89$), and the variation ranged from 12.7% to 20.4%. Therefore, when the RW was buried in the soil excessively, it was easy to make the yield increase or decrease in a large range by the influence of irrigation way.

3.5 Comprehensive evaluation

According to the experiment on the impact of RW on farmland ecology, the comprehensive weight was (0.147.0.393.0.211.0.081.0.081.0.086). The results showed that the weights of the indicators are: biomass > SWSC > yield > TP loss ≈ TN loss ≈ runoff, so the biomass was most drastically affected by the volume of RW embedding, while yield, nitrogen, and phosphorus loss were relatively less affected. In addition, Comparing the CWM, EWM, and CEWM, the evaluation and rank results had some difference in the A1, A2, A3, and B4 experiment groups, the results of which changed all within ±10.7%, compared with the mean value, while other experiment groups varied with ±4.2%. The comprehensive evaluation ranking is: B3>A2>B2>B4>A4>A1>A3>B1 (Table 4), so the comprehensive benefits are influenced by the rainfall intensity or rainfall duration, while the appropriate amount of RW embedding could help promote the stability of farmland ecosystems. Moreover, under natural conditions, high rainfall intensity and short-duration rainfall events can cause weaker impacts on farmland ecosystems than long-duration rainfall events. Finally, we considered the comprehensive application effect in two rainfall events, and RW could obtain the best comprehensive benefit in the embedding volume of the A2 and B2 groups (536.73 m^3/ha).

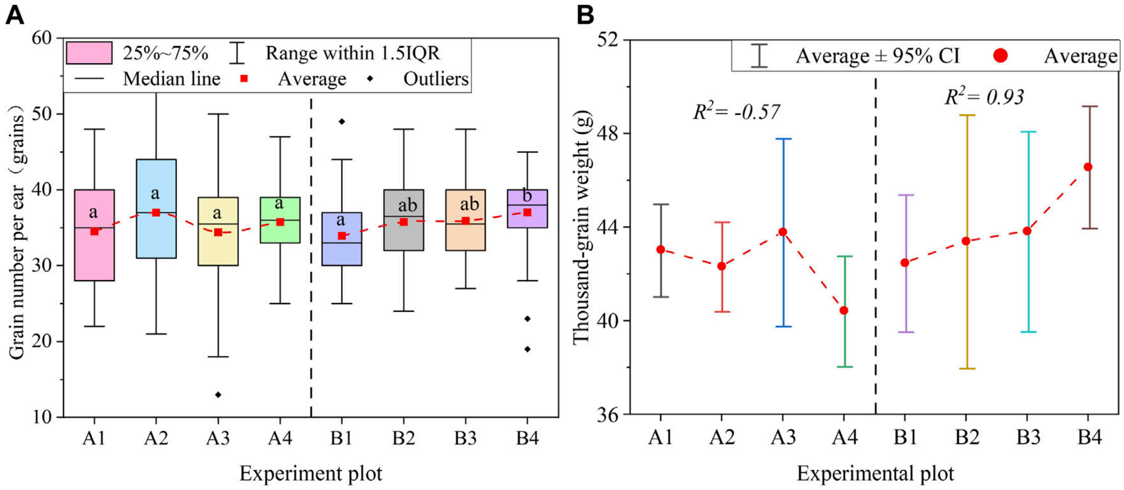

FIGURE 9
Grain number and thousand-grain weight in different experiment groups [**(A, B)** indicate the significant difference between different RW volumes, $p < .05$].

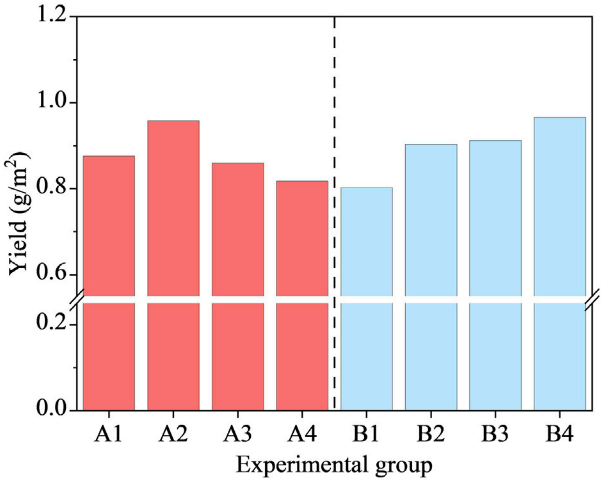

FIGURE 10
Theoretical yield.

4 Discussion

4.1 Effect of RW embedding on the TN and TP loss

RW embedding can increase infiltration and decrease surface runoff (Lv et al., 2020), because the RW improves the soil structure, and increases the specific surface area and soil porosity (Sandoval et al., 2017). At the same time, the huge pore can provide sufficient space for water storage, which easily changes the movement path of the soil water and absorbs a large amount of free water (Libutti et al., 2021). So, RW embedding is beneficial for the local consumption of rainfall water or surface ponding. When the soil moisture gradually decreased to an unsaturated state after rainfall, the RW continuously exuded water to alleviate the soil moisture deficit (Lv et al., 2020; Li W. et al., 2022).

RW can effectively reduce nitrogen and phosphorus loss. Soil erosion often occurs on the surface of the soil, due to the limitation of RW embedding depth, RW cannot directly affect the runoff water quality, and it may indirectly affect the nitrogen and phosphorus content in the topsoil by increasing infiltration (Wang et al., 2020). However, the concentrations

TABLE 4 Comprehensive evaluation and rank.

Experimental plot	Entropy weight method (EWM)	Critic weight method (CWM)	Critic-Entropy weight method (CEWM)
A1	2.48 (7)	2.38 (7)	2.12 (6)
A2	3.48 (4)	4.23 (2)	3.95 (2)
A3	2.63 (6)	2.55 (6)	2.07 (7)
A4	2.97 (5)	2.94 (5)	2.64 (5)
B1	1 (8)	1 (8)	1 (8)
B2	3.48 (3)	3.45 (3)	3.13 (3)
B3	4.5 (1)	4.67 (1)	4.73 (1)
B4	3.53 (2)	2.99 (4)	3.05 (4)

Note: numbers in the bracket represent the rank of comprehensive benefit.

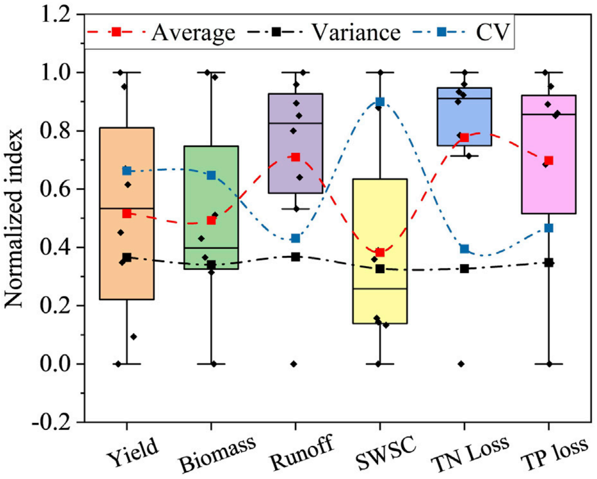

FIGURE 11
The distribution of the normalized index.

of TN and TP in the RW groups may be lower than in the control groups, because the concentrations of TN and TP in the runoff water often reach their peaks within a short period after the runoff starts (Li J. N. et al., 2022). As the runoff continues, the dilution effect plays an increasingly important role in the runoff process, which results in nitrogen and phosphorus elements infiltrating the soil profile with the movement of water, and the concentrations of TN and TP decrease continuously with the delay of the rainfall duration (Li et al., 2017; Yan et al., 2021). Thus RW delayed the runoff process and may have increased the nitrogen and phosphorus concentration.

RW reduces nitrogen and phosphorus concentration, but the difference of which in RW groups was within ±8%. The above phenomenon may be related to the form of nitrogen and phosphorus. The previous study showed that phosphorus is in a mostly granular state in the runoff, while nitrogen was mostly lost by NO_3^-(Zhou et al., 2021). Some scholars think raindrops with high kinetic energy directly hit the surface and transfer some of the kinetic energy to the soil and cause a splash effect, and soil particles are lost with surface runoff after runoff is formed (Ao et al., 2019), which makes it easier for the phosphorus in the topsoil to lose, while the loss of nitrogen is not sensitive to rainfall intensity, and there is no significant difference in TN concentration under different rainfall intensity (de Almeida et al., 2021; Li X. N. et al., 2021). When the runoff process continues, a large amount of nitrogen begins to dissolve, and the nitrogen content in the runoff water increases within a certain period (Yan et al., 2021). Therefore, the TN concentration under long-duration rainfall may be greater than under short-duration rainfall. When the runoff continues, the dilution effect makes the TN concentration continue to decline, that is, the phosphorus loss is more sensitive to the rainfall intensity, while the nitrogen element is more affected by the rainfall duration (Yan et al., 2021).

4.2 Effect of the RW embedding on the crop growth

RW embedding promotes early crop proliferation and tillering. In the jointing period, the number of tillers in RW experimental groups increased by 0.5%–15.3%. It has a positive correlation between the RW embedding volume and the number of tillers (R^2 = .43 and .99), because the RW improves soil water storage capacity and promotes crop root water absorption (Choi and Shin, 2019; Gu et al., 2021). However, the water absorption capacity of hydrophilic RW increased with irrigation time (Choi and Shin, 2019). When extreme rainfall events occur frequently, RW can fully play its advantages of rapid water absorption and drainage, which can effectively reduce soil erosion and nutrient loss, and promote root material absorption and photosynthesis (Lee et al., 2015). In addition, on account of the rainfall duration and the applicability of RW, RW cannot fully absorb sufficient water in short-duration and high-rainfall irrigation events, which may result in insufficient water released in drought seasons to alleviate soil water deficit (VanWoert et al., 2005; Yu et al., 2018). For example, the grain-filling period is the key water-requiring period for crop growth, and the TGW and PD have a certain downward trend due to the applicability of RW, which may cause crop failure in the A3 and A4 groups (Chen et al., 2021). To sum up, RW can promote water drainage, water, and nutrient retention, which is beneficial to crop photosynthesis and biomass accumulation. However, when the volume of RW embedding is too large, likely, the properties of rock wool cannot be fully utilized in short-duration rainfall events. The result of the above phenomenon easily exacerbates the risk of farmland drought and crop failure, which seriously destabilizes the farmland ecosystem.

4.3 Comprehensive evaluation

Different evaluation methods result in different indicator weights (Liu et al., 2021). RW significantly reduces runoff and nitrogen and phosphorus loss, the variation of which is above 50%, so the above indexes relatively present the characteristics of high mean value and small variance (Figure 11). Some objective weighting methods consider that the above indexes contain less information or more repeated information, so the weighting is significantly lower than that of other indicators (Lu et al., 2022). Nevertheless, the different response degrees of RW embedding for different indicators, makes the distribution of normalized index significantly different, and it represents some characteristics like low mean value and high variance.

Different indicator weights make the evaluation results various. The evaluation results in EWM objectively reflect the comprehensive benefits to some extent, but there is little change in the evaluation result of the A2 and B4 groups when we used the CWM and EWM respectively, because the effect of RW on the biomass and SWSC made the evaluation results significantly different, and the weights of the above two indicators increase. The objective method mostly relies on the laws of the data to respond to the amount of information, and the CEWM considers the contrast intensity, dispersion degree, and conflict, which is more reasonable than the other evaluation systems (Lu et al., 2022). In this study, the evaluation results are the same basically when using singularly the EWM and CWM, while the SWSC and biomass have the higher weighting so the importance of both in the CEWM is significantly increased, which causes the weighting of the TN and TP loss to have a certain decrease, and resulting in some changes in the evaluation results when RW has the excellent effect in this index, such as the A1, A2, A3, and B4 groups. The response of each index to RW is influenced by various external conditions, which may make the RW embedding different in other application scenarios.

When RW with appropriate volume is buried in the winter wheat farmland, it can obtain the highest comprehensive benefits like soil and water conservation and farmland production in different conditions, but we must know the expense of RW restricted its application on a large scale at present, and the average price of a RW ranges from ¥1,000 to ¥2,000 m^{-3}, so we can use it in intensive agriculture or economic crop planting. In addition, we must realize that RW cannot create water or reduce the soil water consumption of farmland, and it only plays a role in enhancing soil water storage capacity to delay drought events (Li W. et al., 2022). To sum up, we should consider the application of RW in long periods and multiple environments like agricultural production, flower cultivation, and urban greening, and the effectiveness and feasibility of RW in complex environments should be investigated through models or field studies, which aim to expand the production of RW and achieve comprehensive applications under multiple scenarios and objectives.

5 Conclusion

RW embedding affects farmland soil structure, which influences the farmland runoff process, nitrogen and phosphorus loss, and crop growth in turn. Based on the above assumption, we took winter wheat as the experimental object to explore the impact of RW on the farmland's ecological environment. The results show that RW could reduce runoff and enhance the soil water storage capacity, which effectively alleviates the risk of drought and flood disasters in farmland. When extreme rainfall occurs, RW reduces the total amount of nitrogen and phosphorus losses by 51.9%–70.3% and 72.4%–77.9%, by reducing runoff, the TN, and TP concentration. The above effects generally increase with the increase of RW volume. Finally, plant biomass and yield increase by a maximum of 12.1% and 20.4%, respectively. To sum up, based on the Entropy-Critic comprehensive evaluation method, it is concluded that RW could obtain the highest comprehensive benefit under the embedding volume of 536.73 m^3/ha. Overall, this study is conducive to clarifying the comprehensive application effect of RW in agricultural production, pollution control, and urban landscape. It provides an important basis for expanding its application field and promoting the stability of farmland ecosystems.

Data availability statement

The datasets presented in this article are not readily available because this is confidential data. Requests to access the datasets should be directed to weil01234@163.com.

Author contributions

WL, SL, and TQ conceived the main idea of this manuscript and performed the experiment. YW helped to revise this manuscript. WL wrote the manuscript and all authors contributed to the article and approved the submitted version.

Funding

This research was supported by the National Science Fund Project (Grant No. 52130907) and the National Science Fund Project for Distinguished Young Scholars (Grant No. 51725905).

Acknowledgments

We thank the reviewers for their useful comments and suggestions.

Conflict of interest

The authors declare that the research was conducted in the absence of any commercial or financial relationships that could be construed as a potential conflict of interest.

Publisher's note

References

Ao, C., Yang, P. L., Zeng, W. Z., Chen, W. L., Xu, Y., Xu, H. L., et al. (2019). Impact of raindrop diameter and polyacrylamide application on runoff, soil and nitrogen loss via raindrop splashing. *Geoderma* 353, 372–381. doi:10.1016/j.geoderma.2019.07.026

Arunrat, N., Sereenonchai, S., Chaowiwat, W., and Wang, C. (2021). Climate change impact on major crop yield and water footprint under CMIP6 climate projections in repeated drought and flood areas in Thailand. *Sci. Total Environ.* 807 (2), 150741. doi:10.1016/j.scitotenv.2021.150741

Bi, W. X., Weng, B. S., Yan, D. H., Wang, M. K., Wang, H., Wang, J. J., et al. (2020). Effects of drought-flood abrupt alternation on phosphorus in summer maize farmland systems. *Geoderma* 363, 114147–114212. doi:10.1016/j.geoderma.2019.114147

Cai, W. L., Huang, H., Chen, P. N., Huang, X. L., Gaurav, S., Pan, Z., et al. (2020). Effects of biochar from invasive weed on soil erosion under varying compaction and slope conditions: Comprehensive study using flume experiments. *Biomass Convers. Biorefinery.* doi:10.1007/s13399-020-00943-3

Chen, X. Y., Zhu, Y., Ding, Y., Pan, R. M., Shen, W. Y., Yu, X. R., et al. (2021). The relationship between characteristics of root morphology and grain filling in wheat under drought stress. *Peerj* 9, e12015. doi:10.7717/peerj.12015

Choi, Y. B., and Shin, J. H. (2019). Analysis of the changes in medium moisture content according to a crop irrigation strategy and the medium properties for precise moisture content control in rock wool. *Hortic. Environ. Biotechnol.* 60 (3), 337–343. doi:10.1007/s13580-019-00134-8

Dai, C. T., Liu, Y. J., Wang, T. W., Li, Z. X., and Zhou, Y. W. (2018). Exploring optimal measures to reduce soil erosion and nutrient losses in southern China. *Agric. Water Manag.* 210, 41–48. doi:10.1016/j.agwat.2018.07.032

De Almeida, W. S., Seitz, S., de Oliveira, L. F. C., and de Carvalho, D. F. (2021). Duration and intensity of rainfall events with the same erosivity change sediment yield and runoff rates. *Int. Soil Water Conservation Res.* 9 (1), 69–75. doi:10.1016/j.iswcr.2020.10.004

Du, X., Jian, J. S., Du, C., and Stewart, R. D. (2022). Conservation management decreases surface runoff and soil erosion. *Int. Soil Water Conservation Res.* 10 (2), 188–196. doi:10.1016/j.iswcr.2021.08.001

Fan, Y. H., Tian, M. Y., Jing, Q., Tian, Z. W., Han, H. M., Jiang, D., et al. (2015). Winter night warming improves pre-anthesis crop growth and post-anthesis photosynthesis involved in grain yield of winter wheat (*Triticum aestivum* L). *Field Crops Res.* 178, 100–108. doi:10.1016/j.fcr.2015.04.001

Gu, J. Y., Fang, W., Gao, J., Yan, S. X., Feng, G. L., Liu, C. X., et al. (2020). Improving soil water retention capacity of economic forest using rock wool in hilly area. *Agric. Res. Arid Areas* 38 (3), 10–18. doi:10.7606/j.issn.1000-7601.2020.03.02

Gu, J. Y., Shao, S., Deng, Y. J., Yu, C. B., Chen, J. H., Qin, H., et al. (2021). Response of growth and physiological indicators of Lycopersicone sculentum to water stress relieved by rock wool. *J. Zhejiang A&F Univ.* 38 (2), 311–319. doi:10.11833/j.issn.2095-0756.20200221

Hawrot-Paw, M., Mikiciuk, M., Koniuszy, A., and Meller, E. (2022). Influence of organomineral fertiliser from sewage sludge on soil microbiome and physiological parameters of maize (Zea mays L). *Agronomy-Basel* 12 (5), 1114. doi:10.3390/agronomy12051114

He, L. Z., Zhong, H., Liu, G. X., Dai, Z. M., Brookes, P. C., and Xu, J. (2019). Remediation of heavy metal contaminated soils by biochar: Mechanisms, potential risks and applications in China. *Environ. Pollut.* 252, 846–855. doi:10.1016/j.envpol.2019.05.151

Lee, S. S., Shah, H. S., Awad, Y. M., Kumar, S., and Ok, Y. S. (2015). Synergy effects of biochar and polyacrylamide on plants growth and soil erosion control. *Environ. Earth Sci.* 74 (3), 2463–2473. doi:10.1007/s12665-015-4262-5

Li, J. N., Chou, J., M., Zhao, W. X., Xu, Y., Hao, Y. D., and Li, Y. M. (2022). Future drought and flood vulnerability and risk prediction of China's agroecosystem under climate change. *Sustainability* 14 (16), 10069. doi:10.3390/su141610069

Li, J. Y., Tong, J. X., Xia, C. N., Hu, B. X., Zhu, H., Yang, R., et al. (2017). Numerical simulation and experimental study on farmland nitrogen loss to surface runoff in a raindrop driven process. *J. Hydrology* 549, 754–768. doi:10.1016/j.jhydrol.2017.01.035

Li, S. P., Li, Z. L., Feng, X., Zhou, F. W., Wang, J. P., and Li, Y. (2021). Effects of biochar additions on the soil chemical properties, bacterial community structure and rape growth in an acid purple soil. *Plant Soil Environ.* 67 (3), 121–129. doi:10.17221/390/2020-pse

Li, W., Liu, S. S., Qin, T. L., Xiao, S. B., Li, C. H., Zhang, X., et al. (2022). Experiment study of porous fiber material on infiltration and runoff of winter wheat farmland in Huaibei Plain, China. *Front. Earth Sci.* 10. doi:10.3389/feart.2022.817084

Li, X. N., Zhang, W. W., Wu, J. Y., Li, H. J., Zhao, T. K., Zhao, C. Q., et al. (2021). Loss of nitrogen and phosphorus from farmland runoff and the interception effect of an ecological drainage ditch in the North China Plain-A field study in a modern agricultural park. *Ecol. Eng.* 169, 106310. doi:10.1016/j.ecoleng.2021.106310

Li, Y., Mei, L. P., Zhou, S. L., Jia, Z. Y., Wang, J. X., Li, B. J., et al. (2018). Analysis of historical sources of heavy metals in lake taihu based on the positive matrix factorization model. *Int. J. Environ. Res. Public Health* 15 (7), 1540. doi:10.3390/ijerph15071540

Libutti, A., Francavilla, M., and Monteleone, M. (2021). Hydrological properties of a clay loam soil as affected by biochar application in a pot experiment. *Agronomy-Basel* 11 (3), 489. doi:10.3390/agronomy11030489

Liu, S. M., Wang, H., Yan, D. H., Qin, T. L., Wang, Z. L., and Wang, F. X. (2017). Crop growth characteristics and waterlogging risk analysis of Huaibei Plain in Anhui Province, China. *J. Irrigation Drainage Eng.* 143 (10), 04017042. doi:10.1061/(asce)ir.1943-4774.0001219

Liu, X. Q., Liu, Z. J., Zhong, H. M., Jian, Y. Q., and Shi, L. N. (2021). Multi-dimension evaluation of rural development degree and its uncertainties: A comparison analysis based on three different weighting assignment methods. *Ecol. Indic.* 130, 108096. doi:10.1016/j.ecolind.2021.108096

Liu, Y. F., Sun, D. S., Wang, H. J., Wang, X. J., Yu, G. Q., and Zhao, X. J. (2020). An evaluation of China's agricultural green production: 1978–2017. *J. Clean. Prod.* 243, 118483. doi:10.1016/j.jclepro.2019.118483

Lu, H. A., Zhao, Y. M., Zhou, X., and Wei, Z. K. (2022). Selection of agricultural machinery based on improved CRITIC-entropy weight and GRA-TOPSIS method. *Processes* 10 (2), 266. doi:10.3390/pr10020266

Lv, Z. Y., Qin, T. L., Liu, S. S., Nie, H. J., Liu, F., and Wang, J. W. (2020). Porous-fiber module increases infiltration and reduces runoff. *Agron. J.* 112 (5), 4420–4436. doi:10.1002/agj2.20317

Lv, Z. Y., Qin, T. L., Wang, Y., Liu, S. S., Nie, H. J., and Wang, J. W. (2021). Hydraulic properties of the porous-fiber module and its effects on infiltration and runoff. *Agron. J.* 113 (3), 2913–2925. doi:10.1002/agj2.20630

Meresa, H., Tischbein, B., and Mekonnen, T. (2022). Climate change impact on extreme precipitation and peak flood magnitude and frequency: Observations from CMIP6 and hydrological models. *Nat. Hazards* 111 (3), 2649–2679. doi:10.1007/s11069-021-05152-3

Pu, S. H., Li, G. Y., Tang, G. M., Zhang, Y. S., Xu, W. L., Li, P., et al. (2019). Effects of biochar on water movement characteristics in sandy soil under drip irrigation. *J. Arid Land* 11 (5), 740–753. doi:10.1007/s40333-019-0106-6

Sandoval, V., Bonilla, C. A., Gironas, J., Vera, S., Victorero, F., Bustamante, W., et al. (2017). Porous media characterization to simulate water and heat transport through green roof substrates. *Vadose Zone J.* 16 (4), 1–14. doi:10.2136/vzj2016.10.0101

Swain, D. L., Langenbrunner, B., Neelin, J. D., and Hall, A. (2018). Increasing precipitation volatility in twenty-first-century California. *Nat. Clim. Change* 8 (5), 427–433. doi:10.1038/s41558-018-0140-y

VanWoert, N. D., Rowe, D. B., Andresen, J. A., Rugh, C. L., and Xiao, L. (2005). Watering regime and green roof substrate design affect Sedum plant growth. *Hortscience* 40 (3), 659–664. doi:10.21273/hortsci.40.3.659

Vijayaraghavan, K., and Raja, F. D. (2014). Design and development of green roof substrate to improve runoff water quality: Plant growth experiments and adsorption. *Water Res.* 63, 94–101. doi:10.1016/j.watres.2014.06.012

Wang, R., Min, J., Kronzucker, H. J., Li, Y. L., and Shi, W. M. (2020). N and P runoff losses in China's vegetable production systems: Loss characteristics, impact, and management practices. *Sci. Total Environ.* 698, 971–979. doi:10.1016/j.scitotenv.2019.01.368

Wang, T., Xiao, W. F., Huang, Z. L., and Zeng, L. X. (2022). Interflow pattern govern nitrogen loss from tea orchard slopes in response to rainfall pattern in Three Gorges Reservoir Area. *Agric. Water Manag.* 269, 107684. doi:10.1016/j.agwat.2022.107684

Wu, L., Liu, X., and Ma, X. Y. (2021). How biochar, horizontal ridge, and grass affect runoff phosphorus fractions and possible tradeoffs under consecutive rainstorms in loessial sloping land? *Agric. Water Manag.* 256, 107121. doi:10.1016/j.agwat.2021.107121

Wu, X. L., Tang, Y. L., Li, C. S., Wu, C., and Huang, G. (2015). Chlorophyll fluorescence and yield responses of winter wheat to waterlogging at different growth stages. *Plant Prod. Sci.* 18 (3), 284–294. doi:10.1626/pps.18.284

Xia, M., Jia, K., Zhao, W. W., Liu, S. L., Wei, X. Q., and Wang, B. (2021). Spatio-temporal changes of ecological vulnerability across the Qinghai-Tibetan Plateau. *Ecol. Indic.* 123, 107274. doi:10.1016/j.ecolind.2020.107274

Yan, L., Xue, L. H., Petropoulos, E., Qian, C., Hou, P. F., Xu, D. F., et al. (2021). Nutrient loss by runoff from rice-wheat rotation during the wheat season is dictated by rainfall duration. *Environ. Pollut.* 285, 117382. doi:10.1016/j.envpol.2021.117382

Yu, H. Q., Zhang, Q., Sun, P., and Song, C. Q. (2018). Impact of droughts on winter wheat yield in different growth stages during 2001-2016 in eastern China. *Int. J. Disaster Risk Sci.* 9 (3), 376–391. doi:10.1007/s13753-018-0187-4

Yu, H. W., Zou, W. X., Chen, J. J., Chen, H., Yu, Z. B., Huang, J., et al. (2019). Biochar amendment improves crop production in problem soils: A review. *J. Environ. Manag.* 232, 8–21. doi:10.1016/j.jenvman.2018.10.117

Zhang, C., Huang, X., Zhang, X. W., Wan, L., and Wang, Z. H. (2021). Effects of biochar application on soil nitrogen and phosphorous leaching loss and oil peony growth. *Agric. Water Manag.* 255, 107022. doi:10.1016/j.agwat.2021.107022

Zhang, Y. F., Wang, Y. F., and Liu, L. X. (2001). Function mechanism between the drought and waterlogging disaster and the soil-structure of the shajiang soil in Huaibei Plain. *Prog. Geogr.* 20 (2), 169–176.

Zhao, J., Khan, S., Anwar, S., Mo, F., Min, S., Yu, S., et al. (2019). Plastic Film-mulching with appropriate seeding rate enhances yield and water use effciency of dryland winter wheat in loess plateau, China. *Appl. Ecol. Environ. Res.* 18 (1), 1107–1127. doi:10.15666/aeer/1801_11071127

Zhou, P. G., Zhang, D. H., Zhuang, L., Zhang, L., Yuan, W. R., and Singh, R. P. (2021). Assessment of runoff nutrients loss in Phyllostachys praecox cv. prevernalis forest land under simulated rainfall conditions. *Environ. Sci. Pollut. Res.* 28 (17), 21874–21886. doi:10.1007/s11356-020-11871-0

Zhu, L. (2020). Research and application of AHP-fuzzy comprehensive evaluation model. *Evol. Intell.* 15 (4), 2403–2409. doi:10.1007/s12065-020-00415-7

frontiers | Frontiers in Environmental Science

TYPE Review
PUBLISHED 27 January 2023
DOI 10.3389/fenvs.2023.1084888

OPEN ACCESS

EDITED BY
Hu Liu,
Northwest Institute of Eco-Environment and Resources (CAS), China

REVIEWED BY
Peng Zhang,
Guangdong Ocean University, China
Dongmei Zhang,
Northwest Institute of Eco-Environment and Resources (CAS), China

*CORRESPONDENCE
Wenlong Chen,
48708209@qq.com

SPECIALTY SECTION
This article was submitted to Freshwater Science,
a section of the journal
Frontiers in Environmental Science

RECEIVED 31 October 2022
ACCEPTED 12 January 2023
PUBLISHED 27 January 2023

CITATION
Chen W, Guo F, Huang W, Wang J, Zhang M and Wu Q (2023), Advances in phytoplankton population ecology in the Pearl river estuary.
Front. Environ. Sci. 11:1084888.
doi: 10.3389/fenvs.2023.1084888

Advances in phytoplankton population ecology in the Pearl river estuary

Wenlong Chen[1,2,3]*, Fang Guo[1,2,3], Weijie Huang[1,2,3], Jianguo Wang[1,2,3], Min Zhang[1,2,3] and Qian Wu[1,2,3]

[1]Pearl River Water Resources Research Institute, Pearl River Water Resources Commission of the Ministry of Water Resources, Guangzhou, China, [2]Key Laboratory of the Pearl River Estuary Regulation and Protection of Ministry of Water Resources, Guangzhou, China, [3]Guangdong Provincial Engineering Technology Research Center for Life and Health of River & Lake, Guangzhou, China

Phytoplankton is an important primary producer of the estuarine ecosystem, which is essential for the biogeochemical cycle of water elements and nutrient transfer. The Pearl River estuary (PRE) is a dynamically complex estuary, and the environment of PRE is significantly impacted by anthropogenic activities, variation of phytoplankton community structure in the PRE are complex. This review aims to compare phytoplankton species, species diversity, and abundance variation characteristics from the 1980s and 2020s, evaluate the overall trend of phytoplankton in the PRE, and discuss the main environmental factors affecting phytoplankton growth in the PRE. The data from the past 40 years in PRE showed that the number of phytoplankton species significantly decreased ($p < 0.05$). There was no significant difference in the abundance of phytoplankton at the 10-year scale, however, the fluctuation range of the abundance has increased. Under the conditions of a decreasing species number and no significant difference in abundance, the species diversity of phytoplankton showed a downward trend. In addition, the dominant phytoplankton species in the nearshore waters were relatively homogenous, and the abundance of phytoplankton in the nearshore waters was higher than that in the open waters, which suggested that human activities have a great influence. This review can form the basis for facilitating health management in the PRE ecosystem. Further, relevant guidelines can be developed and implemented for promoting the ecological health of the Guangdong-Hong Kong-Macao Greater Bay Area and ensuring its sustainable development.

KEYWORDS

phytoplankton, the Pearl river estuary, estuarine ecosystem, species characteristics, spatio-temporal variation

1 Introduction

Figure 1 phytoplankton account for 1% of the photosynthetic biomass on Earth, and it is an important primary producer in aquatic ecosystems. Meanwhile, phytoplankton are the base of aquatic food webs and of global importance for ecosystem functioning and services (Winder and Sommer, 2012). Therefore, it plays a vital role in the biogeochemical processes of water elements and the process of nutrient transfer. Phytoplankton have important applications in the assessment of water quality and ecosystem health (Villegas and Giner, 1973; Guo et al., 2020). For example, the balance between phytoplankton, the environment, and the quality of water health can be evaluated using phytoplankton diversity and biological integrity index (Tan et al., 2017; Liu et al., 2020).

The eutrophic conditions lead to phytoplankton blooms, Phytoplankton proliferate and cover the water surface in eutrophic water, blocking the transmission of light to the bottom, inhibiting the growth and proliferation of aquatic plants at the bottom, and reducing the release of oxygen. In addition, when the nutrients are exhausted, a large area of phytoplankton death will occur, and a large amount of oxygen will be consumed when they are decomposed by bacterial communities. The result of both actions is a decrease in the concentration of dissolved oxygen in the water (Anderson et al., 2002). Reduced concentrations of dissolved oxygen can cause the death of aquatic animals, especially fish. Some algae give off a fishy odor, which makes the water smell bad. The final development of eutrophication will reduce the water storage capacity due to organic residue deposition, destroy the ecological structure of water, break the biological chain, species tend to be single, and water function degradation (Anderson et al., 2002; Qi and Liu, 2004; Salk et al., 2022).

The Pearl River is the third longest river in China, with an annual runoff more than 349.2 billion cubic meters, which size is second only to that of the Yangtze River in China (Qiu et al., 2010). It comprises eight outlets and three main tributaries of the Pearl River—the North River, the East River, and the West River, which empty into the Pearl River Estuary (PRE) (Luo et al., 2007; Zhang, et al., 2009). The PRE in southern China is characterized by a typical subtropical climate, rich in natural resources, and the main water source for Zhuhai and Macao, therefore, it is recognized as the central development hub of the Guangdong-Hong Kong-Macao Greater Bay Area with salient natural geographical advantages. However, the PRE has faced substantial environmental pressure under the influence of frequent human activities and intensified global climate change in recent decades. The water developed from a mesotrophic system to undergoing local eutrophication since the 1900s, and this trend is currently being exacerbated (Jia et al., 2002; Zhang et al., 2009; Niu et al., 2020). Jia et al. (2002) revealed the increasing trend of eutrophication in the PRE over the past century through the sedimentary column. The sedimentary budget of organic carbon, biogenic silica and total nitrogen, which are related to the primary productivity of aquatic ecosystems, basically maintained in a relatively low and stable range before the early 20th century, whereas the sedimentary budget of each component showed an obvious increasing trend after 1920. Furthermore, Guo et al. (2022) showed that the overall water quality of the coastal waters of Zhuhai city was extremely poor in November 2017 and March 2018. The input of nutrients, especially nitrogen, has resulted in aquatic eutrophication in this estuary (Huang et al., 2003; Zhu et al., 2018).

Huge environmental pressure causes frequent occurrences of red tides in the PRE. Such tides severely affect the water supply security and threaten the sustainable utilization of natural resources in the Guangdong-Hong Kong-Macao Greater Bay Area. Thus, it is essential to study the phytoplankton population ecology to understand the health of the PRE ecosystem and its underlying drivers. Estuarine habitats are unique, while phytoplankton composition and distribution patterns are both complex. However, there is no review previously published about phytoplankton in the PRE, the existing ecological surveys and published data in the PRE are not continuous. Therefore, the phytoplankton status and change trend in the PRE are both poorly understood. New techniques for phytoplankton monitoring and evaluation, such as remote sensing inversions, may close this gap; however, they require substantial data support (Peng, 2021).

This review focuses on the species composition, dominant species, spatiotemporal distribution, and species diversity trends of phytoplankton in the PRE and summarizes the main findings on the phytoplankton community in the region. Our summary can facilitate health management in the PRE ecosystem and provide relevant guidelines for promoting the ecological health and sustainable development of the Guangdong-Hong Kong-Macao Greater Bay Area.

2 Materials and methods

This manuscript refers only to published data, the graph and significance difference analysis (Student t test) of phytoplankton species and abundance in different periods were performed by R package ggplot2, RColorBrewer, ggsignif and stats. The graphical abstract was drawn with CorelDraw X8.

3 Results and discussion

3.1 Phytoplankton species composition and dominant species

Estuaries are transitional zones between rivers and oceans, where brackish and fresh water interact and the evolution mechanism of biogeochemical processes is complex, thus forming a unique complex ecological environment (Lu and Gan, 2015; Niu et al., 2020). Estuarine phytoplankton groups, such as saltwater, freshwater, and semi-saline water species, are also unique. Eight phytoplankton taxa, namely Diatom, Dinoflagellate, Chlorophyta, Cyanobacteria, Chrysophyta, Cryptophyta, and Xanthophyta, have been reported in the PRE since the 1980s (Huang et al., 2004; Li et al., 2014). Similar to the phytoplankton community structure in the 1980s, diatom was determined as the dominant group (especially in the dry season), followed by Chlorophyta (Song, 1991; Xu et al., 2022). During the upstream period of saltwater intrusion, the dominant taxa in the PRE significantly changed, whereas diatoms predominated in the upper estuary, and dinoflagellates predominated in the lower estuary (Li et al., 2010). According to the published data (Figure 2), the data from the past 40 years in PRE showed that the number of phytoplankton species significantly decreased ($p < 0.05$). Previous studies identified ~300 species of phytoplankton in the PRE in the early 1980s, mainly represented by the widespread and warm-water species (Liu, 2008). Compared with the 1980s, the overall number of phytoplankton species in the PRE exhibited a downward trend because only 84 phytoplankton species were identified during two voyage surveys in the PRE during 2010–2011 (Song, 1991). Moreover, in 2020, only 50 species of phytoplankton were identified at 14 survey stations in the PRE in the summer and winter (Xu S. et al., 2022). During the saltwater intrusion period, less than 80 species were detected (Xiong and Liu, 2018). The number of species in the PRE varies between seasons; an upward trend exists from spring to summer, where the number of species peaks in the summer and decreases as autumn approaches (Zhou et al., 2016).

As mentioned, the dominant species in the PRE and adjacent waters are mainly represented by diatoms, which are affected by the interleaving of two heterogeneous water masses, tidal current, and runoff, thereby causing severe water disturbance and distinct seasonal

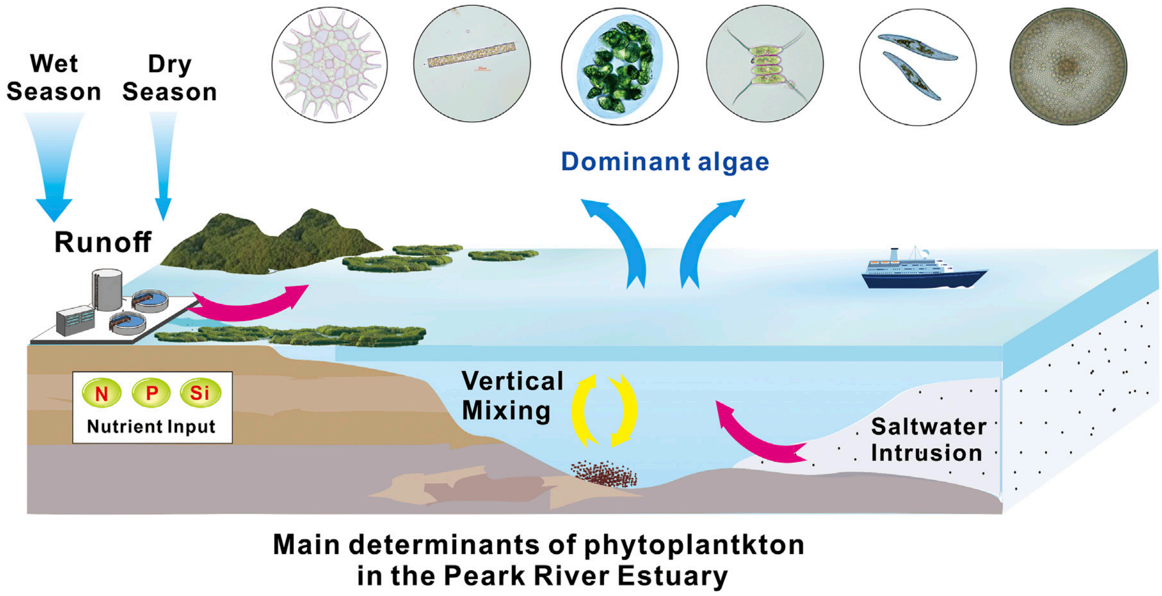

FIGURE 1
Graphical Abstract (Guo and Shen, 2003, Harrison et al., 2008, Huang et al., 2021).

succession of dominant species in the PRE (Li et al., 2007). In the wet season, the dominant species are represented by *Aulacoseira granulata* and *Aulacoseira granulata* var. *angustissima*. Meanwhile, *A. granulata* is a common dominant species in the upper reaches of the PRE (Wang et al., 2012; 2013). *Skeletonema costatum* is arguably the dominant species in the PRE during the dry season, especially during the upstream salt-tide period. *Skeletonema costatum*, characterized by ectothermic and halotolerant organisms, is also the dominant species in the PRE, with a relative abundance of > 80%. Moreover, in some years, *Skeletonema costatum* was reported as the dominant species during wet seasons (Huang et al., 2004; Feng et al., 2012). In addition, the species of *Cerochaete* and *Rhombic* were also reported to be more abundant in the dry season. Similarly, *Nitzschia pungens*, *Nitzschia delicatissima*, *Thalassiosira* sp., *Chaetoceros affinis* etc., were found to be dominant species in the dry season (Dai et al., 2004; Wang et al., 2013). Compared with that in the wet season, the number of red tide species in estuaries increased in the dry season, and dinoflagellates were the species that increased the most (Dong et al., 2009). The statistics from the 2000–2014 period revealed that the the dominant red tide algae in the PRE were *Cochlodinium polykrikoides*, *Cochlodinium geminatum*, *Gyrodinium instriatum*, and *Akashiwo sanguinea* (Liu, 2008; Wei et al., 2012; Huan et al., 2016).

3.2 Distribution characteristics of abundance and diversity trends in phytoplankton

The abundance distribution of phytoplankton in the PRE exhibits distinct spatiotemporal variability. More specifically, the interactions between multiple environmental factors complicates the distribution of phytoplankton in the PRE. Consequently, the abundance of phytoplankton is higher in summer than in winter and higher in the wet season than in the dry season (Si, 2018; Xiong and Liu, 2018; Wang et al., 2021). The abundance of phytoplankton in the PRE has been mainly reported downstream in the wet season. Given the high dilution intensity in the upper estuary, a large amount of suspended matter is formed, thereby limiting the access of phytoplankton to nutrients and light. Consequently, phytoplankton growth is also hindered. By contrast, the downstream of the river water is largely devoid of suspended matter, the dilution intensity is small, and phytoplankton bloom, so the abundance is relatively high (Yin et al., 2004; Feng et al., 2012). The high value of phytoplankton abundance in the dry season was clustered in the middle of the estuary; previous studies also showed that the spatial distribution of chlorophyll a in the dry season was characterized by low variability due to the strong mixing of water bodies (Lu and Gan, 2015). Ma and Zhao (2021) determined that the spatial distribution of phytoplankton in the PRE was irregular in the summer. Li et al. (2010) analyzed the phytoplankton community in the PRE during brackish tides and found that phytoplankton exhibited a decreasing trend from the upper to the lower parts of the estuary during both high and low tides. Furthermore, historical data indicated that the abundance of phytoplankton in the PRE increased at small scale. The abundance of phytoplankton in the wet season was significantly higher during 2010–2019 than that in the 1980s, while there was no significant difference in the abundance of phytoplankton at the 10-year scale (Figure 3), however, the fluctuation range of the abundance has increased, and the inter-annual variation range of phytoplankton in the dry season was somewhat narrow (Song, 1991; Liu, 2008; Xu et al., 2017; Niu et al., 2020).

The diversity of phytoplankton species in the PRE is greatly affected by anthropogenic activities. Indicatively, Wang et al. (2012) examined the phytoplankton in the Pearl River Delta River network and reported that the diversity of dominant species was low in the survey stations near Guangzhou. However, the authors found that the diversity of dominant species that were spatially distant from

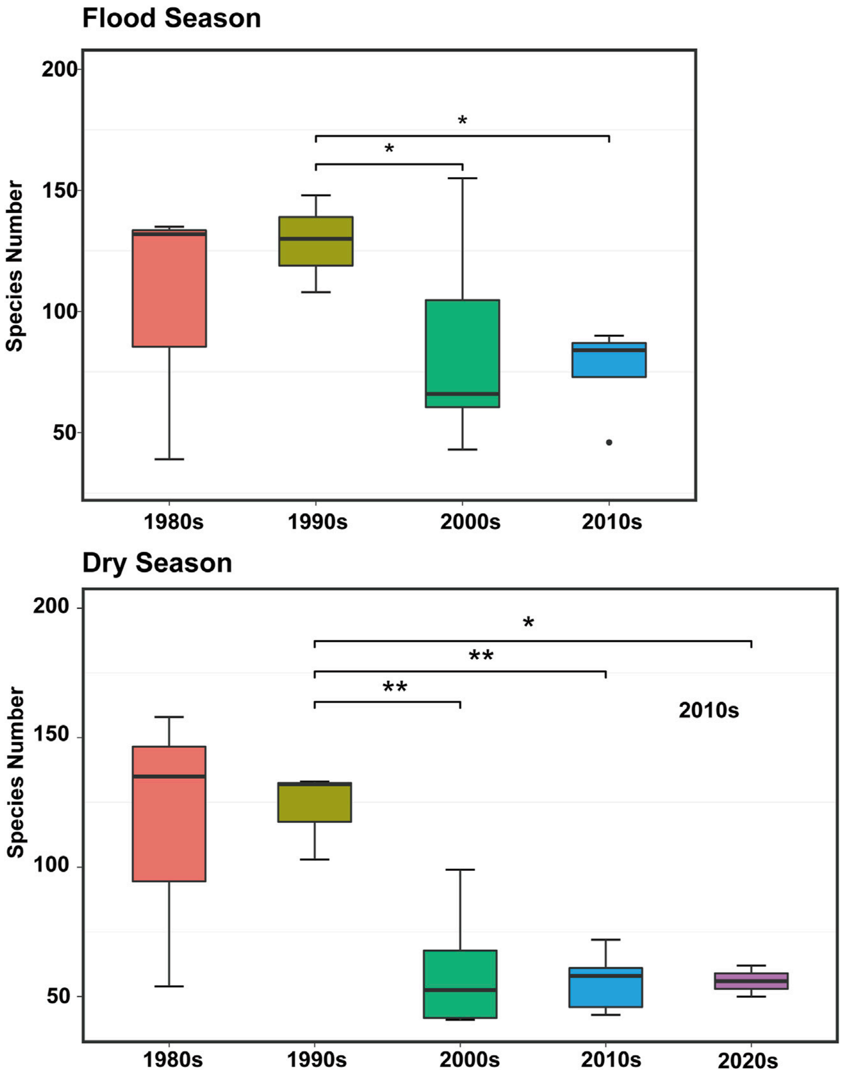

FIGURE 2
Variation characteristics of phytoplankton species number in the Pearl River Estuary during the flood seasons from the 1980s–2020s. Asterisks indicate significant differences (*$p < 0.05$, **$p < 0.01$) (Song, 1991; Dai et al., 2004; Huang et al., 2004; Liu, 2008; Dong et al., 2009; Li et al., 2010; Feng et al., 2012; Wang et al., 2013; Zhou et al., 2016; Xu et al., 2017; Xiong and Liu, 2018; Xu et al., 2022).

Guangzhou was high in the survey stations, while the frequent human activities in Guangzhou weakened the diversity of phytoplankton. Generally, the diversity of phytoplankton species in the PRE peaked in summer, was low in the estuary, and gradually increased outside the estuary. Overall, it has been shown that the greater the distance from the shore, the higher the salinity, and the higher the diversity (Dai et al., 2004). The diversity of phytoplankton species was found to be higher offshore than inshore because the abundance of phytoplankton is high near the PRE. However, the species distribution is uneven in the region, and the dominant species is concentrated and homogenous, thereby inducing weak diversity near the PRE (Feng et al., 2012). From the late 1990s to the early 2000s, phytoplankton diversity in the PRE was found to be slightly average (Liu, 2008). Zhang et al. (2015) focused on the PRE and its adjacent waters from 2006 to 2007. They clearly identified the dominant phytoplankton species in the PRE, while also showing that the overall diversity was low; unlike in the previous period, it exhibited a downward trend. Compared with that 20 years ago, the diversity of phytoplankton in the PRE has significantly decreased in recent years (Xu et al., 2022). Because it is associated with the diversity of phytoplankton species in the PRE, the diversity of phytoplankton species in the upper estuary is also highly important. Therefore, Cui (2019) investigated the Pearl River Basin and found that compared with that in the 1980s, the phytoplankton diversity in the Dongjiang and Beijing rivers exhibited downward trends in the 1990, with the exception of Xijiang River. The phytoplankton diversity input from the upper reaches of the Pearl River to the estuary was weak.

3.3 Main influencing factors of phytoplankton in the PRE

3.3.1 Nutrients

Estuaries are affected by the interaction between freshwater discharge and brackish water invasion, while the environmental factors controlling phytoplankton growth are highly complex. The

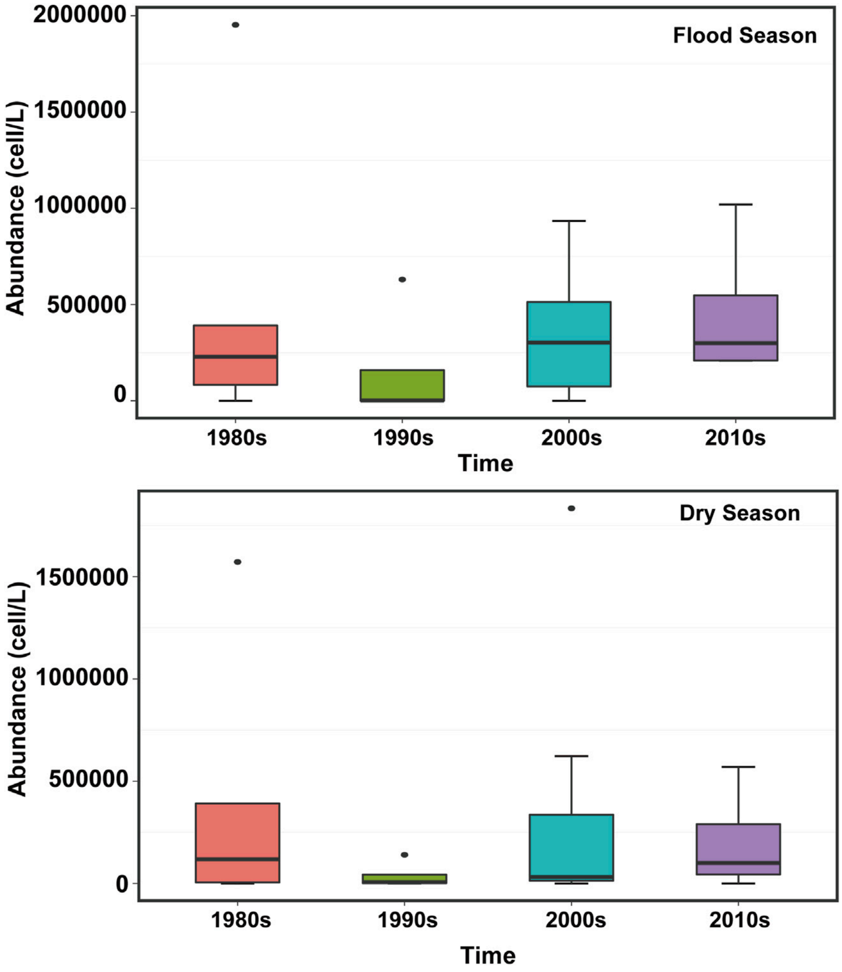

FIGURE 3
Variation characteristics of phytoplankton abundance in the Pearl River Estuary during the flood and dry seasons from the 1980s–2020s (Lin et al., 1994; Huang and Wang, 1997; Huang et al., 2004; Liu, 2008; Li et al., 2010; Feng et al., 2012; Wang et al., 2012; Li et al., 2022; Zhang et al., 2015; Li et al., 2019; Li et al., 2022; Xu et al., 2022).

main nutrients are nitrogen, phosphorus, and silicon (Yin et al., 2000; Xu S. et al., 2022). The concentration of phosphorus in the PRE is low, and the contribution of runoff to PO_4-P formation is not significant; PO_4-P mainly originates from the decomposition of sediment organic matter and the release of sediment, which is exacerbated by the incomplete treatment of domestic sewage discharge and excessive use of nitrogen fertilizers. Therefore, the PRE is characterized by high nitrogen and low phosphorus content. Spatially, nitrogen and phosphorus pollution trends are more prominent in the east but inconspicuous in the west. Dissolved inorganic nitrogen (DIN) in the PRE indicated that upstream of the mouth is dominated by NH_4-N, and the concentration of NO_3-N was the highest at the mouth, accounting for 51.2%–80.4% (Niu et al., 2020b; Li et al., 2022). Generally, the level of nitrogen and phosphorus nutrients is one of the key drivers of red tides in the PRE. Huang et al. (2016) determined that there was a highly significant positive correlation between NO_3-N and the accumulated red tide area in the PRE. In this context, Li et al. (2022) argued that the large increase in PO_4-P may be the cause of the large increase in the abundance of *Skeletonema costatum*, and the transformation of dominant species was mainly associated with the decrease in the concentration of PO_4-P. Previously, Yin and Harrison (2008) had suggested that the excessive nitrogen enrichment in the PRE does not induce the high biomass of phytoplankton, and that limited phosphorus is one of the main drivers of this phenomenon. The surface distribution of nutrients in the PRE is mainly affected by terrestrial input and biological consumption. Given the influence of estuarine diluted water in the summer, the dilution of phosphorus in the PRE basin surface waters outside the estuary waters because of the water level change prevents the upper nutrient exchange between water and bottom water, which lead to the surface of phosphorus are exhausted, and phytoplankton growth is limited by phosphorus (Yin et al., 2011; Li et al., 2017). Additionally, phosphorus limitation has predetermined the miniaturization of phytoplankton in the PRE (Dai et al., 2008). Li et al. (2007) examined the characteristics of phytoplankton community structure in the PRE and found that, compared with the surrounding waters, the PRE was dominated by small phytoplankton. Si (2018) investigated the PRE in 2017 and found that the biomass of picophytoplankton was notably dominant, among which *Prochlorococcus* and *Synechococcus* contributed the most. A previous study demonstrated that phytoplankton communities with large particle sizes are dominant in nutrient rich environmentsand are more susceptible to phosphorus limitation (Litchman et al., 2007). However, other studies showed that ultra-micro phytoplankton with small particle sizes have a higher specific surface area. Thus, they can adapt to the poor nutrient niche and reproduce rapidly, thereby manifesting advantages in the water (Moutin et al., 2002; Zhou et al., 2016). In the winter, given the strong vertical mixing and low bioavailability, the phosphorus in the bottom sediment is replenished in the surface water, thereby elevating all the forms of phosphorus above the levels recorded in the summer. This increase alleviates the phosphorus restriction in phytoplankton growth, thereby causing more frequent winter blooms (Li et al., 2017; Ye et al., 2020).

Notably, the N/P ratio is crucial for phytoplankton growth, while the Redfield ratio (N: $p = 16{:}1$) can be used as a quantitative indicator to evaluate water eutrophication (Sañudo-Wilhelmy et al., 2004). Niu et al. (2020) elucidated the driving factors of the phytoplankton environment in the PRE from 1974 to 2017 and found that DIN and PO_4-P both increased. Given the influence of the non-point source inputs from the PRE, the N/P at most survey stations in the PRE was substantially higher than the ratio optimal for phytoplankton growth. The increase in N/P is mainly driven by the enhanced use of nitrogen compared with that of phosphorus, where nitrogen has higher mobility and more dispersed sources than phosphorus (Peñuelas et al., 2012; Yu and Gan, 2022).

The estuarine biogeochemistry process is generally complex, while the main factors limiting phytoplankton growth differ depending on the season. Some studies have shown that Portland considerably limits phytoplankton growth in spring and summer. Phytoplankton quickly multiply in spring and summer as silicates, which are closely associated with the growth in most dominant species and represents one of the important conditions, showing the advantages of diatoms (Yin and Harrison, 2007; Dai et al., 2008). However, when silicate and phosphate contents are both very low, a dinoflagellate red tide can easily occur.

3.3.2 Salinity

Brackish and freshwater species normally coexist in an estuary; therefore, salinity plays a decisive role in phytoplankton types in the PRE. In recent years, the inter-annual variability of salinity in the PRE has not been significant in the dry season. Despite the insignificance, the frequency, intensity, duration, and range of salt-tide invasion have all exhibited upward trends; salinity in the wet season also showed an upward trend (Zhang et al., 2017). Given the dilution effect of diluting water from the Pearl River in the summer, the salinity of the PRE was found to be higher in dry season than in wet season (Niu et al., 2020). Moreover, the spatial gradient of salinity is negatively correlated with the phytoplankton community in the PRE; as the salinity increases, the number of phytoplankton species decreases (Xiong and Liu, 2018). During the period of upstream saltwater intrusion, the salinity of the upper part of the estuary increases. Some species show weak adaptability to salinity, evident by the decrease in Chlorophyta species, which accounts for a high proportion in the estuary, and the dominant species change from freshwater and brackish water species to marine brackish water species (Wang et al., 2013; Zhang et al., 2017). Spatially, the salinity in the PRE is high in the south and east and low in the north and west. Zhang et al. (2015) showed that the vertical distribution of salinity in the PRE exhibited an increasing trend from the surface layer to the bottom layer and is stratified in the water column. The occurrence of haloclines in the summer hindered the exchange of nutrients between the bottom layer and the surface water, while the phytoplankton had limited access to nutrients, especially phosphate, thereby exacerbating the phosphorus limitations in the PRE.

3.3.3 Hydrodynamic forces

Hydrodynamic conditions represent another important factor for phytoplankton explosion in estuaries (Zhang et al., 2009). Streamflow and tides both affect phytoplankton growth by altering salinity, salt, and light in the PRE (Lu and Gan, 2015; Niu et al., 2020). Because it is exposed to a monsoon climate, the water dynamics of the PRE exhibit clear seasonality. Ma and Zhao (2021) argued that runoff was the main driver of phytoplankton spatial distribution in the PRE. In particular, during the wet season, the river runoff is large and the water column is stratified, thereby forming the thermohalocline. The vertical exchange of nutrients is hindered, limiting the growth of phytoplankton in the PRE. Niu et al. (2020b) showed that the annual average sediment load in the PRE was mainly carried by runoff during 1974–2016. Moreover, they found that a large amount of suspended matter affected the growth of phytoplankton by influencing their photosynthesis. Furthermore, the runoff decreased during the dry season, while the strong vertical mixing of water created a large amount of suspended matter, thereby potentially inducing limited light conditions for phytoplankton.

4 Existing deficiencies

Phytoplankton is an important factor to consider in environmental water quality assessment. Specifically, by monitoring the dynamic changes in phytoplankton, the optimal conditions of the PRE water ecological system and how these conditions are related to other estuarine ecosystems can be elucidated. Thus far, this interaction is more complex, fragile, and less understood because anthropogenic activities affecting aquatic systems have caused the eutrophication of the PRE. Furthermore, the lack of continuous phytoplankton monitoring in the PRE heightens both the complexity and poor understanding of these processes. Numerous scholars have previously used chlorophyll-a instead of phytoplankton monitoring, especially to study phytoplankton community composition. However, such an approach is not conducive for in-depth analysis of the water ecological health status of the PRE. Moreover, the sampling time of the phytoplankton community in the PRE was somewhat arbitrary in previous studies, causing a divergence in survey results. Consequently, there is no holistic study which summarizes, elucidates, and discusses the existing research results, while interpreting the ecological characteristics of the PRE.

A remote sensing approach to phytoplankton analysis is more beneficial compared to traditional methods for determining the distribution and dynamics of phytoplankton. Although such studies are becoming increasingly popular, remote sensing of phytoplankton has some limitations. In particular, for efficient inversion using remote sensing observations, the empirical model must be optimized and a large number of monitoring data must be provided. In other words, the monitoring of phytoplankton in the PRE should be considerably strengthened.

Moreover, the ongoing miniaturization of phytoplankton in the PRE should be further analyzed. In practice, the function of phytoplankton is closely related to its morphology. Phytoplankton, a key primary producer of estuarine ecosystems, plays an important role in the estuarine food chain. Overall, the existing literature demonstrated that phytoplankton in the PRE tend to be miniaturized. However, it is poorly understood whether the change in phytoplankton body size yields a change or loss in the functional needs, thereby prompting further studies on this topic. Finally, the environmental implications of phytoplankton miniaturization in the PRE and the physiological and functional changes in phytoplankton should be elucidated in detail in future studies.

5 Conclusion

In conclusion, the PRE data from the past 40 years showed that the number of phytoplankton species significantly decreased ($p < 0.05$). The dominant phytoplankton species in the nearshore waters were relatively homogenous, and the abundance of phytoplankton in the nearshore waters was higher than that in the open waters. There was no significant difference in the abundance of phytoplankton at the 10-year scale, however, the fluctuation range of the abundance has increased. Under the conditions of a decreasing species number and no significant difference in abundance, the species diversity of phytoplankton showed a downward trend.

Author contributions

WC was responsible for the structure and writing of the article; FG, WH, and JW, contributed to writing the article; MZ was responsible for drawing figures and proofreading; QW was responsible for proofreading.

Funding

This study was supported by the Special Foundation for National Science and Technology Basic Research Program of China (2019FY101900) and Guangdong Natural Science Foundation (2019A1515110131).

Acknowledgments

We thank all the members of the laboratory for their help in writing this article and colleagues for their active comments on this article.

Conflict of interest

The authors declare that the research was conducted in the absence of any commercial or financial relationships that could be construed as a potential conflict of interest.

Publisher's note

References

Anderson, D. M., Glibert, P. M., and Burkholder, J. M. (2002). Harmful algal blooms and eutrophication: Nutrient sources, composition, and consequences. *Estuaries* 25 (4), 704–726. doi:10.1007/bf02804901

Cui, W. Z. (2019). *Temporal and spatial variation of water environment and its impact on the ecosystem of the Pearl River estuary [doctoral dissertation]*. Nanjing: Hohai University.

Dai, M., Li, C. H., Jia, X. P., Zhang, H. H., and Chen, R. W. (2004). Ecological characteristics of phytoplankton in coastal area of Pearl River estuary. *Chin. J. Appl. Ecol.* 15, 1389–1394.

Dai, M., Zhai, W., Cai, W., Callahan, J., Huang, B., Shang, S., et al. (2008). Effects of an estuarine plume-associated bloom on the carbonate system in the lower reaches of the Pearl River Estuary and the coastal zone of the northern South China Sea. *Contin. Shelf Res.* 28, 1416–1423. doi:10.1016/j.csr.2007.04.018

Dong, Y. H., Cai, J. D., and Qian, H. L. (2009). Nutrient ratios and its relationship with phytoplankton in the Pearl River estuary. *Mar. Sci. Bull.* doi:10.3969/j.issn.1001-6392.2009.01.001

Feng, J. P., Jiang, S., Qiao, Y. M., Li, W. X., Guan, X., and Feng, J. H. (2012). Study on characteristics of phytoplankton community in Guangzhou segment of the Pearl River estuary. *Ecol. Sci.* 31, 284–288. doi:10.3969/j.issn.1008-8873.2012.03.010

Guo, F., Gu, J. G., Zhao, J., Yu, H. Z., and Xiao, L. J. (2020). Effects of phytoplankton classifications on the relationship between phytoplankton community and environment in summer subtropical reservoirs, Southern China. *Environ. Sci.* 41, 5050–5059. doi:10.13227/j.hjkx.202005106

Guo, K., Long, C., Dang, E., and Zhang, L. (2022). Assessment of water quality and eutrophication in the coastal area of Zhuhai city. *Mar. Environ. Sci.* 02, 222–229. doi:10.13634/j.cnki.mes.2022.02.002

Guo, P. Y., and Shen, H. T. (2003). Research advance in estuarine phytoplankton ecology. *Chin. J. Appl. Ecol.* 01, 139–142.

Harrison, P. J., Yin, K., Lee, J. H. W., Gan, J., and Liu, H. (2008). Physical–biological coupling in the pearl River Estuary. *Cont. Shelf Res.* 28 (12), 1405–1415. doi:10.1016/j.csr.2007.02.011

Huang, F., Lin, X., Hu, W., Zeng, F., He, L., and Yin, K. (2021). Nitrogen cycling processes in sediments of the Pearl River Estuary: Spatial variations, controlling factors, and environmental implications. *CATENA* 206, 105545. doi:10.1016/j.catena.2021.105545

Huang, L., Jian, W., Song, X., Huang, X., Liu, S., Qian, P., et al. (2004). Species diversity and distribution for phytoplankton of the Pearl River Estuary during rainy and dry seasons. *Mar. Pollute. Bull.* 49, 588–596. doi:10.1016/j.marpolbul.2004.03.015

Huang, L. Q., Pang, R., S., Zhou, Q. L., and Leng, K. M. (2016). Variation trends of nitrogen and phosphorus and the relationship with HABs in Shenzhen coastal waters. *Mar. Environ. Sci.* 06, 908–914. doi:10.13634/j.cnki.mes.2016.06.017

Huang, L., and Wang, H. (1997). Basic organisms composition and environment status of the Zhujiang estuary and adjacent waters. *Mar. Environ. Sci.* 16 (3), 1–7. doi:10.1007/BF02951625

Huang, X. P., Huang, L. M., and Yue, W. Z. (2003). The characteristics of nutrients and eutrophication in the Pearl River estuary, South China. *Mar. Pollute. Bull.* 47 (1-6), 30–36. doi:10.1016/s0025-326x(02)00474-5

Jia, G. D., Peng, P. A., and Fu, J. M. (2002). Sedimentary records of accelerated eutrophication for the last 100 years at the pearl river estuary. *Quat. Sci.* 22 (2), 158–165. doi:10.3321/j.issn:1001-7410.2002.02.009

Li, G., Lin, Q., Lin, J., Song, X., Tan, Y., and Huang, L. (2014). Environmental gradients regulate the spatial variations of phytoplankton biomass and community structure in surface water of the Pearl River Estuary. *Acta Ecol. Sin.* 34, 129–133. doi:10.1016/j.chnaes.2014.01.002

Li, J., Chen, Z., Jing, Z., Zhou, L., Li, G., Ke, Z., et al. (2019). *Synechococcus* bloom in the Pearl River Estuary and adjacent coastal area–With special focus on flooding during wet seasons. *Sci. Total Environ.* 692, 769–783. doi:10.1016/j.scitotenv.2019.07.088

Li, K. Z., Huang, L. M., Zhang, J. L., Yin, J. Q., and Luo, L. (2010). Characteristics of phytoplankton community in the PREPEARL RIVER ESTUARY during saline water intrusion period. *J. Trop. Oceanogr.* 29, 62–68. doi:10.3969/j.issn.1009-5470.2010.01.010

Li, L., Ma, F. F., Zhai, X. H., Yang, W. S., Ye, P. H., and Liu, Y. (2022). Analysis on the key factors for the population evolution and early warning of harmful algal blooms based on an algal bloom in Shenzhen Bay, the South China Sea. *Ecol. Sci.* 41, 82–89.

Li, R., Xu, J., Li, X., Shi, Z., and Harrison, P. J. (2017). Spatiotemporal variability in phosphorus species in the pearl River Estuary: Influence of the river discharge. *Sci. Rep.* 7, 13649. doi:10.1038/s41598-017-13924-w

Li, T., Liu, S., Huang, L. M., and Zhang, J. M. (2007). Comparative study on the community structure of phytoplankton in autumn in different oceanic function of zones of Guangdong seacoast. *Mar. Sci. Bull.* 26, 50–59. doi:10.3969/j.issn.1001-6392.2007.02.008

Litchman, E., Klausmeier, C. A., Schofield, O. M., and Falkowski, P. G. (2007). The role of functional traits and trade-offs in structuring phytoplankton communities: Scaling from cellular to ecosystem level. *Ecol. Lett.* 10, 1170–1181. doi:10.1111/j.1461-0248.2007.01117.x

Liu, K. R. (2008). *The tendency of biodiversity variation of phytoplankton in the Pearl River Estuary [masters dissertation]*. Dalian: Dalian Maritime University.

Liu, Y. Y., AYI, Q. L., Zhang, S. R., Wu, X. R., Wan, B. N., Zhang, X. P., et al. (2020). Comparative study on the suitability of periphytic algae and phytoplankton in river health assessment. *Acta Ecol. Sin.* 11, 3833–3843. doi:10.5846/stxb201812062679

Lu, Z. M., and Gan, J. P. (2015). Controls of seasonal variability of phytoplankton blooms in the Pearl River Estuary. *Deep Sea Res. II* 117, 86–96. doi:10.1016/j.dsr2.2013.12.011

Luo, X. L., Zeng, E. Y., Ji, R. Y., and Wang, C. P. (2007). Effects of in-channel sand excavation on the hydrology of the Pearl River Delta, China. *J. Hydrol.* 343 (3-4), 230–239. doi:10.1016/j.jhydrol.2007.06.019

Ma, B., and Zhao, H. (2021). Distribution characteristics of chlorophyll a and nutrients in the PREPEARL RIVER ESTUARY in summer and their relationship with environmental factors. *Mar. Environ. Sci.* 05, 707–716. doi:10.13634/j.cnki.mes.2021.05.008

Moutin, T., Thingstad, T. F., Van Wambeke, F., Marie, D., Slawyk, G., Raimbault, P., et al. (2002). Does competition for nanomolar phosphate supply explain the prePearl River Estuarydominance of the cyanobacterium Synechococcus? *Limnol. Oceanogr.* 47, 1562–1567. doi:10.4319/lo.2002.47.5.1562

Niu, L., Luo, X., Hu, S., Liu, F., Cai, H., Ren, L., et al. (2020). Impact of anthropogenic forcing on the environmental controls of phytoplankton dynamics between 1974 and 2017 in the Pearl River Estuary, China. *Ecol. Indic.* 116, 106484. doi:10.1016/j.ecolind.2020.106484

Niu, L., van Gelder, P., Luo, X., Cai, H., Zhang, T., and Yang, Q. (2020b). Implications of nutrient enrichment and related environmental impacts in the pearl River Estuary, China: Characterizing the seasonal influence of riverine input. *Water* 12, 3245. doi:10.3390/w12113245

Peng, Y. S. (2021). *Remote sensing inversion of phytoplankton particle size classes and its spatial-temporal characteristics in the Pearl River Estuary [master's dissertation]*. Nanchang: East China University.

Peñuelas, J., Sardans, J., Rivas-Ubach, A., and Janssens, I. A. (2012). The human-induced imbalance between C, N and P in Earth's life system. *Glob. Change Biol.* 18, 3–6. doi:10.1111/j.1365-2486.2011.02568.x

Qi, M., and Liu, F. (2004). Ecological hazards of urban water eutrophication and its prevention measures. *Environ. Sustain. Dev.* 01, 44–46. doi:10.19758/j.cnki.issn1673-288x.2004.01.022

Qiu, D., Huang, L., Zhang, J., and Lin, S. (2010). Phytoplankton dynamics in and near the highly eutrophic pearl River Estuary, south China sea. *Cont. Shelf Res.* 30, 177–186. doi:10.1016/j.csr.2009.10.015

Salk, K. R., Venkiteswaran, J. J., Couture, R. M., Higgins, S. N., Paterson, M. J., and Schiff, S. L. (2022). Warming combined with experimental eutrophication intensifies lake phytoplankton blooms. *Limnol. Oceanogr.* 67 (1), 147–158. doi:10.1002/lno.11982

Sañudo-Wilhelmy, S. A., Tovar-Sanchez, A., Fu, F. X., Capone, D. G., Carpenter, E. J., and Hutchins, D. A. (2004). The impact of surface-adsorbed phosphorus on phytoplankton Redfield stoichiometry. *Nature* 432, 897–901. doi:10.1038/nature03125

Si, Y. Y. (2018). *Study on Mesozooplankton grazing and reproduction in Pearl River Estuary and north-central south China Sea [master's dissertation]*. Xiamen: Xiamen University.

Song, S. X. (1991). Preliminary study on plankton in pearl River Estuary. *Mar. Fish.* 01, 24–27.

Tan, Q., Ma, Q., Li, B. B., Lu, H. J., Fu, M., and Yao, W. (2017). Ecological health assessment of the upper reaches of the Yangtze River, based n biotic integrity index of phytoplankton. *Freshw. Fish.* 03, 97–104. doi:10.13721/j.cnki.dsyy.2017.03.015

Villegas, I., and de Giner, G. (1973). Phytoplankton as a biological indicator of water quality. *Water Res.* 7 (3), 479–487. doi:10.1016/0043-1354(73)90028-6

Wang, C., Jia, H., Wei, J., Yang, W., Gao, Y., Liu, Q., et al. (2021). Phytoplankton functional groups as ecological indicators in a subtropical estuarine river delta system. *Ecol. Indic.* 126, 107651. doi:10.1016/j.ecolind.2021.107651

Wang, C., Lai, Z. N., Li, Y. F., Li, X. H., Sovan, L., Hong, Y., et al. (2012). Population ecology of *Aulacoseira granulata* in Xijiang river. *Acta Ecol. Sin.* 32, 4793–4802. doi:10.5846/stxb201111031657

Wang, C., Li, X., Lai, Z. N., Zeng, Y. Y., Gao, Y., Liu, Q. F., et al. (2013). Temporal and spatial pattern of the phytoplankton biomass in the Pearl River Delta. *Acta Ecol. Sin.* 33, 5835–5847. doi:10.5846/stxb201305191112

Winder, M., and Sommer, U. (2012). Phytoplankton response to a changing climate. *Hydrobiol.* 698 (1), 5–16. doi:10.1007/s10750-012-1149-2

Wei, G., Q., Wang, H., Cai, W. X., and Yi, B. (2012). 10-year retrospective analysis on the harmful algal blooms in the Pearl River Estuary. *Mar. Sci. Bull.*, 1001–6392. 2012.4.017. doi:10.11840/j.issn

Xiong, Y. J., and Liu, J. F. (2018). Can saltwater intrusion affect a phytoplankton community and its net primary production? A study based on satellite and field observations. *Estuaries Coasts* 41, 2317–2330. doi:10.1007/s12237-018-0427-2

Xu, M. N., Wu, Y., Zhang, X., Tang, J. M., Tan, E., Zheng, Z. Z., et al. (2022). Diel change in inorganic nitrogenous nutrient dynamics and associated oxygen stoichiometry along the Pearl River Estuary. *Water Res.* 222, 118954. doi:10.1016/j.watres.2022.118954

Xu, S., Liu, Y., Fan, J., Xiao, Y., Qi, Z., and Lakshmikandan, M. (2022). Impact of salinity variation and silicate distribution on phytoplankton community composition in Pearl River Estuary, China. *Ecohydrol. Hydrobiol.* 22, 466–475. doi:10.1016/j.ecohyd.2022.01.004

Xu, S., Yang, Y., Su, L., Gong, Y., and Chen, Z. (2017). Community structure of phytoplankton in the Nansha sea area of pearl river estuary. South China Fisher. *Sci* 13 (4), 26–33. doi:10.3969/j.issn.2095-0780.2017.04.004

Ye, H., Yang, C., Tang, S., and Chen, C. (2020). The phytoplankton variability in the Pearl River Estuary based on VIIRS imagery. *Contin. Shelf Res.* 207, 104228. doi:10.1016/j.csr.2020.104228

Yin, K. D., Harrison, P. J., Broom, M., and Chung, C. H. (2011). Ratio of nitrogen to phosphorus in the Pearl River and effects on the estuarine coastal waters: Nutrient management strategy in Hong Kong. *Phys. Chem. Earth Parts A B C.* 36, 411–419. doi:10.1016/j.pce.2010.04.014

Yin, K. D., and Harrison, P. J. (2007). Influence of the Pearl River Estuary and vertical mixing in Victoria Harbor on water quality in relation to eutrophication impacts in Hong Kong waters. *Mar. Pollut. Bull.* 54, 646–656. doi:10.1016/j.marpolbul.2007.03.001

Yin, K. D., and Harrison, P. J. (2008). Nitrogen over enrichment in subtropical Pearl River estuarine coastal waters: Possible causes and consequences. *Contin. Shelf Res.* 28, 1435–1442. doi:10.1016/j.csr.2007.07.010

Yin, K. D., Qian, P. Y., Chen, J. C., Hsieh, D. P., and Harrison, P. J. (2000). Dynamics of nutrients and phytoplankton biomass in the pearl River estuary and adjacent waters of Hong Kong during summer: Preliminary evidence for phosphorus and silicon limitation. *Mar. Ecol. Prog. Ser.* 194, 295–305. doi:10.3354/meps194295

Yin, K. D., Zhang, J., Qian, P., Jian, W., Huang, L., Chen, J., et al. (2004). Effect of wind events on phytoplankton blooms in the Pearl River Estuary during summer. *Contin. Shelf Res.* 24, 1909–1923. doi:10.1016/j.csr.2004.06.015

Yu, L., and Gan, J. (2022). Reversing impact of phytoplankton phosphorus limitation on coastal hypoxia due to interacting changes in surface production and shoreward bottom oxygen influx. *Water Res.* 212, 118094. doi:10.1016/j.watres.2022.118094

Zhang, J. P., Huang, X. P., Jiang, Z. J., and Huang, D. J. (2009). Seasonal variations of eutrophication and the relationship with environmental factors in the Zhujiang Estuary in 2006–2007. *Acta Oceanol. Sin.* 31, 113–120. doi:10.3321/j.issn:0253-4193.2009.03.013

Zhang, M., Cui, B., Zhang, Z., and Jiang, X. (2017). Salinity-oriented environmental flows for keystone species in the Modaomen Estuary, China. *Front. Earth Sci.* 11, 670–681. doi:10.1007/s11707-016-0609-9

Zhang, W., Sun, J., Lie, H. T., Jiang, G., Q., and Tao, J. H. (2015). Seasonal and spatial variations of nutrient and the response of phytoplankton in PREPEARL RIVER ESTUARY and adjacent sea areas. *Acta Ecol. Sin.* 12, 4034–4044. doi:10.5846/stxb201308262158

Zhang, W., Yan, Y., Zheng, J., Li, L., Dong, X., and Cai, H. (2009). Temporal and spatial variability of annual extreme water level in the Pearl River Delta region, China. *Glob. Planet. Change* 69 (1-2), 35–47. doi:10.1016/j.gloplacha.2009.07.003

Zhou, W., Jie, G., Liao, J., Shi, R., and Long, A. (2016). Characteristics of phytoplankton biomass, primary production and community structure in the modaomen channel, PRE, with special reference to the influence of saltwater intrusion during neap and spring tides. *PLoS ONE* 11 (12), e167630. doi:10.1371/journal.pone.0167630

Zhu, J., Hong, Y., Zada, S., Hu, Z., and Wang, H. (2018). Spatial variability and coacclimation of phytoplankton and bacterioplankton communities in the Pearl River Estuary, China. *Front. Microbiol.* 9, 2503. doi:10.3389/fmicb.2018.02503

frontiers | Frontiers in Environmental Science

TYPE Original Research
PUBLISHED 07 February 2023
DOI 10.3389/fenvs.2023.1097049

OPEN ACCESS

EDITED BY
Yiping Wu,
Xi'an Jiaotong University, China

REVIEWED BY
Chunhua Zhang,
Ludong University, China
Wenqiang Xu,
Xinjiang Institute of Ecology and Geography (CAS), China
Xingcai Liu,
Institute of Geographic Sciences and Natural Resources Research (CAS), China
Weili Duan,
Xinjiang Institute of Ecology and Geography (CAS), China

*CORRESPONDENCE
Wenzhi Zhao,
✉ zhaowzh@lzb.ac.cn
Hu Liu,
✉ lhayz.lh@gmail.com

SPECIALTY SECTION
This article was submitted to Drylands, a section of the journal Frontiers in Environmental Science

RECEIVED 13 November 2022
ACCEPTED 17 January 2023
PUBLISHED 07 February 2023

CITATION
Bai X, Zhao W, Liu H, Zhang Y, Yang Q, Liu J and Chang X (2023), Effects of precipitation changes and land-use alteration on streamflow: A comparative analysis from two adjacent catchments in the Qilian Mountains, arid northwestern China.
Front. Environ. Sci. 11:1097049.
doi: 10.3389/fenvs.2023.1097049

Effects of precipitation changes and land-use alteration on streamflow: A comparative analysis from two adjacent catchments in the Qilian Mountains, arid northwestern China

Xuelian Bai[1,2,3], Wenzhi Zhao[1,2]*, Hu Liu[1,2]*, Yongyong Zhang[1,2], Qiyue Yang[1,2], Jintao Liu[4] and Xueli Chang[5]

[1]Linze Inland River Basin Research Station, Chinese Ecosystem Research Network, Lanzhou, China, [2]Northwest Institute of Eco-Environment and Resources, Chinese Academy of Sciences, Lanzhou, China, [3]University of Chinese Academy of Sciences, Beijing, China, [4]State Key Laboratory of Hydrology-Water Resources and Hydraulic Engineering, Hohai University, Nanjing, China, [5]College of Resources and Environmental Engineering, Ludong University, Yantai, China

Comparative analysis of the impacts of precipitation and land use on streamflow from adjacent catchments is critical to exploring pathways toward water security and sustainable development. In this work, two adjacent catchments (the Mayinghe and Xidahe, abbreviated as MYC and XDC, respectively) in northwestern China were selected to compare the impacts of precipitation change and land use alteration on streamflow change during 1956–2019 using field observation streamflow data and satellite data. An opposite trend of streamflow was found for the two catchments from 1956 to 2019: the streamflow decreased significantly in the MYC ($-0.63 \times 10^7 m^3/10a$, $p < 0.05$), while it increased in the XDC ($0.71 \times 10^7 m^3/10a$, $p < 0.05$). Land conversion dominated the streamflow reduction in the MYC, with a contribution of about 68.3%. In the XDC, precipitation was confirmed to be the major factor driving the increase in streamflow. The streamflow for farmland irrigation reached $27.97 \times 10^4\ m^3/km^2$ in the MYC, which was the leading factor of streamflow reduction in the basin. The findings obtained from this work can shed light on the quantitative understanding of streamflow changes in small catchments and offer a scientific basis for sustainable water management in other inland river basins.

KEYWORDS

streamflow, inland river basin, northwestern China, land use alteration, precipitation change

1 Introduction

Climate change and human activities have affected hydrology in several ways and to varying degrees (Piao et al., 2010; Cooley et al., 2021). Global warming leads to the acceleration of the hydrological cycle, increasing the frequency of extreme hydrological events such as floods and droughts (Piao et al., 2010; Asadieh and Krakauer, 2015; Duan et al., 2022). It also affects the temporal and spatial distribution of water resources, and thus threatens the stability of the ecosystem and thereby of human society (Dey and Mishra, 2017; Lebek et al., 2019; Palmer and Ruhi, 2019; Satge et al., 2019; Darvini and Memmola, 2020). Intensive human activities have caused changes in the underlying surface, such as the conversion from grassland and forest land to farmland and cities, in turn increasing the uncertainty of the availability of water resources, often leading to water resource shortages (Rust et al., 2014; Senbeta and Romanowicz, 2021). Streamflow is one of the main components of the hydrological process, and it plays an important role in water resource security. It is also a key factor in controlling vegetation distribution and species diversity in basins (Dey and Mishra, 2017; Palmer and Ruhi, 2019). Streamflow is affected by various factors including climate, land use, topography, human activities, and so on (Beck et al., 2015; Pourmokhtarian et al., 2017; Guzha et al., 2018; Williamson and Barton, 2020). Climate variability and land use change are considered to be two key factors that control streamflow dynamics in many regions (Fenta et al., 2017; Anache et al., 2018; Lebek et al., 2019; Darvini and Memmola, 2020). For example, precipitation change directly leads to the variation of streamflow, and there is a strong correlation between extreme precipitation and extreme flood (Pall et al., 2011; Duan et al., 2022). And land use change affects the utilization efficiency of water resources, while increasing farmland area leads to an increase in streamflow consumption, although the implementation of water conservation measures could mitigate some of these negative impacts. For sustainable water management and exploring pathways toward water security, understanding streamflow dynamics under precipitation and land-use change is essential.

Numerous researches have reported on streamflow variation, based on long-term observation data, remote sensing data, hydrological simulation data (Zhang et al., 2015; Liu et al., 2017), and even analyzed the driving mechanism behind the observed variation trends (Huo et al., 2021; Su et al., 2021). Models such as the Soil and Water Assessment Tool (SWAT) and the Budyko-based models (Yang et al., 2014; Dey and Mishra, 2017; Zhai and Tao, 2017), the paired catchment method (Rangecroft et al., 2019) and statistical methods based on the double mass curve (Gao et al., 2017) are now available, to elucidate the role of climate change and anthropogenic stressors in shaping the streamflow hydrograph. Comparative studies have also been carried out in many regions throughout the world to further explore the relative and combined effects of climate change and anthropogenic stressors on streamflow (Liu et al., 2017; Cheng and Yu, 2019). These studies have conducted in-depth research on streamflow variations, but there remains a constant need for a better quantitative understanding of this subject through a comparative study of small adjacent catchments experiencing different agricultural intensities, for the following reasons. First, most available comparison researches have been conducted at the mesoscale, but compensating effects in complex watersheds with a variety of land use types, and the impacts of land use changes on hydrology, are relatively less significant at large scales, while they are much more pronounced at smaller scales (Cao et al., 2009; Bieger et al., 2015). Secondly, few comparative studies have been conducted in arid or semi-arid regions, even though the driving mechanisms of streamflow variation have been widely reported in northwestern China (Yang et al., 2017; He et al., 2019; Xue et al., 2021). Furthermore, these driving mechanisms present complex characteristics because it is difficult to ensure the consistency of the natural background in comparative studies, as there are obvious differences in geographical location, terrain and climate, among various catchments (Yang et al., 2014; Darvini and Memmola, 2020).

Northwestern China has an arid or semiarid continental climate, with an average annual rainfall of 130 mm (about 15% of the average annual precipitation globally) (Arora 2001; Shen et al., 2013). It is one of the areas where ecological resources are restricted mainly by water resources, and where streamflow changes have had significant effects on environmental and socioeconomic resources, so that ill-advised utilization of streamflow may lead to the degradation of natural vegetation and aggravate desertification (Lesk et al., 2016; Fereidoon and Koch, 2018). As one of the region most sensitive to climate change (Chen et al., 2015), Northwestern China is highly vulnerable to variabilities in precipitation and temperature; yet it is a place where future streamflow dynamics are complex and uncertain (Ning et al., 2020). In addition, rapid population growth and urbanization have led to oasis expansion and increasing demand for farmland, significantly changing the land cover over the past several decades, and changes such as farmland expansion and grassland loss have led to the redistribution of streamflow in the region (Brath et al., 2006; Sharma et al., 2019). Although many studies have been conducted on streamflow changes and its influencing factors in Northwest China (Wang et al., 2006; Zhang et al., 2014; Yang et al., 2017; Xue et al., 2021), most of them were concentrated in single watershed such as Heihe River Basin (HRB) and Shiyang River Basin (SRB), lacking comparative studies on small catchments. Therefore, a comparative analysis of the causes of streamflow variation in small catchments in Northwestern China is critical to the management of water resources in this region.

The purpose of this work is to analyze the impacts of precipitation change and land use alteration on streamflow of two small adjacent catchments in arid northwestern China, the Mayinghe catchments (MYC) and Xidahe catchments (XDC). The objectives were i) to compare streamflow variations and land use change during 1956–2019 in the MYC and XDC; ii) to quantify the impacts of land use alteration and precipitation change on streamflow; and iii) to estimate water consumption by farmland in different periods from 1956 to 2019. The study could shed light on the understanding of the hydrological process in inland river basins, and provide a valuable reference for coordinating the relationship between human activities and water resources in the context of climate change.

2 Materials and methods

2.1 Study area

The MYC (100°56′35″-101°18′7″ E, 37°54′58″-38°30′4″ N) and XDC (101°7′34″-101°29′19″ E, 37°47′24″-38°4′34″ N) are first-order catchments of two larger adjacent inland river basins (HRB and SRB, respectively) of arid northwestern China (Figure 1). Both of them originate from the northern part of the middle Qilian Mountains in Shandan County, Gansu Province, and share similar geographical settings (climate, soil and vegetation, et al.), but are under different levels of anthropogenic stressors from agriculture. The advantage of this selection is to ensure the consistency of the natural background of the selected catchments as much as possible, to reduce the potential uncertainties involved in the comparison analysis. The mainstream lengths of XDC and MYC are 30.6 km and 153km, and the areas are 660 km^2 and 1163 km^2, respectively. The terrain of both the catchments is the high elevation in the south and low in the north: it ranges from 2157 m above sea level (m asl.) in the mountain valley to 4423 m asl. at the peak. Both catchments are continental alpine plateaus with a semi-arid climate, with the characteristics of cold, but still distinctive four seasons, concentrated rainfall and obvious vertical zonation (Zhang and Kang, 2021). The precipitation is mostly

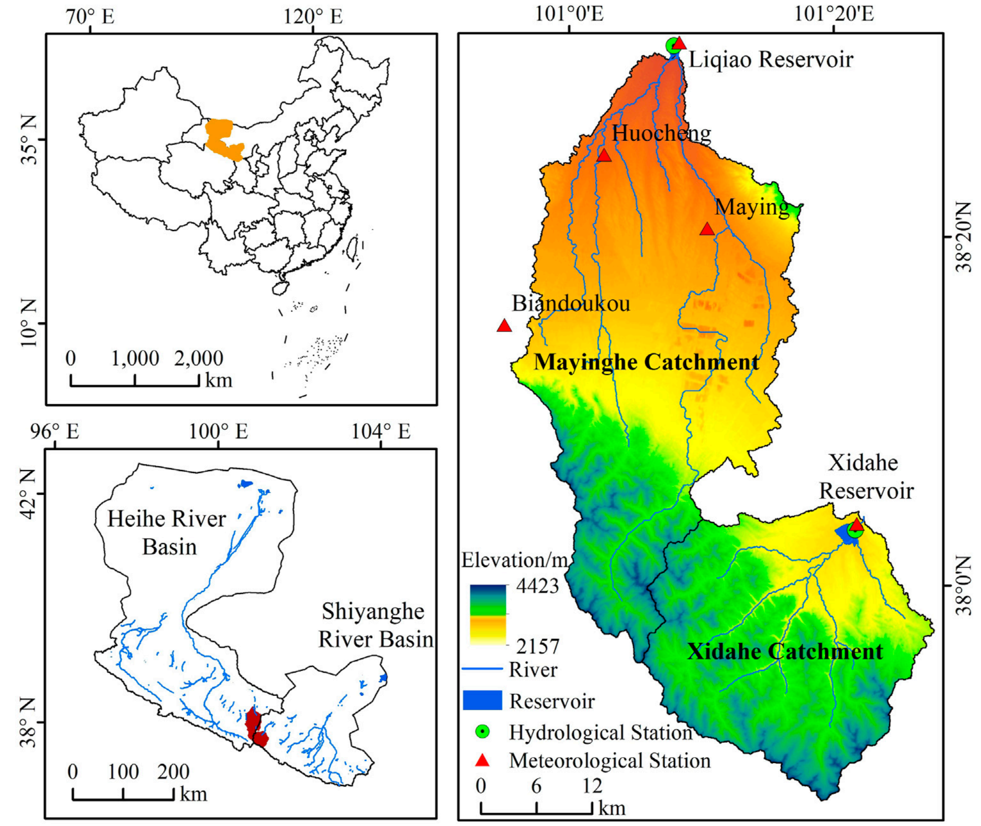

FIGURE 1
Geographical location, river and topographic characteristics and locations of meteorological and hydrological stations of XDC (Xidahe Catchment) and MYC (Mayinghe Catchment).

concentrated in the summer, with the highest temperatures from June to September, a period that also accounts for about 80% of the total annual precipitation. The main recharge source of the surface runoff is precipitation, followed by ice and snow melt.

In the MYC, the annual average precipitation and evaporation were 395 mm and 2153.6 mm from 1956 to 2019, respectively. The annual average streamflow was 6.16 × 10^7 m^3 and the annual temperature varied from -29.8°C to 39.8°C with a mean of 7°C, the average depth of frozen soil was generally between 1.2 m and 1.6 m, and the annual frost-free period was 214 days. The total amount of water resources available in the basin is 0.91 × 10^8 m^3, and the *per capita* water resources are less than 0.06 × 10^8 m^3, which is lower than the internationally recognized water shortage warning line of 0.17 × 10^8 m^3. The upstream section of the MYC is home to the Shandan Army Horse Breeding Farm, the oldest such farm in the world, and the largest in Asia. It is also an important water conservation area of the MYC. However, it is greatly affected by human activities, as large areas of land reclamation have changed the land cover pattern and also significantly affected streamflow in the region. From 1967 to 2000, the conversion of forest and grassland to farmland in the MYC resulted in the reduction of the annual streamflow by 28% (Wang et al., 2006). These developments and the resulting utilization of water resources have resulted in serious ecological deterioration and led to a water resource crisis in the entire basin. The vegetation is vertically distributed in the mountains, with scrub-steppe zones and forest-steppe zones appearing from the foothills to the tops of the mountains in turn. In the corridor plains, it is mainly covered by scrubs and sparse trees. And the main soil types are chestnut and calcareous soil. There are 53,300 people in MYC, and the population is mainly concentrated in the downstream plain, while the upstream is relatively small.

In the XDC, the annual temperature varies from - 27°C to 35.3°C with a mean of 5.7°C from 1956 to 2019, the average depth of frozen soil was generally between 1.4 m and 1.7 m, and the annual frost-free period was 134 days, and annual average precipitation and evaporation were 395 mm and 2098.8 mm, respectively. The annual average streamflow was 1.68 × 10^8 m^3 during 1956–2019, the implementation of a water diversion project since 2003 has introduced an average of 0.25 × 10^8 m^3 per year into the total streamflow of the basin. The annual average sediment concentration was 0.26 kg/m^3, and the annual sediment discharge was 41,600 kg. Contrary to the situation of MYC, the XDC was relatively less affected by human activities, and its land cover has remained a relatively pristine state. It is mainly covered by scrubs, the middle and high mountains are covered by trees, shrubs and grasslands, and some areas in the middle reaches are covered by grasslands and forests. The soil is mostly mountain grey cinnamon soil and subalpine meadow soil. The terrain of the basin is mainly mountainous and the population is relatively small.

2.2 Data sources and pre-processing

The products of land use in the Qilian Mountains from 1985 to 2019 were provided by National Tibetan Plateau Data Center (http://data.tpdc.ac.cn). The dataset was produced by using Landsat data. There were 10 land use categories in the products, and we classified them into six categories. The spatial resolution was 30 m, and the accuracy reached 92.2% as evaluated by Google Earth images and field survey data (Zhong and Jue, 2019). Six satellite images, Landsat MSS (1975), Landsat TM (1985, 1995, 2005), and Landsat OLI (2015, 2019), obtained from USGS through Google Earth Engine (GEE) were also used to interpret previous land use changes, and land use categories were identified based on spectral characteristics of the watershed using supervised classification. Finally, all land use types were classified into six categories, namely forest, grassland, farmland, residential, barren land, and water. To improve the accuracy of the final land use change data, we combined the land use data of the Qilian Mountains with the supervised data and then calibrated them using visual interpretation and the third national land survey data of China.

Streamflow and precipitation data were observed data, with a period of 64 years from 1956 to 2019, acquired from the Shandan Hydrology Bureau. Hydrological stations were built above the dams of the Liqiao and Xidahe reservoirs, and these accurately record the inflow and outflow of the catchments. There are five meteorological stations involved in the precipitation data. The precipitation of MYC involved four meteorological stations, the data of Huocheng, Maying and Liqiao Reservoir were used to represent the precipitation status in the middle and lower reaches of MYC. Since there was no meteorological station in the upper reaches of MYC, we selected the precipitation data of Biandukou, which was the nearest to MYC, to represent the upstream precipitation. Finally, the average of these four stations represents the precipitation status of the whole MYC. There were relatively few meteorological stations involved in the XDC, only Xidahe Reservoir.

Digital Elevation Model (DEM) data were downloaded from the Geospatial Data Cloud (http://www.gscloud.cn/), the data type was ASTER GDEM, and the spatial resolution was 30 m, and it was used to extract the catchment.

2.3 Methods

2.3.1 Mann-Kendall test

A change point indicates the starting time of an abrupt change in streamflow and precipitation. The non-parametric Mann-Kendall (M-K) test (Mann 1945; Kendall 1975) was used to detect change points of annual streamflow and precipitation in the XDC and MYC. It is based on the correlation between the rank of a time series and the time order, which can handle non-normalcy with high asymptotic efficiency and is commonly used to analyze the trend and abrupt points in various hydrological and meteorological series. The test is given as follows:

$$\mathrm{UF}_i = \frac{S_i - E(S_i)}{\sqrt{var(S_i)}} \quad (i = 1, 2, \ldots, \mathrm{n}) \tag{1}$$

$$S_k = \sum\nolimits_{i=1}^{k} r_i \quad (k = 2, 3, \ldots, \mathrm{n}) \tag{2}$$

$$r_i = \begin{cases} 1, & x_i > x_j \\ 0, & x_i \le x_j \end{cases} \quad (j = 1, 2, \ldots, i - 1) \tag{3}$$

Following the assumption that x_i is an independent and identically distributed random variable, the expected value E (Si) and variances var (Si) are given by (Hamed 2008; Bao et al., 2012):

$$E(S_i) = \frac{i(i-1)}{4} \tag{4}$$

$$var(S_i) = \frac{i(i-1)(2i+5)}{72} \tag{5}$$

Then, the curve of UF_i and UB_i can be shown after calculating UB_i based on the inverse time series x_n, x_{n-1}, . . . , x_1 of UF_i and the $\mathrm{UB}_i = -\ \mathrm{UF}_i$, $i = n, n\text{-}1, \ldots, 1$. The change year can be found if there was an intersection of two curves and the series trend is statistically significant.

2.3.2 Correlation analysis

In this study, Pearson correlation was used to evaluate the linear correlation between runoff, precipitation and various land use types. The equation is given as follows:

$$\mathrm{r} = \frac{\sum_{i=1}^{n}(x-\bar{x})(y-\bar{y})}{\sqrt{\sum_{i=1}^{n}(x-\bar{x})^2 \sum_{i=1}^{n}(y-\bar{y})^2}} \tag{6}$$

$$\bar{x} = \frac{1}{n}\sum\nolimits_{i=1}^{n} x_i,\ \bar{y} = \frac{1}{n}\sum\nolimits_{i=1}^{n} y_i \tag{7}$$

where x, y were the variables, such as runoff and precipitation, and $\bar{x}$, $\bar{y}$ were the mean values of the two variables. The significance level of the correlation was obtained by querying the correlation coefficient table, and n is the number of observations in x and y variables.

2.3.3 Streamflow for farmland irrigation

In the MYC, the main soil types are Chestnut and Calcareous soil, the soil structure and water permeability are relatively poor, and both types have obvious calcium accumulation and a high content of carbonate, which is not conducive to streamflow leakage; hence any water loss caused by river channel and soil water infiltration can be ignored. Therefore, the XDC rainfall-streamflow linear regression was considered as the reference model to estimate the streamflow consumption of the MYC under farmland expansion. First, the chi-square test was applied to verify whether precipitation, streamflow and land use data are independent of each other, if they are independent of each other, the rainfall-streamflow model of the XDC was established through linear regression. Then the precipitation of the MYC was brought into the model to obtain the streamflow without the effects of farmland reclamation. The streamflow for farmland irrigation was obtained by calculating the difference between the observed streamflow and the estimated streamflow. The specific method is as follows:

$$Q_X = aP_X + b \tag{8}$$

$$Q_{farmland} = \frac{Q_{estimated} - Q_{observed}}{A} \tag{9}$$

where Q_X and P_X are the streamflow and precipitation of the XDC, respectively; a is the regression coefficient and b is the regression intercept. $Q_{estimated}$ and $Q_{observed}$ are the estimated streamflow and observed streamflow in the MYC, respectively; A is the farmland area during the different periods in the MYC, and $Q_{farmland}$ is the streamflow for farmland irrigation.

2.3.4 Separating the impacts of land use alteration and precipitation change

Human activities and climate variability were considered to be the two main factors impacting streamflow. Since in water-limited regions, annual streamflow is more sensitive to precipitation than to other climate factors (Donohue et al., 2011; Liang and Liu, 2014), we applied linear regression to estimate the impacts of precipitation and land use (Koster and Suarez, 1999; Sankarasubramanian et al., 2001; Milly and Dunne, 2002), which was displayed by:

$$\triangle Q = \triangle Q_{precipitation} + \triangle Q_{land\ use} \tag{10}$$

$$\triangle Q = Q_2 - Q_1 \tag{11}$$

where ΔQ is the streamflow difference before and after the division point, Q_1 is the streamflow before the division point, Q_2 is the streamflow after the division point; and $\Delta Q_{precipitation}$ and $\Delta Q_{land\ use}$ are the streamflow changes caused by precipitation change and land use change, respectively.

The division points were set based on the corresponding years of existing land use data and 10-year intervals, and a total of seven periods are divided from the initial year. In the study of a period, the years before the division was regarded as pre-division, and the years after the division point and before the next division point were considered as post-division. The streamflow change of the pre-division point was a reference period for considering the initial land use, and the post-division year was a period after the land use change occurred. First, it was assumed that precipitation change had the same effects on streamflow variability in both of the two periods, and that streamflow change was therefore only impacted differently, during the two periods, by land use changes (Zhang et al., 2014; Chen et al., 2020). Hence the relationship (*R1*) between annual precipitation and annual streamflow at the pre-division point was established by linear regression, and the hypothetical Q'_2 (streamflow changes without the effects of land use change) can be determined by substituting the annual precipitation after the division point period into *R1*. Before applying these assumptions, it was necessary to verify them based on available data. One step was to check whether the change of regression coefficients in pre- and post-division periods was not significant, another step was to check whether any land use class changed significantly than others. If these conditions were true, the assumptions can be applied to the study. Subsequently, separating the impacts of precipitation variability and land use change can be given by:

$$\triangle Q_{precipitation} = Q_1 - Q'_2 \tag{12}$$

$$\triangle Q_{land\ use} = Q'_2 - Q_2 \tag{13}$$

Finally, the contributions of the two factors can be quantified by:

$$C_{precipitation} = \frac{|\triangle Q_{precipitation}|}{|\triangle Q_{precipitation}| + |\triangle Q_{land\ use}|} \times 100\% \tag{14}$$

$$C_{land\ use} = \frac{|\triangle Q_{land\ use}|}{|\triangle Q_{precipitation}| + |\triangle Q_{land\ use}|} \times 100\% \tag{15}$$

where $C_{precipitation}$ and C_{land_use} are the contributions of precipitation change and land use change to streamflow variation.

3 Results

3.1 Precipitation and streamflow variation

Increasing trends were detected in the XDC and MYC precipitation data collected during the period of 1956–2019 (Figure 2), with change rates of 19.37 mm/10a and 4.33 mm/10a, respectively. The annual mean precipitation amounts were 395.54 mm and 395.28 mm in the two catchments, respectively. The abrupt point of precipitation was determined as 1981 in the XDC, while there was no remarkable abrupt point in the MYC. Increasing trends in precipitation during the period of 1956–1980 (with mean precipitation of 351.81 mm and a change rate of 14.01 mm/10a) were lower than those of the period of 1981–2019 (423.58 mm and 11.09 mm/10a), in the XDC. A significant increasing trend appeared in the annual streamflow of the XDC during 1956–2019, while there was a significant decreasing trend in the MYC ($p < 0.05$) with streamflow change rates of 0.071×10^8 m^3/10a and 0.063×10^8 m^3/10a, and annual mean streamflows of 1.68×10^8 m^3 and 0.62×10^8 m^3 in the XDC and MYC, respectively. In the XDC, the abrupt point of streamflow change was determined as 2003, with the decreasing trends during the period of 1956–2002 (with mean streamflow of 1.55×10^8 m^3 and change rate of 0.03×10^8 m^3/10a) being lower than those of the 2003–2019 period (2.02×10^8 m^3 and 0.21×10^8 m^3/10a). In the MYC, the abrupt point of streamflow was considered to be 1991, with the increasing trends during the period of 1956–1990 (with mean streamflow of 0.74×10^8 m^3 and change rate of 0.006×10^8 m^3/10a) being higher than those of the period of 1991–2019 (0.46×10^8 m^3 and 0.008×10^8 m^3/10a).

3.2 Spatial-temporal changes of land use

The dominant land use types in the MYC are farmland and grassland (Figure 3), which together account for more than 80% of the area. The grassland area is the largest, accounting for 58.8% and 55.3% in 1975 and 1985, respectively, while it was less than 50% of the area during 1995–2019. Although the farmland area was larger than forest, water or residential land in the MYC, its proportion ranged from only 21%–37% of the entire area. In the XDC, forest and grassland were the main land uses, accounting for about 58% and 35%, respectively, while only 1% of its area was used for agriculture. A significant change was detected in MYC farmland, grassland and residential ($p < 0.05$) while the change in forest, water and barren were not significant. And there were two main trends of land use changes in the MYC during 1975–2019: a decrease of grassland and an increase of farmland and construction land. The farmland increased by 181 km^2 while the grassland decreased by 187 km^2 from 1975 to 2019. The grassland area increased by 13.76 km^2 in the XDC, and no other land use types there increased by more than 5 km^2. The land conversions in the MYC and XDC were relatively small from 1975 to 2019 (Figure 3), accounting for only 25.9% (300.76 km^2) and 12.0% (79.48 km^2) of the catchments, respectively. There were four main types of land area change (all more than 5%), of which the grassland conversion area was the largest, reaching 226.5 km^2, and accounting for 75.3% of the conversion area. Conversions from forest land and grassland were the main forms of land use change in the XDC. The area converted from forest land to grassland was 23.91 km^2, from grassland to forest land, 13.46 km^2, which accounted for 30.1% and 16.9% of the area, respectively.

3.3 Impacts of precipitation change and land use alteration on streamflow variation

Significantly correlated relationships were detected between streamflow and both farmland and grassland in the MYC

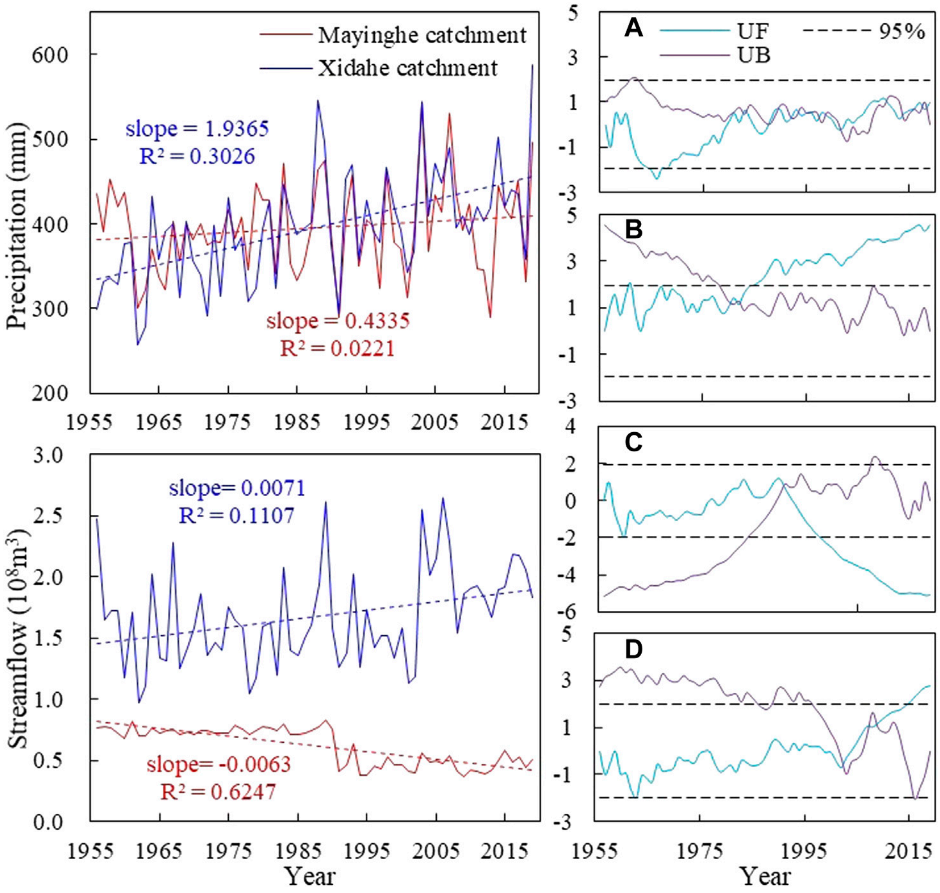

FIGURE 2
Trends of precipitation and streamflow (left column); M-K tests of precipitation and streamflow (right column): **(A)** precipitation M-K test of MYC; **(B)** precipitation M-K test of XDC; **(C)** streamflow M-K test of MYC; **(D)** streamflow M-K test of XDC. The slope is the regression coefficient of linear regression, which means that streamflow and precipitation change with time.

(Table 1). In particular, there was a significant negative correlation between streamflow and farmland ($p < 0.01$). However, a significantly correlated positive relationship was detected between streamflow and precipitation in the XDC. Streamflow variation and the contributions of land use change and precipitation change were different during various periods between 1956 and 2019 in the MYC (Figure 4). The streamflow variation was largest during the periods of 1986–1995 and 1996–2005, although during the period of 1996–2005 the streamflow decreased by 14.01×10^6 m^3 more than it did during the previous period. And the minimum streamflow change was only 0.92×10^6 m^3 in the period of 1966–1975, compared to the other periods. The streamflow variation caused by precipitation change was highest in the period of 2006–2019, especially during 2006–2015 (17.99×10^6 m^3), while the highest streamflow difference caused by land use change occurred during the period of 1986–2019, especially in 1996–2005 and 2006–2015, which were 25.19×10^6 m^3 and 19.76×10^6 m^3, respectively.

The contributions of precipitation change and land use alteration to streamflow variation were 31.7% and 68.3%, respectively, during the overall study period in the MYC. Land use change first increased streamflow and then decreased it, and the contribution of land use change was more than 60% during the period of 1956–2005, with a maximum of 98.9% during the period of 1976–1985, after which it began to decrease. After 2015, the contribution rate of land use change was less than that of precipitation. The estimated streamflow was highest (162.42×10^6 m^3 and 167.43×10^6 m^3, respectively) during the periods of 2006–2015 and 2016–2019; the smallest was 156.18×10^6 m^3, during the period of 1956–1975 (Figure 5). The biggest differences between estimated and measured streamflow were found during the two periods of 2006–2015 and 2016–2019 (117.36×10^6 m^3 and 118.32×10^6 m^3), respectively. Streamflow for farmland irrigation first increased and then decreased, from 1956 to 2019, with a change rate of 27.97×10^4 m^3/km^2. Farmland had the greatest impact on streamflow reduction during the period of 1956–1975 (33.5×10^4 m^3/km^2). However, the least impact of farmland expansion on streamflow reduction occurred during 1986–1995 (26.07×10^4 m^3/km^2).

4 Discussion

4.1 Factors affecting streamflow variations in the selected catchments

Streamflow was generally affected by many factors, such as farmland reclamation, urban expansion, geomorphic properties,

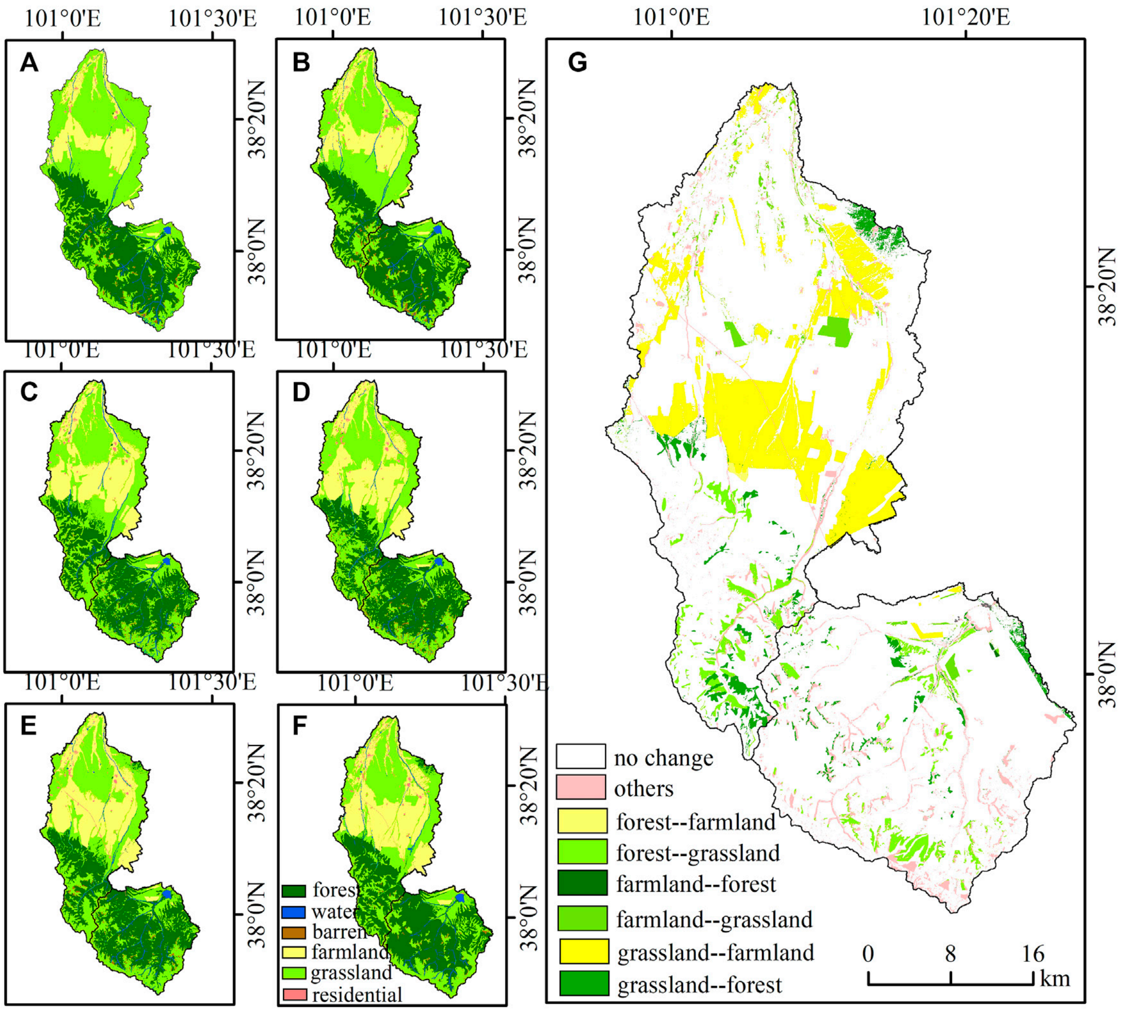

FIGURE 3
Distribution of land use and major land use conversions during 1975–2019 in the MYC and XDC **(A)**, 1975; **(B)**, 1985; **(C)**, 1995; **(D)**, 2005; **(E)**, 2015; **(F)**, 2019; **(G)**, major land use conversions from 1975 to 2019.

TABLE 1 Correlation coefficients between streamflow and precipitation, land use in MYC and XDC.

Catchment	Precipitation	Farmland	Forest	Grassland	Water	Residential	Barren
MYC	0.057	-0.86**	0.36	0.778*	0.501	-0.627	0.397
XDC	0.688*	0.106	0.102	0.101	-0.363	-0.046	-0.393

MYC, mayinghe catchment; XDC, xidahe catchment.
$^{**}p < 0.01$, $^{*}p < 0.05$.

climate warming and so on, but on the whole, it is mainly affected by climate change and land use (Cooley et al., 2021; Huo et al., 2021; Su et al., 2021). An opposite trend of streamflow was detected for the MYC and XDC during 1956–2019. We compared the correlations between streamflow and precipitation for these two adjacent small catchments and noticed that the increase of annual precipitation should be the dominant reason for the increase of streamflow in the XDC. Xue (2021) showed that the significant increase in streamflow was mainly affected by the increased precipitation of XDC from 1961 to 2018, which also supported our results. Along with the increased precipitation in northwestern China over the past decades (Qin et al., 2021), the increased temperature caused by global warming is also expected to bring more streamflow from glacier melt (Harper et al., 2012; Winkelmann et al., 2012; Zhang et al., 2017; Smith et al., 2020; Azam et al., 2021; Zhang and Kang, 2021). In contrast to the XDC, the correlation between streamflow and precipitation was no longer significant in the MYC. Our results indicated that significant changes occurred in farmland (the area increased by 15.6%) and grassland (the area decreased by 16%) in the MYC during this period, but the land use change detected in the XDC was almost negligible (the increase in farmland area was less than 1%) compared with that in the MYC. Considering that both catchments have experienced the same

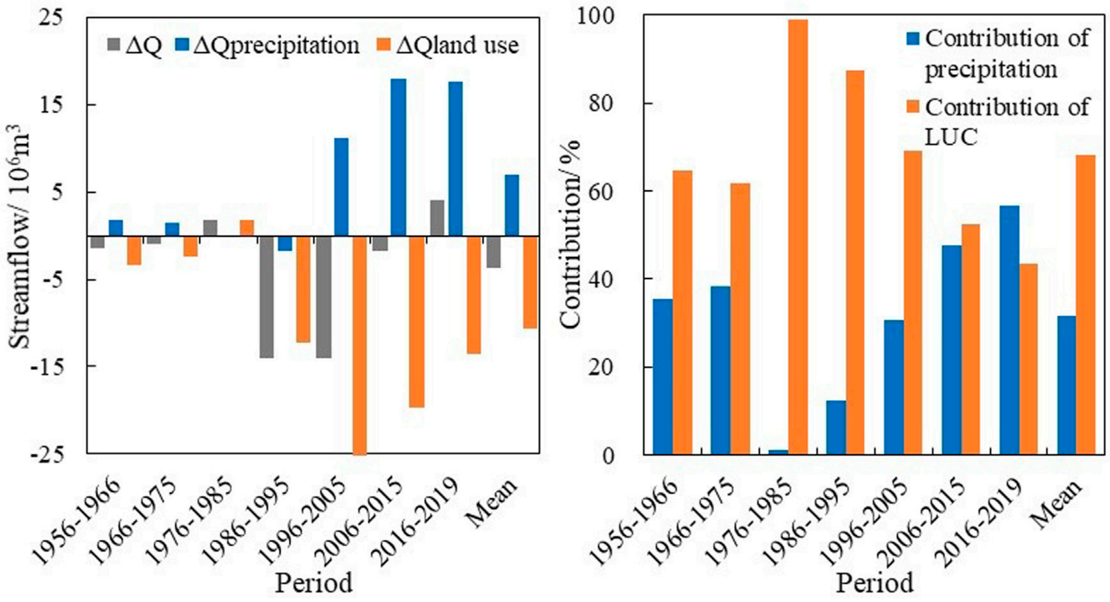

FIGURE 4
Streamflow difference before and after division point and contributions of land use change and precipitation change in various periods from 1956 to 2019 in the MYC. (ΔQ is the streamflow change based on the comparison of before and after the division point; $\Delta Q_{precipitation}$ and $\Delta Q_{land\ use}$ are the streamflow changes caused by precipitation change and land use change, respectively).

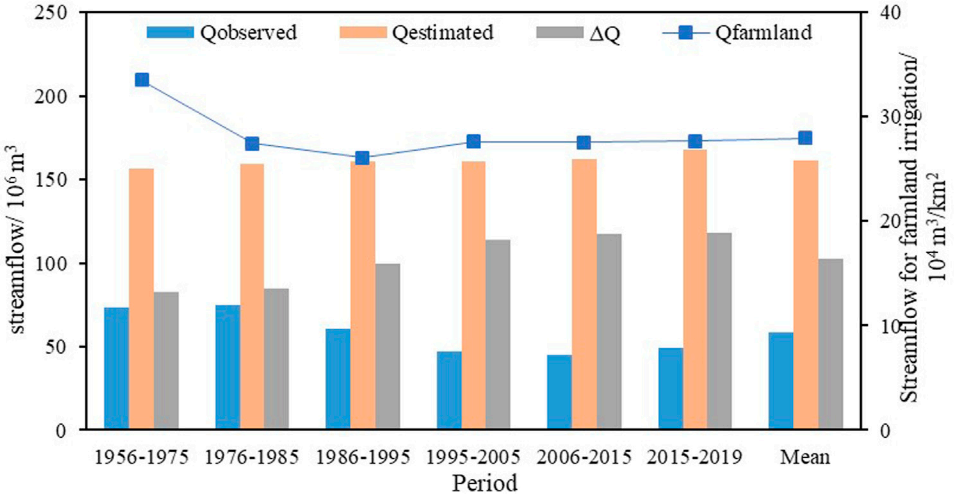

FIGURE 5
Differences (ΔQ) between observed streamflow ($Q_{observed}$) and estimated streamflow ($Q_{estimated}$), and streamflow for farmland irrigation ($Q_{farmland}$) in various periods during 1956–2019 in the MYC.

climate change background, the different streamflow regimes between the MYC and the XDC appear to have been caused mainly by their different land use histories (Table 1).

By comparing the abrupt change points detected in the measured time series, the above conclusions could be further enhanced. For example, a sharp decrease of about 0.34 × 10^8 m^3 was detected in streamflow of the MYC around 1991. This time was roughly coincident with the implementation of household contract responsibility system (in the 1980s), which stimulated agricultural land reclamation from other types of land use (Huang et al., 2014), and thus reduced streamflow through irrigation-intensive farming (Bao and Fang, 2007; Xie et al., 2018). The cumulative contribution of land-use changes to streamflow reduction in the MYC reached 68% during the past 64 years, and the contribution even exceeded 90% during 1976–1985, when farmland expanded rapidly (Figure 4). A previous study also showed that farmland expansion has been the main cause of streamflow change in the MYC from 1967 to 2000 with a contribution of 77%–80% (Wang et al., 2006). Human activities also have a great impact on streamflow in the other regions of inland river basins of Northwestern China, such as the whole HRB, Taohe Upstream Basin and SRB (Wang et al., 2007; Yang et al., 2017; Xue et al., 2021). Although the contribution of land-use change to streamflow has gradually decreased in recent years due to the policy of returning farmland to forest and grassland, land-use change is still the main reason for streamflow reduction in the MYC, primarily because compensating effects are much more pronounced at smaller scales (Cao et al., 2009; Zhang et al., 2014; Bieger et al., 2015). In the XDC, a sharp increase of about $0.47 \times 10^8\ m^3$ was detected in streamflow around 2003, which was coincident with the implementation of a water diversion project (in 2003), which increased streamflow *via* input from other rivers. These shifts also prove that land use history has a great impact on streamflow variations. This mutation time was also consistent with Xue's result (Xue et al., 2021), which confirmed the reliability of our results.

Although the general global climate change trend is toward warmer and wetter weather, and glacier melt has accelerated in the Qilian Mountains (Guo et al., 2018), there is no obvious response of streamflow change in the XDC, which further indicates that other factors besides human activities also affect this result, such as permafrost coverage, catchment elevation and groundwater level (Niu et al., 2011; He et al., 2019). Viola et al. (2017) pointed out that the amount of rainfall converted into streamflow in a high-altitude catchment is higher than that in a low-altitude catchment, which indicates that the XDC, with an average altitude of 3465 m, has great potential for converting precipitation into streamflow. In addition, the groundwater level rose under the influence of the policy of prohibiting overexploitation of groundwater, reducing streamflow infiltration of the XDC and maintaining a normal circulation of surface water (Hochmuth et al., 2015; Huang et al., 2017). Moreover, the proportion of grassland and forest land was considered as the main factor affecting the annual streamflow of basins in temperate continental climate regions (Huo et al., 2021), and the XDC, with a total proportion of grassland and forest land accounting for 93% of the area, may not be greatly affected by the warming and wetting climate. All of these influences affect streamflow variations and increase the complexity of hydrological processes, and indicate that human activities and climate change play different roles in different regions and at different scales.

4.2 Uncertainty involved in the quantification analysis

Although we quantified the impacts of precipitation change and land use change on streamflow, uncertainties remain in the assessment of their respective contributions. Uncertainties could be induced by data representation. For example, the sparsely distributed stations may ignore the hydrological processes in upstream of MYC. Considering that Biandoukou was close to MYC and its altitude was similar to that of the upstream of MYC, it is acceptable to replace the upstream precipitation from this meteorological station when there is no suitable data available. The hydrological data and land use data are not well matched in terms of their spatial scales and resolution. The hydrological data (i.e., precipitation and streamflow) were collected at individual stations, while the land use data were extracted from satellite images (Zhu et al., 2018; Duan et al., 2021). Given that the evaluation of streamflow and land use change was largely based on trend analysis rather than data points, the errors introduced by the data resolution could be largely ignored. Multi-sourced data (i.e., Landsat data, products of land use in the Qilian Mountains) were used to classify land use. In addition, we assumed that streamflow change is only influenced by land use and precipitation, the effect of evapotranspiration and other climate variables may not be representative. This assumption also may not be applicable to catchments with large land area, low gradient, slow water flows and rich water, but it could be considered plausible for the XDC and MYC, with their high gradients and limited water resources, because annual streamflow is more sensitive to precipitation than to evapotranspiration in these regions (Donohue et al., 2011; Berghuijs et al., 2016; Zhang et al., 2021). Moreover, in the water consumed by human activities, only farmland irrigation was considered, while domestic and industrial production use were neglected, which may have led to calculation errors in streamflow consumption. Considering, however, that the proportions of industrial production and domestic water use in these catchments are small and mainly come from groundwater, these errors could be largely ignored.

4.3 Implications for regional development

Streamflow guarantees regional ecosystem stability and ecological protection in arid northwestern China (Dey and Mishra, 2017; Palmer and Ruhi, 2019). But streamflow also serves as the primary source of irrigation water for agriculture (which in turn is the dominant source of livelihood in arid regions like the study area). Because each of the systems, including vegetation, water, soil and atmosphere, will be affected in a variety of ways by reduced streamflow, if too much water is used for irrigation and streamflow continues to decrease, irreversible ecological disasters are probable, although rarely does one know just when such an event will happen (Palmer and Ruhi, 2019; Morganstein and Ursano, 2020). Balancing water use between human food production and the needs of the environment is extremely important for local communities and governments, but also complex and difficult to achieve in practice (Qin et al., 2022). Thus, an explicitly formulated strategy for streamflow forecasting and management is needed, especially in the climate change context. In streamflow management, water allocation among various ecosystems should be coordinated to prevent excessive water use in any given ecosystem, especially in agriculture, which may reduce the water available for natural vegetation, causing desertification (Satge et al., 2019). It is necessary to find the threshold of ecological water demand in different regions, to realize the maximum benefit by using the minimum amount of water for human needs. And the water resources should be reasonably allocated in the upper, middle and lower reaches of a river, through a series of policies and the coordination of various departments, to alleviate the contradiction between the supply and demand of water resources and prevent downstream interruption caused by excessive water use in the upper and middle reaches.

In the context of global climate change, the uncertainty of precipitation and snowmelt in arid northwestern China leads to instability in streamflow, which in turn could lead to an increase in the number of extreme events such as floods and droughts, posing a threat to both the natural environment and human life (Lesk et al., 2016; Fereidoon and Koch, 2018; Duan et al., 2022). For example, drought, flood and unpredictable rainfall distribution threaten food security by increasing the uncertainty of agricultural production, and an increase in drought frequency and intensity will increase desertification and lead to serious land degradation (Akbari et al., 2020; Qin et al., 2022). Although climate change is not considered to be the main driving factor of streamflow variation in some regions, glacier retreats and the melting of previously frozen soil caused by climate change have important impacts on streamflow regulation (Niu et al., 2011; He et al., 2019). The reduction of large-scale snow cover will aggravate spring droughts in the future, and the reliability of snow melt for river runoff will be greatly reduced (Qi et al., 2022). Therefore, the multi-scale variation characteristics of hydrological processes such as precipitation, streamflow and the melting of alpine snow and glaciers should be the focus of future research, to increase the accuracy of predictions and help humans prepare for possible water insecurity, in the future. In addition, vegetation can play an important role in ameliorating streamflow instability (Zhang et al., 2012; Aires et al., 2020; Huo et al., 2021). The impact of vegetation patterns and spatial allocation modes, on the temporal and spatial variation of streamflow, should be studied, to regulate the dynamic process of streamflow. The possible impact of the construction of large-scale restoration projects on the decrease of natural streamflow in arid Northwest China should be considered. One suggestion is that vegetation restoration should focus on restoring natural areas, and that artificial vegetation restoration projects should be properly controlled (Zastrow, 2019). Appropriate vegetation coverage, matching the sustainable utilization of water and soil resources in the basin, should be based on the water-carrying capacity, to give full play to the ecological, economic and social benefits of vegetation.

5 Conclusion

In this study, hydrological and satellite data were used to compare the streamflow variations, the contributions of precipitation change and land use alteration to the streamflow, and the water consumption attributable to farmland expansion for two adjacent basins in the Qilian Mountains, in northwestern China. Opposite trends in streamflow were detected in the two catchments during the period of 1956–2019; the streamflow in the MYC decreased significantly ($-0.63 \times 10^7 m^3/10a$) while it increased in the XDC ($0.71 \times 10^7 m^3/10a$). A sharp decrease of about 0.34×10^8 m^3 in streamflow was detected in the MYC around 1991, while an abrupt increase of about 0.47×10^8 m^3 was detected in the XDC around 2003. The land conversions within the MYC were relatively small, accounting for only 25.9% (300.76 km^2) of the streamflow changes in the catchment, yet land conversion was the dominant reason for streamflow reduction in the MYC, as its contribution reached 68.3%. The streamflow consumed by farmland irrigation first increased and then decreased, from 1956 to 2019, with a change rate of 27.97×10^4 m^3/km^2. The greatest impact of farmland irrigation on streamflow occurred during 1956–1975 (33.5×10^4 m^3/km^2). In the XDC, however, changes in precipitation were confirmed to be the dominant factor driving the increase of streamflow. We conclude that although streamflow is affected by both human activities and climate change, these influences vary greatly among different regions. The relationship between the intensity of human activities and the availability of water resources should be studied more closely, and anthropogenic stressors and water resource allocation should be coordinated to maintain water resource security and prevent regional water resource crises.

Data availability statement

The original contributions presented in the study are included in the article/Supplementary Material, further inquiries can be directed to the corresponding authors.

Author contributions

XB, WZ, HL, and YZ contributed to conception and writing. QY, JL, and XC interpreted the data. XB wrote the first draft of the manuscript. All authors contributed to manuscript revision, read, and approved the submitted version. WZ and HL received funding for the project detailed in the Funding.

Funding

This work was jointly supported by the Strategic Priority Research Program of the Chinese Academy of Sciences (XDA2003010102), the National Key Research and Development Program of China (2019YFC0507400), and the National Natural Science Foundation of China (42171117).

Conflict of interest

The authors declare that the research was conducted in the absence of any commercial or financial relationships that could be construed as a potential conflict of interest.

The reviewer CZ declared a shared affiliation with the author XC to the handling editor at time of review.

Publisher's note

References

Aires, U. R. V., da Silva, D. D., Moreira, M. C., Ribeiro, C. A. A. S., and Ribeiro, C. B. M. (2020). The use of the normalized difference vegetation index to analyze the influence of vegetation cover changes on the streamflow in the manhuacu River Basin, Brazil. *Water Resour. Manag.* 34 (6), 1933–1949. doi:10.1007/s11269-020-02536-1

Akbari, M., Shalamzari, M. J., Memarian, H., and Gholami, A. (2020). Monitoring desertification processes using ecological indicators and providing management programs in arid regions of Iran. *Ecol. Indic.* 111, 106011. doi:10.1016/j.ecolind.2019.106011

Anache, J. A. A., Flanagan, D. C., Srivastava, A., and Wendland, E. C. (2018). Land use and climate change impacts on runoff and soil erosion at the hillslope scale in the Brazilian Cerrado. *Sci. Total Environ.* 622, 140–151. doi:10.1016/j.scitotenv.2017.11.257

Arora, V. K. (2001). Streamflow simulations for continental-scale river basins in a global atmospheric general circulation model. *Adv. Water Resour.* 24 (7), 775–791. doi:10.1016/s0309-1708(00)00078-6

Asadieh, B., and Krakauer, N. Y. (2015). Global trends in extreme precipitation: Climate models versus observations. *Hydrol. Earth Syst. Sci.* 19 (2), 877–891. doi:10.5194/hess-19-877-2015

Azam, M. F., Kargel, J. S., Shea, J. M., Nepal, S., Haritashya, U. K., Srivastava, S., et al. (2021). Glaciohydrology of the himalaya-karakoram. *Science* 373 (6557), eabf3668. doi:10.1126/science.abf3668

Bao, C., and Fang, C. (2007). Water resources constraint force on urbanization in water deficient regions: A case study of the hexi corridor, arid area of NW China. *Ecol. Econ.* 62, 508–517. doi:10.1016/j.ecolecon.2006.07.013

Bao, Z. X., Zhang, J. Y., Wang, G. Q., Fu, G. B., He, R. M., Yan, X. L., et al. (2012). Attribution for decreasing streamflow of the Haihe River basin, northern China: Climate variability or human activities? *J. Hydrol.* 460, 117–129. doi:10.1016/j.jhydrol.2012.06.054

Beck, H. E., Roo, A. D., and Dijk, A. V. (2015). Global maps of streamflow characteristics based on observations from several thousand catchments. *J. Hydrometeorol.* 16 (4), 1478–1501. doi:10.1175/JHM-D-14-0155.1

Berghuijs, W. R., Woods, R. A., Hutton, C. J., and Sivapalan, M. (2016). Dominant flood generating mechanisms across the United States. *Geophys. Res. Lett.* 43 (9), 4382–4390. doi:10.1002/2016gl068070

Bieger, K., Hoermann, G., and Fohrer, N. (2015). The impact of land use change in the Xiangxi Catchment (China) on water balance and sediment transport. *Reg. Envir. Chang.* 15 (3), 485–498. doi:10.1007/s10113-013-0429-3

Brath, A., Montanari, A., and Moretti, G. (2006). Assessing the effect on flood frequency of land use change via hydrological simulation (with uncertainty). *J. Hydrol.* 324 (1-4), 141–153. doi:10.1016/j.jhydrol.2005.10.001

Cao, W., Bowden, W. B., Davie, T., and Fenemor, A. (2009). Modelling impacts of land cover change on critical water resources in the motueka river catchment, New Zealand. *Water Resour. Manag.* 23 (1), 137–151. doi:10.1007/s11269-008-9268-2

Chen, H., Fleskens, L., Baartman, J., Wang, F., Moolenaar, S., and Ritsema, C. (2020). Impacts of land use change and climatic effects on streamflow in the Chinese loess plateau: A meta-analysis. *Sci. Total Environ.* 703, 134989. doi:10.1016/j.scitotenv.2019.134989

Chen, Y., Zhi, L., Fan, Y., Wang, H., and Deng, H. (2015). Progress and prospects of climate change impacts on hydrology in the arid region of Northwest China. *Environ. Res.* 139, 11–19. doi:10.1016/j.envres.2014.12.029

Cheng, Z., and Yu, B. (2019). Effect of land clearing and climate variability on streamflow for two large basins in Central Queensland, Australia. *J. Hydrol.* 578, 124041. doi:10.1016/j.jhydrol.2019.124041

Cooley, S. W., Ryan, J. C., and Smith, L. C. (2021). Human alteration of global surface water storage variability. *Nature* 591 (7848), 78–81. doi:10.1038/s41586-021-03262-3

Darvini, G., and Memmola, F. (2020). Assessment of the impact of climate variability and human activities on the runoff in five catchments of the Adriatic Coast of south-central Italy. *J. Hydrol.-Reg. Stud.* 31, 100712. doi:10.1016/j.ejrh.2020.100712

Dey, P., and Mishra, A. (2017). Separating the impacts of climate change and human activities on streamflow: A review of methodologies and critical assumptions. *J. Hydrol.* 548, 278–290. doi:10.1016/j.jhydrol.2017.03.014

Donohue, R. J., Roderick, M. L., and McVicar, T. R. (2011). Assessing the differences in sensitivities of runoff to changes in climatic conditions across a large basin. *J. Hydrol.* 406 (3-4), 234–244. doi:10.1016/j.jhydrol.2011.07.003

Duan, W., Maskey, S., Chaffe, P., Luo, P., He, B., Wu, Y., et al. (2021). Recent advancement in remote sensing technology for hydrology analysis and water resources management. *Remote Sens.* 13 (6), 1097. doi:10.3390/rs13061097

Duan, W., Zou, S., Christidis, N., Schaller, N., Chen, Y., Sahu, N., et al. (2022). Changes in temporal inequality of precipitation extremes over China due to anthropogenic forcings. *npj Clim. Atmos. Sci.* 5 (1), 33–13. doi:10.1038/s41612-022-00255-5

Fenta, A. A., Yasuda, H., Shimizu, K., and Haregeweyn, N. (2017). Response of streamflow to climate variability and changes in human activities in the semiarid highlands of northern Ethiopia. *Reg. Envir. Chang.* 17 (4), 1229–1240. doi:10.1007/s10113-017-1103-y

Fereidoon, M., and Koch, M. (2018). SWAT-MODSIM-PSO optimization of multi-crop planning in the Karkheh River Basin, Iran, under the impacts of climate change. *Sci. Total Environ.* 630, 502–516. doi:10.1016/j.scitotenv.2018.02.234

Gao, P., Li, P., Zhao, B., Xu, R., Zhao, G., Sun, W., et al. (2017). Use of double mass curves in hydrologic benefit evaluations. *Hydrol. Process.* 31 (26), 4639–4646. doi:10.1002/hyp.11377

Guo, H., Bao, A., Liu, T., Jiapaer, G., Ndayisaba, F., Jiang, L., et al. (2018). Spatial and temporal characteristics of droughts in Central Asia during 1966-2015. *Sci. Total Environ.* 624, 1523–1538. doi:10.1016/j.scitotenv.2017.12.120

Guzha, A. C., Rufino, M. C., Okoth, S., Jacobs, S., and Nóbrega, R. (2018). Impacts of land use and land cover change on surface runoff, discharge and low flows: Evidence from East Africa. *J. Hydrol.-Reg. Stud.* 15, 49–67. doi:10.1016/j.ejrh.2017.11.005

Hamed, K. H. (2008). Trend detection in hydrologic data: The Mann-Kendall trend test under the scaling hypothesis. *J. Hydrol.* 349 (3-4), 350–363. doi:10.1016/j.jhydrol.2007.11.009

Harper, J., Humphrey, N., Pfeffer, W. T., Brown, J., and Fettweis, X. (2012). Greenland ice-sheet contribution to sea-level rise buffered by meltwater storage in firn. *Nature* 491 (7423), 240–243. doi:10.1038/nature11566

He, Y., Jiang, X., Wang, N., Zhang, S., Ning, T., Zhao, Y., et al. (2019). Changes in mountainous runoff in three inland river basins in the arid Hexi Corridor, China, and its influencing factors. *Sust. Cities Soc.* 50, 101703. doi:10.1016/j.scs.2019.101703

Hochmuth, H., Thevs, N., and He, P. (2015). Water allocation and water consumption of irrigation agriculture and natural vegetation in the Heihe River watershed, NW China. *Environ. Earth Sci.* 73 (9), 5269–5279. doi:10.1007/s12665-014-3773-9

Huang, S., Zhou, L., Chen, Y., and Lu, H. (2014). Impacts of polices on eco - environment of Minqin county during the past 60 years. *J. Arid. Land Resour. Environ.* 28 (7), 73–78.

Huang, S., Zhou, L., Feng, Q., Lu, Z., and Xiao, J. (2017). Evaluation of eco-environment effects of management policy implementing in inland River Basin of China: A case in the minqin oasis. *J. Desert Res.* 37 (3), 580–586.

Huo, J., Liu, C., Yu, X., Jia, G., and Chen, L. (2021). Effects of watershed char and climate variables on annual runoff in different climatic zones in China. *Sci. Total Environ.* 754, 142157. doi:10.1016/j.scitotenv.2020.142157

Kendall, M. G. (1975). *Rank correlation methods*. London: Griffin.

Koster, R. D., and Suarez, M. J. (1999). A simple framework for examining the interannual variability of land surface moisture fluxes. *J. Clim.* 12 (7), 1911–1917. doi:10.1175/1520-0442(1999)012<1911:asffet>2.0.co;2

Lebek, K., Senf, C., Frantz, D., Monteiro, J. A. F., and Krueger, T. (2019). Interdependent effects of climate variability and forest cover change on streamflow dynamics: A case study in the upper umvoti River Basin, south Africa. *Reg. Envir. Chang.* 19 (7), 1963–1971. doi:10.1007/s10113-019-01521-8

Lesk, C., Rowhani, P., and Ramankutty, N. (2016). Influence of extreme weather disasters on global crop production. *Nature* 529 (7584), 84–87. doi:10.1038/nature16467

Liang, L., and Liu, Q. (2014). Streamflow sensitivity analysis to climate change for a large water-limited basin. *Hydrol. Process.* 28 (4), 1767–1774. doi:10.1002/hyp.9720

Liu, J., Zhang, Q., Singh, V. P., and Shi, P. (2017). Contribution of multiple climatic variables and human activities to streamflow changes across China. *J. Hydrol.* 545, 145–162. doi:10.1016/j.jhydrol.2016.12.016

Mann, H. B. (1945). Nonparametric tests against trend. *Econometrica* 13, 245–259. doi:10.2307/1907187

Milly, P. C. D., and Dunne, K. A. (2002). Macroscale water fluxes - 2. Water and energy supply control of their interannual variability. *Water Resour. Res.* 38 (10), 24-1–24-9. doi:10.1029/2001wr000760

Morganstein, J. C., and Ursano, R. J. (2020). Ecological disasters and mental health: Causes, consequences, and interventions. *Front. Psychiatry* 11 (1), 1. doi:10.3389/fpsyt.2020.00001

Ning, T., Feng, Q., Li, Z., and Li, Z. (2020). Recent changes in climate seasonality in the inland river basin of Northwestern China. *J. Hydrol.* 590, 125212. doi:10.1016/j.jhydrol.2020.125212

Niu, L., Ye, B., Li, J., and Sheng, Y. (2011). Effect of permafrost degradation on hydrological processes in typical basins with various permafrost coverage in Western China. *Sci. China Ser. D-Earth Sci.* 54 (4), 615–624. doi:10.1007/s11430-010-4073-1

Pall, P., Aina, T., Stone, D. A., Stott, P. A., Nozawa, T., Hilberts, A. G. J., et al. (2011). Anthropogenic greenhouse gas contribution to flood risk in England and Wales in autumn 2000. *Nature* 470 (7334), 382–385. doi:10.1038/nature09762

Palmer, M., and Ruhi, A. (2019). Linkages between flow regime, biota, and ecosystem processes: Implications for river restoration. *Science* 365 (6459), eaaw2087. doi:10.1126/science.aaw2087

Piao, S., Ciais, P., Huang, Y., Shen, Z., Peng, S., Li, J., et al. (2010). The impacts of climate change on water resources and agriculture in China. *Nature* 467 (7311), 43–51. doi:10.1038/nature09364

Pourmokhtarian, A., Driscoll, C. T., Campbell, J. L., Hayhoe, K., Stoner, A. M. K., Adams, M. B., et al. (2017). Modeled ecohydrological responses to climate change at seven small watersheds in the northeastern United States. *Glob. Change Biol.* 23(2), 840–856. doi:10.1111/gcb.13444

Qi, W., Feng, L., Yang, H., and Liu, J. (2022). Warming winter, drying spring and shifting hydrological regimes in Northeast China under climate change. *J. Hydrol.* 606, 127390. doi:10.1016/j.jhydrol.2021.127390

Qin, J., Duan, W., Chen, Y., Dukhovny, V. A., Sorokin, D., Li, Y., et al. (2022). Comprehensive evaluation and sustainable development of water–energy–food–ecology systems in Central Asia. *Renew. Sust. Energ. Rev.* 157, 112061. doi:10.1016/j.rser.2021.112061

Qin, J., Su, B., Tao, H., Wang, Y., Huang, J., Li, Z., et al. (2021). Spatio-temporal variations of dryness/wetness over Northwest China under different SSPs-RCPs. *Atmos. Res.* 259, 105672. doi:10.1016/j.atmosres.2021.105672

Rangecroft, S., Van Loon, A. F., Coxon, G., Breña-Naranjo, J. A., Van Ogtrop, F., and Van Lanen, H. A. J. (2019). Using paired catchments to quantify the human influence on hydrological droughts. *Hydrol. Earth Syst. Sci.* 23 (3), 1725–1739. doi:10.5194/hess-23-1725-2019

Rust, W., Corstanje, R., Holman, I. P., and Milne, A. E. (2014). Detecting land use and land management influences on catchment hydrology by modelling and wavelets. *J. Hydrol.* 517, 378–389. doi:10.1016/j.jhydrol.2014.05.052

Sankarasubramanian, A., Vogel, R. M., and Limbrunner, J. F. (2001). Climate elasticity of streamflow in the United States. *Water Resour. Res.* 37 (6), 1771–1781. doi:10.1029/2000wr900330

Satge, F., Hussain, Y., Xavier, A., Zola, R. P., Salles, L., Timouk, F., et al. (2019). Unraveling the impacts of droughts and agricultural intensification on the Altiplano water resources. *Agric. For. Meteorol.* 279, 107710. doi:10.1016/j.agrformet.2019.107710

Senbeta, T. B., and Romanowicz, R. J. (2021). The role of climate change and human interventions in affecting watershed runoff responses. *Hydrol. Process.* 35, e14448. doi:10.1002/hyp.14448

Sharma, P. J., Patel, P. L., and Jothiprakash, V. (2019). Impact of rainfall variability and anthropogenic activities on streamflow changes and water stress conditions across Tapi Basin in India. *Sci. Total Environ.* 687, 885–897. doi:10.1016/j.scitotenv.2019.06.097

Shen, Y., Li, S., Chen, Y., Qi, Y., and Zhang, S. (2013). Estimation of regional irrigation water requirement and water supply risk in the arid region of Northwestern China 1989-2010. *Agric. Water Manage.* 128, 55–64. doi:10.1016/j.agwat.2013.06.014

Smith, B., Fricker, H. A., Gardner, A. S., Medley, B., Nilsson, J., Paolo, F. S., et al. (2020). Pervasive ice sheet mass loss reflects competing ocean and atmosphere processes. *Science* 368 (6496), 1239–1242. doi:10.1126/science.aaz5845

Su, X., Li, X., Niu, Z., Wang, N. a., and Liang, X. (2021). A new complexity-based three-stage method to comprehensively quantify positive/negative contribution rates of climate change and human activities to changes in runoff in the upper Yellow River. *J. Clean. Prod.* 287, 125017. doi:10.1016/j.jclepro.2020.125017

Viola, F., Caracciolo, D., Forestieri, A., Pumo, D., and Noto, L. V. (2017). Annual runoff assessment in arid and semiarid Mediterranean watersheds under the Budyko's framework. *Hydrol. Process.* 31 (10), 1876–1888. doi:10.1002/hyp.11145

Wang, G., Liu, J., Kubota, J., and Chen, L. (2007). Effects of land-use changes on hydrological processes in the middle basin of the Heihe River, northwest China. *Hydrol. Process.* 21 (10), 1370–1382. doi:10.1002/hyp.6308

Wang, G., Zhang, Y., Liu, G., and Chen, L. (2006). Impact of land-use change on hydrological processes in the Maying River basin, China. *Sci. China Ser. D-Earth Sci.* 49 (10), 1098–1110. doi:10.1007/s11430-006-1098-6

Williamson, T. N., and Barton, C. D. (2020). Hydrologic modeling to examine the influence of the forestry reclamation approach and climate change on mineland hydrology. *Sci. Total Environ.* 743 (15), 140605. doi:10.1016/j.scitotenv.2020.140605

Winkelmann, R., Levermann, A., Martin, M. A., and Frieler, K. (2012). Increased future ice discharge from Antarctica owing to higher snowfall. *Nature* 492 (7428), 239–242. doi:10.1038/nature11616

Xie, Y., Bie, Q., Lu, H., and He, L. (2018). Spatio-temporal changes of oases in the hexi corridor over the past 30 years. *Sustainability* 10 (12), 4489. doi:10.3390/su10124489

Xue, D. (2021). *Attribution analysis of runoff changes in the Shiyang River Basin*. Gansu, China: Northwest Normal University. doi:10.27410/d.cnki.gxbfu.2021.000174

Xue, D., Zhou, J., Zhao, X., Liu, C., Wei, W., Yang, X., et al. (2021). Impacts of climate change and human activities on runoff change in a typical arid watershed, NW China. *Ecol. Indic.* 121, 107013. doi:10.1016/j.ecolind.2020.107013

Yang, H., Qi, J., Xu, X., Yang, D., and Lv, H. (2014). The regional variation in climate elasticity and climate contribution to runoff across China. *J. Hydrol.* 517, 607–616. doi:10.1016/j.jhydrol.2014.05.062

Yang, L., Feng, Q., Yin, Z., Wen, X., Si, J., Li, C., et al. (2017). Identifying separate impacts of climate and land use/cover change on hydrological processes in upper stream of Heihe River, Northwest China. *Hydrol. Process.* 31 (5), 1100–1112. doi:10.1002/hyp.11098

Zastrow, M. (2019). China's tree-planting drive could falter in a warming world. *Nature* 573 (7775), 474–475. doi:10.1038/d41586-019-02789-w

Zhai, R., and Tao, F. (2017). Contributions of climate change and human activities to runoff change in seven typical catchments across China. *Sci. Total Environ.* 605, 219–229. doi:10.1016/j.scitotenv.2017.06.210

Zhang, A., Zheng, C., Wang, S., and Yao, Y. (2015). Analysis of streamflow variations in the Heihe River Basin, northwest China: Trends, abrupt changes, driving factors and ecological influences. *J. Hydrol.-Reg. Stud.* 3, 106–124. doi:10.1016/j.ejrh.2014.10.005

Zhang, F., Zhang, M., Wang, S., Qiang, F., Che, Y., and Wang, J. (2017). Evaluation of the tourism climate in the hexi corridor of northwest China's Gansu Province during 1980-2012. *Theor. Appl. Climatol.* 129 (3-4), 901–912. doi:10.1007/s00704-016-1814-x

Zhang, L., Moges, E., Kirchner, J. W., Coda, E., Liu, T., Wymore, A. S., et al. (2021). Chosen: A synthesis of hydrometeorological data from intensively monitored catchments and comparative analysis of hydrologic extremes. *Hydrol. Process.* 35 (11). doi:10.1002/hyp.14429

Zhang, L., Podlasly, C., Ren, Y., Feger, K.-H., Wang, Y., and Schwaerzel, K. (2014). Separating the effects of changes in land management and climatic conditions on long-term streamflow trends analyzed for a small catchment in the Loess Plateau region, NW China. *Hydrol. Process.* 28 (3), 1284–1293. doi:10.1002/hyp.9663

Zhang, M., Wei, X., Sun, P., and Liu, S. (2012). The effect of forest harvesting and climatic variability on runoff in a large watershed: The case study in the Upper Minjiang River of Yangtze River basin. *J. Hydrol.* 464, 1–11. doi:10.1016/j.jhydrol.2012.05.050

Zhang, Q., and Kang, S. (2021). Glacier elevation change in the Western Qilian mountains as observed by TerraSAR-X/TanDEM-X images. *Geocarto Int.* 36 (12), 1365–1377. doi:10.1080/10106049.2019.1648563

Zhong, B., and Jue, K. (2019). Land cover dataset with 30m spatial resolution over Qilian Mountain area (1985-2017) V1.0. Beijing, China. *National Tibetan Plateau Data Center*. doi:10.11888/Geogra.tpdc.270130

Zhu, H., Li, Y., Huang, Y., Li, Y., Hou, C., and Shi, X. (2018). Evaluation and hydrological application of satellite-based precipitation datasets in driving hydrological models over the Huifa river basin in Northeast China. *Atmos. Res.* 207, 28–41. doi:10.1016/j.atmosres.2018.02.022

frontiers | Frontiers in Environmental Science

TYPE Original Research
PUBLISHED 16 February 2023
DOI 10.3389/fenvs.2023.1119605

OPEN ACCESS

EDITED BY
Hu Liu,
Northwest Institute of Eco-Environment and Resources (CAS), China

REVIEWED BY
Dejin Wang,
Kunming University of Science and Technology, China
Quanyan Tian,
Northwest Institute of Eco-Environment and Resources (CAS), China

*CORRESPONDENCE
Lihui Tian,
✉ lhtian@qhu.edu.cn

SPECIALTY SECTION
This article was submitted to Drylands, a section of the journal Frontiers in Environmental Science

RECEIVED 09 December 2022
ACCEPTED 03 February 2023
PUBLISHED 16 February 2023

CITATION
Zhang H, Tian L, Hasi E, Zhang D and Wu W (2023), Vegetation–soil dynamics in an alpine desert ecosystem of the Qinghai Lake watershed, northeastern Qinghai–Tibet Plateau.
Front. Environ. Sci. 11:1119605.
doi: 10.3389/fenvs.2023.1119605

Vegetation–soil dynamics in an alpine desert ecosystem of the Qinghai Lake watershed, northeastern Qinghai–Tibet Plateau

Hongwei Zhang[1,2], Lihui Tian[3]*, Eerdun Hasi[1], Dengshan Zhang[3] and Wangyang Wu[3,4]

[1]Faculty of Geographical Science, Beijing Normal University, Beijing, China, [2]Academy of Forestry Inventory and Planning, National Forestry and Grassland Administration of China, Beijing, China, [3]State Key Laboratory of Plateau Ecology and Agriculture, Qinghai University, Xining, China, [4]School of Earth Sciences, East China University of Technology, Nanchang, China

Different types of dunes cause habitat differences, which can affect vegetation growth. In turn, water utilized by vegetation leads to the differential distribution of soil moisture in different dunes. However, vegetation–soil dynamics in the alpine desert of the Qinghai–Tibet Plateau remain poorly understood. We chose the largest section of desert along the eastern shore of Qinghai Lake as a study area to test the hypotheses that plant community characteristics and soil physicochemical properties show differences in different sand-binding communities, in addition to soil moisture content, based on methods of field investigations and *in situ* observations. The main results were as follows:1) Plant community species diversity and herb coverage increased with the stabilization status of dunes; meanwhile, coverage increased with the age of the added artificial semi-fixed dunes. 2) Surface deposits were mainly composed of medium sand, leading to low organic matter and nutrient content in the study area; this being different from other deserts in northern China. 3) Soil moisture's seasonal variation was consistent with rainfall seasonality and lacked significant interannual differences, while its vertical distribution was influenced by precipitation infiltration. 4) Soil crust forms beneath specific species, such as leguminous plants in the study area, which should be effective at preventing wind erosion. Our findings will facilitate a mechanistic understanding of plant–soil–water relationships in alpine deserts and provide timely information for screening introduced species for enhancing sand-fixation effectiveness.

KEYWORDS

vegetation communities, soil properties, soil moisture, sand dunes, Qinghai Lake

1 Introduction

Desertification has attracted much international attention as one of the most serious land degradation problems, and establishing suitable land rehabilitation projects in sensitive areas would be the best strategy for slowing desertification worldwide (D'Odorico et al., 2013; Huang et al., 2020). Vegetation restoration and reconstruction have become the most important and effective measures and methods for mitigating desertification in drylands (Li et al., 2014; Qi et al., 2018). Shrubs are often used as priority individuals for planting in desertification restoration projects, as they can generally maintain a high coverage rate and strong protective performance under the most severe wind erosion conditions in spring and winter. Once pioneer plant species have been established on mobile dunes, aeolian sediments tend to be fine-grained and biological crusts begin to appear under the canopy (Zuo et al., 2008; Li et al., 2013). Yet, vegetation coverage undergoes a self-thinning process that declines during the succession of vegetation from artificial ecosystems to natural ecosystems (Wang et al., 2005). A previous study showed that vegetation coverage is close to being maximally coordinated with local soil moisture carrying capacity, rendering soil moisture a key limiting factor leading to shrubs' mortality and leaving herbs to gradually become the dominant species in a semi-arid desert in China (Li et al., 2014). Nevertheless, that would be a long-term succession process, one that is still poorly understood in alpine deserts. There is no doubt that vegetation–soil dynamics are the principal focus of study for understanding the stability of a desert ecosystem, where characteristics of vegetation and soil properties strongly interact with each other (Maxwell et al., 2018). On one hand, artificial measures can weaken aeolian activities and promote organic matter's increase on the surface due to the interception of dust; on the other hand, soil structure can influence the rainfall infiltration rate and pattern of plants' water and nutrient absorption by roots (Noy-Meir, 1979; Silva and Lambers, 2018). Therefore, understanding the dynamics of both the plant community and soil at the initial restoration stage is useful to gain insight into the evolution of alpine desert ecosystems.

Qinghai Lake is the largest inland saltwater lake in China. It is not only the convergence zone of China's three major climate types but also a buffer zone between the Qaidam Basin and Huangshui Valley in the Qinghai–Tibet Plateau (Li et al., 2018). Providing ecological security for the northeastern Qinghai–Tibet Plateau, and a natural barrier blocking off desertification that is spreading eastward, Qinghai Lake plays a paramount ecological role in the stable development of the Qinghai–Tibet Plateau. Currently distributed around Qinghai Lake is about 134 295 ha of desert, which has expanded by 2.2% annually since the 1950s (Wu et al., 2019a). Desertification of the Qinghai Lake watershed provides a hotspot for research investigating the influence of climate change on the Tibetan Plateau (Li et al., 2018). The local Qinghai Province government has encouraged afforestation and conducted several sand-fixation projects to impede the spread of mobile dunes along the nearby Qinghai–Tibet Railway and Eastern Surrounding Road (Tian et al., 2019). Desertification has been effectively curbed by a relatively stable pattern of "fixed lowlands," "semi-fixed dunes," and "mobile dunes" from the lakeshore to the foothills of Riyue Mountain, the eastern boundary of Qinghai Lake.

Recent studies in this area have mainly focused on desert formation, dynamic changes of desertification, desertification control measures, soil particle composition, soil moisture dynamics, effective control and evaluation of straw checkerboards, and individuals' effects on reducing wind-driven sand erosion (Tian et al., 2015; Tian et al., 2019; Tian et al., 2020), in addition to water use sources of afforestation species (Wu et al., 2016; Wang et al., 2022). Work by Wu H et al. (2019) has analyzed species characteristics (richness and traits) and other afforestation community features over several years. Earlier, Lu et al. (2013) focused on the effect of rainfall on replenishing soil moisture in newly afforested areas. Yet, little attention has been paid to the interaction between community features and soil properties in the alpine desert ecosystem of the Qinghai–Tibet Plateau, especially in the Qinghai Lake watershed.

To fill these knowledge gaps, here we illustrate community characteristics and soil physicochemical properties during growing seasons in an alpine semi-arid desert in the northeastern region of the Tibetan Plateau. The tested hypotheses were that 1) plant community diversity and coverage and soil physicochemical properties showed differences in different sand-binding communities; 2) soil moisture content was higher in natural dunes than in afforested dunes. This study's findings will facilitate a mechanistic understanding of plant–soil–water relationships in alpine desert ecosystems, while also providing information for screening introduced species for sand-fixation effectiveness according to local soil conditions and soil water content. This could have far-reaching significance for the ecological engineering of desertification control in the Qinghai–Tibet Plateau.

2 Materials and methods

2.1 Study area

The study was conducted at the eastern shore of Qinghai Lake, which belongs to the Ketu Wind Prevention and Sandfixation Experimental Range (hereafter, WPSER; 36°46.9′ N, 100°46.8′ E; 3,224 m; for more details about WPSER, refer to Tian et al. (2019) and Tian et al. (2020)). Mega-dunes and continuous mobile dunes are distributed across the WPSER. After 5 years of treatment, the amount of vegetation covering the mobile dunes, semi-fixed dunes, and fixed dunes has increased by 30.4%, 20.2%, and 11.6%, respectively (Tian et al., 2015).

The WPSER is situated within an alpine semi-arid climatic zone, having a relatively wet summer and cold winter. Based on data from the Haiyan County National Meteorological Station, located ca. 20 km away from the WPSER, the annual mean temperature is 0.93°C, with the lowest mean monthly temperature occurring in January (−13.1°C) and the highest occurring in July (12.4°C). The annual average precipitation is 438.6 mm, approximately 80% of which falls between July and September (Wang et al., 2022). Precipitation and temperature have both increased since 2004, especially from 2010 onward (Cui and Li, 2015; Wu H et al., 2019). The WPSER is a low-wind energy environment whose aeolian activity is strongest from late autumn to early spring, being controlled by the north-west wind direction. The threshold wind velocity for sand movement on a mobile dune is 6.5 m s^{-1}, but it is greater than 8 m s^{-1} on afforestation dunes (Tian et al., 2020). The natural shrub species distributed in natural fixed dunes are mainly *Artemisia ordosica* and *Caragana jubata*, while natural herbs

TABLE 1 Study sites in the WPSER.

No.	Status of dunes	Dominant species	Afforestation time	Biological measures	Technical measures
SD	Natural fixed	*Artemisia ordosica*	—	—	—
SSD	Natural semi-fixed	*A. ordosica*	—	—	—
MD	Mobile	—	—	—	—
SJD	Artificial semi-fixed	*Hippophae rhamnoides*	2007	Planting seedlings	1.5 m × 1.5 m straw checkerboard
WLD	Artificial semi-fixed	*Salix cheilophila*	2009	High-stem deeply planting	1.5 m × 1.5 m straw checkerboard

Note: "—" means not applicable.

are *Carex qinghaiensis* and *Achnatherum splendens*. The soil in the study area consists of sand without a typical soil development sequence. The growing season of vegetation begins in May and ends in September or early October.

In spring 2011, we selected five dunes in the WPSER: a natural fixed dune (SD), a natural semi-fixed dune (SSD), a mobile dune (MD), and two dunes with artificial measures (SJD and WLD). Their corresponding plots are summarized in Table 1. We investigated vegetation features and soil properties on the top of each dune from 2011 through 2013.

2.2 Methods

2.2.1 Vegetation dynamics

Three randomized 5 m × 5 m plots were established at the top of each dune type. Then, traditional measurements in ecology were used to survey the shrub species and their canopy and height in each plot. According to these data, we calculated shrub coverage and defined the dominant species in each plot community. Within fixed shrub plots, we set up five quadrats (each 1 m × 1 m: one in the center, four at the corners) and then measured the height and number of herbaceous species to calculate herb coverage. In this study, the Simpson index D, Shannon–Wiener index H, and Pielou evenness index E were used to measure the species diversity of communities, as follows:

$$D = 1 - \sum p_i^{\,2}, \tag{1}$$

$$H = -\sum p_i \ln p_i, \tag{2}$$

$$E = H/\ln S, \tag{3}$$

where p_i is the relative importance value of species i (relative height plus relative coverage) and S is the total number of species i in the plot or quadrat, that is, an abundance index.

2.2.2 Soil properties

A total of 75 soil cores were collected from all 15 plots to a depth of 80 cm, by digging sections from each plot in triplicate. The depth profile was divided into five layers from the surface to 80 cm depth: 0–10 cm, 10–20 cm, 20–40 cm, 40–60 cm, and 60–80 cm. Soil samples were analyzed in the Key Laboratory of Environmental Change and Natural Disaster [ECND] at Beijing Normal University for particle size, organic matter content (OM), and available nitrogen (N), phosphorus (P), and potassium (K) content. The fractions of sand, silt, and clay were obtained following the standard defined by Blott and Pye (2001): sand ($0.063 < d < 2.00$ mm), silt ($0.002 < d < 0.063$ mm), and clay ($d < 0.002$ mm). Organic matter content was determined by the method of Walkley and Black (1934).

2.2.3 Soil moisture dynamics

Soil moisture data have been collected in the WPSER using an automatic sensor network. This includes the aforementioned five dune (plot) sites, where it has been operating since August 2009. Capacitance-type soil moisture probes (ECH2O-5, Decagon Devices Inc., USA) were variously installed in five soil horizons according to five layers of soil samples (mentioned previously). All the cables were carefully buried below the depth of the installed probes and then laid horizontally away from each probe location. We obtained continuous 10-min time-series data from August 2009 through December 2013. In this study, we only used soil moisture data for the entire year, from 2011 to 2013, for consistency with the data obtained for the investigated vegetation and soil properties.

2.2.4 Data analysis

The variation in community diversity or plant coverage among the five dune types was distinguished by one-way analysis of variance (ANOVA) combined with a least significant difference (LSD). ANOVAs were also used to detect differences in soil particle size, organic content, and bulk density for each community. The alpha = 0.05 significance level was set for the statistical analyses, all of which were performed in SPSS 26.0 software (SPSS Inc., Chicago, IL, USA). All figures were drawn in the Origin 2018 software (OriginLab, Northampton, MA, USA).

3 Results

3.1 Plant community characteristics

3.1.1 Species-forming communities on dunes

As seen in Table 2, there were nine families and 13 species at the study sites after afforestation. These consisted of five species of Leguminosae, two species of Poaceae, and other families that were composed of only one species. Except for

TABLE 2 Species composition of plant communities on the sites (in accordance with family classification).

Family	Species	Family	Species
Elaeagnaceae	*Hippophae rhamnoides*	*Rosaceae*	*Potentilla fruticosa*
Salicaceae	*Salix cheilophila*	*Poaceae*	*Leymus racemosus* and *Achnatherum splendens*
Pinaceae	*Pinus sylvestris*	*Cyperaceae*	*Carex tristachya*
Cupressaceae	*Sabina vulgaris*	*Asteraceae*	*Artemisia ordosica*
Leguminosae	*Caragana korshinskii, Astragalus adsurgens, Astragalus polycladus, Hedysarum scoparium,* and *Oxytropis aciphylla*		

TABLE 3 Species and richness of plant communities on the study sites (2013).

No.	Shrubs	Herbs	Richness
SD	*A. ordosica, H. rhamnoides, O. aciphylla,* and *S. vulgaris*	*C. tristachya, C. splendens, A. adsurgens, A. polycladus,* and *L. racemosus*	9
SSD	*A. ordosica, H. rhamnoides,* and *S. vulgaris*	*L. racemosus, C. tristachya,* and *C. splendens*	6
MD	—	—	0
SJD	*H. rhamnoides*	*L. racemosus*	2
WLD	*S. cheilophila, H. rhamnoides, P. sylvestris, P. fruticosa, C. korshinskii,* and *A. ordosica*	*C. tristachya, L. racemosus,* and *H. scoparium*	9

Note: the sequence was in accordance with relative coverage, and "—" means no species present.

TABLE 4 α-diversity of communities on study sites (2011–2013).

Year	α-diversity index	SD	SSD	SJD	WLD
2011	Simpson index (D)	0.479^{a}	0.634^{a}	0.510^{a}	0.767^{a}
	Shannon–Weiner index (H)	0.964^{a}	0.750^{a}	0.798^{a}	1.401^{b}
	Pielou index (E)	0.533^{a}	0.883^{a}	1.151^{b}	0.848^{a}
2012	Simpson index (D)	0.626^{a}	0.568^{a}	0.607^{a}	0.706^{a}
	Shannon–Weiner index (H)	1.157^{a}	1.055^{a}	0.959^{a}	1.318^{a}
	Pielou index (E)	0.719^{a}	0.758^{a}	0.802^{a}	0.950^{a}
2013	Simpson index (D)	0.604^{a}	0.730^{a}	0.526^{a}	0.788^{a}
	Shannon–Weiner index (H)	1.689^{a}	1.525^{a}	1.045^{a}	1.678^{a}
	Pielou index (E)	0.689^{a}	0.829^{a}	0.950^{a}	0.884^{a}

Note: Different letters within a row table indicate significant differences between the mean values of the communities.

Carex tristachya, Artemisia ordosica, *Astragalus adsurgens*, and *Astragalus polycladus*, all other species had been artificially planted. Since the 1980s, *Hippophae rhamnoides* has been most commonly used in afforestation projects in the WPSER. Starting in 2007, *Salix cheilophila*, *Pinus sylvestris*, *Potentilla fruticosa*, and *Sabina vulgaris* were planted to implement China's 11th Five-Year Plan in the study area. The greater the dune fixation, the higher its community richness and number of perennial herb species, as shown in Table 3. *Salix* stems were deep-planted in 2009 on WLD and then replanted with *H. rhamnoides*, *P. fruticosa*, and *P. sylvestris*; breeding of *Caragana korshinskii*, *A. ordosica*, and *Hedysarum scoparium* was undertaken in 2010. Therefore, the increased richness was human-induced.

3.1.2 Diversity of plant communities on dunes

Table 4 shows that the greater a dune's fixation, the higher the species diversity in its community. However, there were no significant differences among dune types in terms of H nor for evenness (E) and richness (D) ($p > 0.05$). With each subsequent fixation year, the species diversity increased. Because artificial species were abundant in the WLD, its α-diversity index exceeded that of other dune types, but *S. cheilophila* remained the dominant species.

3.1.3 Coverage dynamics of different dunes

Afforestation stabilized mobile dune surfaces, which provided a favorable condition for the recovery of natural species. As Figure 1 shows, the total vegetation cover on artificial semi-fixed dunes

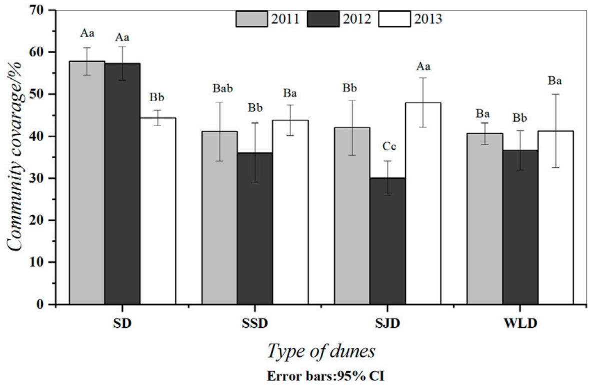

FIGURE 1
Coverage dynamics of different dunes. Note: Differing capital letters indicate that coverage in different communities was significantly different ($p < 0.05$), while differing lower-case letters indicate that the coverage of the same communities in different years was significantly different ($p < 0.05$). The same letter indicates no significant difference ($p > 0.05$).

TABLE 5 Features of *Artemisia ordosica* in different dunes (M±SE).

Year	Index	SD	SSD	SJD	WLD
Plots area/m^2		25	25	25	25
2011	*cover*/%	36.03 ± 17.37	21.72 ± 8.42	—	16.02 ± 10.41
	density	45.67 ± 6.39	11.00 ± 6.00	—	11.50 ± 9.50
	height/cm	24.13 ± 2.87	33.96 ± 1.76	—	54.41 ± 3.60
2012	*cover*/%	52.01 ± 4.52	25.42 ± 8.87	0.77 ± 0.42	22.37 ± 7.73
	density	25.00 ± 3.51	11.67 ± 3.76	6.00 ± 1.00	15.33 ± 4.00
	height/cm	23.21 ± 1.77	42.38 ± 6.38	22.75 ± 1.66	41.63 ± 2.21
2013	*cover*/%	30.16 ± 5.59	18.76 ± 3.53	2.29 ± 0.52	0.42 ± 0.00
	density	17.67 ± 4.81	10.67 ± 1.86	5.00 ± 0.00	3.00 ± 0.00
	height/cm	30.22 ± 4.84	43.30 ± 1.38	30.88 ± 5.28	29.70 ± 0.00

Note: M ± SE denotes the mean ± standard error.

(WLD and SJD sites) reached more than 40% in 2013. The vegetation cover exhibited an increasing trend during the study period. Meanwhile, the vegetation cover on artificial mobile dunes in the initial restoration years was similar to that on natural semi-fixed dunes. In addition, the vegetation cover was low due to lower precipitation in 2012, except for natural fixed dunes.

A. ordosica was not only the dominant species in SD and SSD but also the most abundant naturally established species in the study area. As seen in Table 5, according to an overall survey of its vegetation recovery level, *A. ordosica* increased in cover with elapsed years of recovery growth, though its density varied negligibly while its plant height increased. The *A. ordosica* growing on SJD came from seedling afforestation in 2009, whereas the *A. ordosica* on WLD had high coverage and arose from both artificial seedlings and natural recovery.

3.2 Soil properties in different dunes

3.2.1 Particle size composition

Table 6 shows that on SD, there was minimal clay, whose concentrations were <1%. The silt was the most evident conversion feature that emerged during the evolution from sand to the soil, being closely related to sediment nutrients. Meanwhile, it was also the main substance carried by wind in the sand–wind flow. The silt was more prominent in SD than in the other dune types ($p < 0.05$). Fine and medium sand were the main particles in the sediments and nearly equal in the content on SD, whereas medium sand predominated in mobile dunes more than fixed dunes. However, coarse sand was not regular between dunes.

3.2.2 Organic content and nutrient dynamics

As Figure 2 shows, SD had the highest organic matter content at 4.56 g kg^{-1}. Organic matter content was closely related to clay content. There were significant variations in organic matter content among SSD, SJD, and WLD ($p < 0.05$) while it was different between SD and MD ($p > 0.05$).

Soil nutrient content was relatively low in the WPSER. The average content of available nitrogen, phosphorus, and potassium was 0.07 g kg^{-1}, 0.002 g kg^{-1}, and 0.17 g kg^{-1}, respectively. The content of available nitrogen in SD exceeded that in other dune types ($p < 0.05$). In this region, phosphorus would be negligible, being found only on SD in a very small amount, i.e., 0.004 g kg^{-1}. There was no significant difference ($p > 0.05$) in potassium content among the dune types, except for SJD.

3.2.3 Soil bulk density dynamics

Analyzing the bulk density of the soil in the dune types (Figure 3) revealed little difference between them ($p > 0.05$), with an average content of 1.54–1.67 g cm^{-3}. This was attributable to higher vegetation amelioration on dunes, which may also be associated with the functional types of species; e.g., soil amelioration that was significantly superior in *H. rhamnoides* with rhizobia than *S. cheilophila*.

3.3 Soil moisture dynamics

Soil moisture content (SMC) was the highest in SD and SSD in the study area, and its value was more than or similar to 9% from 2011 to 2013 (Figure 4). Meanwhile, the volumetric moisture content in the other three dunes was below 9%. There were no significant interannual differences for the same dune type ($p > 0.05$). Nevertheless, within the same year, SMC was different among various dunes; in general, that of SJD was the lowest.

3.3.1 Seasonal dynamics of soil moisture

As seen in Figure 5, from December to the following February, a freezing period occurred with low soil

TABLE 6 Particle size composition (M±SE, %) in the surface 10 cm of deposits in different dunes.

Type of dunes	*Clay*	*Silt*	*Very fine sand*	*Fine sand*	*Medium sand*	*Coarse sand*
	>0.002 mm	0.002–0.063 mm	0.063–0.125 mm	0.125–0.25 mm	0.25–0.5 mm	0.5–1 mm
SD	0.22 ± 0.19^A	3.74 ± 0.49^A	9.76 ± 1.19^A	40.44 ± 3.11^A	40.13 ± 2.70^B	5.71 ± 2.14^C
SSD	0	1.52 ± 0.76^C	6.14 ± 0.85^B	33.94 ± 1.47^B	44.20 ± 1.78^B	13.95 ± 3.39^B
MD	0	1.03 ± 0.54^C	4.46 ± 0.93^C	31.52 ± 3.77^B	51.30 ± 2.50^A	11.68 ± 1.94^B
SJD	0	0.51 ± 0.51^D	4.86 ± 0.26^C	37.95 ± 0.95^A	48.71 ± 0.75^A	7.96 ± 0.29^C
WLD	0	2.27 ± 0.74^B	6.39 ± 1.53^B	22.12 ± 1.91^C	50.51 ± 1.84^A	18.70 ± 1.41^A

Note: M ± SE denotes the mean ± standard error. Different capital letters indicate soil particle classes in different communities that differed significantly ($p < 0.05$). The same letter indicates no significant difference ($p > 0.05$).

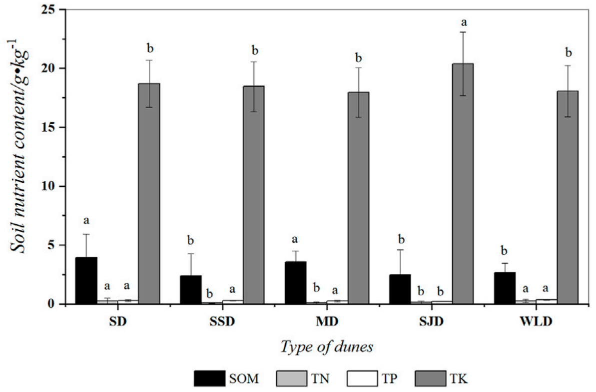

FIGURE 2
Organic matter and nutrient content 80 cm below the surface of deposits in dunes examined. Note: different letters indicate organic matter and nutrient content differed significantly between communities ($p < 0.05$); the same letter indicates no significant difference ($p > 0.05$).

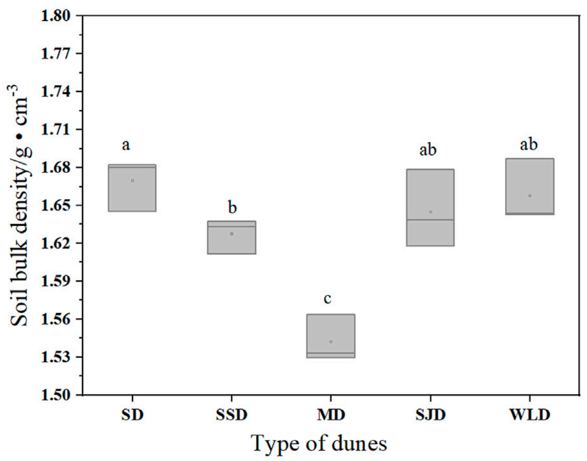

FIGURE 3
Soil bulk density 80 cm below the surface of deposits in dunes examined in the WPSER. Note: different letters indicate soil bulk density differed significantly between communities ($p < 0.05$); the same letter indicates no significant difference ($p > 0.05$).

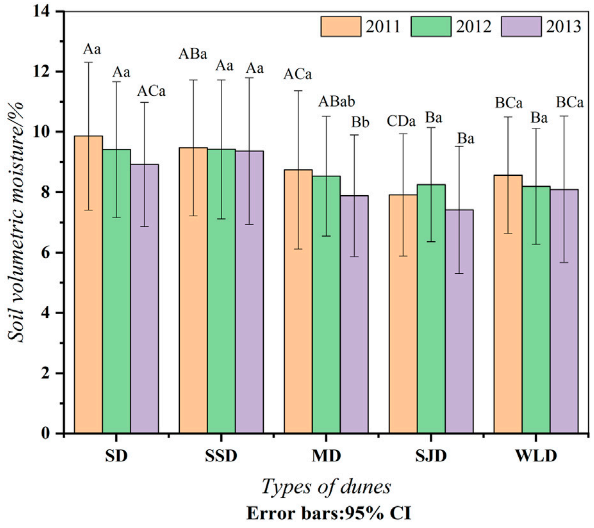

FIGURE 4
Soil moisture dynamics from 2011 to 2013 in dunes examined. Note: different capital letters indicate the SWC differed significantly between communities ($p < 0.05$), while different small letters mean the SWC of the same communities varied significantly from year to year ($p < 0.05$). The same letter indicates no significant difference ($p > 0.05$).

temperatures and the lowest soil moisture. However, soil moisture remained relatively stable during the winter. In March, soil thawing and snow melting led to a rapid replenishment of soil moisture. Plants began germinating in early April when soil water consumption was still low *via* transpiration. Thus, soil moisture increased at the onset of vegetation growth. Whereas *H. rhamnoides* consumed a large amount of water during its early growth stage, soil moisture at the SJD site was lower in April. In May, rainfall increased, followed by a gradual increase in vegetation transpiration, when soil moisture increases were unlikely to occur. From July to August, plants were in a vigorous phase of the growing season, distinguished by a stronger evapotranspiration rate and peaks in yearly rainfall. Rainfallaugmented soil moisture and soil moisture loss *via* evaporation were almost equal.

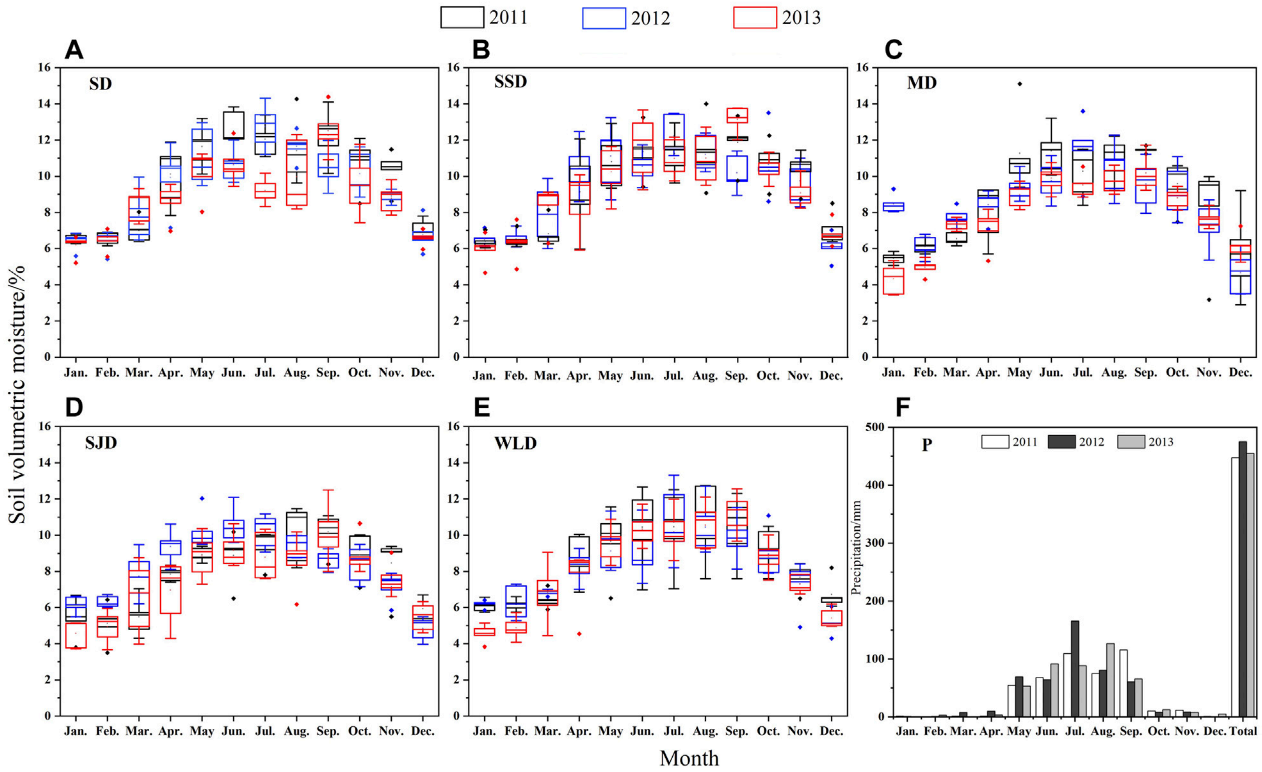

FIGURE 5
Seasonal variation of soil moisture dynamics 80 cm below the surface from 2011 to 2013 in different dunes **(A–E)** and precipitation **(F)** in the study area.

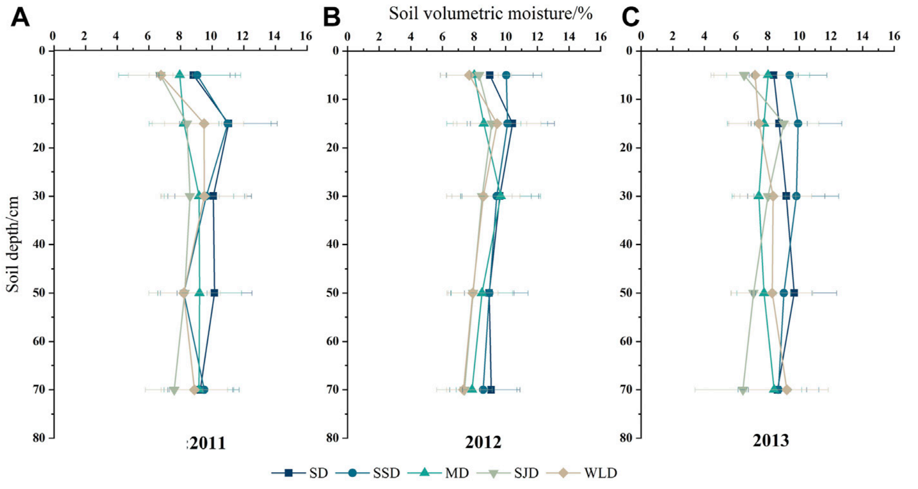

FIGURE 6
Vertical soil moisture variation 80 cm below the surface between 2011 and 2013 in different dunes.

Therefore, soil moisture remained stable at this stage. In September, plants underwent a decline in their growth. Soil moisture was at its yearly peak because of the large amount of soil water stored and a small quantity of rainfall supplement. Then, soil moisture exhibited a sharp decline due to the little precipitation in October. At this point, plants have completed a year of growth and begin to go dormant, and the soil begins to freeze.

TABLE 7 Features of crusts in different types of dunes in the WPSER.

Types of dunes	Types of crust	Thickness of crust/cm	Distribution
SD	Biological crust and physical crust	0.75 ± 0.25	70% soil surface
SSD	—	—	—
MD	—	—	—
SJD	Physical crust	3.50 ± 2.50	Only under *H. rhamnoides* canopy
WLD	Biological and physical crust	0.30 ± 0.20	Only under shrub individuals' canopy

3.3.2 Vertical variation in soil moisture

According to Figure 6, the vertical depth of soil moisture in the different dune types varied predictably. Differences in annual precipitation led to significant interannual variability in SWC at 20 cm depth. Contrasting the vertical differentiation of soil moisture from 2011 to 2013, the soil moisture content was highest at the 10–20 cm depth in dunes except for MD, which attained its greatest value at the 20–40 cm depth in both 2011 and 2012 but at the 60–80 cm depth in 2013. Overall, the point of the highest soil moisture content was deeper in 2013 than in the first two years, except for SJD and SSD, whose interannual variation was not pronounced.

3.4 Soil crusts in different dunes

Table 7 describes the crusts present on the soil surface at SD, SJD, and WLD. Soil crusts developed under *O. aciphylla*, *A. ordosica*, and *H. rhamnoides* canopies, covering up to 70% of the surface with a 0.5–1.0 cm thickness at SD. Biological crusts were covered by the two former plant species, whereas a physical crust formed under the third species. There were no crusts under any herbs. Atop SSD, *A. ordosica* nebkhas formed without any soil crusts. No crusts were yet found on MD.

Straw checkerboard barriers placed atop SJD had an average height of 2–3 cm. *H. rhamnoides* were planted in the northwest checkerboard in 2007, where they grew well with few dry stems. A hard physical crust has formed under the canopy of that species since 2011. Crust thickness—including the thickness of the adhesive sand—was 0.5–6 cm.

In 2009, we deeply planted *S. cheilophila* with tall stems on WLD and then replanted with *H. rhamnoides* and *P. fruticosa* in 2010. The biological crust thickness was 0.1–0.2 cm in the *A. ordosica* nebkhas. Underneath *S. cheilophila* plants, we found biological crusts with a thickness of 0.2–0.5 cm. The physical crust was 1.5 cm thick under *H. rhamnoides*.

4 Discussion

In drylands, abiotic processes such as wind- and water-driven erosion significantly influence surface processes (Turnbull et al., 2012). Before artificial measures were taken, sand movements were extremely strong on mobile dunes because of forceful winds in winter and spring. Once plantations were established on dunes, wind-related hazards decreased considerably (Tian et al., 2020).

4.1 How does vegetation respond to the local soil regime in the alpine desert?

Soil texture is a key factor in the coupled relationships between climate, soil, and vegetation, which affect soil erosion, soil accumulation, and soil physicochemical processes (Fernandez-Illescas et al., 2001; Renne et al., 2019). In other words, soil particle composition is one of the most important soil physical properties because it directly affects soil moisture transport and vegetation distribution patterns (Pan and Wang, 2009; Bayat et al., 2015). Medium and fine sands were the dominant particles in the study area (Table 6), whose content was more than 72.36% at some dune sites. Also, sand has a stronger infiltration capacity for precipitation than either silt or clay, thus creating an "inverse texture effect" in arid and semi-arid ecosystems (Noy-Meir, 1973; Porporato et al., 2002). Overall, the coarser the sand, the greater the water infiltration capacity that is exploitable by plant individuals in a water-limited environment (Pan et al., 2015). In our study area, the particles of natural fixed dunes were significantly finer than those of mobile or semi-fixed dunes, both artificial and natural, which ultimately resulted in less infiltration into deeper soils, allowing direct uptake by vegetation for survival (Wang et al., 2022).

Soil is the most basic and important part of an ecosystem, and fertile soil is an important guarantee for the healthy and sustainable development of plant communities (Noy-Meir, 1973). Our analysis of the physical and chemical characteristics of soil in the alpine desert uncovered a low content of organic matter and nutrients, particularly phosphorus, and the deposits mainly consisted of fine sand or medium sand with little clay present (Table 6; Figure 2). However, in this study, plantations on the artificial semi-fixed dunes were in an early stage of succession, and their deposits were still coarse in soil texture. With more years of vegetation restoration, the physical and chemical properties of soil become more robust indicators of soil development (Yu and Jia, 2014); good examples of this include soil texture refinement, soil organic matter, and nutrient content increases, soil bulk density decreases, and biological crust development.

The groundwater level at a dune's topmost position is above 10 m in depth in our study area (Wang et al., 2022). Furthermore, there were few rainfall events from January to April, so precipitation had little effect on soil water content. However, the amount of soil water replenishment *via* soil melting increases significantly in May. Moreover, Qinghai Lake is located in the distribution area of seasonally frozen soil. The high-water zone formed by gaseous water condensation in this seasonally frozen soil, namely, a cold-generated wet sand layer, is beneficial for the growth of desert plants

(Wan et al., 2005). However, in this area, the depth of the groundwater in the sand dunes is too significant for gaseous water transport to be utilized by artificial sand fixation vegetation.

Desertification control measures consist mainly of biological measures, or these are combined with mechanical measures, and soil moisture is one of the main limiting factors for vegetation restoration in the study area (Lu et al., 2013). Precipitation quantity and seasonality interact with soils to determine the spatiotemporal patterning of plant-available water in the soil, thereby influencing the differential success of plant growth forms in water-limited systems (Renne et al., 2019). Soil moisture seasonal dynamics in our study area could be divided into three periods. The first is a stage where stagnant water is frozen from December to the following February when the soil moisture content is low and relatively stable. The second stage lasts from March to June when losses in soil moisture are compensated by increases in soil moisture. The third and final stage occurs during a period of dehydration from July to November when high soil moisture levels gradually decrease. Overall, the highest soil moisture occurs in summer and autumn, when plants need water the most to maintain their growth, as proven by Rodriguez-Iturbe et al. (1999).

4.2 How do plantations affect soil properties after afforestation in the alpine desert?

Community features and soil properties are mutually reinforcing (Maxwell et al., 2018). On one side, vegetation cover reduces radiation and wind speed at the soil surface, thus reducing evaporation (Porporato et al., 2002). On the other side, once the vegetation has established on a mobile dune, leafy plants begin to control, to some extent, the loss of their own resources and create a favorable microenvironment for other plants and animals (Noy-Meir, 1973). Furthermore, vegetation also affects soil particle size composition, mainly in two ways. First, soil layers under the influence of different vegetation will have different root systems and their associated rhizosphere secretions, which in turn change the physicochemical properties of soil and its particle composition (Zhu et al., 2014). Second, the capacity of vegetation to intercept rainfall and lessen surface soil erosion depends on the canopy density and coverage of plants, leading to different retention capacities of surface soil particles (Gu et al., 2018). By comparing the particle size characteristics of the five dune types (Table 6), we conclude that artificial measures can significantly impact the soil surface by promoting the deposition of fine particles and by effectively reducing surface wind erosion.

In terms of the vegetation's vertical structure, its above-ground components, such as plant type, canopy structure, surface cover, and litter, can reduce water erosion by intercepting rainfall and attenuating the energy of raindrops. Furthermore, root systems can slow surface runoff and weaken soil erodibility by improving soil structure and its biophysical properties (Xu et al., 2006). A recent study shows that precipitation in the studied region can strongly influence the moisture content at the surface (0–20 cm), while deeper soil moisture is less replenished (Wang et al., 2022), as was the case in our study.

In addition, vegetation restoration affects soil properties and hydrological processes in drylands by increasing soil organic matter content (Wu et al., 2023). In arid and semi-arid areas, individual plants' canopies and collective vegetation cover are the main factors affecting soil water content, which is negatively correlated with soil water content in the community (Pan and Wang, 2009). The greater the width of a plant's canopy, the more water it requires and the greater its water consumption (Wang et al., 2011). Yet, the soil water content of natural fixed dunes in the study area exceeded that of mobile dunes (Figure 4), due to the fast precipitation infiltration rate of mobile dunes and the lack of effective interception of precipitation by ground vegetation and shielding of surface evaporation by the canopy. Seasonal variation in soil moisture was similar among the dune types, but differences in water consumption among individual plants can also lead to changes in soil water content (Tian et al., 2021).

The shade and higher surface soil moisture under a shrub canopy enhance biocrust formation, which can significantly bolster the resistance of the soil surface to wind erosion by increasing the wind friction velocity threshold of the soil (Li et al., 2021). Once the straw checkerboard barrier is established, the prerequisite microenvironment for physical crust formation has been created. When *H. rhamnoides* is planted in the checkerboard's corners, rainfall is intercepted by straw, and its mulched leaves form hard black physical crusts. We find that crust formation is strongly related to the kind of vegetation growing locally (Table 7). Furthermore, the length of formed crusts on dunes was generally longer in the north–south direction than the east–west direction, likely due to the prevailing westerly and northwesterly winds that disrupt the presence of crusts (Jiang et al., 2018). Previous research has shown that the amount of biocrust cover has a negative effect on rainfall infiltration, leading to the death of mature shrubs in Chinese temperate deserts (Li et al., 2013). The hydrological roles of biocrusts in the alpine desert warrant further investigation.

4.3 Implications for the ecological management of the alpine desert

Given the short recovery times of three-five years for SJD and WLD, fewer herbs will have settled on these dunes in the WPSER. In winter and spring, the contribution of herbaceous cover to the plant community is almost negligible, unlike that from shrubs and subshrubs, chiefly due to strong winds and low temperatures that hasten graminoid mortality. For example, the above-ground segments of *L. racemosus* and *C. tristachya* dried out in October and were later blown off in winter; hence, both species had to produce new branches from their roots in May of the following year. As a result, the Poaceae family has a very low density and contributes little to the composition of the desert community.

With the successive establishment of plantations, higher surface cover from plants leads to excessive moisture and intense local competition among individuals, which eventually leads to poor shrub growth (Yu et al., 2016; Yu et al., 2020). Based on a sound understanding of the spatiotemporal distribution of soil moisture, it is necessary to select appropriate plant species and allocate their densities rationally to achieve robust long-term effects on blocking alpine desert winds and reducing sand erosion (Yu et al., 2017; Li and Sawada, 2022). The differences in plant morphology and community characteristics of dune plantations reflect the ecological adaptations of sand-fixing species in alpine deserts (Wu et al., 2019b). Under similar climatic and soil conditions, species diversity in communities is determined by physiological and innate ecological adaptation mechanisms. Nonetheless, afforestation practices and structural patterns deserve more attention in future desert research and management.

An ecosystem is a collection of organic and inorganic components that are open to being influenced by human disturbances (Hill, 1975). In this very complex dune ecosystem, there is a self-regulating, buffering, and repair mechanism operated by the external environment (Noy-Meir, 1979–80). If the pressure from the external environment reaches a tolerable threshold, the vegetation can restore itself to some stable state after normal environmental conditions recover. Once the threshold is exceeded, however, both soil properties and vegetation will likely undergo a series of changes (Zhou et al., 2020). During this process, the alterations to the physical and chemical properties of the soil are not as pronounced as those of the vegetation, but when they do occur, it is difficult to restore them to their original state (Dormaar and Willms, 1990). Soil properties and vegetation are closely related; for example, high levels of ecosystem biodiversity with a complex vegetation composition are resilient, that is, able to withstand external disturbances. By contrast, plantations that are monoculture systems are less resilient and thus easier to change because their resistance to disturbance is minimal. In the study area, the reduced vegetation cover in SD was mainly caused by human damage to the biological crusts and the expansion of bare areas detected by yearly field surveys in spring during the study period (Figure 1). Finally, strong wind erosion occurred in spring and winter, ultimately leading to reductions in vegetation cover. However, soil moisture infiltration may increase, and vegetation could likely recover in the coming years. Thus, plant community management should be carefully carried out in the future.

Regardless of the dominant woody plant species, planting increases soil water content. Previous studies have shown that plants have prominent regulating and storage functions and that the water regulation exercised by plants becomes more pronounced as restoration is prolonged (Li et al., 2014). Afforestation increases vegetation cover and suppresses surface evaporation, thereby augmenting soil water content, which ultimately improves sand-driven wind speed and effectively reduces the impact of wind erosion in alpine deserts. Hence, the reasonable planting of artificial vegetation plays a pivotal role in improving the ecological environment in terms of its soil water content balance during alpine desert restoration.

5 Conclusions

Overall, vegetation growth and soil features of the alpine desert along the eastern shore of Qinghai Lake have gradually improved after desertification control measures were implemented. The species diversity of the community has increased with the extension of the fixed growth time of the dunes, while the coverage of herbaceous plants has also increased. Soil surface deposits were mainly concentrated in medium sands, whose organic matter and nutrient content are both low. Influenced by precipitation, soil moisture reaches its highest state on natural dunes rather than mobile dunes but lacks interannual variation for all dune types. However, the vertical distribution of soil moisture is seasonal, showing variation from precipitation and exhibiting interannual variability. The dynamic patterns of vegetation and soil properties are similar to those of other deserts in northern China, despite the severe impact of climatic conditions on plant survival in the alpine desert, which makes it more difficult to control the expansion of desertification.

Data availability statement

The raw data supporting the conclusions of this article will be made available by the authors without undue reservation.

Author contributions

HZ started the formal analysis and wrote the original draft. LT played a guiding role in conceptualizing the field experiment and editing the manuscript. EH helped with editing and reviewing the manuscript. DZ and WW assisted in the data curation and editing of the manuscript.

Funding

This research was funded by the Chinese Western Youngest Scientist Program supported by CAS (2021_1_1), the Leading Talent Program supported by Qinghai Province (2022), the Qinghai Three Rivers Ecological Protection and Construction Phase II (2018-S-1), and the Open Project of the State Key Laboratory of Plateau Ecology and Agriculture, Qinghai University (2022-KF-07).

Acknowledgments

We thank Dengfeng Zhang for his kind assistance with this study's field experiments.

Conflict of interest

The authors declare that the research was conducted in the absence of any commercial or financial relationships that could be construed as a potential conflict of interest.

Publisher's note

References

Bayat, H., Rastgo, M., Mansouri Zadeh, M., and Vereecken, H. (2015). Particle size distribution models, their characteristics and fitting capability. *J. Hydrology* 529, 872–889. doi:10.1016/j.jhydrol.2015.08.067

Blott, S. J., and Pye, K. (2001). Gradistat: A grain size distribution and statistics package for the analysis of unconsolidated sediments. *Earth Surf. Process. Landforms* 26, 1237–1248. doi:10.1002/esp.261

Cui, B. L., and Li, X. Y. (2015). Stable isotopes reveal sources of precipitation in the Qinghai Lake Basin of the northeastern Tibetan Plateau. *Sci. Total Environ.* 527-528, 26–37. doi:10.1016/j.scitotenv.2015.04.105

D'odorico, P., Bhattachan, A., Davis, K. F., Ravi, S., and Runyan, C. W. (2013). Global desertification: Drivers and feedbacks. *Adv. Water Resour.* 51, 326–344. doi:10.1016/j.advwatres.2012.01.013

Dormaar, J. F., and Willms, W. D. (1990). Sustainable production from the Rough Fescue Prairie. *J. of Soil and Water Conservation* 45, 4.

Fernandez-Illescas, C. P., Porporato, A., Laio, F., and Rodriguez-Iturbe, I. (2001). The ecohydrological role of soil texture in a water-limited ecosystem. *Water Resour. Res.* 37, 2863–2872. doi:10.1029/2000wr000121

Gu, C., Mu, X., Gao, P., Zhao, G., Sun, W., Tatarko, J., et al. (2018). Influence of vegetation restoration on soil physical properties in the Loess Plateau, China. *J. Soils Sediments* 19, 716–728. doi:10.1007/s11368-018-2083-3

Hill, A. R. (1975). Ecosystem stability in relation to stress caused by human activities. *Canadian Geographer* 3, 15.

Huang, J., Zhang, G., Zhang, Y., Guan, X., Wei, Y., and Guo, R. (2020). Global desertification vulnerability to climate change and human activities. *Land Degrad. Dev.* 31, 1380–1391. doi:10.1002/ldr.3556

Jiang, Z.-Y., Li, X.-Y., Wei, J.-Q., Chen, H.-Y., Li, Z.-C., Liu, L., et al. (2018). Contrasting surface soil hydrology regulated by biological and physical soil crusts for patchy grass in the high-altitude alpine steppe ecosystem. *Geoderma* 326, 201–209. doi:10.1016/j.geoderma.2018.04.009

Li, S., and Sawada, Y. (2022). Soil moisture-vegetation interaction from near-global *in-situ* soil moisture measurements. *Environ. Res. Lett.* 17, 114028. doi:10.1088/1748-9326/ac9c1f

Li, X., Hui, R., Tan, H., Zhao, Y., Liu, R., and Song, N. (2021). Biocrust research in China: Recent progress and application in land degradation control. *Front. Plant Sci.* 12, 751521. doi:10.3389/fpls.2021.751521

Li, X., Yang, X., Ma, Y., Hu, G., Hu, X., Wu, X., et al. (2018). Qinghai Lake basin critical zone observatory on the Qinghai-Tibet Plateau. *Vadose Zone J.* 17, 1–11. doi:10.2136/vzj2018.04.0069

Li, X., Zhang, Z., Huang, L., and Wang, X. (2013). Review of the ecohydrological processes and feedback mechanisms controlling sand-binding vegetation systems in sandy desert regions of China. *Chin. Sci. Bull.* 58, 1483–1496. doi:10.1007/s11434-012-5662-5

Li, X., Zhang, Z., Tan, H., Gao, Y., Liu, L., and Wang, X. (2014). Ecological restoration and recovery in the wind-blown sand hazard areas of northern China: Relationship between soil water and carrying capacity for vegetation in the tengger desert. *Sci. China Life Sci.* 57, 539–548. doi:10.1007/s11427-014-4633-2

Lu, R., Tang, Q., and Zhang, D. (2013). Rainwater infiltration at dunes under various rainfall events in sandy land to the East of Qinghai Lake. *J. Desert Res.* 33, 6.

Maxwell, T. M., Silva, L. C. R., and Horwath, W. R. (2018). Integrating effects of species composition and soil properties to predict shifts in montane forest carbon-water relations. *Proc. Natl. Acad. Sci. U. S. A.* 115, E4219–E4226. doi:10.1073/pnas.1718864115

Noy-Meir, I. (1973). desert ecosystems: Environment and producers. *Annu. Rev. Ecol. Syst.* 4, 25–51. doi:10.1146/annurev.es.04.110173.000325

Noy-Meir, I. (1979). Structure and function of desert ecosystem. *Israel J. Bot.* 28, 19.

Pan, Y.-X., and Wang, X.-P. (2009). Factors controlling the spatial variability of surface soil moisture within revegetated-stabilized desert ecosystems of the Tengger Desert, Northern China. *Hydrol. Process.* 23, 1591–1601. doi:10.1002/hyp.7287

Pan, Y.-X., Wang, X.-P., Zhang, Y.-F., and Hu, R. (2015). Spatio-temporal variability of root zone soil moisture in artificially revegetated and natural ecosystems at an arid desert area, NW China. *Ecol. Eng.* 79, 100–112. doi:10.1016/j.ecoleng.2015.04.019

Porporato, A., Odorico, P. D., Laio, F., Ridolfi, L., and Rodriguez-Iturbe, I. (2002). Ecohydrology of water-controlled ecosystems. *Adv. Water Resour.* 25, 1335–1348. doi:10.1016/s0309-1708(02)00058-1

Qi, Y., Chen, T., Pu, J., Yang, F., Shukla, M. K., and Chang, Q. (2018). Response of soil physical, chemical and microbial biomass properties to land use changes in fixed desertified land. *Catena* 160, 339–344. doi:10.1016/j.catena.2017.10.007

Renne, R. R., Bradford, J. B., Burke, I. C., and Lauenroth, W. K. (2019). Soil texture and precipitation seasonality influence plant community structure in North American temperate shrub steppe. *Ecology* 100, e02824. doi:10.1002/ecy.2824

Rodriguez-Iturbe, I., D'odorico, P., Porporato, A., and Ridolfi, L. (1999). On the spatial and temporal links between vegetation, climate, and soil moisture. *Water Resour. Res.* 35, 3709–3722. doi:10.1029/1999wr900255

Silva, L. C. R., and Lambers, H. (2018). *Soil–Plant–Atmosphere Interact.* 35, 29–60.

Tian, L., Wang, H., Zhang, D., Wang, Q., and Liu, R. (2021). Water use patterns for a typical afforested shrub among topographic positions in an alpine desert of Qinghai-Tibet Plateau using stable isotopes tracers. *Acta Ecol. Sin.* 41, 12.

Tian, L., Wu, W., Zhang, D., Lu, R., and Wang, X. (2015). Characteristics of erosion and deposition of straw checkerboard barriers in alpine sandy land. *Environ. Earth Sci.* 74, 573–584. doi:10.1007/s12665-015-4059-6

Tian, L., Wu, W., Zhang, D., and Yu, Y. (2020). Airflow field around Hippophae rhamnoides in alpine semi-arid desert. *Land* 9, 140. doi:10.3390/land9050140

Tian, L., Wu, W., Zhou, X., Zhang, D., Yu, Y., Wang, H., et al. (2019). The ecosystem effects of sand-binding shrub Hippophae rhamnoides in alpine semi-arid desert in the northeastern Qinghai–Tibet Plateau. *Land* 8, 183. doi:10.3390/land8120183

Turnbull, L., Wilcox, B. P., Belnap, J., Ravi, S., D'odorico, P., Childers, D., et al. (2012). Understanding the role of ecohydrological feedbacks in ecosystem state change in drylands. *Ecohydrology* 5, 174–183. doi:10.1002/eco.265

Walkley, A. J., and Black, I. A. (1934). Estimation of soil organic carbon by the chromic acid titration method. *Soil Sci.* 37, 10.

Wan, L., Cao, W., Hu, F., Liang, S., and Jin, X. (2005). Eco-hydrology and eco-hydrogeology. *Geol. Bull. China* 24, 4.

Wang, H., Tian, L., Zhang, H., Yu, Y., and Wu, H. (2022). Water uptake by Artemisia ordosica roots at different topographic positions in an alpine desert dune on the northeastern Qinghai–Tibet Plateau. *Front. Earth Sci.* 10. doi:10.3389/feart.2022.686441

Wang, X.-P., Li, X.-R., Xiao, H.-L., and Pan, Y.-X. (2005). Evolutionary characteristics of the artificially revegetated shrub ecosystem in the Tengger Desert, northern China. *Ecol. Res.* 21, 415–424. doi:10.1007/s11284-005-0135-9

Wang, X. P., Wang, Z. N., Berndtsson, R., Zhang, Y. F., and Pan, Y. X. (2011). Desert shrub stemflow and its significance in soil moisture replenishment. *Hydrology Earth Syst. Sci.* 15, 561–567. doi:10.5194/hess-15-561-2011

Wu, H., Li, X.-Y., Jiang, Z., Chen, H., Zhang, C., and Xiao, X. (2016). Contrasting water use pattern of introduced and native plants in an alpine desert ecosystem, Northeast Qinghai–Tibet Plateau, China. *Sci. Total Environ.* 542, 182–191. doi:10.1016/j.scitotenv.2015.10.121

Wu, H., Li, X. Y., Zhang, J., Li, J., Liu, J., Tian, L., et al. (2019). Stable isotopes of atmospheric water vapour and precipitation in the northeast Qinghai-Tibetan Plateau. *Hydrol. Process.* 33, 2997–3009. doi:10.1002/hyp.13541

Wu, W., Chen, G., Meng, T., Li, C., Feng, H., Si, B., et al. (2023). Effect of different vegetation restoration on soil properties in the semi-arid Loess Plateau of China. *Catena* 220, 106630. doi:10.1016/j.catena.2022.106630

Wu, W., Zhang, D., Tian, L., Gao, S., Zhang, M., and Zhou, X. (2019a). Erosion-deposition characteristics and fencing life of straw checkerboard in alpine sandy lands. *Environ. Eng. Sci.* 36, 60–70. doi:10.1089/ees.2018.0155

Wu, W., Zhang, D., Tian, L., Zhang, M., and Zhou, X. (2019b). Features of artificial plant communications from the east sand region of the Qinghai Lake over the last 10 years. *Acta Ecol. Sin.* 39, 13.

Xu, X., Ma, K., Li, C., Fu, B., Liu, X., Huang, Y., et al. (2006). Research review of the relationship between vegetation and soil loss. *Acta Ecologica Sinica* 26, 7.

Yu, X., Huang, Y., Li, E., Li, X., and Guo, W. (2017). Effects of vegetation types on soil water dynamics during vegetation restoration in the Mu Us Sandy Land, northwestern China. *J. Arid Land* 9, 188–199. doi:10.1007/s40333-017-0054-y

Yu, Y., and Jia, Z. Q. (2014). Changes in soil organic carbon and nitrogen capacities of *Salix cheilophila* Schneid along a revegetation chronosequence in semi-arid degraded sandy land of the Gonghe Basin, Tibet Plateau. *Solid Earth.* 5, 1045–1054. doi:10.5194/se-5-1045-2014

Yu, Y., Wei, W., Chen, L., Feng, T., Daryanto, S., and Wang, L. (2016). Land preparation and vegetation type jointly determine soil conditions after long-term land stabilization measures in a typical hilly catchment, Loess Plateau of China. *J. Soils Sediments* 17, 144–156. doi:10.1007/s11368-016-1494-2

Yu, Y., Zhao, W., Martinez-Murillo, J. F., and Pereira, P. (2020). Loess Plateau: From degradation to restoration. *Sci. Total Environ.* 738, 140206. doi:10.1016/j.scitotenv.2020.140206

Zhou, G., Xia, J., Zhou, P., Shi, T., and Li, L. (2020). Not vegetation itself but mis-revegetation reduces water resources. *Sci. China Earth Sci.* 51, 8.

Zhu, B.-Q., Yu, J.-J., Rioual, P., and Ren, X.-Z. (2014). Particle size variation of aeolian dune deposits in the lower reaches of the Heihe River basin, China. *Sediment. Geol.* 301, 54–69. doi:10.1016/j.sedgeo.2013.12.006

Zuo, X., Zhao, H., Zhao, X., Zhang, T., Guo, Y., Wang, S., et al. (2008). Spatial pattern and heterogeneity of soil properties in sand dunes under grazing and restoration in Horqin Sandy Land, Northern China. *Soil Tillage Res.* 99, 202–212. doi:10.1016/j.still.2008.02.008

Frontiers in Environmental Science

TYPE Original Research
PUBLISHED 23 February 2023
DOI 10.3389/fenvs.2023.1116633

Check for updates

OPEN ACCESS

EDITED BY
Yang Yu,
Beijing Forestry University, China

REVIEWED BY
Jiabo Yin,
Wuhan University, China
Siyu Cai,
China Institute of Water Resources and Hydropower Research, China

*CORRESPONDENCE
Hengjia Zhang,
✉ 596088683@qq.com

SPECIALTY SECTION
This article was submitted to Freshwater Science, a section of the journal Frontiers in Environmental Science

RECEIVED 05 December 2022
ACCEPTED 15 February 2023
PUBLISHED 23 February 2023

CITATION
Yu J, Yu S, Zhang H, Wang Z, Zhou C and Chen X (2023), Determination of ecological flow thresholds for rainfall-recharging rivers based on multiple hydrological methods.
Front. Environ. Sci. 11:1116633.
doi: 10.3389/fenvs.2023.1116633

Determination of ecological flow thresholds for rainfall-recharging rivers based on multiple hydrological methods

Jiandong Yu[1,2], Shouchao Yu[2], Hengjia Zhang[1,2]*, Zeyi Wang[1], Chenli Zhou[1] and Xietian Chen[1]

[1]College of Water Conservancy and Hydropower Engineering, Gansu Agricultural University, Lanzhou, China, [2]College of Agronomy and Agricultural Engineering, Liaocheng University, Liaocheng, China

Given the threats to the regional river ecological flow, including the sharp increase in *per capita* water demand, the increase in the number of hydraulic engineering, and the strong seasonal runoff of rainfall recharge channels, we clarified the appropriate ecological flow thresholds for the middle reaches of Bailong River of northwest China. Based on the monthly runoff data in the Wudu Hydrological Station of Bailong River from 1990 to 2020, seven suitable hydrological methods were used to couple the estimation of the ecological flow in the middle reaches of Bailong River, which were tested by runoff satisfaction level analysis, using quadratic fit and 95% confidence interval to determine the monthly ecological flow and threshold of the river in the study area. The results by using the single hydrological methods showed that the calculation results from the monthly minimum ecological runoff calculation method, the improved RVA method, the Tennant method, and the DC method were four better estimation methods, which had a satisfaction level of more than 90% in the whole year. The improved RVA method and the Tennant method were more suitable for the diversion power station whose main task aimed at power generation. Although the economic benefits of hydropower stations were better when the improved RVA method was used to calculate ecological flow, the calculation results from the improved RVA method were tested and analyzed by the Tennant method, which were extremely poor from November to April in the following year, and could not meet the minimum ecological water requirements for the biological community in the river channel. While the other five methods all meet this requirement. We suggest that the minimum ecological flow in the middle reaches of the Bailong River maintained at 27.28 m^3/s, and the maximum retained at 116.33 m^3/s. The calculation results were in line with the dynamics of runoff in the study area, which could improve the accuracy of water ecological protection. The calculation results of this study could be used for the middle reaches of the Bailong River and may provide a reference for follow-up ecological restoration research and management in similar ecological zones.

Abbreviations: CI, Confidence Interval; IFIM, Instream Flow Incremental Methodology; BBM, Building Block Methodology; NGPRP, Northern Great Plains Resource Program; RVA, Range of Variability Approach; DC, Duration Curve; FDC, Flow Duration Curve.

KEYWORDS

ecological flow threshold, rainfall recharge runoff, hydrological method, middle reaches of Bailong River, 95% confidence intervals

1 Introduction

With the population growth as well as economic and social development, human intervention in regional soil and water resource and the surrounding ecological environment has been continuously intensified, among which human activities such as damming, sand panning, and shipping have significantly changed the hydrological situation of rivers, leading to increasingly prominent problems such as river drying, aquatic species extinction and ecological environment degradation (Angus Webb et al., 2013; Brown et al., 2015; Ren et al., 2018; Harper et al., 2022). As the main living water source for most urban and village residents, the reasonable and accurate measurement of ecological flow within inland river channels has become an important part of protecting the ecological security of rivers and lakes and promoting regional coordinated sustainable development (Wu and Chen, 2018; Hairan et al., 2021). According to incomplete statistics, about 1/3 of global inland river runoff originates from recent rainfall recharge, and in the global warming environment, extreme weather is occurring frequently. The intensity (duration) of these precipitation extremes is intensifying (decreasing), persistent high temperatures, droughts and erratic rainfall are becoming increasingly synchronised, and a sense of crisis is increasingly evident in the process of balancing the relationship between water allocation, use and ecological and economic development (Bevacqua et al., 2022; Yin et al., 2022; Yin et al., 2023). This general environment will result in frequent intra- and inter-annual instability in rainfall-supplemented river runoff, which greatly affects the accuracy of rivers and lakes even ecological protection decisions in the basin (Wu and Chen, 2018; Kang et al., 2020). Therefore, how to accurately determine the ecological flow of rivers, then scientifically allocate water rights, rationally develop water resources, and protect water ecological security has become a hot global research topic and an urgent problem to be solved (Bhaduri et al., 2016).

The research on river ecological flow began in the early 1940s (Poff and Matthews, 2013), and the concept of basic ecological environment water demand was proposed by Gleick at the end of the last century (Gleick, 1998), after which he deepened and enriched this concept. At the beginning of this century, with the “European Union Water Framework Directive,” The Nature Conservancy of the United States, China’s “Guidelines for Ecological Water Demand Assessment of Rivers and Lakes (Trial) (SL/Z 479-2010)” and other relevant authorities and provisions promulgated as well as the definition and further analysis on the concept of Environmental Water Demand (or Ecological Water Demand) proposed and promoted, domestic and foreign research on the ecological water demand of rivers and lakes began to develop rapidly (Poff and Matthews, 2013). At present, there are more than 200 methods for calculating ecological flow in rivers worldwide (Tharme, 2003), mainly including: i) The hydrological methods (Shaeri Karimi et al., 2012; Abdi and Yasi, 2015; Dai et al., 2019), through which are simple and convenient to calculate the ecological flow, such as the Tennent method, Average Flow method of the Driest Month in the Last 10 Years (Ministry of Water Resources of the People’s Republic of China, 2015), and Typical Hydrological Frequency Year method (Yao et al., 2021), etc.; ii) The hydrodynamic methods, which takes hydraulic elements (or hydraulic parameters) as influencing factors (also called hydraulic index methods) (Abdi and Yasi, 2015; Książek et al., 2019), such as Wet Cycle method (Gippel and Stewardson, 1998), R2CROSS method (Mosley, 1982), etc.; iii) The habitat simulation methods (also known as habitat quorum methods, or habitat simulation methods) that relate biological communities in the region with hydrological information, such as IFIM method (Instream Flow Incremental Methodology) (PHABSIM for Windows User’s Manual and Exercises, 2022), etc.; iv) The holistic or integrated analysis methods that combines multiple natural information in the area, such as BBM method (Building Block Methodology) (Hughes, 2001), Overall Research method (Liu et al., 2016), etc.

Different estimation methods of river ecological flow have corresponding proposed backgrounds and application scopes. Among them, the hydrological methods are based on multi-year hydrological elements of the river. It is simple to calculate and has strong operability, and is widely used by scholars and institutions in many developing countries (Shaeri Karimi et al., 2012; Abdi and Yasi, 2015). However, different hydrological methods have a different focus when calculating ecological flow in different rivers. For rainfall recharge rivers, due to the influence of extreme weather such as heavy rainfall and continuous drought, the inter-annual fluctuation of runoff is big, resulting in great differences in the final calculation results (Zhang et al., 2022). Therefore, the objectives of the present study were to determine: 1) To compare the differences in the calculation results of seven hydrological methods for calculating ecological flow applied in the study area; 2) To establish a set of hydrological methods by coupling a variety of methods that were consistent with the calculation of rainfall supplementary runoff ecological flow. 3) Using the combining polynomial fitting method and 95% confidence interval to explore the threshold range of ecological flow value. It is worth mentioning that the seven hydrological methods applied in this study are very applicable to calculating the ecological flow of rainfall supplemental runoff. Unfortunately, the selection of the most appropriate calculation methods requires a comprehensive analysis of the study area and is also beyond the scope of this study. Thereby, this methodological study is to provide a reference for accurate and scientific analysis and calculation of ecological flow in rainfall supplemental runoff-type channels.

2 Materials and methods

2.1 Study area

The middle reaches of Bailong River basin were selected as the study area, which is located between the 103°30′E and 105°40′E and between the 32°20′N and 34°10′N (Zhou, 2014). The Bailong River is the largest tributary of the Jialing River, a first-class tributary of the Yangtze River. It originates from Langmu Temple, Luqu County,

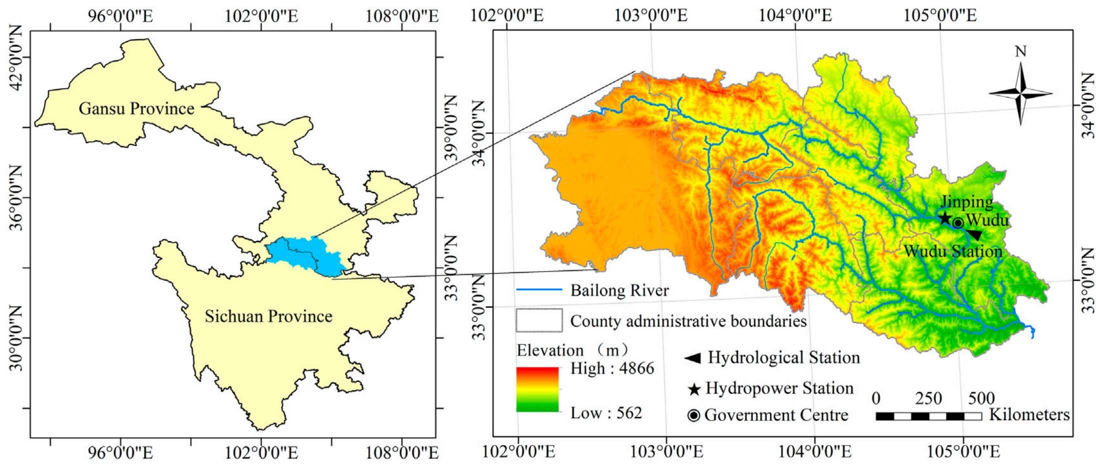

FIGURE 1
Overview of the water system and hydrological station distribution in Bailong River Basin, China.

Gansu Province, China. The total length of the river is 576 km, the drop between the river source and estuary is 3,607 m, and the average ratio drop of the river is 0.54%. The river runoff is mainly recharged by rainfall, and the average annual runoff is 389 m^3/s. There are abundant hydraulic resources available for development, and many hydropower stations have been put into operation, such as the Qilin Temple Hydropower Station and the Bikou Hydropower Station, etc. The general situation of the water system and the distribution of hydrological stations in Bailong River Basin were shown in Figure 1.

2.2 Data collection

In this study, the Wudu Hydrological Station in Bailong River was selected as the study hydrological station, which is located in the urban area of Longnan City with a large population and a high level of hydropower development, a more important hydrological control station in the Bailong River basin. The basic data sources mainly originated from "Gansu Provincial Water Resources Bulletin" (Gansu Provincial Water Resources Department, 2020) and the actual measurement data by the Wudu Hydrological Station. Additionally, a total of 31 years of runoff data from 1990 to 2020 and those of multi-year average monthly runoff from 1956 to 2020 were also obtained.

2.3 Methodologies of data analysis

This study refers to the relevant research in the same type of area and selects the following seven methods based on the local hydrological conditions as the assessment methods to determine the ecological flow in the middle reaches of the Bailong River.

2.3.1 NGPRP method

The NGPRP method (Northern Great Plains Resource Program method) calculates the ecological flow in the river channel as follows:

TABLE 1 Classification basis of the year types.

Model year	Dry year	Normal water year	Wet year
Percentage anomaly	$P_i < -10\%$	$-10\% \le P_i \le 10\%$	$P_i > 10\%$

i) Dividing the known historical runoff data in the study area into three groups: wet years, normal years, and dry years; ii) Regarding the runoff in the normal year corresponding to the 90% guarantee rate as the ecological flow (Dai et al., 2019).

Use the percentage of anomalies to determine the wet, normal and dry years of a long series of historical runoff data. The calculation equation was as following:

$$\boldsymbol{P_i} = \frac{(\boldsymbol{Q_i} - \boldsymbol{Q_n})}{\boldsymbol{Q_n}} \times \mathbf{100\%} \tag{1}$$

where: P_i—the percentage of anomalies of the runoff data, %; Q_i—the monthly average flow in the i-th year, m^3/s; Q_n—the average value of the runoff data within n years. The results of the year-type classification were shown in Table 1.

The percentage of anomalies and average annual flows for each of the year in the normal flow year group (a total of 9 years) were shown in Table 2, and the year corresponding to the 90% cumulative frequency was 1998. The final ecological flow values were obtained for each month of the year.

2.3.2 Improved dynamic calculation method

The dynamic calculation method introduces the contemporaneous mean ratio as an index to calculate the ecological water demand of the river, which is more suitable for the natural runoff characteristics of the river (Pan et al., 2013). In the original method, the improved dynamic calculation method introduces the mean ratio of annual runoff to the multi-year average method runoff under the 90% guarantee rate corresponding to the P-III curve. This method reduces the influence of decreasing or increasing ratio in the same season in the calculation process due to the increase or decrease of the runoff

TABLE 2 Percentage of anomalies and average annual flow in each year's group.

Year	1998	2008	2001	2015	2007	2003	1999	2012	2014
Percentage anomaly (%)	−9.7%	−8.8%	−8.8%	−8.0%	−3.6%	−3.2%	−1.3%	6.8%	9.7%
Average monthly traffic (m^3/s)	104.00	104.99	105.00	105.87	111.00	111.41	113.60	122.96	126.29

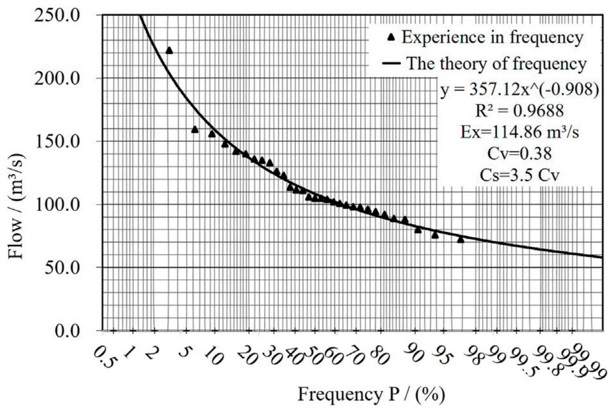

FIGURE 2
Historical flow-frequency curve of Wudu Hydrological Station.

TABLE 3 P-III curve wiring results.

Project	$\overline{q_i}$ (m^3/s)	C_v	C_s	$q_{90\%}$ (m^3/s)
The Numerical	114.86	0.38	3.5	82.81

data time series, thus reducing the error of the ecological flow value (Zhao et al., 2018). The calculating steps of the improved dynamic calculation method are as follows.

① According to the known long series of historical runoff data, the average monthly flow for a long time was calculated, and the calculation equation was as following:

$$\overline{q_i} = \frac{1}{n}\sum_{j=1}^{n} q_{ij} \tag{2}$$

② The P-III curve adaptation method was used to determine the annual runoff value of the river under a 90% guarantee rate, and the alignment results were shown in Figure 2. The results of the multi-year monthly mean flow ($\overline{q_i}$), variation coefficient C_V, deviation coefficient C_S and annual river runoff $q_{90\%}$ for the 90% guaranteed rate were shown in Table 3.

③ The mean value ratio in the same season was obtained using the annual runoff value ratio $q_{90\%}$ of the river channel under 90% guarantee rate to the average runoff in each month for a long time. The calculating method was Eq. 3, and the mean value ratio in the same season was 0.72.

$$\eta = \frac{q_{90\%}}{\overline{q_i}} \tag{3}$$

④ The ecological flow in the river in this study area was calculated for each month, and the equation was as following:

$$Q_{ec} = \overline{q_i} \times \eta \tag{4}$$

where: $\overline{q_i}$—Multi-year average monthly flow for month i of the year, m^3/s; q_{ij}—Runoff for month i of the year j, m^3/s; n—A total year number of the historical runoff information in the long series; $q_{90\%}$—The annual river runoff volume under 90% guarantee rate, which was calculated using the P-III curve alignment method, m^3/s; η—The mean ratio in the same season; Q_{ec}—Monthly ecological flow in the study area in the river channel, m^3/s.

The ecological flow of the river at Wudu Hydrological Station was calculated according to Eq. 4; Table 3, and the calculation results in ③.

2.3.3 Improved RVA method

The RVA method (Range of Variability Approach method), also known as the range of variation method or the range of variability method, was proposed by Richter et al. (1997), which considers the changes in hydrological elements such as flow, duration, and frequency before and after human impact (construction of hydraulic engineering, etc.) on the river and its environment as well as stipulates that 25% and 75% of the incoming water frequencies are the upper and lower limits of the estimated river ecological flow, that is, the RVA threshold. Many scholars have continuously improved and revised the RVA method. Zhang et al. (2017) proposed the improved RVA method to divide the annual rainfall into four seasons including the non-flood season, pre-flood season, main flood season, and post-flood season, and calculated the ecological flow, respectively. To a certain extent, the improvement reduced the influence of the small ecological flow value calculated in the dry season due to the small range of the RVA threshold values in the same season. The minimum ecological flowvalue of the river for the non-flood, pre-flood, and post-flood seasons in the study area were calculated according to Eq. 5, while that for the main flood season was calculated by Eq. 6. The results of the calculations were shown in Table 4.

$$Q_{ec} = (Q_u - Q_l) \times 50\% \tag{5}$$

$$Q_{ec} = (Q_u - Q_l) \times 75\% \tag{6}$$

where: Q_{ec}—Minimum ecological flow value of the river; Q_u—Runoff corresponding to the upper limit of the RVA threshold (p = 25%); Q_l—Flow rate corresponding to the lower limit of the RVA threshold (p = 75%).

2.3.4 Monthly minimum ecological runoff calculation method

This method reduces the errors in ecological flow calculation due to uneven distribution of precipitation in each month of the year with seasonal characteristics, and the calculated value fits the

TABLE 4 Ecological Flow values calculated by the improved RVA method for each month at Wudu station.

Month	Jan	Feb	Mar	Apr	May	Jun	Jul	Aug	Sept	Oct	Nov	Dec
Q_u (p = 25%)	58.3	50.45	51.11	87.19	162	189	223.01	195	225	211	109	71.7
Q_l (p = 75%)	43.1	38.7	38.79	58.7	102	123	120	113	124	129	82.99	55.5
Ecological flow (m^3/s)	7.6	5.87	6.16	14.25	45	49.5	77.25	61.5	75.75	61.5	13.01	8.1

Note: Months were indicated by abbreviations in all figures and tables in this study. For example, January was indicated by Jan.

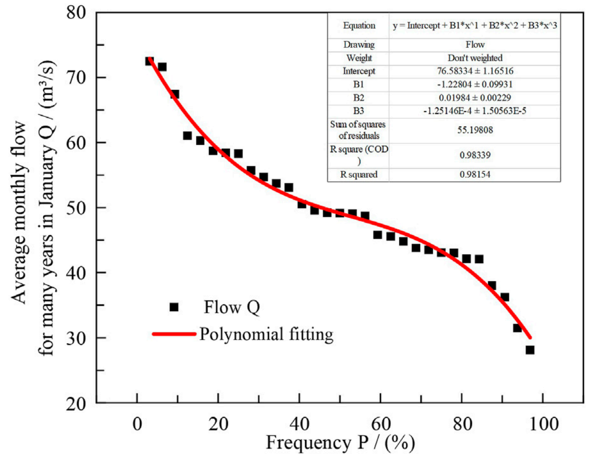

Equation	y = Intercept + B1*x^1 + B2*x^2 + B3*x^3
Drawing	Flow
Weight	Don't weighted
Intercept	76.58334 ± 1.16516
B1	-1.22804 ± 0.09931
B2	0.01984 ± 0.00229
B3	-1.25146E-4 ± 1.50563E-5
Sum of squares of residuals	55.19808
R square (COD)	0.98339
R squared	0.98154

FIGURE 3
Cumulative frequency corresponding to multi-year average runoff in January.

characteristics of intra-annual variation of river runoff, which is more consistent with the calculation of the river ecological flow based on rainfall recharge (Wu et al., 2020).

The calculating steps are as follows: 1) From the known historical long series runoff data, pool the runoff volume of January each year and take the minimum value as the ecological flow of January; 2) Obtaining a total of 12 ecological flow values in February, March, ..., and December following above method.

2.3.5 DC method

The DC method (Duration Curve method) (Tharme, 2003) is an improved method of the Flow Duration Curve (FDC) method (Men et al., 2012). Various indexes can be obtained in the calculation of river ecological flow by the DC method: multi-year average minimum ecological flow, typical annual minimum ecological flow, minimum ecological flow in four seasons, and monthly ecological flow. Therefore, the flow rate $Q_{95\%}$ (the minimum flow value of the protected river) corresponding to the cumulative frequency p = 95% in each month of the year was selected to calculate the river ecological flow according to the DC method. The calculation steps are as follows:

Firstly, sorting the long series of historical runoff data of no less than 20 years from the maximum to minimum recorded as q_i, $(i = 1, 2, \ldots, N)$, in which q_i is the maximum runoff in the long series of historical data and q_N indicates the minimum. Secondly, calculating the cumulative frequency corresponds to the monthly runoff in the historical year according to Eq. 7. Thirdly, plotting the historical curve (Figure 3). Finally, determining the ecological flowbased on the corresponding cumulative frequency.

$$\boldsymbol{P_i} = \frac{\boldsymbol{i}}{\boldsymbol{N+1}} \tag{7}$$

where: P_i—the percentage of anomalies of the runoff data, %; i—ordinal number corresponding to the sorting of the runoff; N—the total year number of historical runoff data.

By accurately fitting the cumulative frequency curve corresponding to the multi-year average runoff in January (Figure 3), the runoff corresponding to a cumulative frequency of 95% was selected to calculate the ecological flow value using the DC method.

2.3.6 Improved monthly frequency calculation method

The monthly frequency calculation method divides the month of the year into three seasons (wet water season, 50% guaranteed rate; normal water season, 70% guaranteed rate; and dry water season, 90% guaranteed rate). The runoff obtained under the guaranteed rate for these three seasons are always used as the ecological flowvalue of the river (Dong et al., 2012). To avoid the lack of ecological flowvalues when seasonal river breaks occurred, we did not divide the season of the year in the improved monthly frequency method and took 50% as the guaranteed rate for each month within the year to calculate the corresponding ecological flow values (Chen, 2005).

2.3.7 Tennant method

The Tennant method, also known as the Montana method, uses the percentage of the average annual runoff in a river as a benchmark for evaluating the biological ecological water demand (Karakoyun et al., 2018) and is one of the most widely used methods for calculating river ecological flow through hydrology (Tennant, 1976). Around 1974, Donald Leroy Tennant (1976) conducted the "Montana method" test and the correlation analysis by the "Montana method" under different flow regimes in hundreds of rivers of 24 states in the United States (Hamidifar et al., 2022), and the results showed that: i) The minimum instantaneous flow to maintain the survival conditions of aquatic organisms in the habitat for a short season was 10% of the annual average flow; ii) The base flow in maintaining good living conditions for most aquatic organisms in the habitat was 30% of the annual average flow; iii) The flow used to provide excellent biological habitat for most aquatic organisms in the habitat during the main growing season and the rest of the resting phase was 60% of the average annual flow.

TABLE 5 Calculating ecological flow assessment criteria in the Tennant method.

Narrative description of the flow	Recommended base flow regimens (percentages of average annual flow) (%)	
	Dry season	Wet season
Flushing or maximum	200	200
Optimal range	60–100	60–100
Outstanding	40	60
Excellent	30	50
Good	20	40
Fair	10	30
Minimum	10	10
Severe degradation	0–10	0–10

Note: Data source: Karakoyun et al. (2016)

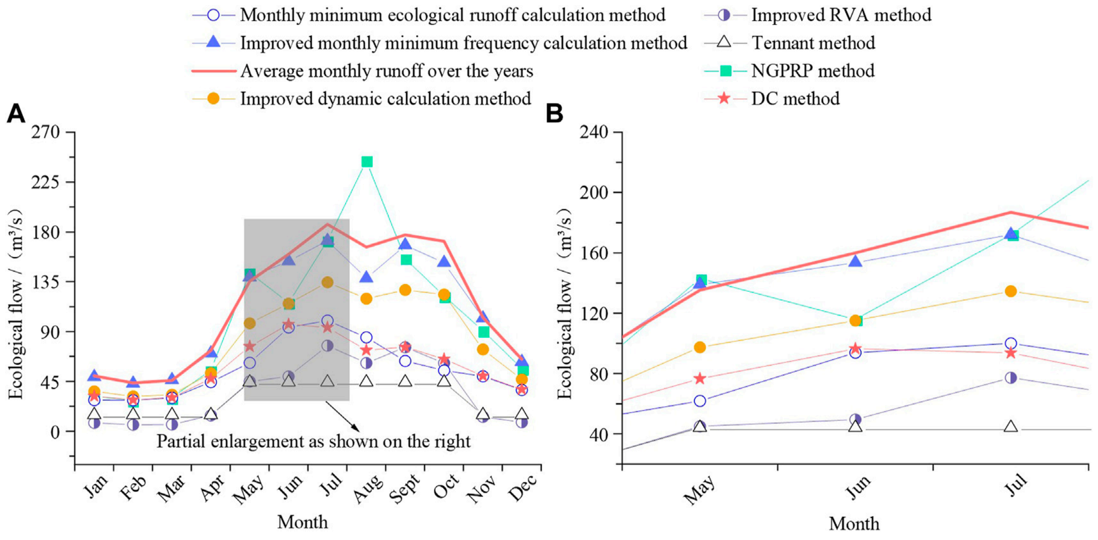

FIGURE 4
Ecological flow for each month of the year calculated by various methods at Wudu Hydrological Station. **(A)** shows the ecological flow values calculated by seven methods. **(B)** shows the 'abrupt change' in ecological flow calculated by various methods for the months of May-July.

The Tennant method calculation steps are as follows: firstly, dividing the months of the year into the dry season (general water use season: October–March of the next year) and the wet season (fish spawning and rearing season: April–September), and then the ecological flow of this river stretch was calculated according to the Tennant method assessment criteria. The evaluation criteria of the Tennant method were shown in Table 5.

Since the Tennant method has more typical data characteristics when calculating ecological flow values in rivers, it was used in this study as a comparative method to test and analyze the results of ecological flow calculation by various hydrological methods (Guo et al., 2009). According to the characteristics of runoff and rainfall distribution in the study area, the months of the year are divided into the dry season (general water use season: November–April of the following year) and the wet season (fish spawning and fattening season: May to October), and the 10% of the average annual flow during the dry season and 30% of the average annual flow during the wet season were selected as the ecological flow of the river.

3 Results and analysis

3.1 Estimation results

Taking the middle reaches of Bailong River basin as the study area, the river ecological flow was calculated, and the historical hydrological data of the Wudu Hydrological Station were analyzed

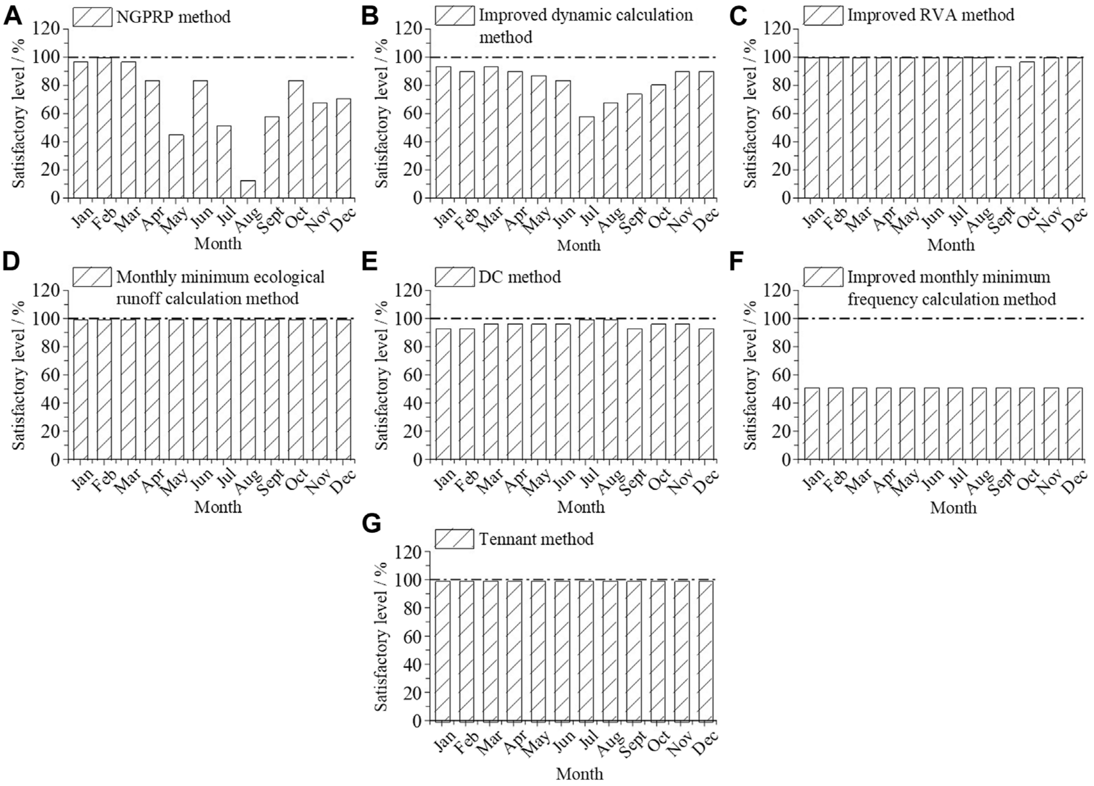

FIGURE 5
Monthly ecological flow satisfactory level within the year. **(A)** shows the Satisfactory level of ecological flow calculated according to the NGPRP method. **(B)** shows the Satisfactory level of ecological flow values calculated according to the Improved dynamic calculation method. **(C)** shows the Satisfactory level of ecological flows calculated according to the Improved RVA method. **(D)** shows the Satisfactory level of ecological flows calculated according to the Monthly minimum ecological runoff calculation method. **(E)** shows the Satisfactory level of ecological flows calculated according to the DC method. **(F)** shows the Satisfactory level of ecological flows based on the Improved monthly minimum frequency calculation method. **(G)** shows the Satisfactory level of the ecological flow calculated according to Tennant's method.

and calculated according to the previous seven methods. The results were shown in Figure 4A.

On the whole, the distribution patterns of the ecological flow values calculated by each hydrological methods were consistent with the multi-year monthly average flow (1956–2020), not only reflecting the change of ecological flow with seasonal rainfall replenishment or deficit of runoff but also conforming to the variation of the actual survival water demand of biological communities in the rivers during the reproductive season (fish spawning and nursery season) and the general water use season described in the Tennant method.

Taking the multi-year average monthly runoff curve and the Tennant method calculation results curve were used as a reference, the calculation results for the seven methods selected for this study were grouped into three categories: i) The results were closed to multi-year average monthly runoff. Includes the improved monthly frequency calculation method. Due to the high demand for domestic water and agricultural irrigation on both sides of the Wudu Hydrological Station, the ecological flow should be less than the average monthly runoff, so this method calculation results were on the large side; ii) The results were closed to the Tennant method calculation results. Includes the improved RVA method. The results obtained by this method were calculated based on the minimum ecological flow in the river. Therefore, it could be used as a lower limit for the ecological flow of the river in this study. However, the determination of a lower limit ecological flow requires further analysis and calculation; iii) The results lay between the multi-year average monthly runoff curve and the Tennant method calculation results curve. A total of four methods, including the DC method, the NGPRP method, the Improved Dynamic Calculation method, and the Monthly minimum ecological runoff calculation method. All four methods focus on the study of the guaranteed rate of runoff for each month of the year and had similar calculation principles. Although the calculations were superior, further analysis was required to avoid sudden changes in ecological flow caused by extreme weather, as shown in Section 3.2 of this study.

As shown in Figure 4B, the results of the NGPRP method had an "inflection point" in May. Comparison with multi-year average monthly runoff, which was no non-linear change from May to June. On the one hand, as the NGPRP method was used to calculate, 1998 was the year corresponding to the 90% guarantee rate of the normal water year group, while the low rainfall, relatively high evaporation capacity and water demand in June of that year, and the predominance of rainfall recharge for river runoff in this study area, resulted in a smaller runoff volume in that month than the multi-

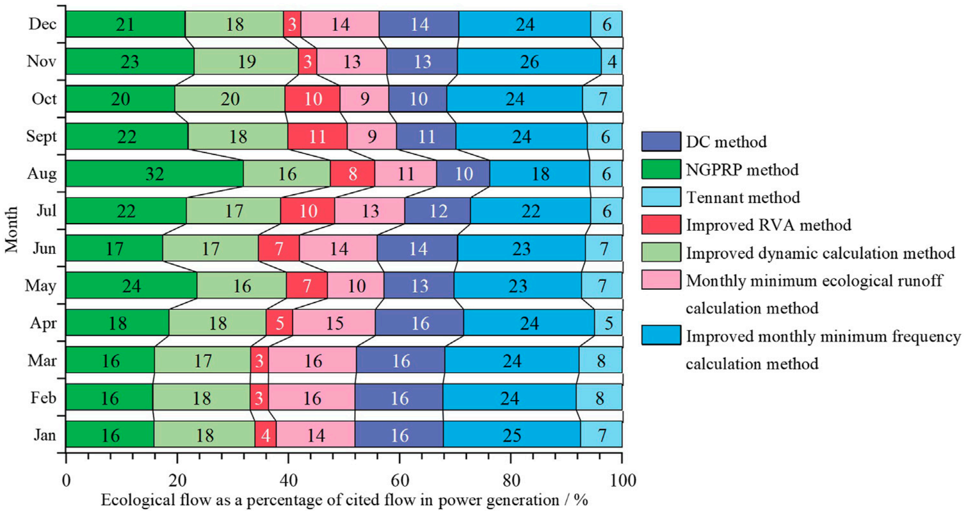

FIGURE 6
Percentage of monthly ecological flow in a generation diversion one within the year.

year average monthly runoff volume, as well as a dramatically smaller ecological flowvalue. On the other hand, for all six methods except the NGPRP method, the results in June follow the same trend as the multi-year average monthly runoff. Therefore, compared to the calculation results of the remaining six methods, the NGPRP method calculation results had another "inflection point" in August for similar reasons as described above. To sum up, the occurrence of the "inflection point" was an accidental phenomenon, which had no significant impact on the calculation of the river ecological flow values in the study area.

As shown in Figure 4A, the ecological flow values calculated by the various methods varied from 11.12 to 62.69 in standard deviations within the same month, with a large level of dispersion. To determine the river ecological flow values at Wudu Hydrological Station of Bailong River Basin with a more scientific and reasonable way, it was necessary to further analyze the accuracy of the calculation results using above mentioned methods, as shown in Section 3.2 and Section 3.3 of this study.

3.2 Preliminary analysis

3.2.1 Satisfactory level analysis

The ecological flow satisfactory level analysis of each method to calculate ecological flow values is a frequent evaluation method often used by many scholars and management agencies in the process of determining the ecological flow (Ge et al., 2019). The evaluation method is based on the preliminary calculation of ecological flow values for each month of the year by each method compared with historical data of monthly runoff, which is calculated as follows:

$$\omega = \frac{n}{N} \tag{8}$$

where: ω—the level of ecological flow satisfaction, %; n—the total number of months in which the monthly runoff is greater than or equal to the ecological flow of the month in the historical runoff data corresponding to a certain month; N—the total year number of historical runoff data. The ecological flow satisfactory level of the Wudu Hydrological Station was calculated according to each method as shown in Figure 5.

As can be seen from Figure 5, the Tennant method, the monthly minimum ecological runoff calculation method, the DC method, and the improved RVA method had satisfactory levels of more than 90% in each month of the year. However, under the improved monthly frequency calculation method, since the ecological flow value in each month was calculated according to the monthly runoff corresponding to the 50% guarantee rate, the calculated satisfactory level was 51.61%. The other two methods (the NGPRP method and the improved DC method) showed a low or extremely low level of satisfaction in the rest of the months, although the satisfactory levels were higher in January, February, and March, with more than 90%. Taking the NGPRP method as an example, this was mainly due to the representative year selected in the calculation process. The ratios of annual mean ecological flow values in May and August exceed 85%, thus showing a low-level ecological flow satisfaction in Figure 5, a phenomenon that also fully illustrates the disadvantages in the single hydrological method calculation of river ecological flow values the occasional extreme deviation (Liu et al., 2016).

3.2.2 Economic benefit test analysis

The unique geological resources and water resources conditions of Bailong River basin promoted the development and construction of many large, medium, and small hydroelectric projects in the study area, among which most of the hydropower stations took power generation as their main task, often leading to the economic benefits and ecological protection conflict (Shen and Xie, 2020). Therefore, we conducted the economic benefit analysis on river ecological flow to provide theoretical analysis for the determination of ecological flow, but the main research object of the economic benefit test analysis was the diverse type power station taking power generation as the main or only task. The principle of this method was in line with the characteristic that the flow rate of power generation quoted

TABLE 6 Tennant method analysis of monthly ecological flow within the year.

Month	General water use season (November–April) (%)						Fish spawning and fattening season (May–October) (%)					
Method	Jan	Feb	Mar	Apr	Nov	Dec	May	Jun	Jul	Aug	Sept	Oct
Improved RVA method	5.16	3.99	4.19	9.68	8.84	5.5	30.57	33.63	52.49	41.79	51.47	41.79
NGPRP method	21.4	19.02	20.65	37.57	61.83	38.46	97.16	78.82	116.86	165.78	105.99	82.89
DC method	21.48	19.28	20.65	32.36	34.03	25.78	51.96	65.55	63.64	49.72	51.66	44.2
Monthly minimum ecological runoff calculation method	19.09	19.02	20.52	30.17	33.7	25.28	41.98	63.73	67.94	57.62	43.08	37.3
Improved monthly minimum frequency calculation method	33.39	29.26	31.39	47.84	69.31	42.63	94.41	104.29	116.86	93.76	114.16	103.27
Improved dynamic calculation method	24.45	21.35	22.41	35.68	50.22	31.76	66.21	78.25	91.43	81.38	86.68	83.93

by the turbine of the diverse type of power station determined the economic benefit of the power station within a certain range. In the research process of this study, we adopted Jinping Power Station close to Wudu Hydrological Station on Bailong River as the reference benchmark, which is located in Liangshui Town, Wudu District of Gansu Province and is a typical artificial open channel diversion power station, with the main design task of power generation. The flow rate used to generate electricity was 176 m^3/s. The calculation results were shown in Figure 6.

As shown in Figure 6, the 6 months of January–April, November and December had the lowest percentage of cited flow in power generation, calculated using the improved RVA method and Tennant method, indicating that in such case the power generation efficiency of the Jinping Hydropower Station on Bailong River was much better, while the ecological flow released from the sluice gate was less, thereby, further research was needed to determine whether the limited ecological flow could meet water demand of normal survival of the aquatic biological community in this river section. Each of the remained five methods respectively accounted for about 17% of the total calculated results of the 6 months, with no significant difference. The calculated results by the improved RVA method, DC method, monthly minimum ecological runoff method, and Tennant method from May to October accounted for about 8%, indicating that the economic benefit of the hydropower station under such flow allocation was relatively better, which could both meet the ecological flow demand in the river channel and obtain high economic benefits at the same time. From the perspective of the whole year, the calculation results by the NGPRP method and the improved monthly frequency calculation method accounted for a large proportion of each month within the year. For hydropower plants whose main task aiming at generating electricity, such flow allocation would affect the profitability of hydropower plants to a greater extent. Therefore, it is necessary to further balance the relation-ship between environmental protection and economic benefits.

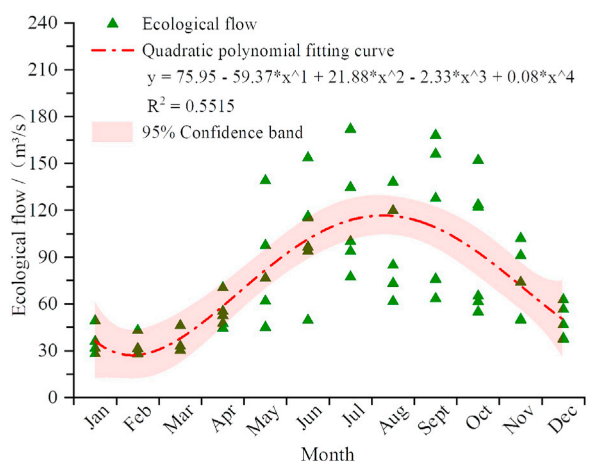

FIGURE 7
Ecological flow threshold fitting analysis.

3.2.3 Tennant method test analysis

The Tennant method test analysis was introduced to determine the mean ratio of ecological flow in each category to annual average monthly runoff (Table 5), and the comparative analysis was carried out during the breeding season of aquatic organisms (fish spawning and nursery season) and general water use season in the river channel. The calculated results were shown in Table 6.

Table 6 revealed that the calculated results from the improved RVA method showed extremely poor performance in January, February, March, April, November, and December, which could not meet the minimum instantaneous flow rate for aquatic organisms to maintain habitat survival conditions in a short season of the river, so that the ecological function of this river section could not maintained. Therefore, these data should be excluded from the subsequent overall analysis of the river ecological flow, which could reduce the error of the overall analysis.

3.3 Comprehensive analysis

In determining the reasonable thresholds for river ecological water demand, it is necessary to clarify the variability characteristics of natural runoff (As shown in Figure 4) to meet the specific ecological function objectives in various reaches of the river at different times within a year (Pan et al., 2013). To reduce the

TABLE 7 Upper and lower threshold of the ecological flow.

Month		Jan	Feb	Mar	Apr	May	Jun	Jul	Aug	Sept	Oct	Nov	Dec
Ecological flow (m^3/s)	Fitted value	36.21	27.28	37.9	58.59	81.71	101.42	113.69	116.33	108.94	92.96	71.61	49.97
	Threshold Lower limit	11.7	11.59	21.72	44.63	69.01	88.08	100.39	103.92	95.73	77.68	56.42	25.48
	Threshold Upper limit	60.72	42.98	54.08	72.56	94.41	114.75	126.99	128.74	122.15	108.23	86.8	74.45

TABLE 8 Evaluation of fitted monthly ecological flow.

Month		Jan	Feb	Mar	Apr	May	Jun	Jul	Aug	Sept	Oct	Nov	Dec
Ecological flow(m^3/s)	Fitted value	36.21	27.28	37.9	58.59	81.71	101.42	113.69	116.33	108.94	92.96	71.61	49.97
	Tennant's method test analysis [annual mean ratio (%)]	24.6	18.54	25.75	39.81	55.52	68.91	77.25	79.04	74.02	63.16	48.65	33.95
	Satisfactory level (%)	93.55	100	80.65	77.42	96.77	93.55	87.10	70.97	93.55	90.32	90.32	87.10

influence on the river ecological flow calculation results due to the extreme rainfall conditions within a year, the satisfactory level of ecological flow, economic benefit, and Tennant method analysis were combined, and the Origin 2021 software was applied in fitting comparison analysis of the monthly ecological flow obtained by each method within a year. Simulation analysis showed that the final fitted equation was optimally simulated by a quartic polynomial, with R^2 marked as the maximum and the reliability the highest. The specific fitting results were shown in Figure 7.

Related studies had shown that the 95% Confidence Interval (CI) was often used as a reference value to determine the interval for estimating the overall parameters of hydrological sample statistics (Babbar, 2014; Jiang et al., 2015; Wang et al., 2018). In the present study, this method was also used to quantify the upper and lower limits of the ecological flow of the river. The month ecological flow threshold interval of Wudu Hydrological Station in Bailong River Basin was shown in Table 7.

To ensure the reliability and reasonableness of the fitted results, we once again analyzed the satisfactory level and Tennant method for fitted values of each month's ecological flow, and the specific calculation results were shown in Table 8.

4 Discussion

4.1 Evaluation of fitted monthly ecological flow

The results of ecological flow calculated based on one hydrological method have low confidence, but after coupling multiple hydrological developments and taking 95% confidence intervals, all the ecological flow values were satisfied to a high level (McCluney et al., 2014). As shown in Table 8. It could be seen that the monthly ecological flow values in the middle reaches of Bailong River basin (Wudu Hydrological Station) might meet the requirements of the inter-annual variation of monthly runoff and had a relatively high satisfactory level for the monthly runoff in the last 31 years, which were also sufficient for the minimum ecological water demand of the aquatic communities in the river during the dry and wet seasons. Thus, the results could be used as a reference value for the ecological flow at Wudu Hydrological Station in Bailong River Basin, providing theoretical reference for relevant research and management institutions.

The calculation results showed a high satisfactory level for the survival needs of the runoff and biological communities, which was mainly because the coupled assessment ecological flow of multiple hydrological methods established a threshold range for the survival needs of aquatic species at different times in the study area. Firstly, the selection of the calculation method was mainly in line with the river runoff types of rainfall recharge, meeting the characteristics of the temporal and spatial variation of river runoff with rainfall (Han et al., 2012). Secondly, when coupling multiple hydrological methods were applied to evaluate the ecological flow threshold in Bailong river middle reaches, the data that were beyond the evaluation range in the preliminary calculation results from the seven calculation methods were deleted, making this data more reliable overall. Finally, Origin 2021 was used to perform quadratic fitting and 95% confidence interval threshold calculations obtained from the three test methods, making the model more generalizable and better fitting, thus reducing the underfitting impact on the calculated results and improving fitting accuracy and science (Li and Lin, 2022).

4.2 Credibility demonstration of coupled multiple hydrological methods for calculating ecological flow

In this study, our work was consistent with the characteristics of runoff changes in Bailong River's middle reaches, and the satisfactory level of water ecological protection was maintained at a relatively high level, which was of great significance for water ecology management and protection in Bailong River's middle reaches. Domestic and foreign research on ecological water demand has undergone nearly half a century of development. Although some studies have been conducted in some regions using related methods, due to the influence of uncertain factors such as the large span of river basins, runoff variation population dynamics, and the prevalence of specific case studies and analyses, the concept and connotation of ecological flow has not been uniformed, although many countries have issued corresponding regulations on ecological civilization at national levels (Han et al., 2012; Chen et al., 2016). As the largest tributary in Jialing River, Bailong River has an abundant water volume, which is responsible for various major tasks such as residential water demand in southern Gansu Province and northern Sichuan Province, ecological water demand and hydroelectric power generation, among others. Previous research found that protecting river water ecological security and biodiversity was of great significance for maintaining regional coordination and unity, as well as green and healthy development (Shenton et al., 2012; Wang et al., 2017). We used the multi-year average monthly runoff from 1956 to 2020 as a comparison and made a comparison description of the preliminary calculation results of ecological flow in the middle reaches of Bailong River. The inadequacy of this study is that the known hydrological data has not been analyzed by proper methods such as models or empirical formulas, thereby further re-searches on this aspect need to have proceeded in the future.

4.3 Application of multiple hydrological methods coupled to calculate ecological flow in watershed management

The coupling of multiple hydrological methods to calculate ecological flow is mainly applied to water ecology restoration and water resource allocation management in some of the basins in China (Wu et al., 2022). The amount of inland river water resources has gradually become a major influencing factor for regional economic development, and in order to avoid over-exploitation of water resources and to protect aquatic biodiversity and the original ecological structure of the river, rational allocation of water resources has gradually been emphasized, and government agencies have developed mechanisms for dividing water rights of watershed water resources to balance water for domestic, agricultural irrigation, hydropower generation and ecological water demand (Liu, 2012). Taking the Yellow River as an example, over-exploitation of river water will not only affect the normal survival of aquatic organisms in the river, but also cut off the flow of the river downstream (Yin, 2002). As the ecological flow of the river is related to the normal survival of aquatic organisms and regional water resources distribution, and the hydrological method to calculate ecological flowis a low-cost, simple and fast method, many scholars have conducted research in this area, but there are differences in the ecological flow calculation methods and evaluation methods for different types of rivers (Ma et al., 2019). Su et al. (2022) used six hydrological methods to calculate the ecological flow in Dahuangkou estuary of the Xi River based on the hydrological data of the river before the anthropogenic disturbance, and the calculated results were compared with those based on the simulation of the fish spawning habitat in this river section in related studies, and the satisfactory level was high. Ren et al. (2018) proposed a complex ecological flow study framework, which considered the impact of intra and inter-annual variation of runoff caused by climate change on ecological flow, but the final calculated ecological flow values were not analyzed in terms of the satisfactory level, and their generalizability needs further analysis. The ecological flow threshold calculation method proposed in this study not only took into account the influence of river type on the calculation method, but also removed the data with low satisfactory levels from the calculation results through various satisfactory level analysis methods, effectively improving the accuracy of the calculation of ecological flow thresholds in rivers, which can provide a reference for the calculation of ecological water demand in watershed water management for rivers where rainfall is the main form of recharge runoff.

5 Conclusion

In this study, we assessed the performance of ecological flow in river by comparing multiple hydrological methods, using multiple hydrological methods coupled to assess ecological flow, while evaluating the results, and applied it to the Jinping Hydropower Station, where the Wudu Hydrological Station of Bailong River is located, to obtain ecological flow thresholds for each month of the year at the Wudu Hydrological Station. The coupling of multiple hydrological methods to assess river ecological flow took into account the differences between inter-annual monthly variations in river runoff, primarily in the form of rainfall rechange runoff, and the single hydrological method when calculating river ecological flow, and took into account the analysis of ecological flow satisfactory level, the analysis of economic benefits of hydropower station. The Tennant's method test analysis and the comprehensive analysis, the overall satisfactory level of the calculation results was higher than the satisfactory level of the single hydrological method results, and the results were more practical than the results of the Tennant method test analysis alone, in line with the ecological meaning, and meet the water needs of the biological communities within the river, which could be used as a reference value for the ecological flow threshold in the river of study area. Furthermore, the conflict between power generation benefits and ecological protection during fish spawning and growth seasons would have an impact on the guaranteed rate of ecological flow, necessitating gradient cooperation, joint scheduling, and reasonable development of water conservancy projects upstream and downstream of the river.

Data availability statement

The datasets presented in this study can be found in online repositories. The names of the repository/repositories and accession number(s) can be found in the article/Supplementary Material.

Author contributions

JY prepared the data, calculated the methodology, conceptualized and drafted the article. HZ performed the funding acquisition. SY and HZ wrote-reviewed and edited. SY and HZ supervised, reviewed and edited. ZW validated and investigated. CZ performed the visualization, and XC organized the data. All authors have read and agreed to the published version of the manuscript.

Funding

This work was supported by the National Natural Science Foundation of China (No. 51669001, 52269008), the Industrial

Support Plan Project of the Gansu Provincial Department of Education (No. 2022CYZC-51), and the Key Research and Planning Projects of Gansu Province (No. 18YF1NA073).

Acknowledgments

The authors would like to thank the National Natural Science Foundation of China (No. 51669001, 52269008), the Industrial Support Plan Project of the Gansu Provincial Department of Education (No. 2022CYZC-51), and the Key Research and Planning Projects of Gansu Province (No. 18YF1NA073) for the funding and lab facilities. We also thank the editor and two referees for careful reading and comments which will greatly improve the paper.

Conflict of interest

Publisher's note

References

Abdi, R., and Yasi, M. (2015). Evaluation of environmental flow requirements using eco-hydrologic–hydraulic methods in perennial rivers. *Water Sci. Technol.* 72, 354–363. doi:10.2166/wst.2015.200

Angus Webb, J., Miller, K. A., King, E. L., Little, S. C., Stewardson, M. J., Zimmerman, J. K. H., et al. (2013). Squeezing the most out of existing literature: A systematic re-analysis of published evidence on ecological responses to altered flows. *Freshw. Biol.* 58, 2439–2451. doi:10.1111/fwb.12234

Babbar, R. (2014). Pollution risk assessment based on QUAL2E-UNCAS simulations of a tropical river in Northern India. *Environ. Monit. Assess.* 186, 6771–6787. doi:10.1007/s10661-014-3888-1

Bevacqua, E., Zappa, G., Lehner, F., and Zscheischler, J. (2022). Precipitation trends determine future occurrences of compound hot–dry events. *Nat. Clim. Change* 12, 350–355. doi:10.1038/s41558-022-01309-5

Bhaduri, A., Bogardi, J., Siddiqi, A., Voigt, H., Vörösmarty, C., Pahl-Wostl, C., et al. (2016). Achieving sustainable development goals from a water perspective. *Front. Environ. Sci.* 4, 64. doi:10.3389/fenvs.2016.00064

Brown, C. M., Lund, J. R., Cai, X., Reed, P. M., Zagona, E. A., Ostfeld, A., et al. (2015). The future of water resources systems analysis: Toward a scientific framework for sustainable water management: The future of water resources systems analysis. *Water Resour. Res.* 51, 6110–6124. doi:10.1002/2015WR017114

Chen, A., Wu, M., Chen, K., Sun, Z., Shen, C., and Wang, P. (2016). Main issues in research and practice of environmental protection for water conservancy and hydropower projects in China. *Water Sci. Eng.* 9, 312–323. doi:10.1016/j.wse.2017.01.008

Chen, Z. Q. (2005). *Ecological flow requirements for the middle and lower reaches of the Yangtze River*. Nanjing: Hohai Univ. Available at: https://kns.cnki.net/KCMS/detail/detail.aspx?dbcode=CMFD&dbname=CMFD0506&filename=2005074300.nh&v=.

Dai, L., Fang, G., Huang, X., and Zhong, J. (2019). Ecological flow process evaluation of a hydropower STATION'S dehydration river. *Appl. Ecol. Environ. Res.* 17. doi:10.15666/aeer/1703_57075722

Dong, Z.-H., Yang, X. H., Guo, Y. N., Mei, Y., Li, Y. Q., and Li, J. Q. (2012). Modified frequency computation method for optimal environmental flows. *Therm. Sci.* 16, 1539–1543. doi:10.2298/TSCI1205539D

Gansu Provincial Water Resources Department (2020). *Gansu provincial water resour.* Lanzhou: Bulletin. Available at: http://slt.gansu.gov.cn/slt/index.shtml (Accessed October 14, 2021).

Ge, J. J., Peng, W. Q., Zhang, W. H., and Qu, X. D. (2019). Comparison of several hydrological methods to determine the ecological flow for instream river—A case study of Zhoukou hydrological station in Shaying River. *South-to-North Water Divers. Water Sci. Technol.* 17, 75–80. doi:10.13476/j.cnki.nsbdqk.2019.0036

Gippel, C. J., and Stewardson, M. J. (1998). . Use of wetted perimeter in defining minimum environmental flows. *River Res. Appl.* 14, 53–67. doi:10.1002/(sici)1099-1646(199801/02)14:1<53::aid-rrr476>3.0.co;2-z

Gleick, P. H. (1998). Water in crisis: Paths to sustainable water use. *Ecol. Appl.* 8, 571–579. doi:10.1890/1051-0761(1998)008[0571:WICPTS]2.0.CO;2

Guo, L. D., Xia, Z. Q., Lin, H., and Wang, Y. (2009). Researches on application of the tennant method in ecological flow evaluention. *Acta Ecol. Sin.* 29, 1787–1792. doi:10.3321/j.issn:1000-0933.2009.04.020

Hairan, M. H., Jamil, N. R., Azmai, M. N. A., Looi, L. J., and Camara, M. (2021). Environmental flow assessment of a tropical river system using hydrological index methods. *Water* 13, 2477. doi:10.3390/w13182477

Hamidifar, H., Akbari, F., and Rowiński, P. M. (2022). Assessment of environmental water requirement allocation in anthropogenic rivers with a hydropower dam using hydrologically based methods—case study. *Water* 14, 893. doi:10.3390/w14060893

Han, S. M., Yang, Y. H., Fan, T., Xiao, D. P., and Moiwo, J. P. (2012). Precipitation-runoff processes in Shimen hillslope micro-catchment of Taihang Mountain, north China. *Hydrol. Process* 26, 1332–1341. doi:10.1002/hyp.8233

Harper, M., Rytwinski, T., Taylor, J. J., Bennett, J. R., Smokorowski, K. E., Olden, J. D., et al. (2022). How do changes in flow magnitude due to hydropower operations affect fish abundance and biomass in temperate regions? A systematic review. *Environ. Evid.* 11, 3. doi:10.1186/s13750-021-00254-8

Hughes, D. A. (2001). Providing hydrological information and data analysis tools for the determination of ecological instream flow requirements for South African rivers. *J. Hydrol.* 241, 140–151. doi:10.1016/S0022-1694(00)00378-4

Jiang, S., Jomaa, S., Büttner, O., Meon, G., and Rode, M. (2015). Multi-site identification of a distributed hydrological nitrogen model using Bayesian uncertainty analysis. *J. Hydrol.* 529, 940–950. doi:10.1016/j.jhydrol.2015.09.009

Kang, S. C., Guo, W. Q., Zhong, X. Y., and Xu, M. (2020). Change in the mountain cryosphere ang their impacts and measures. *Clim. Chang. Res.* 16, 143–152. doi:10.12006/j.issn.1673-1719.2019.257

Karakoyun, Y., Yumurtaci, Z., and Dönmez, A. H. (2016). Environmental flow assessment for energy generation sustainability employing different hydraulic evaluation methods: Çambaşi hydropower plant case study in Turkey. *Clean. Technol. Environ. Policy* 18, 583–591. doi:10.1007/s10098-015-1023-9

Karakoyun, Y., Dönmez, A. H., and Yumurtacı, Z. (2018). Comparison of environmental flow assessment methods with a case study on a runoff river–type hydropower plant using hydrological methods. *Environ. Monit. Assess.* 190, 722. doi:10.1007/s10661-018-7107-3

Książek, L., Woś, A., Florek, J., Wyrębek, M., Młyński, D., and Wałęga, A. (2019). Combined use of the hydraulic and hydrological methods to calculate the environmental flow: Wisloka river, Poland: Case study. Environ. *Monit.* Assess. 191, 254. doi:10.1007/s10661-019-7402-7

Li, Y., and Lin, J. (2022). Calculation of minimum ecological flow in dewatering section of small hydropower stations: Taking Panxi cascade hydropower stations as an example. *South-to-North Water Divers. Water Sci. Technol.* 20, 536–543. doi:10.13476/j.cnki.nsbdqk.2022.0054

Liu, J. (2012). *A tentative analysis of the concept and system of water rights: From the perspective of the division of resource water and product water*. Nanchang: Contemporary Finance & Economics, 26–34. Available at: https://kns.cnki.net/KCMS/detail/detail.aspx?dbcode=CJFD&dbname=CJFD2012&filename=DDCJ201206002&v=.

Liu, Y. Y., Zhu, J. F., and Zhao, J. S. (2016). Development history and frontiers of river environmental flow research. *J. Hydroe. Eng.* 35, 23–34. doi:10.11660/slfdxb.20161203

Ma, D. Y., Luo, W. G., Yang, G. L., Lu, J., and Fan, Y. Z. (2019). A study on a river health assessment method based on ecological flow. *Ecol. Model.* 401, 144–154. doi:10.1016/j.ecolmodel.2018.11.023

McCluney, K. E., Poff, N. L., Palmer, M. A., Thorp, J. H., Poole, G. C., Williams, B. S., et al. (2014). Riverine macrosystems ecology: Sensitivity, resistance, and resilience of whole river basins with human alterations. *Front. Ecol. Environ.* 12, 48–58. doi:10.1890/120367

Men, B. H., Lin, C. K., Li, Z. F., and Sun, B. Y. (2012). Application of flow duration curve method in calculating instream minimum ecological water demand in guanting gorge of yongding river. *South-to-North Water Divers. Water Sci. Technol.* 10, 52–56+92. doi:10.3724/SP.J.1201.2012.02052

Ministry of Water Resources of the People's Republic of China (2015). Ministry of Water Resources on the approval of the release of water industry standards announcement (Specification of calculation of environmental flow in rivers and lakes). *Tech. Superv. Water Resour.* 23, 90.

Mosley, M. P. (1982). Analysis of the effect of changing discharge on channel morphology and instream uses in a Braided River, Ohau River, New Zealand. *Water Resour. Res.* 18, 800–812. doi:10.1029/WR018i004p00800

Pan, Z. R., Ruan, X. H., and Xu, J. (2013). A new calculation method of instream basic ecological water demand. *J. Hydrau. Eng.* 44, 119–126. doi:10.13243/j.cnki.slxb.2013.01.005

PHABSIM for Windows User's Manual and Exercises (2022). *PHABSIM for Windows User's manual and Exercises*. Available at: https://pubs.er.usgs.gov/publication/ofr2001340 (Accessed December 1, 2022).

Poff, N. L., and Matthews, J. H. (2013). Environmental flows in the anthropocence: Past progress and future prospects. *Curr. Opin. Environ. Sustain.* 5, 667–675. doi:10.1016/j.cosust.2013.11.006

Ren, K., Huang, S., Huang, Q., Wang, H., and Leng, G. (2018). Environmental flow assessment considering inter- and intra-annual streamflow variability under the context of non-stationarity. *Water* 10, 1737. doi:10.3390/w10121737

Richter, B., Baumgartner, J., Wigington, R., and Braun, D. (1997). How much water does a river need? *Freshw. Biol.* 37, 231–249. doi:10.1046/j.1365-2427.1997.00153.x

Shaeri Karimi, S., Yasi, M., and Eslamian, S. (2012). Use of hydrological methods for assessment of environmental flow in a river reach. *Int. J. Environ. Sci. Technol.* 9, 549–558. doi:10.1007/s13762-012-0062-6

Shen, M. H., and Xie, H. M. (2020). Transboundary ecological compensation in the Xin'an River Basin and its institutional arrangement of sustainability. *China Popul. Resour. Environ* 30, 156–163. doi:10.12062/cpre.20200304

Shenton, W., Bond, N. R., Yen, J. D. L., and Mac Nally, R. (2012). Putting the "ecology" into environmental flows: Ecological dynamics and demographic modelling. *Environ. Manage.* 50, 1–10. doi:10.1007/s00267-012-9864-z

Su, H., Xu, Z. X., Li, P., Ye, C. L., and Wang, J. J. (2022). Estimation of ecological baseflow with several hydrological methods at the Dahuangjiangkou reach of the Xijiang River. *J. Beijing Normal Univ. Nat. Sci.)* 58, 269–276. doi:10.12202/j.0476-0301.2021229

Tennant, D. L. (1976). Instream flow regimens for fish, wildlife, recreation and related environmental resources. *Fisheries* 1, 6–10. doi:10.1577/1548-8446(1976)001<0006:IFRFFW>2.0.CO;2

Tharme, R. E. (2003). A global perspective on environmental flow assessment: Emerging trends in the development and application of environmental flow methodologies for rivers. *River Res. Appl.* 19, 397–441. doi:10.1002/rra.736

Wang, Y., Wang, D., Lewis, Q. W., Wu, J., and Huang, F. (2017). A framework to assess the cumulative impacts of dams on hydrological regime: A case study of the Yangtze river. *Hydrol. Process* 31, 3045–3055. doi:10.1002/hyp.11239

Wang, J., Forman, B. A., and Davis, A. P. (2018). Probabilistic stormwater runoff and water quality modeling of a highway in suburban Maryland. *J. Hydrol. Eng.* 23, 05017034. doi:10.1061/(ASCE)HE.1943-5584.0001600

Wu, M., and Chen, A. (2018). Practice on ecological flow and adaptive management of hydropower engineering projects in China from 2001 to 2015. *Water Policy* 20, 336–354. doi:10.2166/wp.2017.138

Wu, X. J., Lenon, G. P., and Dong, Y. (2020). The calculation of riverine ecological instream flows and runoff profit-loss analysis in a coal mining area of northern China. *River Res. Appl.* 36, 760–768. doi:10.1002/rra.3594

Wu, C. X., Bo, Y., Du, Y. Y., and Zhou, F. (2022). Ecological flow requirement deficit in the Songliao River Basin and its key drivers. *Acta Sci. Circumstantiae* 42, 151–159. doi:10.13671/j.hjkxxb.2021.0470

Yao, Y. Z., Jiang, C. L., and Wan, F. T. (2021). Research on ecological base flow of classical sections in the Luan River using various hydrology methods. *South-to-North Water Divers. Water Sci. Technol.* 19, 941–949. doi:10.13476/j.cnki.nsbdqk.2021.0098

Yin, G. K. (2002). Reflections on the environmental tolerance of water resources development in the Yellow River Basin. *Acta Geogr. Sin.* 224-231. Available at: https://kns.cnki.net/KCMS/detail/detail.aspx?dbcode=CJFD&dbname=CJFD2002&filename=DLXB200202013&v=. doi:10.3321/j.issn:0375-5444.2002.02.013

Yin, J., Slater, L., Gu, L., Liao, Z., Guo, S., and Gentine, P. (2022). Global increases in lethal compound heat stress: Hydrological drought hazards under climate change. *Geophys. Res. Lett.* 49. doi:10.1029/2022GL100880

Yin, J., Guo, S., Wang, J., Chen, J., Zhang, Q., Gu, L., et al. (2023). Thermodynamic driving mechanisms for the formation of global precipitation extremes and ecohydrological effects. *Sci. China Earth Sci.* 66, 92–110. doi:10.1007/s11430-022-9987-0

Zhang, Z. G., Jin, Y., Li, K. F., Li, Y., and He, F. F. (2017). RVA method-based study on river ecological baseflow hydrograph. *Water Resour. hydrop. Eng.* 48, 155–160. doi:10.13928/j.cnki.wrahe.2017.09.024

Zhang, H., Zeng, C. J., Li, T., He, S. F., Mo, K. L., Yang, P. S., et al. (2022). Ecological flow in the mid-lower hanjiang River based on spawning demands of the four major Chinese carps. *J. Hydroe.* 43, 1–8. doi:10.15928/j.1674-3075.202101190013

Zhao, R. H., Peng, T., Wang, H. F., Gao, F., and Qi, Z. (2018). Study on instream basic ecological water demand based on the improved dynamic calculation method. South-to-North Water Diversion. *Water Sci. Technol.* 16, 114–119. doi:10.13476/j.cnki.nsbdqk.2018.0104

Zhou, K. (2014). Bailong River. Gansu water conserve. *Hydrop. Technol.* 50, 60–65.

frontiers | Frontiers in Environmental Science

TYPE Original Research
PUBLISHED 02 March 2023
DOI 10.3389/fenvs.2023.1121248

EDITED BY
Hu Liu,
Northwest Institute of Eco-Environment and Resources (CAS), China

REVIEWED BY
Zhibin He,
Northwest Institute of Eco-Environment and Resources (CAS), China
Yu Hailong,
Ningxia University, China

*CORRESPONDENCE
Guang Yang,
✉ mikeyork@163.com
Xiaolong Li,
✉ lixiaolong409@shu.edu.cn

†These authors have contributed equally to this work and share first authorship.

SPECIALTY SECTION
This article was submitted to Land Use Dynamics, a section of the journal Frontiers in Environmental Science

RECEIVED 11 December 2022
ACCEPTED 21 February 2023
PUBLISHED 02 March 2023

CITATION
Xu X, Tian H, Yang G, Li X, He X, Li Y, Gao Y, Li F, Li P, Liu B and Xue L (2023), Spatial and temporal changes in land and water resources on the northern slopes of the Tianshan mountains from the perspective of "production-living-ecological space". *Front. Environ. Sci.* 11:1121248.
doi: 10.3389/fenvs.2023.1121248

Spatial and temporal changes in land and water resources on the northern slopes of the Tianshan mountains from the perspective of "production-living-ecological space"

Xingang Xu[1,2†], Hao Tian[1,2†], Guang Yang[1,2*], Xiaolong Li[1,2*], Xinlin He[1,2], Yi Li[1,3], Yongli Gao[4], Fadong Li[1,5,6], Pengfei Li[1,2], Bing Liu[1,2] and Lianqing Xue[1,7]

[1]College of Water Conservancy & Architectural Engineering, Shihezi University, Shihezi, China, [2]Key Laboratory of Cold and Arid Regions Eco-Hydraulic Engineering of Xinjiang Production & Construction Corps, Shihezi, China, [3]College of Water Resources and Architectural Engineering, Northwest Agriculture and Forestry University, Yangling, China, [4]Department of Earth and Planetary Sciences, University of Texas at San Antonio, San Antonio, TX, United States, [5]Institute of Geographic Sciences and Natural Resources Research, Beijing, China, [6]College of Resource and Environment, University of Chinese Academy of Sciences, Beijing, China, [7]College of Hydrology and Water Resources, Hohai University, Nanjing, China

The rapidly growing social demand for water and land, along with increasingly constraining economic and social development, have intensified the conflicts between regional production, living, and ecological spaces (PLES). Water and land resources have become major obstacles to long-term growth in arid and semi-arid regions. Therefore, we propose a scenario-based framework for a production, living, and ecological spaces water resource assessment, integrating patch-generating land use simulation (PLUS), Shared Socioeconomic Pathways (SSPs), and multiple regression equations to analyse the spatial and temporal variability of these resources on the northern slopes of the Tianshan Mountains (NSTM) and assess the future development of water resources. The results show: 1) from 2000 to 2020, land use types on the northern slopes of the Tianshan Mountains were dominated by ecological land, which decreased to 11,793 km^2; production and domestic land use increased. Water for production and ecological use accounted for approximately 93% and a minor proportion of the total water use, respectively. 2) Production land is mainly influenced by population density and Gross Domestic Product (GDP), living land by population density, and ecological land by precipitation and topographic factors. 3) The PLUS model had good applicability, with a kappa coefficient, overall accuracy, and FoM of 0.81, 0.88, and 0.28, respectively. 4) The total water use in the northern slopes of the Tianshan Mountains will increase under all three scenarios between 2030 and 2050, but by varying degrees. Production water use accounts for the most significant proportion (93%), with its use decreasing by 305 million m^3 under the SSP3 scenario. Domestic water use shows a slow increase under all three scenarios. Further development of the northern slopes of the Tianshan Mountains should take account of regional ecological vulnerability, and water use for production should be controlled based on existing water resources and ecological capacity to reduce pressure on the environment and provide essential ecological protection and sustainable development.

KEYWORDS

plus model, land use, water resource, shared socioeconomic pathways, sustainable development

1 Introduction

For many years, sustainable development of arid and semi-arid areas has been a critical research topic (Bryan et al., 2018). Environmental problems, such as human activities, climate change, and land desertification, have increased ecological and environmental pressures, resulting in negative impacts on sustainable development (Pokhrel et al., 2021). As the primary carrier of terrestrial ecosystems, the land is an important site for human activities and plays a vital role in human production and life (Jiang et al., 2022a; Lin & Peng, 2022). Since the 1980s, the rapid growth of society has led to tension in human–land relations and the emergence of competition in production and living ecological spaces (Fu et al., 2021; Wang & Wang, 2022). The rapid expansion of production and living space has led to the narrowing of ecological space. The disorderly development of land restricts sustainable development and may lead to a decline in regional development competitiveness and affect the ecology and living environment (Hou & Braham, 2021; Lu et al., 2021; Wang et al., 2021). In terms of water, resources in arid ones are in short supply, with the proportion of water used for production reaching as high as 79.8%. In comparison, water used for ecological purposes accounts for only 5.3% of the total water consumption (Chen et al., 2019). The allocation of water resources is dominated by the economic development planning department, which pays more attention to production and domestic water and ignores ecological water (Hu et al., 2021; Lu et al., 2021; Xu et al., 2022). The misuse of water resources has worsened the ecological environment in fragile inland areas (Eaton et al., 2021).

In terms of land use simulation, the main models for simulating future land use include the CLUE-S model (Stanley et al., 2023), CA-Markov model (Philip et al., 2023), and FLUS model (Lin et al., 2022; Xiang et al., 2022), which are more suitable for simulation studies in small areas, not accurate enough in larger scale simulations, poor simulation effects, and limited to the analysis of the quantity and spatial structure, ignoring the interactive application between models, and not enough for influencing land use The PLUS (Patch-generating Land Use Simulation Model) model (Liang et al., 2021) is a new land use prediction model developed to solve the accuracy problem of larger-scale land use data simulation, which has a better explanation of the influencing factors of various land use changes and higher accuracy of simulation results (Halima and Hiroaki, 2022; hao et al., 2022). Li et al. (2021) used a coupled GMOP-PLUS model to analyse the spatial and temporal evolution of the ecological barrier ESV in Sichuan and Yunnan, China, using LULC and other data from 2000, 2010, and 2018, which can improve the assessment of socioeconomic and environmental factors. Shi et al. (2021) studied to determine the impact of different future land use/cover scenarios on the Ili River, China watershed, and analyed synergistic response characteristics to inform site-specific decisions for implementing ecological projects. hai et al. (2021) investigated in depth the spatial and temporal patterns of land use/cover change under urbaniation in Wuhan, China, based on continuous time in an attempt to understand the development pattern of Wuhan over 20 years, and the results showed rapid urbaniation, which triggered large LUCC with the increased floor area.

A scenario framework was developed by the Intergovernmental Panel on Climate Change (IPCC) in 2010 that described the potential paths of different socioeconomic groups (O'Neill et al., 2017; Wang & Sun, 2022). In 2012, the Chinese government formulated the "Production-Living-Ecological Space (PLES)" strategy in land space planning to achieve sustainable development of the region and ecological environment (Fu et al., 2021). Therefore, many scholars have combined land use with the SSPs. hou et al. (2022) used a spatial-temporal geographically weighted regression (GTWR) model to analye the spatial-temporal evolution characteristics of PLES and its drivers in 73 prefecture-level cities in the middle reach of the Yangte River from 2005 to 2020. Cui et al. (2022) analyzed the spatial and temporal characteristics, coupling coordination, spatial autocorrelation, and influencing factors of PLES in China from 2000–2020. The urban expansion of Hohhot-Baotou-Erdos-Yulin from 2017 to 2050 was simulated by Song et al. (2020) using SSP scenarios and land use; Jiang et al. (2022b) simulated henghou's PLES and ecological effects based on SSPs and multiple methods, and Bao et al. (2022) used linear equations to establish a relationship between land cover type and water use to estimate ecological and agricultural water use in Lake Ebey in 2035.

A glance at the development of land use change and land and water resources research at home and abroad shows that land use change has changed from relying on traditional methods to combining with emerging technologies, which is also an inevitable requirement of the development of the times. After a long period of theoretical research, the configuration of soil and water resources has formed a relatively perfect academic system; with various numerical models as the basic method and the continuous development of innovative soil and water resources information systems, in recent years, the large-scale study of soil and water resources configuration has become more and more accurate and detailed with the support of information technology and 3S system. However, considering the sustainable development of the ecological-social-economic integrated system, the current methods for optimal allocation of soil and water resources still have shortcomings. Most of the existing research methods for land use change are still in the study of the quantification of land use type conversion, and the study of the intrinsic and extrinsic drivers of its conversion is still relatively superficial, and the predictive analysis models used for future land use change aren't mature enough, without considering The models used for predicting and analying

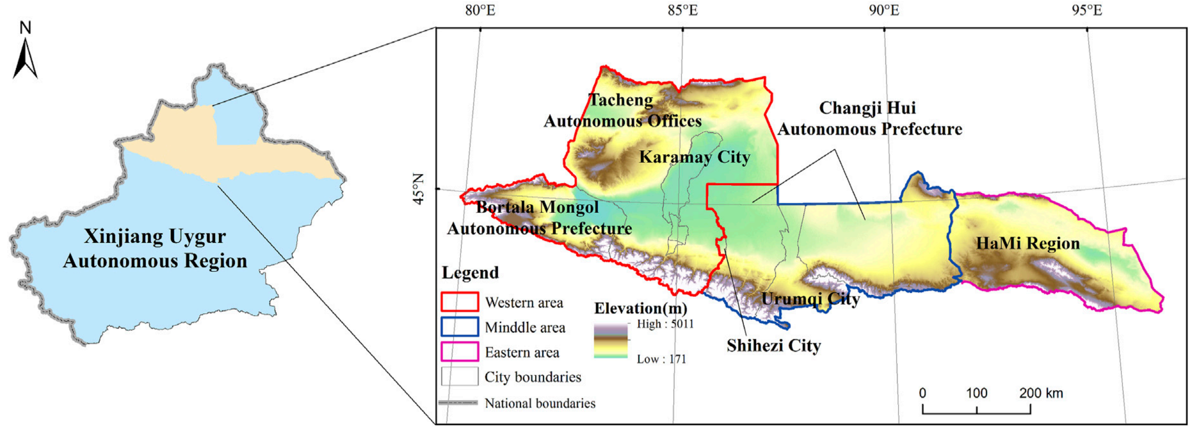

FIGURE 1
Geographical location and segmental boundary on the northern slopes of the Tianshan Mountains.

future land use change aren't mature enough and do not consider the influence of the interaction and change trends of ecosystems and economic and social systems on land use change, so the selection of models should take into account the ecological, economic and social factors and the advantages of model adaptation range and model accuracy. Studies on the optimal allocation of water or land resources alone are predominant, and studies combining the interactions and constraints of the two are limited. The exchange of water and land resources is necessary to consider the interaction of the two, which should be planned, evaluated, protected, and utilied in order to optimie the allocation of resources.

Based on the above problems, this study proposes a research framework for multi-scenario water resource prediction based on the PLUS model and SSPs, which provides a method for water resource assessment. We analyed the spatial and temporal changes in water and land resources on the northern slopes of the Tianshan Mountains (NSTM) from 2000 to 2020 and calculated the contribution rate of driving factors to the dynamic change in land cover. We predicted the water consumption for PLES on the NSTM based on three scenarios of the SSPs. The specific objectives of this study were: 1) to analye the characteristics of water and soil resource changes on the NSTM and explain the reasons for land resource changes, and 2) to analye the temporal and spatial changes of PLES water use on the NSTM under different scenarios from 2020 to 2050. The proposed optimiation method helps to explore regional water and land resource changes. It provides a fundamental basis for the rational planning regional water and land resources and ecological and environmental protection.

2 Materials and methods

2.1 Regional overview

The NSTM is located in an arid one of the Asia-Europe continental hinterland on the southern edge of the Junggar Basin, with the geographical coordinates of 79°53′E–96°06′E and 42°49′N-47°15′N. The NSTM is a crucial area of the Belt and Road Initiative. The main landforms in the south are high mountains, the central part belongs to the oasis, and the north is mainly desert, forming a typical mountain-basin system. At the end of 2020, the total population of NSTM was 8,399,700, accounting for 32% of Xinjiang's population (Fang et al., 2019). We divided the NSTM into three sections based on topographic and climatic features: western, middle, and eastern, as shown in Figure 1.

2.2 Data sources

The SSP data were obtained from the Nanjing University of Information Science and Technology. The data mainly included land use, socioeconomic [population density, Gross Domestic Product (GDP)], road and water system (railways, roads, rivers), climate (rainfall, temperature), and topographic data (Table 1). The geographical coordinate system was unified as D_WGS_1984 with a resolution of 1 km, and the number of data rows and columns was identical. Production, domestic, and ecological water use data were obtained from the Statistical Yearbook and Water Resources Bulletin.

2.3 Research methods

The framework proposed in this study consists of three main parts (Figure 2). Firstly, the spatial and temporal analysis of land and water resources on the NSTM is based on dividing them into three parts: production, living, and ecology; secondly, the PLUS model is used to simulate future changes in the quantity and spatial distribution of land resources on the NSTM, and finally, scenarios are set up to simulate future changes in water resources under different SSP scenarios. In this study, SSPs, PLUS, and multiple regression equations were coupled to predict the water consumption of land use types on the NSTM from the perspective of PLES.

2.3.1 Classification of the dominant functions of land use

The land use data were classified from the perspective of land use cover types, with a total of six primary classifications and

TABLE 1 Data type and sources.

Data type	Details	Data sources
Land use/cover data	Seven periods of data from 2000 to 2020 are selected. Spatial Resolution: 30 m	Resource and environment science and data centre (http://www.resdc.cn)
GDP and population grid data	Select the interpolation data of GDP and population (2000–2020), Spatial Resolution: 1 km	Resource and environment science and data centre (http://www.resdc.cn)
Road network data sets	Road data includes railways, main roads, secondary roads, and tertiary roads. The river system is the main river	OpenStreetMap (https://www.openstreetmap.org/)
Meteorological data sets	Including annual average temperature and annual precipitation (2000–2020)	China Meteorological Data Network (http://data.cma.cn)
Digital elevation model (DEM)	Aster GDEM V2 data, Spatial Resolution: 30 m	Geospatial data cloud (http://www.gscloud.cn)
Soil datasets	China's soil dataset (v1.1) based on the world soil database mainly obtains soil texture, type, and component percentage content	Resource and environment science and data centre (http://www.resdc.cn)
SSPs date	Resolution: 0.5 × 0.5	Nanjing University of Information Science and Technology (https://geography.NUIST.Edu.CN/)
Water consumption for production, living, and ecology	《Statistical yearbook》and《Water Resources Bulletin》	Statistics Bureau of Xinjiang Uygur Autonomous Region (http://tjj.xinjiang.gov.cn/)

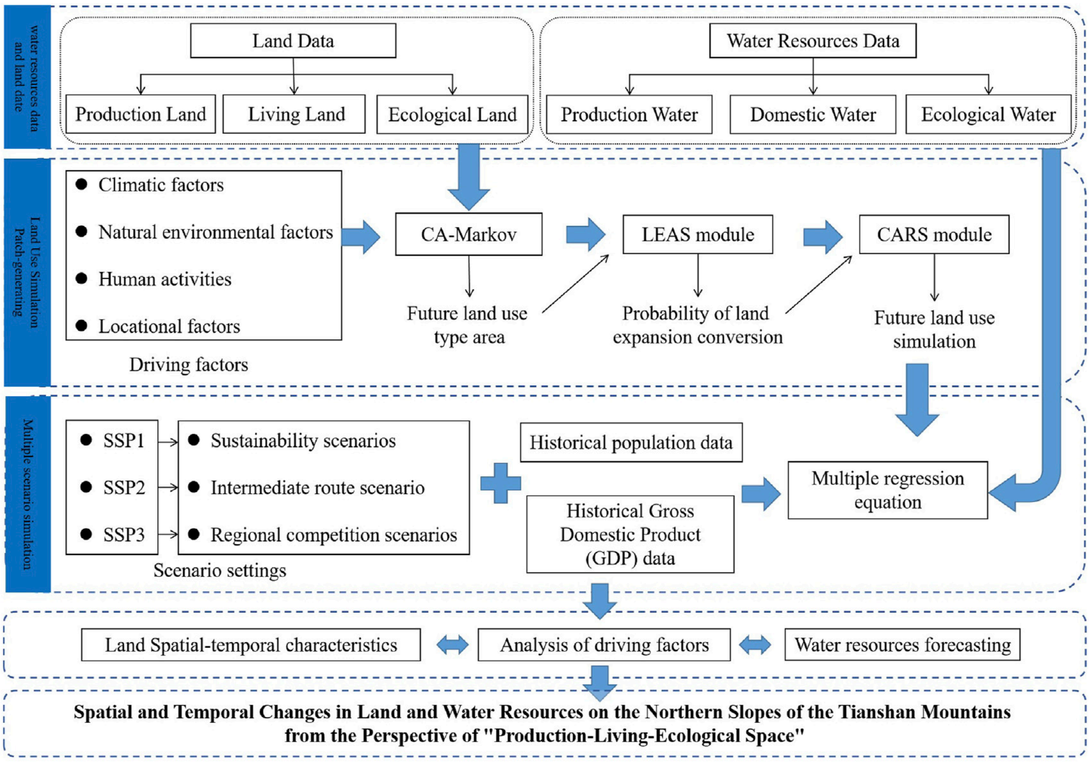

FIGURE 2
Research framework.

25 secondary classifications (Liu et al., 2017). With research on the ecological environment, many scholars have proposed a classification scheme for ecological land from an environmental perspective (Wang J. et al., 2017), and a land use classification scheme based on the perspective of industrial structure and economic development (Liu et al., 2018). This classification uses the above ideas and classification schemes for reference and adopts dominant function classification. For example, forestland can produce fruits, has ecological functions, and may also have the life function of tourism. However, the dominant function of forestland is to maintain the ecological environment, so it is classified as ecological land (Deng and Yang, 2021; Cui et al.,

TABLE 2 Land use types based on the dominant function.

Classification of production–living–ecological land		Secondary classification of the land use classification system
Primary land use type	Secondary land use type	
Production land	Agricultural production land	Paddy fields and dry land
	Industrial production land	Construction land for factories, mines, and salt fields
Ecological land	Forestland ecological land	forest land, shrubbery land, sparse forest land, and other forest lands
	Grassland ecological land	High-coverage grassland, medium-coverage grassland, and low-coverage grassland
	Water ecological land	Rivers, lakes, reservoirs and pits, glaciers, and permanent snow deposits
	Other ecological lands	Sandy land, Gobi, saline-alkali land, marshland, and bare land
Living land	Urban living land	Urban land
	Rural living land	Rural residential area

2022; hou et al., 2022). Based on the perspective of PLES and land use leading functions, the classification scheme of PLES land use leading functions was established by summing up land use types in land use data (Table 2).

2.3.2 Land use dynamics and land transfer matrix

The dynamic degree of land use can quantitatively reflect the change speed of land use quantity in the study area (Yuan et al., 2022), and the formula is as follows:

$$R_t = \frac{\sum_{i=1}^{n}\left|S_{yi} - S_{xi}\right|}{2 \times \sum_{i=1}^{n} S_{xi}} \times \frac{1}{T} \times 100\% \tag{1}$$

where R_t is the comprehensive land use dynamic degree, S_{xi} and S_{yi} are the areas of type I land in the early and later stages, km^2, n is the number of land use types, and T is the time difference between two adjacent periods, a.

The land use transfer matrix can quantitatively analyse the transformation between unearthed land use types and reflect land use change trends (Wang, 2022). The expression is:

$$D_{xy} = \begin{bmatrix} D_{11} & D_{12} & \cdots & D_{1n} \\ D_{21} & D_{22} & \cdots & D_{2n} \\ \vdots & \vdots & \ddots & \vdots \\ D_{n1} & D_{n2} & \cdots & D_{nn} \end{bmatrix} \tag{2}$$

where D is the land area, km^2, x and y are the land use types before and after the transfer, and n is the number of land use types in the study area.

2.3.3 Construction and simulation of the land use PLUS model

With the PLUS model, we can examine the driving factors behind land type expansion at patch scales, as opposed to other land use simulation models, and t is possible to obtain greater simulation accuracy by analying potential land use conversion rules (Liang et al., 2021). Consequently, the model was used in this study to analye the spatial pattern of land use in the study area from 2000 to 2020, as well as to simulate and predict future land use patterns.

Following are the steps and parameters.

1. Land Expansion Analysis Strategy Module (LEAS): A total of twelve factors (Figure 3) inputs were gathered from four aspects: climate factor, social natural factor, and accessibility factor. Samples were selected by random sampling, the sampling rate and the number of decision trees were set to defaults, and four parallel threads were used (Liang et al., 2021).
2. CA-based on muitiple random patch seeds (CARS) parameter settings: The domain effect was set as the default value of the system. The lower the attenuation coefficient, the more difficult it is to convert land types. Therefore, 0.5 was chosen, the diffusion coefficient was set to 0.1, and the probability of random patch seed was set to the default value (Liang et al., 2021).
3. Weighting of used land neighborhoods: agricultural production land is 0.3, industrial production land is 0.9, forestland ecological land is 0.5, grassland ecological land is 0.6, water ecological land is 0.8, urban living land is 0.9, rural living land is 0.9, and other ecological lands are 0.2 (Jiang et al., 2022b).

2.3.4 Model accuracy validation

In this study, a new index (DISO) is selected to describe the overall performance of different models or simulations. This new index is a collection of other statistical indicators, including correlation coefficient (r), absolute error (AE), and root-mean-square error (RMSE), which has the advantage of quantifying the overall performance of different models compared to other indices (Hu et al., 2019). For the observed time series (A = [a1, a2, . . ., an]) and the model-simulated time series (B = (b1, b2, . . ., bn)], the r, AE, and RMSE are calculated as follows:

$$r = \frac{\sum_{k=0}^{n}(a_i - \bar{a})(b_i - \bar{b})}{\sqrt{\sum_{k=0}^{n}(a_i - \bar{a})^2}\sqrt{\sum_{k=0}^{n}(b_i - \bar{b})^2}} \tag{3}$$

$$AE = \frac{1}{n}\sum_{k=0}^{n}(a_i - b_i) \tag{4}$$

$$RMSE = \frac{1}{n}\sum_{k=0}^{n}\sqrt{(a_i - b_i)^2} \tag{5}$$

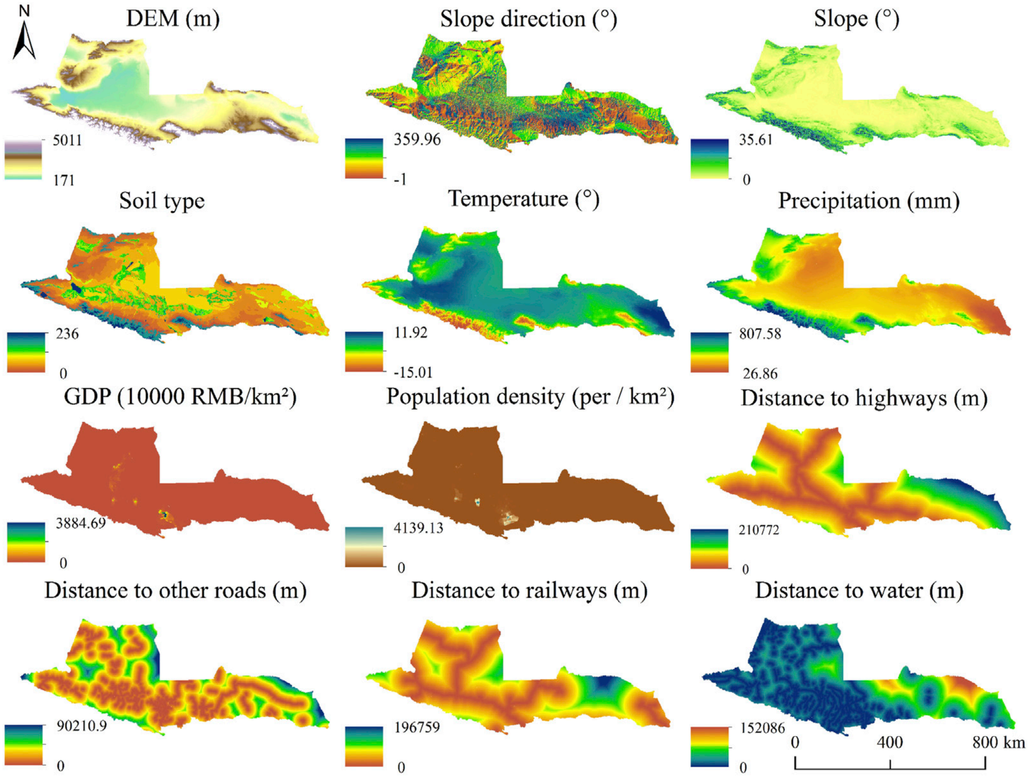

FIGURE 3
Driving factors affecting land use.

where $\bar{a}$ and $\bar{b}$ are the means of A and B, respectively, and n is the length of the time series. To eliminate the influence of dimensions, AE and RMSE are normalied (divided by the absolute observation mean ($|\bar{a}|$)). DISO is then defined as:

$$DISO = \sqrt{(r-1)^2 + NAE^2 + NRMSE^2} \tag{6}$$

where N indicates normalied values of AE and RMSE. The simulation is close to the observation when DISO is close to 0.

2.3.5 Water consumption estimation

The SSPs consist of five future scenarios: a sustainability scenario (SSP1), a middle route scenario (SSP2), a regional competition scenario (SSP3), an inequality scenario (SSP4), and a conventional fossil fuel and development scenario (SSP5) (O'Neill et al., 2017). Each pathway projects regional economic, demographic, and other factors and covers possible future development patterns in different regions, aiming to explore different levels of climate change adaptation and mitigation challenges (O'Neill et al., 2014). Referring to the relevant literature and taking into account the actual conditions on the northern slopes of the Tien Shan, the inequality scenario (SSP4) and the traditional fossil fuel and development scenario (SSP5) do not correspond to the future development trends on the northern slopes of the Tien Shan. In this study, SSP1, SSP2, and SSP3 were selected as the actual conditions of the NSTM and pathway route scenarios.

To estimate the future water consumption of production, living, and ecological land on the NSTM, we constructed a multiple regression equation using historical data. The relationship between the demand for water for the three different types of life is established using GDP, population, and land use type. An equation was developed using historical data of population, GDP, and land use type area on the NSTM from 2000 to 2020 as dependent variables and water consumption as the independent variables. The expression is as follows:

$$WR_{production} = 68.965GDP_i - 1770.866POP_i + 16.485landtype_i + 1471124.53 \tag{7}$$

$$WR_{domestic} = 0.86GDP_i - 64.72POP_i + 2.3landtype_i - 12740.32 \tag{8}$$

$$WR_{ecology} = 1.96GDP_i + 168.65POP_i + 1.12landtype_i - 3617.89 \tag{9}$$

where *WR* is the total water consumption, *POP* is the total population in the year (10^4 people), *GDP* is the value of GDP in the year (100 million RMB), and *land type* is the land use type (km^2) in the year. The R^2 of the multiple equations WR $_{\text{production}}$, WR $_{\text{domestic}}$, and WR $_{\text{ecology}}$ were 0.91, 0.86, and 0.89, respectively. After the t-test, $p < 0.05$, indicated that the multiple regression coefficients were significant at the 5% level. The land use type area was predicted according to the population and GDP data predicted by different SSPs and the PLUS model. The water consumption of different land types in the future was predicted and calculated using Eqs 7–9, and the coupling of SSPs and the PLUS model was realied.

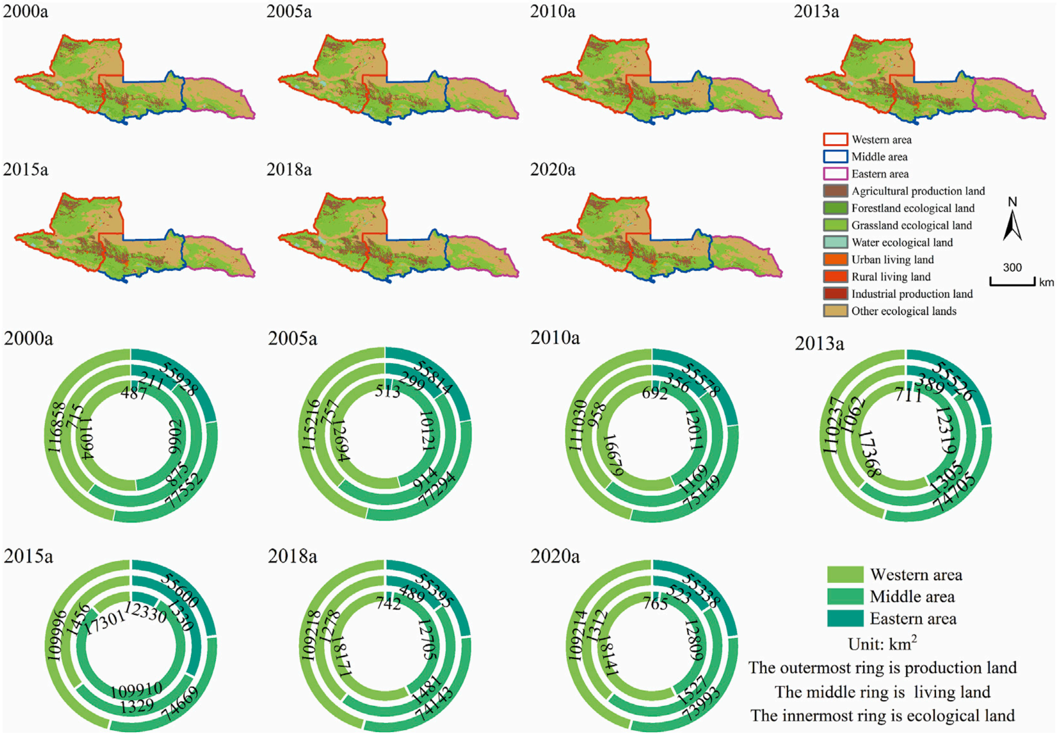

FIGURE 4
Land use distribution and area on the northern slopes of the Tianshan Mountains from 2000 to 2020.

3 Results

3.1 Spatial and temporal variation of land and water resources

The productive, living and ecological land areas in the NSTM were counted in the western, middle, and eastern areas (Figure 4). The results show that in each of these regions, the NSTM is dominated by ecological land, distributed in the southern and northern parts of each section, and mainly composed of other ecological lands (49%) and ecological land for graing (48%). During 2000–2020, ecological land decreased from 116,858 km^2 to 109,214 km^2 at a rate of 382.2 km^2/a in the western area, by 3,559 km^2 at a rate of 177.95 km^2/a in the middle section, and by 29.5 km^2/a in the eastern area. The central oasis developed around rivers and lakes, consists mainly of agricultural production land (96%), with the western area increasing by 7,047 km^2 at a rate of 352.35 km^2/a and multiplying from 2000 to 2010 at a rate of 558.5 km^2/a. Living land is mainly located in the central oasis, surrounded by agricultural production and ecological pastureland. It has increased rapidly over the last 20 years, with the western, middle, and eastern sections of the living land increasing by 83.5%, 49.9%, and 147.9%, respectively.

During the past 20 years, the surface water volume on the NSTM has been stable (Figure 5A). The total water use has been growing, with an increase of nearly three billion m^3 over 20 years, with the most significant proportion of water used for production, with an average value of approximately 93% (Figure 5B), whereas the water consumption per 10,000 RMB of GDP showed a decreasing trend (Figure 5C). The GDP of the NSTM increased 10.7 times between 2000 and 2020, and its population increased by 2,622,000 people (Figure 5C). With the economic development and population growth of the NSTM, the land-use pattern has also significantly changed. According to the dynamic attitude of each section of the NSTM from 2000 to 2010 and 2010–2020 (Figure 5D), the eastern section had the most significant change in living land use from 2000 to 2010 with a dynamic attitude of 7.06%. As shown in Figures 5E, F, the transfer of grassland ecological land and other ecological land to agricultural production land on the NSTM from 2000 to 2010 was 10,157 km^2. From 2010 to 2020, the area of grassland ecological land and forestry ecological land increased by 13,042 km^2 and 2,120 km^2, respectively, and the area of subsistence land increased by 1,768 km^2, mainly agricultural production land (55.09%) and grassland ecological land (18.21%).

3.2 The driving factors of land use on the NSTM

The evolution of land patterns is the result of a combination of many drivers, and the degree of contribution of the drivers varies (Figure 6). Arable land changes are mainly influenced by topographic factors and population density. Woodland was mainly influenced by temperature (21.89%), rainfall (21.32%), and soil type (14.91%) in 2000–2010, while the degree of each driver was more balanced in 2010–2020, not influenced by a single

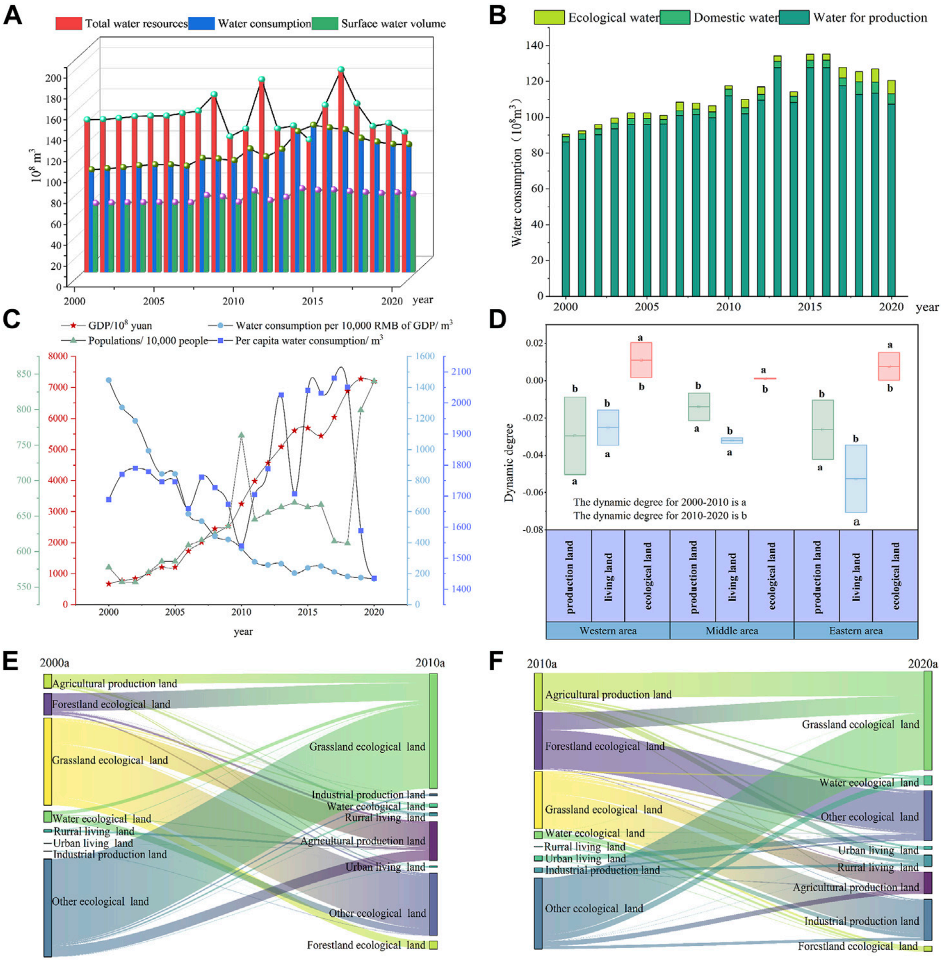

FIGURE 5
(A) The total water resources, surface water, and water consumption **(B)** Water consumption for production, living, and ecological purposes; **(C)** GDP, population, water consumption *per capita*, and water consumption per 10,000 RMB of GDP; **(D)** Dynamic attitudes for the periods 2000–2010 and 2010–2020; **(E) (F)** is land use transfer matrix from 2000 to 2010 and from 2010 to 2020.

factor, and the development was more stable and coordinated. Grassland was more influenced by population density (15.24%) and rainfall (11.97%) in 2000–2010, while the population density factor decreased to 7.73% in 2010–2020. The dominant driver for both urban sites and rural settlements was population density, which was 43.77% and 25.45% in 2010–2020, respectively. Industrial and mining land is influenced more by GDP (18.07%), distance to the railroad (11.52%), and annual rainfall (11.05%). The dominant factors influencing the change in unused land were soil type (12.67%) and precipitation (11.85%), which were mainly influenced by annual precipitation (14.45%), topographic factors (12.59%), and population density (11.23%) from 2010 to 2020.

3.3 Future land use simulation on the NSTM

The land use distribution in 2020 was simulated using 2010 land use data and compared with the actual land use distribution in 2020 to verify that the PLUS model is applicable to the NSTM (Figure 7). The results showed that the kappa coefficient was 0.81, and the overall accuracy was 0.88. As a further validation of the model's simulation accuracy, the coefficient of merit (FoM) was introduced with FoM = 0.28. In the simulation comparison, the PLUS model was found to be more applicable to modeling land and spatial changes in the NSTM over the long term.

Based on the PLUS model simulation, we obtained the land dynamics of the study area from 2030 to 2050 (Figure 8) and counted the areas of production, living, and ecological land by section. Between 2030 and 2050, the production land in the western section increased by 993 km^2, the middle section increased by 1948 km^2, the eastern section increased by 168 km^2, and agricultural production land in the production land increased by approximately 90%. The area of living land in the western section was the largest, increasing by 444 km^2, and the area of the eastern section increased by 56 km^2. The data indicate that ecological land continues to decrease, with the western section decreasing by approximately 1,168 km^2 and the eastern section decreasing by 147 km^2, among which the middle section is grave, decreasing by 2,193 km^2, accounting for approximately 2.5% of the ecological land area in the middle section.

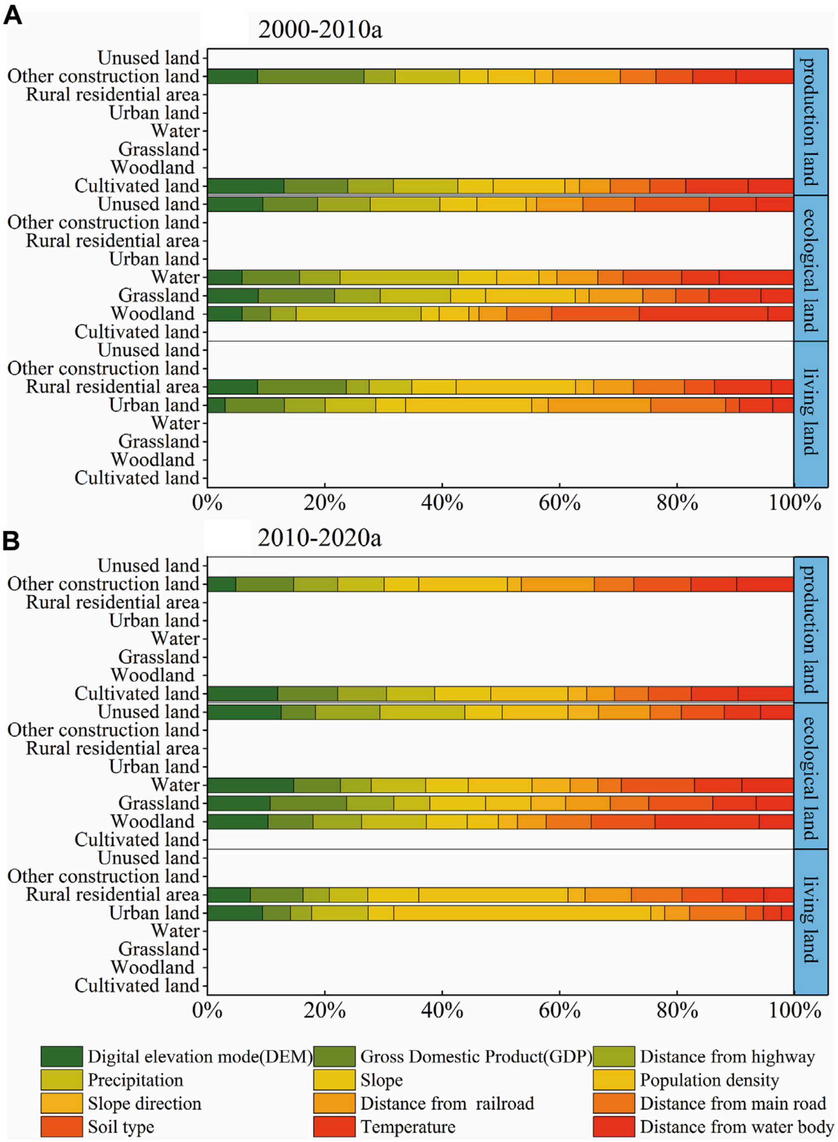

FIGURE 6
(A) The percentage of driving factors of land use changed from 2000 to 2010. **(B)** Contribution percentage of driving factors of land use types from 2010 to 2020.

3.4 Prediction of water use in three lands use SSP scenarios for the NSTM

During 2030–2050, water use for production (Figure 9A) will continue to increase under the SSP1 and SSP2 scenarios, with SSP2 increasing by 2,407 million m^3, while water use decreases under the SSP3 scenario by 305 million m^3. It is noteworthy that water consumption per 10,000 RMB of GDP (Figure 9E) shows a decreasing trend, with SSP3 decreasing the most, by 49.37 m^3, indicating that under the regional competition path, the NSTM is generating less water to create economic value. Regarding domestic water use (Figure 9B), the three scenarios showed a slow growth trend, with the most significant increase of 101 million m^3 in the SSP2 scenario. The growth of domestic water use is slow owing to the completion of the demographic transition in the SSP2 scenario, where the population grows slowly and gradually plateaus. The *per capita* domestic water consumption (Figure 9F) does not differ much among the three scenarios, ranging from 159.4 L/d to 177.04 L/d. In terms of ecological water use (Figure 9C), SSP2 increased the most at 362 million m^3, indicating that under the middle path, it maintains a similar path to the historical period and continues to develop, striving to achieve sustainable development in terms of the ecological environment and human wellbeing. At the same time, the other scenarios also showed an increasing trend. In terms of the total water consumption (Figure 9D), all three scenarios increased, but the degree of increase varied greatly, with SSP3 increasing by only 132 million m^3.

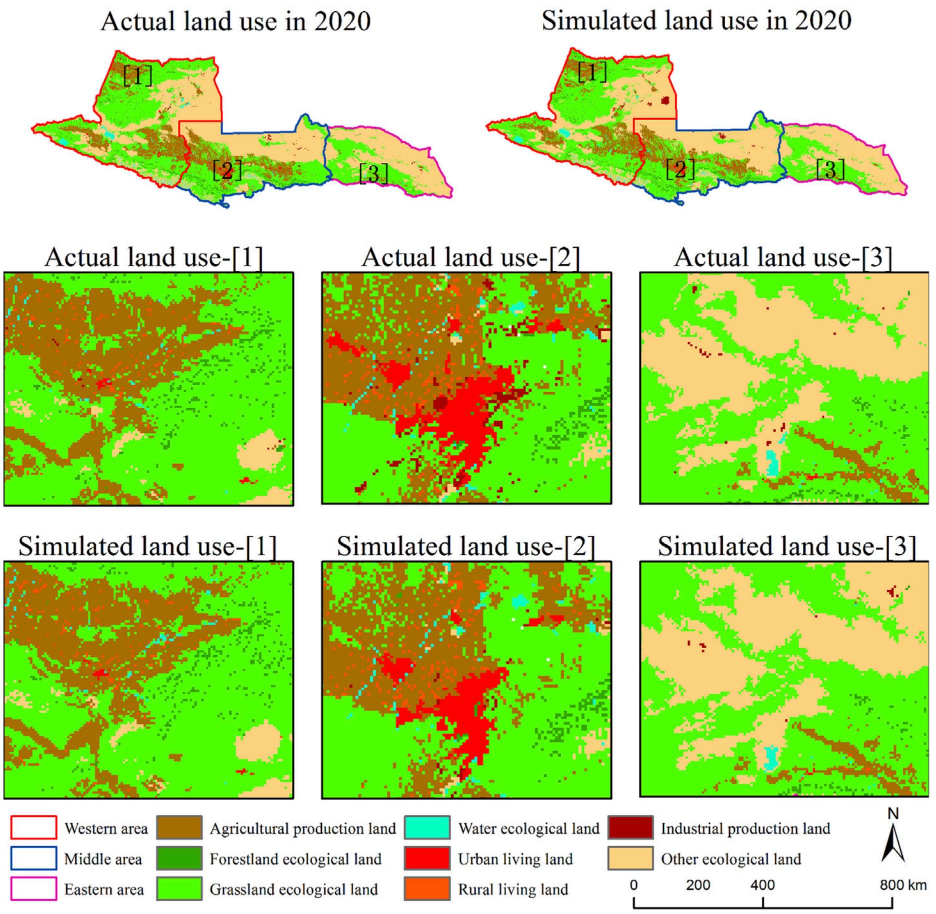

FIGURE 7
Comparison of simulated land use and actual land use in 2020.

4 Discussion

4.1 Factors affecting land change

Land use drivers are dynamic organic systems in which many factors inside and outside the system interact to influence land use type/cover change (Chen et al., 2006). At the same time, land use change is not entirely passive and independent; the results of land use change eventually also affect drivers through various pathways, thus creating feedback (hao et al., 2014; Ouedraogo et al., 2015). The drivers of land use include natural and human drivers, with natural drivers, including changes in the characteristics and processes of the natural environment, and human drivers, including factors such as population change, economic growth, proximity to roads, and policy-making. In this study, the driving forces were analysed based on land use/cover changes in the NSTM from 2000 to 2020. Factors such as topographic factors and soil type played a dominant role in forming land use patterns (Wang et al., 2019). These factors are relatively stable and have cumulative effects on productive and ecological land. In contrast, anthropogenic factors, such as population density, economic growth, and transportation, are relatively active and play a decisive role in the formation of short-term land use patterns, such as for living land (hang et al., 2017; Lamqadem et al., 2019). Fluctuations in meteorological factors affect the spatial and temporal patterns of various types of land. The NSTM is in an arid one, and it is a typical “mountain–oasis–desert” mountain basin system. It has been shown that the average annual precipitation growth rate on NSTM is 10.67 mm/10a. The average temperature growth rate is 0.32°C/10a (Li et al., 2018), with a general trend of continued slow warming and humidification, which is closely linked to the expansion of snow and ice melt water and lake areas, significantly increasing the reservoir area, and indirectly affecting the expansion of the oasis arable land area (Wang N. et al., 2020).

With the implementation of the national strategy of Western development and the construction of cotton plantation bases, land development has been encouraged from a policy perspective (Wang Y. et al., 2017). Simultaneously, the market economy’s developmental needs and the population’s economic growth have made land reclamation a fast and effective means of increasing income (Chen et al., 2020). However, the NSTM is in an arid inland region with little rainfall and high evaporation; increased land reclamation in this area consequently led to a water shortage problem. In the 1980s, large-scale mulched drip irrigation was introduced to improve the utiliation efficiency of farmland water resources. The measures of area drip irrigation by the Xinjiang Production and Construction Corps

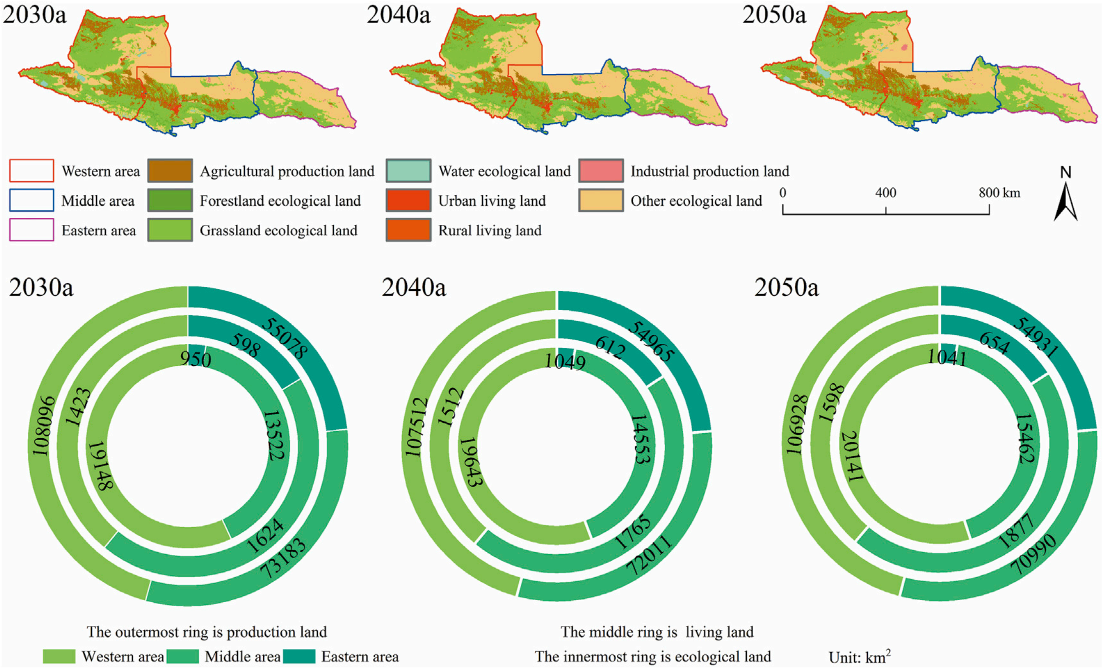

FIGURE 8
Land use distribution and area on the northern slopes of the Tianshan Mountains from 2030 to 2050.

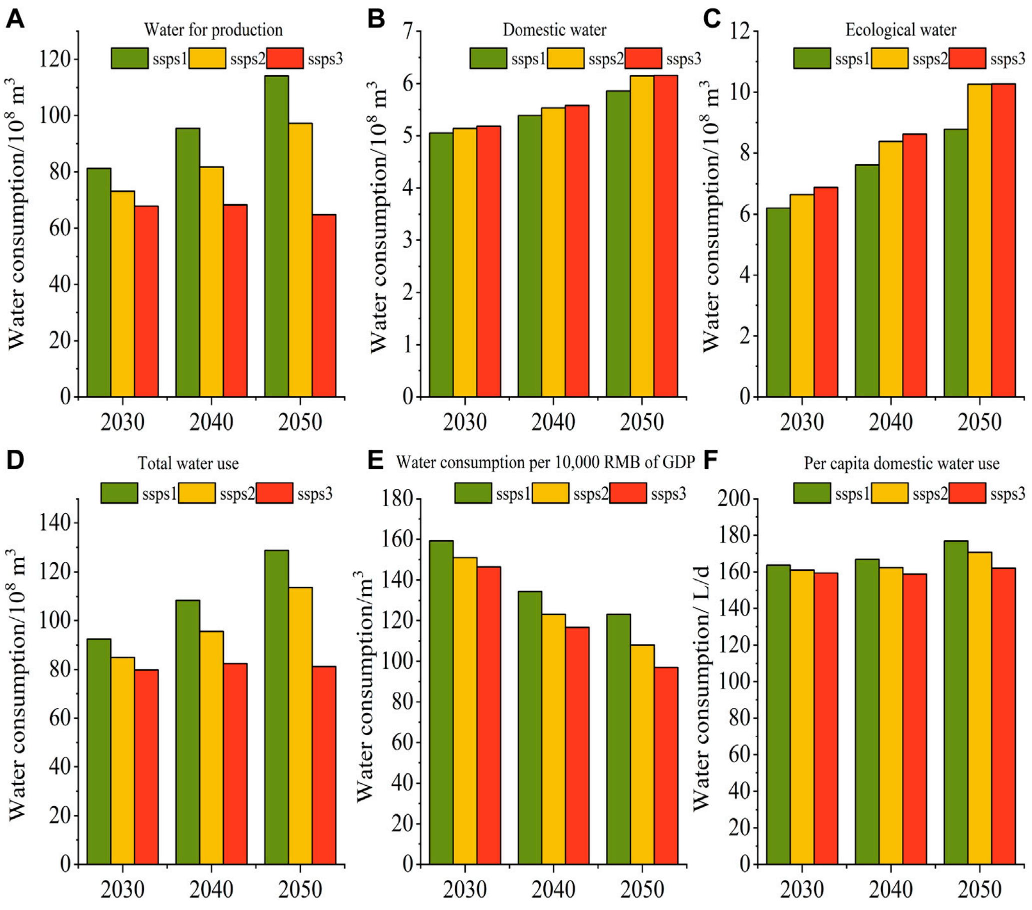

FIGURE 9
(A–D) show the total amount of production, domestic, ecological, and water consumption of the northern slopes of the Tianshan Mountains from 2030 to 2050. **(E)** Water consumption per 10,000 RMB of GDP. **(F)** Per capita domestic water use.

TABLE 3 Simulation accuracy of production land, living land, and ecological land from 2000 to 2020.

Land use type	r	AE	RMSE	DISO
Production land	0.63	43	94.42	0.37
Living land	0.75	9.71	76.57	0.25
Ecological land	0.67	24.57	102	0.33

exceeded 82.4% (Wang . et al., 2020). Applying water-saving irrigation and facility agriculture technologies has led to changes in land use types; farmland has appeared in desert areas previously considered unsuitable for reclamation, and land use types have changed, with technological drivers becoming the motivation for regional land use changes. Natural drivers are essential for land use distribution and play a dominant role in long-term land change. In contrast, human factors played a decisive role in short-term spatial and temporal land use changes.

4.2 Uncertainty analysis in model simulation studies

In terms of model simulation, this study uses the FOM index to quantify the accuracy of the land change model, which is more advantageous than the kappa index. The FOM index provides a unit-by-unit comparison between the simulation and the actual situation, which can increase the reliability of the simulation. Regarding the accuracy indicators of the simulations, using the DISO metric, we were able to determine the level of model performance and summarie the overall evaluation of individual simulations. The PLUS model simulated the slightest deviation for the living land with a DISO value of 0.25, followed by the ecological land, and the most deviation for the production land with a DISO value of 0.37 (Table 3). In terms of the data used, a total of 12 indicators in two aspects, human activities, and natural factors were selected to drive the model to simulate a more realistic land type change, but some factors, such as policy factors and technology, which are difficult to quantify and fail to study comprehensively may have some errors. In addition, the water use of land types is also a complex system involving many factors, which this study fails to consider comprehensively, and has some bias in the numerical estimation. Typical climate scenarios and development models should be chosen for further studies, and a model framework should be established to improve accuracy. As such, we will continue to refine the impact of future land use change on water resources under various scenario models to accommodate the application requirements for future scenarios.

5 Conclusion

This study proposes a research framework for multi-scenario water resource prediction based on the PLUS model and the SSPs, which simulates and analyses the spatial and temporal changes in water and soil resources on the NSTM from 2030 to 2050, predicts the productive, domestic, and ecological land use from 2030 to 2050, quantifies the contribution of each driver to the dynamic changes in land cover, and predicts the water use of the NSTM under the SSPs based on the water consumption for production, living, and ecology. The following conclusions were drawn.

(1) The NSTM is mainly ecological land, which shows a decreasing trend, whereas production and living land show an increasing trend. Land transfer is mainly concentrated between agricultural production land, grassland ecological land, and other ecological lands. The change in production land was mainly influenced by population density (10.05%) and GDP (14.47%), living land was mainly influenced by population density, and ecological land was influenced by annual rainfall (16.33%) and topographic factors (12.07%).

(2) The PLUS model has better applicability in simulating land and spatial changes in the NSTM, with a Kappa coefficient of 0.81, an overall accuracy of 0.88, and an FoM of 0.28. The total future water use in the simulated NSTM increased in all three scenarios, with production water still accounting for the largest share, and production water decreased in the SSP3 scenario with a decrease of 305 million m^3. Domestic water uses: The three scenarios show a slow growth trend. In terms of ecological water use, SSP2 increased the most at 362 million m^3.

Data availability statement

The original contributions presented in the study are included in the article/supplementary material, further inquiries can be directed to the corresponding authors.

Author contributions

The study was conceptualied by GY, XL, and HT. The diagrams were designed and produced by YL and XH. XX, YG, and FL significantly contributed to the analysis and manuscript preparation. XX, PL, BL, and XL performed the analysis. All authors contributed to the article and approved the submitted version.

Funding

This research was supported by the National Natural Science Foundation of China (Grant Number 52269006, U1803244); Xinjiang Production and Construction Corps (Grant Numbers 2021AB021, 2022BC001, 2022DB023); The Third Xinjiang Scientific Expedition Program (Grant No. 2021xjkk0804) and Shihei University (Grant Number CXRC201801, RCK 2018C22).

Conflict of interest

The authors declare that the research was conducted in the absence of any commercial or financial relationships that could be construed as a potential conflict of interest.

The handling editor HL declared shared parent affiliation with author FL at the time of review.

Reviewer ZH declared shared parent affiliation with author FL to the handling editor at the time of review.

Publisher's note

References

Bao, Q., Ding, J., Han, L., Li, J., and Ge, X. (2022). Predicting land change trends and water consumption in typical arid regions using multi-models and multiple perspectives. *Ecol. Indic.* 141, 109110. doi:10.1016/j.ecolind.2022.109110

Bryan, B. A., Gao, L., Ye, Y., Sun, X., Connor, J. D., Crossman, N. D., et al. (2018). China's response to a national land-system sustainability emergency. *Nature* 559 (7713), 193–204. doi:10.1038/s41586-018-0280-2

Chen, X., Chang, C., Bao, A., Wu, S.-x., and Luo, G. (2020). Spatial pattern and characteristics of land cover change in Xinjiang since past40 years of the economic reform and opening up. *Arid. Land Geogr.* 43 (01), 1–11.

Chen, Y., Li, B., Fan, Y., Sun, C., and Fang, G. (2019). Hydrological and water cycle processes of inland river basins in the arid region of Northwest China. *J. Arid Land* 11, 161–179. doi:10.1007/s40333-019-0050-5

Chen, Y., Xu, X., and Wang, S. (2006). Land use/cover change and degradation trend of the ortindag sandy area inInner Mongolia plateau. *Mt. Res.* (01), 60–64.

Cui, X., Ning, X., Wanxu, C., Guanheng, W., Jiale, L., Sipei, P., et al. (2022). Spatio-temporal variation and influencing factors of the coupling coordination degree of production-living-ecological space in China. *Int. J. Environ. Res. Public Health* 19, 10370. doi:10.3390/ijerph19161037019(16)

Deng, Y., and Yang, R. (2021). Influence mechanism of production-living-ecological space changes in the urbaniation process of guangdong province, China. *Land* 10 (12), 1357. doi:10.3390/land10121357

Eaton, W. M., Brasier, K. J., Burbach, M. E., Walt, W., Engle, E. W., Barbara, Q., et al. (2021). A conceptual framework for social, behavioral, and environmental change through stakeholder engagement in water resource management. *Soc. Nat. Resour.* 34 (8). doi:10.1080/08941920.2021.1936717

Fang, C., Gao, Q., hang, X., and Cheng, W. (2019). Spatiotemporal characteristics of the expansion of an urban agglomeration and its effect on the eco-environment: Case study on the northern slope of the Tianshan Mountains. *Sci. China Earth Sci.* 62 (9), 1461–1472. doi:10.1007/s11430-018-9369-x

Fu, X., Wang, X., hou, J., and Ma, J. (2021). Optimiing the production-living-ecological space for reducing the ecosystem services deficit. *Land* 10 (10), 1001. doi:10.3390/land10101001

Halima, I. E., and Hiroaki, S. (2022). A scenario simulation and the prediction of land use and land cover changes in Nigeria. *J. Environ. Inf. Sci.* 2021 (12).

Hou, M., and Braham, W. W. (2021). Land development in an urban megalopolis: A holistic environmental assessment of housing on chongming eco-island, China. *J. Clean. Prod.* 312, 127617. doi:10.1016/j.jclepro.2021.127617

Hu, S., Ma, R., Sun, ., Ge, M., eng, L., Huang, F., et al. (2021). Determination of the optimal ecological water conveyance volume for vegetation restoration in an arid inland river basin, northwestern China. *Sci. Total Environ.* 788, 147775. doi:10.1016/j.scitotenv.2021.147775

Hu, ., Chen, X., hou, Q., Chen, D., and Li, J. (2019). Diso: A rethink of taylor diagram. *Int. J. Climatol.* 39 (5). doi:10.1002/joc.5972

hai, H., Lv, C., Liu, W., Yang, C., Fan, D., Wang, ., et al. (2021). Understanding spatio-temporal patterns of land use/land cover change under urbaniation in wuhan, China, 2000–2019. *Remote Sens.* 13 (16), 3331. doi:10.3390/rs13163331

hang, D., Huang, Q., He, C., and Wu, J. (2017). Impacts of urban expansion on ecosystem services in the beijing-tianjin-hebei urban agglomeration, China: A scenario analysis based on the shared socioeconomic pathways. *Resour. Conservation Recycl.* 125, 115–130. doi:10.1016/j.resconrec.2017.06.003

hao, L., Liu, X., Xu, X., Liu, C., and Chen, K. (2022). Three-dimensional simulation model for synergistically simulating urban horiontal expansion and vertical growth. *Remote Sens.* 14 (6), 1503. doi:10.3390/rs14061503

hao, X., hang, ., Wang, X., uo, L., Liu, B., Yi, L., et al. (2014). Analysis of Chinese cultivated land's spatial-temporal changes and causes inrecent 30 years. *Trans. Chin. Soc. Agric. Eng.* 30 (03), 1–11.

hou, G., Di, ., Qian, ., and Tao, S. (2022). Study on the spatiotemporal evolution characteristics of the "Production–Living–Ecology" space in the Yellow River Basin and its driving factors. *Sustainability* 14 (22), 15227. doi:10.3390/su142215227

Jiang, X., Bingxin, L., Hongyu, ., Qiqi, ., Xiaoya, S., and Haoran, . (2022a). Examining the spatial simulation and land-use reorganisation mechanism of agricultural suburban settlements using a cellular-automata and agent-based model: Six settlements in China. *Land Use Policy* 120, 106304. doi:10.1016/j.landusepol.2022.106304120

Jiang, X., hai, S., Liu, H., Chen, J., hu, Y., and Wang, . (2022b). Multi-scenario simulation of production-living-ecological space and ecological effects based on shared socioeconomic pathways in henghou, China. *Ecol. Indic.* 137, 108750. doi:10.1016/j.ecolind.2022.108750

Lamqadem, A. A., Afrasinei, G. M., and Saber, H. (2019). Analysis of Landsat-derived multitemporal vegetation cover to understand drivers of oasis agroecosystems change. *J. Appl. Remote Sens.* 13 (1), 1. doi:10.1117/1.jrs.13.014517

Li, C., Wu, Y., Gao, B., heng, K., Wu, Y., and Li, C. (2021). Multi-scenario simulation of ecosystem service value for optimiation of land use in the Sichuan-Yunnan ecological barrier, China. *Ecol. Indic.* 132, 108328. doi:10.1016/j.ecolind.2021.108328

Li, J., Chen, Y., and Liu, . (2018). Variations in temperature and precipitation and their influences on surface waterresource in different climate ones of Xinjiang. *J. Univ. Chin. Acad. Sci.* 35 (03), 370–381.

Liang, X., Guan, Q., Clarke, K. C., Liu, S., Wang, B., and Yao, Y. (2021). Understanding the drivers of sustainable land expansion using a patch-generating land use simulation (PLUS) model: A case study in wuhan, China. *Comput. Environ. Urban Syst.* 85, 101569. doi:10.1016/j.compenvurbsys.2020.101569

Lin, J., He, P., Yang, L., He, X., Lu, S., and Liu, D. (2022). Predicting future urban waterlogging-prone areas by coupling the maximum entropy and FLUS model. *Sustain. Cities Soc.* 80, 103812. doi:10.1016/j.scs.2022.103812

Lin, ., and Peng, S. (2022). Comparison of multimodel simulations of land use and land cover change considering integrated constraints - a case study of the Fuxian Lake basin. *Ecol. Indic.* 142, 109254. doi:10.1016/j.ecolind.2022.109254

Liu, C., Xu, Y., Liu, Y., Sun, P., Huang, A., and hou, J. (2018). Research on land use functions classification and evaluation system based onSystem theory. *Acta Sci. Nat. Univ. Pekin.* 54 (01), 181–188.

Liu, J., Liu, Y., and Li, Y. (2017). Classification evaluation and spatial-temporal analysis of "production-living-ecological" spaces in China. *Acta Geogr. Sin.* 72 (07), 1290–1304.

Lu, ., Feng, Q., Xiao, S., Xie, J., ou, S., Yang, Q., et al. (2021). The impacts of the ecological water diversion project on the ecology-hydrology-economy nexus in the lower reaches in an inland river basin. *Resour. Conservation Recycl.* 164, 105154. doi:10.1016/j.resconrec.2020.105154

O'Neill, B. C., Kriegler, E., Ebi, K. L., Kemp-Benedict, E., Riahi, K., Rothman, D. S., et al. (2017). The roads ahead: Narratives for shared socioeconomic pathways describing world futures in the 21st century. *Glob. Environ. Change* 42, 169–180. doi:10.1016/j.gloenvcha.2015.01.004

O'Neill, B. C., Kriegler, E., Riahi, K., Ebi, K. L., Hallegatte, S., Carter, T. R., et al. (2014). A new scenario framework for climate change research: The concept of shared socioeconomic pathways. *Clim. Change* 122 (3), 387–400. doi:10.1007/s10584-013-0905-2

Ouedraogo, I., Mbow, C., Balinga, M., and Neufeldt, H. (2015). Transitions in land use architecture under multiple human driving forces in a semi-arid one. *Land* 4 (3), 560–577. doi:10.3390/land4030560

Philip, A., Simon, B., Ardey, C. S. N., and Mawunyo, D. F. (2023). Land use and land cover change detection and prediction based on CA-Markov chain in the savannah ecological one of Ghana. *Environ. Challenges* 10 (10), 100664. doi:10.1016/j.envc.2022.100664

Pokhrel, Y., Felfelani, F., Satoh, Y., Boulange, J., Burek, P., Gädeke, A., et al. (2021). Global terrestrial water storage and drought severity under climate change. *Nat. Clim. Change* 11 (3), 226–233. doi:10.1038/s41558-020-00972-w

Shi, M., Wu, H., Fan, X., Jia, H., Dong, T., He, P., et al. (2021). Trade-offs and synergies of multiple ecosystem services for different land use scenarios in the yili river valley, China. *Sustainability* 2021 (13), 1577–1580. doi:10.3390/su13031577

Song, S., Liu, ., He, C., and Lu, W. (2020). Evaluating the effects of urban expansion on natural habitat quality by coupling localied shared socioeconomic pathways and the land use scenario dynamics-urban model. *Ecol. Indic.* 112, 106071. doi:10.1016/j.ecolind.2020.106071

Stanley, C., Olang, L. O., and Sitoki, L. (2023). Modelling of land-use/cover change trajectories in a transboundary catchment of the Sio-Malaba-Malakisi Region in East Africa using the CLUE-s model. *Ecol. Model.* 476, 110256. doi:10.1016/j.ecolmodel.2022.110256

Wang, H., Cai, Y., Yang, Q., Gong, Y., and Lv, G. (2019). Factors that alter the relative importance of abiotic and biotic drivers on the fertile island in a desert-oasis ecotone. *Sci. Total Environ.* 697, 134096. doi:10.1016/j.scitotenv.2019.134096

Wang, H., Liu, Y., Cai, L., Fan, D., Wang, Y., and Yao, Y. (2021). Regional differentiation in the ecological effects of land cover change in China. *Land Degrad. Dev.* 33 (2), 346–357. doi:10.1002/ldr.4156

Wang, J., Chen, Y., Wang, W., Qi, Y., He, T., and Wu, R. (2017a). Classification system and spatio-temporal distribution of ecological land in Chinain the period of 1996-2012. *Geogr. Res.* 36 (03), 453–470.

Wang, N., Yang, X., hang, W., Chenand a, A. (2020a). The relationship between area variation of the Aral Sea in the arid Central Asiaand human activities and climate change. *J. Glaciol. Geocryol.* 42 (02), 681–692.

Wang, Q., and Wang, H. (2022). Dynamic simulation and conflict identification analysis of production-living-ecological space in wuhan, central China. *Integr. Environ. Assess. Manag.* 18, 1578–1596. doi:10.1002/ieam.4574

Wang, T., and Sun, F. (2022). Global gridded GDP data set consistent with the shared socioeconomic pathways. *Sci. Data* 9 (1), 221. doi:10.1038/s41597-022-01300-x

Wang, Y. (2022). Spatial–temporal evolution of “production-living-ecologica” function and layout optimiation strategy in China: A case study of liaoning province, China. *Environ. Sci. Pollut. Res. Int.* 30, 10683–10696. doi:10.1007/s11356-022-22899-9

Wang, Y., hou, H., Wu, B., and Li, Y. (2017b). Ecological achievement of Xinjiang production and construction Corps and ItsProblems and countermeasures. *Bull. Chin. Acad. Sci.* 32 (01), 55–63.

Wang, ., Chen, X., hang, X., Fan, W., Li, W., and ong, R. (2020b). Discussion of the future development of field drip irrigation in China. *Agric. Res. Arid Areas* 38 (04), 1–9.

Xiang, L., Jingying, F., Dong, J., Gang, L., and Chenglong, C. (2022). Land use optimiation in Ningbo City with a coupled GA and PLUS model. *J. Clean. Prod.* 375, 134004. doi:10.1016/j.jclepro.2022.134004

Xu, Y., Lu, F., hou, Y., Ruan, B., Dai, Y., and Wang, K. (2022). Dryness–wetness encounter probabilities’ analysis for lake ecological water replenishment considering non-stationarity effects. *Front. Environ. Sci.* 10. doi:10.3389/fenvs.2022.806794

Yuan, ., hou, L., Sun, D., and Hu, F. (2022). Impacts of urban expansion on the loss and fragmentation of cropland in the major grain production areas of China. *Land* 11 (1), 130. doi:10.3390/land11010130

Frontiers in
Environmental Science

Explores the anthropogenic impact on our natural world

An innovative journal that advances knowledge of the natural world and its intersections with human society. It supports the formulation of policies that lead to a more inhabitable and sustainable world.

Discover the latest Research Topics

See more →

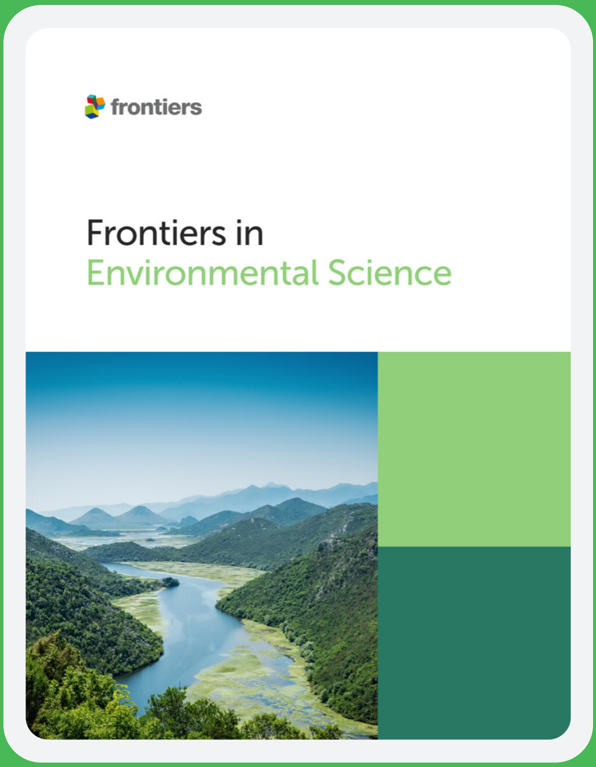

frontiers

Frontiers in
Environmental Science

Frontiers

Avenue du Tribunal-Fédéral 34
1005 Lausanne, Switzerland
frontiersin.org

Contact us

+41 (0)21 510 17 00
frontiersin.org/about/contact

frontiers | Research Topics